THE UNIVERSITY
of EDINBURGH

NUMERICAL STUDY OF MICROFLUIDIC EFFECTS AND RED BLOOD CELL DYNAMICS IN "DETERMINISTIC LATERAL DISPLACEMENT" GEOMETRIES

ROHAN VERNEKAR

THE UNIVERSITY
of EDINBURGH

School of Engineering

This thesis is submitted for the degree of

Doctor of Philosophy

27 May 2019

SUPERVISORS:
Dr. Timm Krüger (University of Edinburgh, UK)

LOCATION:
Edinburgh, Scotland, UK

LAY SUMMARY

Experience of flow phenomena in our daily lives, such as when taking a shower, or making a coffee, has given us an intuitive feel for the behaviour of liquids. Still, markedly different flow behaviour that humans do not generally experience manifests when liquids flow through extremely tiny channels or pores. Channels smaller than the width of the human hair can be manufactured to carry the these liquids. Due to their extremely small size, these channels prove advantageous for handling and manipulating similarly tiny objects, such as cells or DNA. Such channels are called micro-channels, and the science of studying the flow behaviour in these channels is termed as 'microfluidics'.

This thesis deals with one such microfluidic tool, called the 'deterministic lateral displacement' (DLD) device, which was invented for the separation of different types of cells or DNA. Since its advent, the DLD technique has seen a great number of applications aimed at enrichment or separation of different blood cells. Blood cell isolation processes play important roles in many biological operations, e. g. in disease diagnostic tests. The thesis presents an investigation of the DLD technique with the help of computer simulations of red blood cells (RBCs) suspended in water flowing through DLD microchannel devices.

The detailed investigation includes looking at the subtle flow effects, and studying the individual and collective behaviour of RBCs, when flowing through the DLD device. The investigations have come up with a number of design recommendations for improving the DLD technique. Further, the research has pushed forward ideas that could lead to diagnostic tests on the RBCs using this device. The research has also identified some inherent operational limitations when using the DLD technique. The results in this thesis would help improve cell separation tasks in the DLD microfluidic device.

DECLARATION

I declare that this thesis was composed by myself, that the work contained herein is my own except where explicitly stated otherwise in the text, and that this work has not been submitted for any other degree or professional qualification.

Rohan Vernekar
27 May 2019
Edinburgh, Scotland, UK

ABSTRACT

The last two decades have seen microfluidics gaining increasing interest from the fields of medical diagnostics and bio-chemical processes, due to its immense potential for point-of-care diagnostic applications. Since blood plays a crucial role in many physiological and diagnostic processes, red blood cells (RBCs) have been the focus of a large volume of microfluidics research. The isolation of red blood cells and other blood components, based on the manifest morphological characteristics, is required in many applications, e. g. flow cytometry. The deterministic lateral displacement (DLD) is one such popular microfluidic technique that has shown great promise toward cellular separations.

The DLD technique separates particles based on their hydrodynamic size. It has been demonstrated for size-based separations down to unprecedented size resolutions of ~10 nm. The DLD consists of a large number of obstacle pillars placed in a microfluidic channel. The layout of these obstacles is such that the obstacle array presents a fixed angle to the average fluid flow through the microfluidic channel. Size-based separation comes about due to steric interaction of particles with the pillars. Particles larger than a 'critical' size are forced to move along the obstacle array incline. The larger particles, following the array incline, are displaced perpendicular to the average flow direction, and are said to be on the displacement mode. Particles smaller than this critical size flow along the average fluid flow direction, zigzagging around the obstacles. The trajectories followed by these smaller particles are classified as zigzag mode. Micro-particles therefore follow different trajectory modes based on their size, eventually leading to their spatial separation. The particles are separated passively, i. e. other than the pressure drop needed to drive the fluid flow through the DLD micro-channel, there is no need for any external forces for particle sorting.

Numerous studies since the advent of the DLD have focussed on widening the scope of applications covered by the technique. In this thesis, I take a more physical approach, focussing on understanding the microhydrodynamics and RBC dynamics within the DLD geometries. For these investigations, I have used an in-house numerical solver that incorporates ingredients for fluid flow solution, RBC membrane deformation, and an explicit coupling algorithm between the two. The lattice Boltzmann method is used for obtaining a fluid flow solution at low Reynolds numbers, and the finite element method is used for computing the membrane energetics. The immersed boundary method explicitly couples these two solutions with non-matching boundaries, at each time step.

Firstly, I investigate subtle flow hydrodynamic effects through DLD obstacle arrays. Here, fluid-only simulations uncover and map anisotropic flow permeability of the obstacle arrays. The research reveals that if the unit cell of

the obstacle array geometrically forms a parallelogram, the array induces an anisotropic pressure gradient normal to the average flow direction. Contrarily, if the obstacle arrangement reflects a rotated square in its unit cell, anisotropy is entirely absent. Such anisotropic pressure conditions in the DLD cause local flow deviations and can lead to unintended particle motion arising from locally varying critical separation size. I find that elevated levels of such anisotropy are also brought about by pillar shape design and asymmetric array gaps. Furthermore, strategies to minimise anisotropic flow effects are proposed.

The research on deformable RBC flow through the DLD tackles both single and collective cell dynamics in these arrays. Single cell dynamics is studied for special, non-cylindrical obstacle pillar shapes. In addition to the particle-obstacle steric contact, dynamic RBC motion leads to effects that influence cell trajectories in the DLD. Such effects are strongly tied to the interplay between RBC deformability, dynamic motion (such as tumbling and tank-treading) and the flow-field generated by the pillar shape. In certain cases, wall-induced hydrodynamic cell migration becomes significant enough such that the deformed tank-treading RBC undergoes displacement mode without steric contact with the pillars. Here, migration velocity experienced by the cells interacting with special pillar shapes causes a reversal of the phase-bifurcation trend. The uncovering of this mechanism, opens the door for research on novel DLD pillar designs that exploit wall-induced soft particle migration.

Lastly, the research turns to collective RBC dynamics at high volume fractions, in standard DLD arrays with cylindrical pillars. Here, I research the effect of increasing cell volume fraction on the displacement and zigzag modes, with the help of appropriate statistical measures. I find that the displacement mode suffers a breakdown at higher volume fractions, while the zigzag mode remains robust. This has important implications for cell separation applications in the DLD, where smaller particles (e. g. platelets) need to be separated from a dense background of RBCs and *vice versa*.

The investigations undertaken in this thesis identify subtle hydrodynamic and particle effects in DLD arrays that explain previously unresolved particle behaviour. This research should help improve the design and fabrication of DLD devices, especially those targeted at improved separation and manipulation of deformable RBCs.

Dedicated to my loving parents,
Kunda and Ranganath Vernekar.

ACKNOWLEDGMENTS

Foremost, I would like to thank my parents for their love and understanding over the last four years of my PhD life. The final hurdle of writing this thesis would not have been possible without your constant support.

I am also deeply grateful to my PhD supervisor Dr. Timm Kruğer for the opportunity start my PhD, constant guidance, valuable insights, and above all for instilling scientific rigour into my research work. I would also like to thank my second supervisor Dr. Prashant Valluri for his constant encouragement, guidance and support. Furthermore, I would like to thank Dr. David Inglis and Dr. Kerwin Zeming for their insight, help and opportunity for experimental collaboration.

Special thanks to my thesis examiners Dr. Stewart Smith and Prof. Chaouqi Misbah for their valuable time and detailed critique of my thesis, which has significantly helped improve this work, and given me a few ideas for the future.

Also, I would like to thank the other PhD students in Timm's group; Charles, Arunn, Yunzhou, Greg for the discussions over coffee, help, herbal/magic-powder teas, gym lessons, (i could go on...) etc. And all colleagues at the research institute who were constant sources of encouragement during the writing period of my PhD. My friends from India; Priyamrit, Bagu, Prashant, Partha, Alekh and Dipankar — thank you for your continued friendship despite being far away.

University research is only part of a PhD students story — friends and colleagues at the University have made Edinburgh a home away from home for me. I would like to thank my flatmates Davide and Chiara (P) for making the flat a home (albeit an Italian one!) and cooking for me during the writing period (and also my older flatmate, James!). The neighbours cat, Gollum, with his idiosyncratic and incessant demands for petting, however, gets no thanks.

Just as importantly, I would like to thank my buddies-in-arms from Edinburgh; James, Patrick, Ares, Sofia, Charithea, Alessio, Robson, Nelly, Arunn, Chiara (DS), Eva, Agus, James and all the rest of the gang at the University for all the fun times in the last four years. Thank you for being there through the good, the bad and the hungover! These years have flown by because of you and sincere apologies to those whom I have forgotten to mention by name. Thank you for making me feel welcome!

Rohan Vernekar
Edinburgh, Scotland, UK
27 May 2019

PREFACE

This thesis is the culmination of my four years of PhD studies at the *University of Edinburgh*. My PhD project was aimed at studying cell separation in microfluidic geometries, particularly a technique called the 'deterministic lateral displacement' (DLD). The study focussed on numerical simulations of fluid flow through DLD geometries, with a special focus on suspended red blood cell (RBC) dynamics. A majority of these numerical studies are aligned with experimental investigations of the DLD by researchers at other institutes. Coming from a background of pure numerical research, this has indeed been an exciting opportunity.

My PhD studies have spanned multiple 'sub-projects', the ideas for some of which were seeded during stimulating *Skype* calls with experimental investigators. Others have come about from engaging discussions with my PhD supervisor, Dr. Timm Krüger. Of course, not all of these projects have ended up being successful, yet even these dead-ends have had an important influence on my subsequent research and academic outlook. This thesis contains only those successful projects where the results are either published or at a mature stage. In writing this thesis, I have tried my best to present a comprehensive yet readable story of the last four years of my PhD research on the DLD, and the RBCs. Since this thesis is one of only a handful so far to use 3D computer simulations to look at microfluidic particle separations, effort has been made here to provide sufficient details on the numerical approaches used.

HOW TO READ THIS THESIS

This thesis is divided into four parts, each with modular, semi-independent chapters. Part I (INTRODUCTION) has the general motivation for this thesis in chapter 1, the introduction to microfluidic RBC dynamics in chapter 2 and a comprehensive review of the DLD technique in chapter 3. Part II (METHODS) presents the mathematical model in chapter 4, as well as details on the numerical solvers for fluid flow, RBC deformation and their (fluid-solid) coupling algorithm in chapters 5, 6 and 7, respectively. Part III (RESEARCH) contains my research results. Chapter 8 investigates microfluidic anisotropy and its consequences, chapter 9 examines RBC dynamics and migration in the DLD, and chapter 10 studies increased suspension concentration effect in the DLD. Part IV (CONCLUSIONS AND OUTLOOK), with chapters 11 and 12 surmises and culminates this thesis.

All the chapters have been kept as self-contained as possible, and can be read independently. Moreover, current 'gaps in literature' addressed by this work are highlighted in section 3.5, chapter 3. Additionally, the chapter 4 sets the bounds on the physics that is numerically modelled in this work. In gen-

eral, no set sequence need be followed in reading this thesis, and an expert on microfluidics, RBC dynamics and numerical simulations could directly jump to the results presented in Part III. This thesis could be useful for researchers coming from multiple backgrounds; e. g. those investigating RBC dynamic or experimental microfluidics or numerical flow problems. Some critical pathways for reading this thesis, keeping in mind the research background for these three cases, are:

RBC DYNAMICS: Chapters 3, 4, and 8–10.

EXPERIMENTAL MICROFLUIDICS: Chapters 2, 4, and 8–10 (if needed 5–7).

NUMERICAL SIMULATIONS: Chapters 2, 3, and 8–10.

These suggestions are made merely to reduce the reading effort, but I do hope that most of you would prefer to read this thesis from cover to cover. Whichever route you do choose, I hope you enjoy reading this thesis as much as I have enjoyed (mostly. . .) writing it.

Rohan Vernekar
27 May 2019

PUBLICATIONS

Parts of this work have appeared previously in the following publications:

R. Vernekar and T. Krüger (2015). 'Breakdown of deterministic lateral displacement efficiency for non-dilute suspensions: A numerical study'. In: *Medical Engineering & Physics* 37.9, pp. 845–854

R. Vernekar, T. Krüger et al. (2017). 'Anisotropic permeability in deterministic lateral displacement arrays'. In: *Lab on a Chip* 17.19, pp. 3318–3330

CONTENTS

Part I

INTRODUCTION

'Broken symmetry' is one of those fundamental ideas that physicists like but profoundly irritates engineers because it seems to take a simple idea and make it sound mysterious . . .

— Sturm, Cox, Comella and Austin (2014)

1 MICROFLUIDICS FOR DISEASE DIAGNOSTICS

Microfluidics is the branch of fluid dynamics dealing with flow in channels that are tens of micrometres wide. The engineering emerging from microfluidics (and its sister field *nanofluidics*) has seen successful miniaturisation of multiple processes across diverse fields such as bio-assays, chemical synthesis, drug development, single molecule manipulation etc. The advancement of microfluidics has the potential to bring about the next revolution in technology, within our lifetimes. This chapter looks at some of the reasons for studying such flow physics at the micrometre scale, especially cell separation microfluidics.

nanofluidics
Similar to microfluidics, but where the length scales are of the order of 10 *to* 100*'s of nanometres*

Here, I try and convey the broader motives for microfluidics research, focusing on its potential for *point-of-care* (POC) diagnostic devices for disease detection. In particular, the chapter looks at conventional blood tests for disease diagnosis. Taking malaria as an example, I look at how microfluidic technologies could help deliver healthcare in regions without access to conventional medical facilities. This thesis presents research on one particular microfluidic technique termed 'deterministic lateral displacement' (DLD), with focus on the manipulation and dynamics of red blood cells (RBCs) in this device. This chapter aims to present the overall motivation for this thesis, with detailed introduction to RBC dynamics and the DLD device given in upcoming chapters 2 and 3, respectively.

point-of-care
A phrase indicating the location of the patient, outside the hospital, where the medical attention is needed

In section 1.1 of this chapter, we take a look at the current state of disease diagnostics and the malaria *pandemic*. In section 1.2, I go over the field of microfluidics and its inherent adaptability for POC diagnostic devices. I then examine microfluidic techniques for cellular separations/manipulations in section 1.3. The final section 1.4 sets the substance of this thesis in the broader context.

pandemic
Referring to a disease that is prevalent over the whole country or the world

1.1 DISEASE DIAGNOSTICS

Most (if not all) of us have had the experience of having to visit the doctor in order to check one's state of health by getting our bodily fluids (e. g. urine, blood, saliva etc.) tested. Amongst such diagnostic tests, taking blood samples for testing is common and important. A blood sample provides a large amount of information about the physiological and biochemical state of an individuals health (Ryan, 2015). Details on the body's mineral content, organ function, blood glucose and cholesterol levels etc., as well as identification of external pathogens and diseases, and the effectiveness of medication can be gauged from blood tests. For example, diagnosis, treatment and management of diseases like malaria, hepatitis or diabetes relies on accurately measuring or identifying the bio-chemical parameter of interest (the malarial

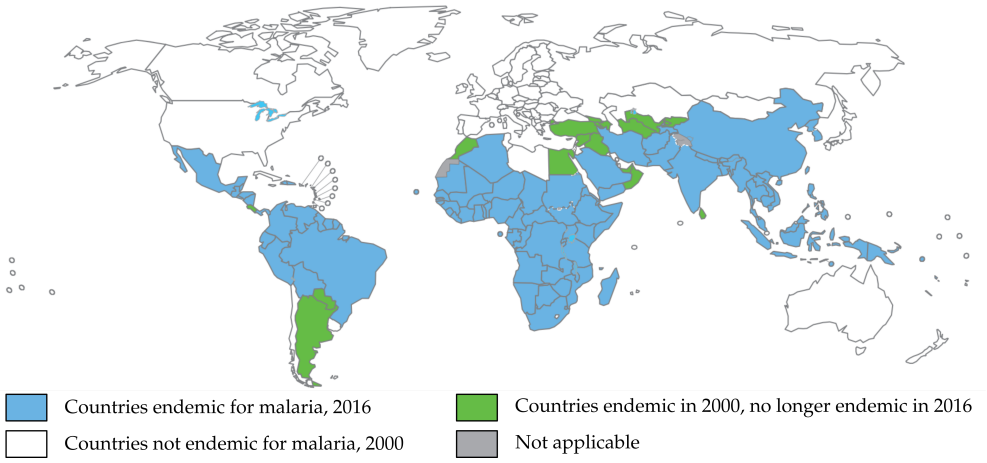

Figure 1.1: Map of the world with the countries where malaria is considered endemic as of 2016 coloured in blue. Note, that the map is not to scale. Sourced from World Health Organization (2017a) report (©CC BY-NC-SA).

parasites, hepatitis viruses, blood glucose levels, respectively) from a blood sample.

The traditional, well-established methods for testing blood or other body fluids involve taking a large blood sample (millilitres in volume) and sending it off to a centralised laboratory. Large sized equipment such as clinical centrifuges, optical microscopes etc. are used to process and examine blood samples in pathology labs, by trained clinicians. The results are then processed and returned to the clinic, and thence to the patient. In many economically poor countries, such centralised labs, with the necessary expensive equipment, are inaccessible to large sections of the populace (Yager et al., 2006). Even if sufficient investment is made in setting up such laboratories, and in training the necessary personnel to run them, we encounter issues of lack of basic support infrastructure, (e. g. uninterrupted electricity supply) in order to operationalise them. Such infrastructure is unreliable or simply absent in many parts of the developing world. This scenario denies basic healthcare to a large portion of the world's population. Bringing affordable basic healthcare to the world's poorest populations is one of the greatest global challenges currently facing world leaders as well as researchers.

1.1.1 *Malaria as an example...*

In developing countries, a large number of deaths occur from treatable infectious diseases simply because large sections of the population do not have access to basic healthcare and diagnostic facilities (Yager et al., 2006). As an example, World Health Organization (2017b) (WHO) estimates that 445,000 worldwide deaths occurred due to malaria in the year 2016 (and 446,000 estimated deaths in the year 2015). This, despite the fact that malarial treatment, in its modern form, has been known since the 1820's (Oliveira and Szczerbowski, 2009). Figure 1.1 shows the countries where malaria was considered

endemic by WHO, as of 2016. There are four parasite species that cause malaria in humans; *Plasmodium vivax, Plasmodium ovale, Plasmodium malariae, and Plasmodium falciparum*. Of these four, *P. vivax and P. falciparum* are dominant, estimated to have caused 216 million cases of malaria across 91 countries in 2016, with falciparum malaria proving to be the deadliest (World Health Organization, 2017b).

endemic
Refers to a disease or condition regularly found in a specific population set or a geographical location

The traditional method of blood stain observations under an optical microscope is still the 'gold standard' for diagnosis of malaria in most countries (Makler, Palmer and Ager, 1998; Patankar et al., 2018). In recent years, disposable POC rapid diagnostic test (RDT) kits for identifying *P. falciparum* infections, have been successfully deployed in the developing world, especially in Africa. These RDTs use *immunochromatographic* strips (ICS) that detect specific *antigens* present in the blood due to the malarial infection and can identify the disease within 15-30 minutes. Thus, the need for expensive and time consuming laboratory testing is overcome. The RDTs are also easy to read, the results mostly being presented in a 'yes or no' format, and therefore can be easily used by semi-skilled healthcare workers.

immunochromatographic assays
simple paper-based devices that are used for rapid diagnosis, that work on the presence of selective antigen affinity

antigen
A molecule that induces an immune response in the body

However, challenges still remain, especially with regards to false positives/negatives in hyper-endemic regions as well as rising drug resistance (Patankar et al., 2018). Such small portable diagnostic kits show the way forward for POC healthcare devices, highlighting their benefit in the economically poor regions of the world. It is in this context of the potential of POC medical devices, that we shall take a look at another nascent but exciting field; that of microfluidics for the manipulation of cells or other bio-particles.

1.2 MICROFLUIDIC DEVICES

Microfluidics is the study of flow phenomena at the scale of tens of microns (micrometres) (Squires and Quake, 2005). Microfluidic devices have channels and features from 1 to 100's of microns in size, and carry fluid volume flow rates in the range of 10^{-18} to 10^{-8} m^3/s. The flow physics at such small scales is markedly different from what we are used to in our everyday observations. Microfluidic devices take advantage of their most obvious attribute — their small size — and the fact that at such small scales, the fluid flow remains *laminar*. Microfluidic flow is dominated by viscous effects in the fluid, and can be in the *Stokes flow* regime. Therefore, microfluidic devices can exploit these small scales and flow characteristics for a range of applications, out of reach for the large sized devices (Beebe, Mensing and Walker, 2002; Stone, Stroock and Ajdari, 2004). Examples of processes that have been successfully miniaturised with microfluidic devices are cellular/molecular separation, chemical treatment and synthesis, reaction kinetics, micro-droplet generation and encapsulation etc. Figure 1.2 shows a few examples of microfluidic applications.

laminar flow
Flow phenomenon where the viscous dissipation due to internal fluid friction dominates flow inertia, and the flow can be visualised as distinct flow laminae

Stokes flow
Flow regime determined by the Stokes equation, which entirely ignores all inertial flow effects

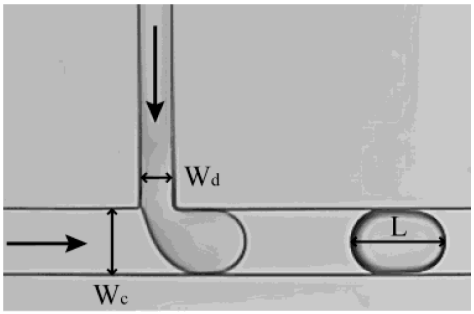

(a) Droplet generation: T-junction

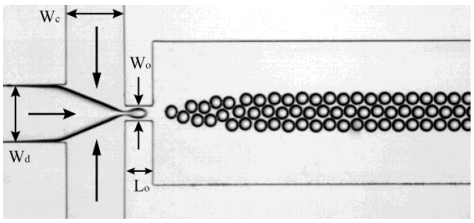

(b) Droplet generation: Flow focussing

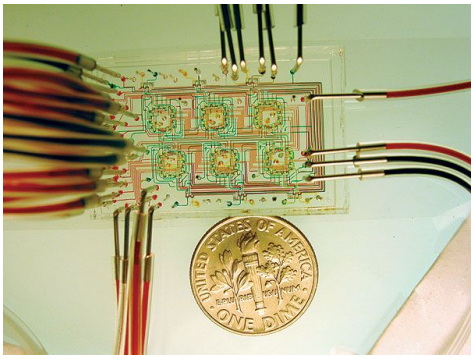

(c) Microchemostat

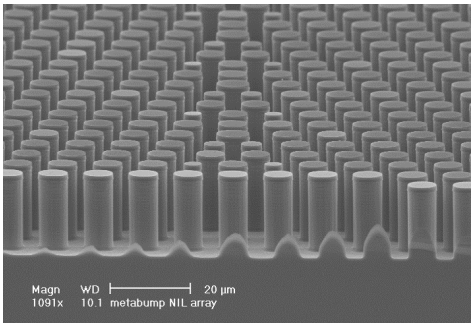

(d) DLD micro-pillar array

Figure 1.2: Examples of a few microfluidic applications. Generation of monodisperse droplets using (a) T-junction geometry and (b) flow focusing geometry. The dimensions in (a) are $W_d = 50\mu m$; $W_c = 100\mu m$, and in (b) are $W_d = W_c = 200\mu m$; $W_o = 50\mu m$. The microscopic images in (a) and (b) are sourced from a review by Gu, Duits and Mugele (2011) (©CC BY). (c) A microfluidic 'chemostat' device, with its connecting channels traced out by coloured dye, used for studying microbial population growth. The image is reproduced with permission from (Balagaddé et al., 2005) (©AAAS). (d) A scanning electron microscopic (SEM) image of a section of a deterministic lateral displacement (DLD) device. The cylindrical pillar array structure is used for separating particles or cells based on size. The SEM image was kindly provided by ©Keith Morton.

1.2.1 *Origin of microfluidics*

The remote origins of microfluidics are to be found in the chemical and biological micro-analytical methods developed to manipulate small fluid volumes. Whitesides (2006) pinpoints four 'parents' that originally nurtured and funded the now adolescent field of microfluidics; namely, molecular analysis, bio-defence, molecular biology and microelectronics. Many early microfluidic devices used glass and silicon, similar to their microelectronics cousins. The pace of development and application of microfluidics technology has accelerated dramatically post the switch to poly(dimethylsiloxane) (PDMS) and other engineering polymers (McDonald et al., 2000). Most of these developments are in the field of biology (Beebe, Mensing and Walker, 2002), with applications from testing of new drugs to disease diagnostics. For the inter-

ested reader, the reviews by Whitesides (2006) and Yager et al. (2006) on the development of microfluidics, and its potential role in public healthcare are recommended.

1.2.2 *Microfluidic point-of-care diagnostics*

As seen from the example of malaria in section 1.1.1, POC disease diagnostics techniques are already having an impact on the ground. Microfluidics shares many of the advantages that makes these ICS techniques attractive for POC diagnostics. Similar to ICS, microfluidic methods use small sample fluid volumes, the devices are inexpensive to fabricate, and can be made (fully or partly) disposable. More importantly, microfluidic chips are small enough to fit in the palm of one's hand making them highly portable. This means that they can be easily adapted into *lab-on-chip* (LOC) diagnostic systems (Stone, Stroock and Ajdari, 2004). Such LOC diagnostic devices would still remain small and portable. In this sense, LOC microfluidics would be more powerful than the current ICS RDTs used for malaria. In fact, such chips could also integrate antigen affinity testing techniques as as part of its diagnostic functionalities.

lab-on-chip
A phrase referring to a miniaturised device that integrates multiple sequential/parallel processes and diagnostic steps, currently carried out in a conventional laboratory

Such LOC devices could theoretically take all diagnostic testing out from the centralised laboratories to the patients bedside. In the future, continuous monitoring of health of patients could become possible with the help of microfluidics. Currently, microfluidic devices are yet to realise their full potential for POC disease diagnostics due to several reasons (Whitesides, 2006). Many of these issues are slowly but surely being ironed out (Moschou and Tserepi, 2017), though this has meant that microfluidic techniques are yet to see their full commercial exploitation (Wyatt Shields IV, Ohiri et al., 2017). If costs are kept low, realisation of such technologies can bring about the next revolution in global healthcare. It goes without saying that for this to happen, continued theoretical and experimental research, as well as microfluidic product development is imperative.

1.3 MICROFLUIDIC CELL SEPARATIONS

Selective separation of cells and bio-particles is an important step in many diagnostic processes. Cellular separation based on morphological differences, such as size, deformability etc. could itself be used as a diagnostic test. In fact, the RDTs for diagnosis of *P. falciparum* infection discussed earlier (in section 1.1.1) rely on immunoaffinity based separation of target bio-molecules through capillary driven flow chromatography (Hage, 1999). Since microfluidic (or nanofluidic) channels can be fabricated down to the scale of the target cells (or molecules), microfluidic devices possess a much greater potential for targeted cell separations or manipulations. Unsurprisingly therefore, microfluidics literature is littered with multiple types of techniques for separating cells or bio-particles by exploiting a variety of physical effects and forces (Salafi, Kwek Zeming and Zhang, 2017; Wyatt Shields IV, Reyes and

Figure 1.3: Cover page from the journal "Lab on a Chip", a leading journal of microfluidic technologies. The image illustrates bi-modal separation of two types of cells using a modified microfluidic dielectrophoresis (DEP) device. The article describing the details of the microfluidic device is referenced in the cover image. Reproduced with permission from 'Front cover' (2018) (©RSC).

López, 2015). Microfluidic particle separation devices are generally classified based on the nature of the force employed for sorting particles.

Separation methods are also categorised based on whether or not pre-treatment of target cells (in order to 'label' them) is needed. The labelling process uses external agents such as fluorescent dyes, *immunomagnetic* beads etc., that selectively mark cells of interest. On the other hand, label-free separation techniques are those that do not use any external labels for the target cells, instead relying on the intrinsic deviations in cell properties (Carey et al., 2018). Here, differences in cell size, shape, electrical impedance, deformability etc. could be exploited for achieving microfluidic separation. Clearly, for diagnostic POC applications we would prefer to have label-free sorting device and avoid the additional overhead of cell labelling.

immunomagnetic
Magnetic beads which can attach to specific receptor antigens on the surface of the target cells

These label-free techniques can be further subdivided into those that require an external physical force field and those that simply rely on flow hydrodynamics for separation. Dielectrophoresis (DEP), magnetoelectrophoresis (MEP), optical trapping, surface acoustic waves (SAW) etc., are some of the non-hydrodynamic force field techniques used for cell separation. Here, the strength and direction of the external force can be used for actively directing

particles into required outlets. The illustration in figure 1.3 shows separation of two cell species, in two different outlets, with the help of DEP.

1.3.1 *Hydrodynamic label-free microfluidics*

When no external forces or cell labelling is present, a microfluidic device has to rely on the forces imposed by the fluid flow, in order to separate particles (Liu and Hu, 2017). In such devices, clever microfluidic geometries are employed to bring out subtle hydrodynamic effects. Such pure hydrodynamic label-free sorting methods are better suited to maintain cellular viability, an important point for diagnostic tests. Some examples of such devices are the deterministic lateral displacement (DLD), inertial focussing (IF) hydrodynamic filtration (HF) etc. The DLD technique can be seen as a generalisation of the HF method. Generally speaking, the IF method has a higher throughput, while the DLD has higher resolution for particle separation.

Deterministic lateral displacement, RBCs and disease diagnosis

The DLD consists of microscopic obstacles, that pattern the fluid flow to separate particles based on size. Figure 1.2d shows a scanning electron microscope (SEM) image of a section of a DLD micro-pillar array. The microfluidic DLD device is generally operated in the Stokes flow regime, and flow rates do not have an influence on particle separation. The DLD principle has been deployed at all scales (nano, micro and macro) for particle separation. We shall learn more about the DLD principle, as well as its applications in chapter 3.

The first DLD device was demonstrated for the separation of DNA and micro-beads, with an unprecedented size-resolution of 10nm (Huang et al., 2004). Since its invention, the DLD has proved to be popular for applications involving fractionation of blood. It has been adopted for de-bulking of RBCs from whole blood as a preprocessing step for on-chip cytometric applications. Thus, RBC dynamics in the DLD is an important research topic. It has practical applications towards RBC separation for disease diagnostic purposes. The rich dynamics displayed by RBCs in shear flows, such as those found the DLD microfluidic devices, are introduced in chapter 2. Engineering the DLD technique for detection of diseases, by taking advantage of differences in such flow dynamics between healthy and infected RBCs, remains an open challenge.

1.4 RELEVANCE OF THIS THESIS

Microfluidic technologies are poised to emerge as the next big disruption in technology. Similar to the impact of electronic communication on the postal system, these devices could potentially have the same effect on conventional laboratory systems. It is hoped that microfluidic POC diagnostic devices would bring about a positive transformation in global healthcare delivery

systems. Significant difference is likely to be felt in cases where a large percentage of the worlds population simply misses out due to the lack of timely disease diagnosis, even though treatment is available and inexpensive. The mortality statistics provided for malaria in section 1.1.1 are a case in point.

This thesis hopes to be a small yet meaningful part in this global effort. The thesis explores subtle flow effects in the DLD with and without particles. These effects have a telling impact on the separation of particles and cells, as well as the overall device effectiveness. The numerical investigations cover particle-free hydrodynamic effects, as well as deformable RBC dynamics in the DLD. There is significant interest in the microfluidic processing of blood, and already there are a number of DLD devices that have been designed to process blood cells for various applications.

DLD designs that take advantage of the changes in RBC deformability for cell separation are presented. As RBC deformability changes drastically in diseases such as malaria, sickle cell anaemia etc., this work is targeted towards microfluidic disease diagnostics. In general, this thesis is aimed towards better DLD design for particle separation. Active collaboration with experimental investigators, wherever possible, was sought for the realisation of the DLD designs. The detailed breakdown of individual problems addressed by this thesis are given at the end of the introduction (part i, chapter 3) to this thesis.

2

RED BLOOD CELL DYNAMICS

This chapter introduces the reader to the rich world of red blood cell (RBC) dynamics in flow. RBCs are the most numerous cells in the human body and, as mentioned in chapter 1, of paramount importance in clinical diagnostics. In essence, an RBC is a fluid-filled bag enclosed by a 2D *closed membrane*. The RBC membrane possesses both elastic as well as fluid-like properties. RBCs are seen to display a wide range of shapes and dynamic behaviours, both collectively as well as individually, under varying hydrodynamic and physiological conditions. A healthy RBC generally has a characteristic biconcave shape under physiological equilibrium conditions.

closed membrane
Membrane made up of a 2D surface that is compact and without boundary

Since this work deals with the ex-*vivo* flow of RBCs in the deterministic lateral displacement (DLD) microfluidic device, we focus on single RBC dynamics relevant to such flows. This chapter is geared towards helping the reader understand the bio-mechanical basis for the mathematical model for RBC deformation (in chapter 4) employed in this thesis and the research results involving RBCs (in chapters 9 and 10). However, this chapter is intentionally kept brief so as not to unnecessarily extend the length of this thesis. Still, the chapter provides sufficient references relevant to the shape and dynamics of RBCs in microfluidics.

The chapter is divided into three major sections. The first section 2.1 is a short introduction on the shape and biological structure of the RBCs. The second section 2.2 outlines the non-equilibrium shapes and the dynamics of RBCs in shear flows. The third section 2.3 talks about the hydrodynamic cross streamline migration experienced by RBCs in flows typical of microvasculature and microfluidic devices. A short concluding summary of the most important takeaways from this chapter is provided in section 2.4.

2.1 SIZE, SHAPE AND BIOLOGY

Red blood cells (RBCs) (or erythrocytes) are the most abundant cell type in the human body and the main components of the circulatory system. RBCs develop from *pluripotential hematopoietic stem cells* (Narla, 2015). Their development into mature red blood cells takes place mainly in the bone marrow and partially in peripheral blood. During the last stages of this evolution, the cells (specifically termed *reticulocytes*) lose all of their internal organelles, such as mitochondria, nucleus etc. This leaves the mature RBC with merely an outer membrane that surrounds an inner cellular fluid called the *cytosol*. The average lifespan of a mature RBC in the blood stream is around 120 days, before their removal in the spleen. Incredibly, 10^{11}–10^{12} new RBCs are produced each day by the human body (Higgs, Roy and Hay, 2015)!

pluripotent
Referring to the cells ability to differentiate into other cell types

hematopoietic stem cell
Primitive cell that can develop into other types of blood cells, such as RBCs, platelets etc.

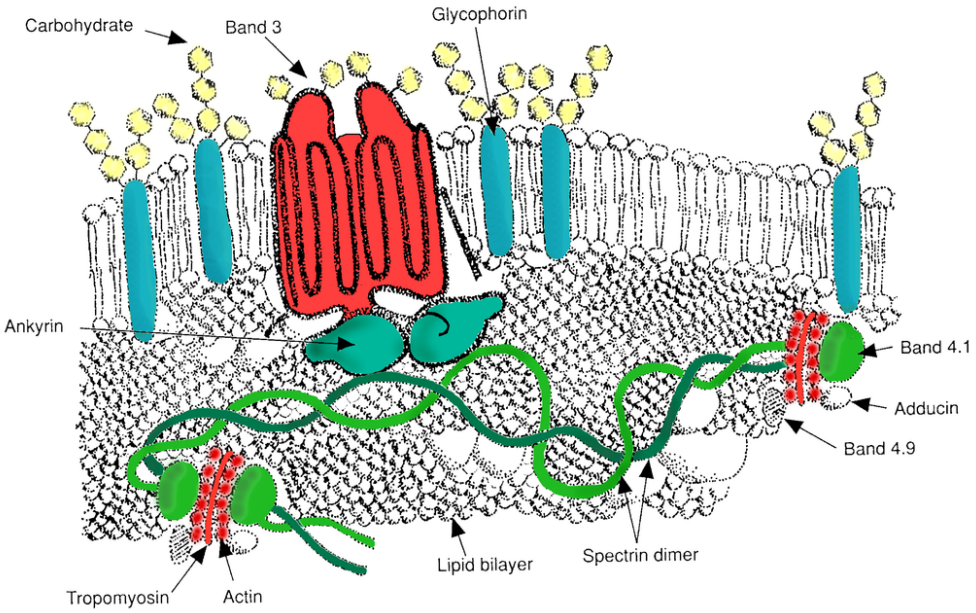

Figure 2.1: Illustration of a nano-meter scale section of the red blood cell (RBC) membrane (by Hempelmann (2009); PUBLIC DOMAIN). The bilayer arrangement of the lipid molecules with the hydrophilic 'head' groups lying on the outside, is seen in black and white. Most types of membrane proteins are also seen, with some highlighted in colour. Some of the proteins such as *Ankyrin, Tropomyosin, Actin, Spectrin* etc. are integral constituents of the cytoskeleton. The cross-linked Spectrin dimer (shown in green) can store elastic energy and gives the membrane its resistance to shear loading. Other proteins such as *Band 3*, anchor the cytoskeletal proteins in the lipid bilayer as well as perform transport function across the membrane.

2.1.1 *Biological composition*

amphipathic *Molecule having both water repulsing (hydrophobic) and water attracting (hydrophilic) parts*

phospholipid *Class of lipids (organic molecules soluble in non-polar solvents) that are a major constituent of all cell membranes, and generally consists of two hydrophobic fatty acid "tails" and a hydrophilic "head" consisting of a phosphate group*

Biologically speaking, the RBC structure is relatively simple; made of an outer deformable membrane that completely surrounds an inner cellular fluid. The enclosing RBC membrane is made up of two coupled parts; an outer self assembled *amphipathic* (predominantly *phospholipid*) 'bilayer' and an inner elastic scaffold of polymerised proteins that supports the outer bilayer, called the *cytoskeleton*. An artistic representation of a typical nano-scale section of the RBC membrane is shown in figure 2.1. As the name suggests, the bilayer is composed of two (uni-molecular) layers or "leaflets" of (mostly) lipid molecules, with their hydrophobic ends (or 'tails') pointing inwards. The lipid bilayer is in fluid phase, behaving like an incompressible 2D fluid. Therefore the bilayer cannot support any shear stresses and is effectively incompressible. Hence, the total surface area of the RBC membrane remains strongly conserved.

The lipid bilayer anchors an inner interlinked protein scaffold made up of multiple types of proteins (Yawata, 2003), some of which are highlighted in colour in figure 2.1. This inner cytoskeleton has elastic properties and therefore can bear shear stresses. Furthermore, the cytoskeleton and the outer

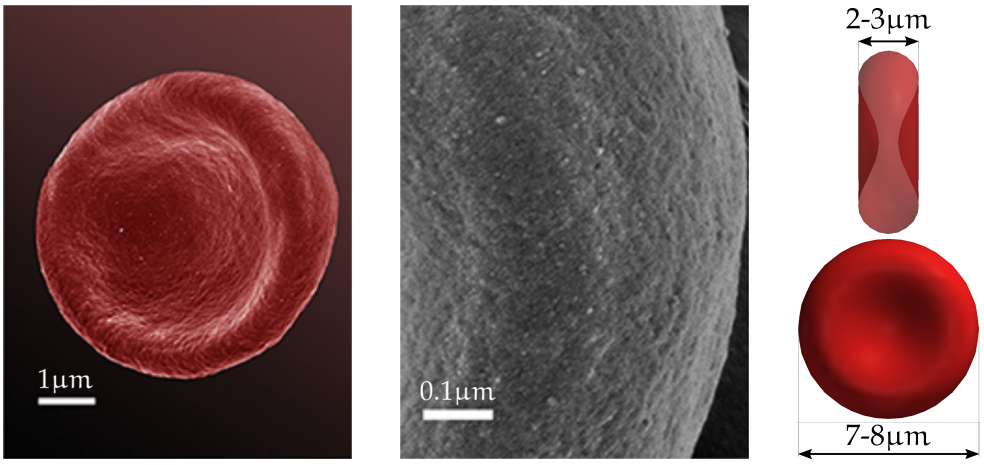

(a) RBC SEM image (b) Zoomed-in RBC rim (c) Dimensions

Figure 2.2: The human red blood cell image and dimensions. (a) A scanning electron microscope (SEM) (false colour) image of a healthy human red blood cell (RBC) and (b) Zoomed-in SEM image of the rim of a RBC, showing the globular structure (from (Bester et al., 2013); CC BY). (c) Sketch showing the diameter and thickness ranges for a healthy RBC.

bilayer can both withstand bending loads. However, bending resistance of the outer bilayer is much greater compared to that of the cytoskeleton, and dominates (Gompper and Schick, 2008). The bending resistance of the bilayer mainly comes from two comparable contributions; the (local as well as non-local) difference in the type, and the number of lipid molecules in the two leaflets of the bilayer. In addition to the lipid bilayer, and the cytoskeletal proteins, the RBC membrane also hosts multiple types of 'transport' proteins that serve mainly bio-chemical functions (Yawata, 2003). A few of these are also highlighted in colour in figure 2.1.

haemoglobin
Large molecule made up of proteins and iron, with 4 binding sites for oxygen molecules

The characteristic red colour of the RBC is given by a molecule called *haemoglobin* dissolved in the cytosol. In fact, the cytosol can primarily be considered to be an aqueous solution of haemoglobin. Cytosolic haemoglobin makes it possible for the RBCs to transport oxygen from the lungs to other organs. The haemoglobin molecule also binds to carbon dioxide given out by the tissues, and releases it in the lungs. The cytosolic fluid viscosity is mainly decided by the concentration of dissolved haemoglobin in it (Narla, 2015). Under normal physiological conditions for the RBCs, the intra-cellular fluid viscosity is approximately 5 times that for the suspending plasma.

2.1.2 *Shape, size and structure*

A mature RBC without any external stresses displays a discoid biconcave shape under physiological conditions. The biconcave shape is seen vividly from a scanning electron microscope (SEM) image in figure 2.2a. The large diameter of the RBC disk lies between 7-8µm (Narla, 2015) and the cell thickness ranges between 2-3µm (Kim, Kim and Park, 2012) as shown in figure 2.2c.

The RBCs also show a variety of other equilibrium shapes, which are induced by physiological changes such as concentration gradients in the cellular environment (Gompper and Schick, 2008). The biconcave and other equilibrium shapes of the RBC results from a minimisation of the bending energy of the bilayer and the elastic energy stored in the cytoskeleton, subject to fixed cell volume and membrane surface area (Lim, Wortis and Mukhopadhyay, 2002). We shall not go further into these shapes here, since such physiological mechanisms are absent in our microfluidic system.

Moreover, the RBC membrane surface area is $\approx 140\mu m^2$ and the enclosed volume is $\approx 90fL$. Therefore, the RBC membrane has nearly 43% 'excess area' compared to that of a membrane enclosing a sphere of similar volume. This excess area, the lack of internal structures and the nature of the membrane makes the RBCs highly deformable. RBCs deform by redistributing the internal volume while conserving their membrane area. This high deformability is vital for the cells to pass through extremely narrow ($3\mu m$ diameter) capillaries in the body for transporting oxygen.

Though highly deformable, the RBC membrane has been shown to possess a 'memory' of its equilibrium biconcave shape (Fischer, 2004). This shape memory means that when deforming external stresses are absent, an elemental portion of the deformed RBC membrane, which was originally located on the membrane rim, will return to the rim. Similarly an elemental portion originally on the central dimple, returns to the dimple. That is, RBC membrane elements have preferred positions relative to the axis of rotational symmetry for the biconcave shape. The shape memory has been attributed to a non-spherical stress free shape for the RBC membrane. This aspect is still a matter of debate and ongoing research (Viallat and Abkarian, 2014).

The degree of bio-mechanical description of the RBC provided here is sufficient to gain an understanding of our RBC model described in chapter 4. For further reading one is referred to detailed descriptions of the red cell biology by Narla (2015) and Yawata (2003).

2.2 RBC DYNAMICS UNDER SHEAR

RBCs have to traverse through micro-capillaries which are as small as $3\mu m$ and cross endothelial slits narrower than $1\mu m$ (Narla, 2015). Thus, their high deformability is a necessary requirement for the healthy functioning of the blood circulatory system. This inherent RBC deformability produces a rich variety of shapes and dynamic motions in shearing flows. Two rather well established RBC dynamic motions in planar linear shear flow are illustrated in figure 2.3. These two classic RBC dynamic modes under simple shear were identified in the 1970s by Fischer, Stöhr-Lissen and Schmid-Schonbein (1978) and Goldsmith, Marlow and MacIntosh (1972). These dynamic modes are termed as 'tumbling' (or 'flipping') and 'tank-treading', and are optically observed in experiments by attaching micro-beads to a small portion of the RBC membrane.

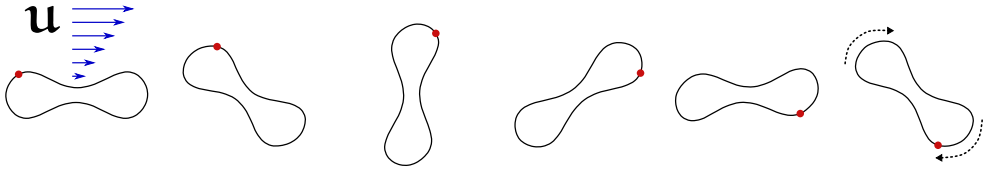

(a) RBC 'tumbling' motion

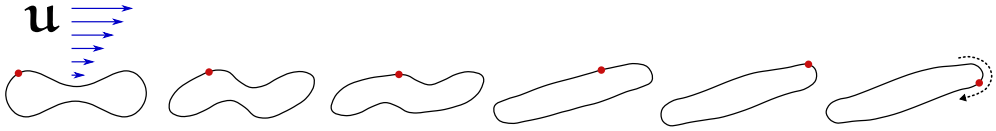

(b) RBC 'tank-treading' motion

Figure 2.3: Illustration of (a) 'tumbling' and (b) 'tank-treading' dynamics of a red blood cell (RBC) in linear shear flow. The RBC membrane is shown as a black outline and the relative deformation of the membrane can be gauged from the attached red coloured bead. (a) In tumbling, the red bead remains in approximately the same relative position on the membrane, indicating an absence of large shearing membrane deformation. Here, the cell rotates about its centre, with its axis of rotational symmetry in the shear plane. (b) In tank-treading, the cell deforms into an ellipsoid-like shape, presenting a fixed inclination to the flow. In this case, the bead revolves about the inner fluid, indicating a membrane shearing. The membrane dynamics appears like the motion of the tread of a tank.

In RBC 'tumbling', the cells axis of rotational symmetry flips (or rotates) through 360° in the shear plane as shown in figure 2.3a. The membrane does not deform significantly in tumbling and relative positions of the membrane elements remain (roughly) the same. At higher shear rates, the RBC membrane deforms and takes up an ellipsoid-like shape, presenting a steady orientation to the shear flow, as seen in figure 2.3b. Here, the RBC membrane displays a 'tank-treading' motion (like the tread of a tank), in which the membrane elements revolve around the inner cellular fluid with a given angular velocity. A wheel-like 'rolling' RBC motion (not illustrated) has also been observed at certain intermediate shear rates (Bitbol, 1986; Goldsmith, Marlow and MacIntosh, 1972).

An early mathematical attempt at describing RBC dynamics in simple linear shear flow was made by Keller and Skalak (1982) (KS theory). They approximate RBCs as fluid-filled ellipsoidal vesicles and obtain the transition from tumbling to tank-treading behaviour. The transition is found to depend on the ratio of the inner to outer fluid viscosities as well as the particles shape parameters. The KS theory has proven very influential in understanding RBC dynamics, even though the simplified KS model fails to identify other dynamic modes nor predict the dependence of the tumbling to tank-treading transition on flow shear rate.

In recent years, with the advent of microfluidic techniques, a much more complete picture of the dynamics of RBCs and vesicles in simple linear shear flow has emerged (Abkarian, Faivre and Viallat, 2007; Dupire, Socol and

Viallat, 2012; Kantsler and Steinberg, 2006). The detailed experimental observations by Dupire, Socol and Viallat show a rich complexity of the RBC dynamic modes in simple shear flow. The RBCs undergo tumbling, rolling, spinning, swinging and tank-treading dynamics at different shear rates and viscosity contrasts. Modified KS theories, incorporating elastic contribution from the RBC membrane cytoskeleton, have shown greater success in explaining these intermediate dynamical motions (Abkarian, Faivre and Viallat, 2007; Skotheim and Secomb, 2007). These results expose the importance of accounting for RBC membrane shear elasticity to capture their dynamics.

In quadratic (*Poiseuille*) flows, in addition to their complex dynamics, the RBCs also display a number of characteristic shapes and clustering phenomenon (McWhirter, Noguchi and Gompper, 2009). Such non-linear shear flow conditions are always present in blood micro-circulation and also in pressure-pump driven microfluidics. Amongst others, the two well known characteristic shapes in Poiseuille flow are the asymmetric 'slipper' and the symmetric 'parachute' shape. The appearance of an asymmetric stable shape such as the slipper, in parabolic flow, is indeed surprising. Kaoui, Biros and Misbah (2009) answer the question "why..?" the shape is stable, though a comprehensive understanding of the phenomenon leading to the slipper shape is still lacking (Kaoui, Biros and Misbah, 2009). The emergence of these RBC shapes, (e. g. parachute, slipper etc.) is influenced by the curvature of the velocity-field, the excess area of the membrane as well as confinement by bounding walls (Fedosov, Peltomäki and Gompper, 2014; Noguchi and Gompper, 2005). A recent study suggests that the emergence of these shapes could also depend on the initial conditions (Guckenberger et al., 2018).

In conclusion, the shape and dynamics of the RBCs in shearing flows show a remarkable complexity and richness. These shapes and dynamics have been shown to be governed by three major factors (Viallat and Abkarian, 2014):

- The in-plane membrane properties such as cytoskeletal elasticity, the lipid bilayer viscosity, strong area conservation and bending resistance.
- The viscosity contrast of the cytosol with the outer suspending fluid.
- The large excess surface area of the RBC membrane relative to the enclosed volume, and its shape memory.

2.3 HYDRODYNAMIC 'LIFT'

As briefly mentioned in the previous chapter 1, a neutrally buoyant solid spherical particle in the Stokes flow cannot migrate transverse to the flow direction, without an external push. This classic result follows from the mathematical form of the Stokes equation, which possesses fore-aft symmetry for flow around symmetric bodies, thus ruling out lateral particle migrations (Leal, 2007). However, RBCs are highly deformable and can break this symmetry by undergoing asymmetric shape changes under shear. Hence, RBCs can experience lateral-to-flow 'lift' even in the Stokes flow regime. In fact, such flow

physics is crucial for healthy blood circulation in human vasculature. In arterioles and capillaries, where Stokes flow prevails, a wall induced repulsive migration causes the RBCs to move away from the capillary walls. This creates a cell free layer close to the vessel walls, which reduces the overall flow resistance in such vessels (Fåhræus and Lindqvist, 1931). This cell free layer has been the subject of much research over the last century.

Olla has carried out an analytical evaluation of this wall induced cross streamline migration velocity experienced by tank-treading particle in shear flow (Olla, 1997; Olla, 2000). Like Keller and Skalak before, he approximates the tank-treading RBC by an ellipsoidal particle at a large distance y away from a stationary wall. The lateral migration velocity u_m due to wall induced 'lift'[1] is found to scale as $u_m \sim \dot{\gamma} R^3/y^2$, where $\dot{\gamma}$ is the flow shear rate and R the ellipsoidal length scale (or effective radius). Recent experiments with lipid vesicles, carried out in microgravity by Callens et al. (2008), agree well with the analytical scaling predicted by Olla.

Though the shape and dynamic behaviour has been greatly simplified in Olla's analysis, the study gives good insight into the lateral migration of a tank-treading deformable RBC in shear flow. However, Olla study does not address the dynamical behaviour of a cell very close to the wall. Theoretical scaling analysis of such dynamic *unbinding* of a neutrally buoyant vesicle from a wall was carried out by Cantat and Misbah (1999) and Seifert (1999), employing the *lubrication approximation*. The scaling results suggest that there is a critical shear rate for cell detachment from a binding substrate (such as a vessel wall) in linear shear flow, and find that the migration velocity experienced post unbinding scales similarly to the analytical results of Olla. Recent numerical simulations carried by Meßlinger et al. (2009) for a neutrally buoyant vesicle close to the wall also agree well with the $1/y^2$ decay of the lateral migration velocity.

unbinding
When a particle can break free from an attractive potential adhering it to the wall

lubrication approximation
Scaling the Stokes equation in a geometry where one dimension is significantly smaller than the others in order to reduce mathematical complexity

Yet, later experimental results of Abkarian, Lartigue and Viallat (2002), obtained for a negatively buoyant tank-treading vesicle, show significant deviations. Here, the 'lift' force experienced by a non-neutrally buoyant vesicle is found to scale as $\sim \eta g(1-\nu)\frac{\dot{\gamma} R^3}{y}$, where $g(1-\nu)$ is a dimensionless function of the reduced volume ν, and η is the outer fluid viscosity. Since RBCs possess much greater complexity of shape and structure than vesicles, their behaviour is likely to show an even greater variation. As far as I know, single RBC unbinding from a stationary wall and subsequent cross streamline migration remains to be studied.

In addition to wall induced migration, shear gradients in flow (e. g. in Poiseuille flow) are also known to cause vesicle migrations towards regions of low shear (Danker, Vlahovska and Misbah, 2009; Kaoui, Ristow et al., 2008). In microfluidic devices and in human vasculature, the bounding walls are always present and the flow features will exhibit shear gradients. This scenario has an added layer of complexity since in non-constant shear regimes the RBCs can assume asymmetric shapes as seen previously in section 2.2. In a

1 In this chapter, 'lift' is used to indicate cross streamline repulsive migration of a deformable cell, and does not mean that there is a net force acting on the cell.

recent microfluidic experiment, Coupier et al. demonstrate that lateral migration velocity decays as $u_m \sim 1/y$ (Coupier et al., 2008). The velocity enhancement compared to the constant shear case is attributed to compounding of flow non-linearity and wall repulsion effects. Such wall and shear gradient induced 'lift' effects have been successfully exploited in microfluidic devices for separation of cells based on their size and deformability (Geislinger, Eggart et al., 2012; Geislinger and Franke, 2013).

2.4 SUMMARY

In this chapter I have briefly reviewed the rich shapes and dynamics exhibited by RBCs in shear flows. The main factors determining RBC dynamics are the viscoelastic properties of its membrane, the energy dissipation by the cytosolic fluid and the excess membrane area relative to the enclosed volume. RBC dynamics and shapes have a significant influence on overall blood flow in microcirculation as well as in microfluidic applications. Furthermore, RBCs experience 'lift' and undergo lateral-to-flow cross streamline migration in Stokes flow regime, when deformed by shear flow. It is important to note that when the cells deform and 'tank-tread', the classical results of Stokes flow around an ellipsoidal rigid body do not apply, and the migration experienced by a cell close to a wall can become significant. These cross streamline migration mechanisms are responsible for the formation of the cell free layer in blood capillary networks. The application of such wall induced 'lift' for the separation of soft bio-particles based on their size and deformability has already been demonstrated successfully (Geislinger and Franke, 2014).

The understanding of RBC deformation, dynamics and wall induced cross streamline migration presented here is important for our deterministic lateral displacement application results presented in chapters 9 and 10, in this thesis. With the advent of microfluidic devices, the study of the RBC dynamics has seen a revival, and the current state of the art can be found in recent reviews by Viallat and Abkarian (2014) and Vlahovska, Podgorski and Misbah (2009).

3

DETERMINISTIC LATERAL DISPLACEMENT

In chapter 1, we have seen the applications and potential of microfluidics for bio-particle separation, such as sorting of blood cells or DNA molecules. The reader was introduced to the deterministic lateral displacement (DLD) technique, the subject matter of this thesis. In this chapter, we take a detailed look at the DLD. DLD is a microfluidic technique designed to separate particles based on their size, with nanometre scale resolutions. It relies solely on flow hydrodynamics and symmetry-breaking steric interactions between the particles and the device geometry. This makes the technique attractive for *label-free*, *passive* cell sorting. Since its advent, the DLD has proven to be very popular in the field of bio-particle separations. This is mainly due to the high separation resolution and reliability of the DLD.

label-free
No external 'labels', such as fluorescence dye, are required, and particles are differentiated based on inherent properties such as size etc.

passive operation
Particle sorting relies on forces generated due to flow hydrodynamics within the device and external 'active' force manipulation is absent

Like many famous discoveries, the DLD technique was uncovered as the result of an accident. This chapter aims to tell the story of the DLD, such that the reader becomes familiar with the separation physics, the important application milestones, and the challenges involved. Here, I have cited most of the DLD literature. However, this chapter is not a DLD literature review. Also, details about device fabrication, bio-particle treatment and general device setup and operation are not included here. Such additional details and an extensive list of DLD applications can be read from McGrath, Jimenez and Bridle (2014), a recent (tutorial) review. For a reader familiar with the DLD, this chapter brings out the main challenges and open questions from a physical point of view, and briefly presents the research outcomes.

We first take a short look at the rather interesting story of invention in section 3.1. Then, we examine DLD operation physics in section 3.2, and the various DLD parameters affecting separation in section 3.3. In section 3.4, we cover the broad application range for the technique. In the final section 3.5, we provide a synopsis of the open questions, which are dealt with in this thesis.

3.1 STORY OF INVENTION

The deterministic lateral displacement (DLD) microfluidic technique, with more than 20 distinct[1] application spin-offs till date, was discovered by accident (Sturm et al., 2014). The first DLD separation device was developed at Princeton University by Huang, Cox, Austin and Sturm (Huang et al., 2004). For its time, the separation characteristics demonstrated in this new microfluidic device were truly remarkable. Since then, the DLD has proven

1 A conservative estimate based on counting the number of papers published that demonstrate DLD separations for different cell/particle types, as distinct applications.

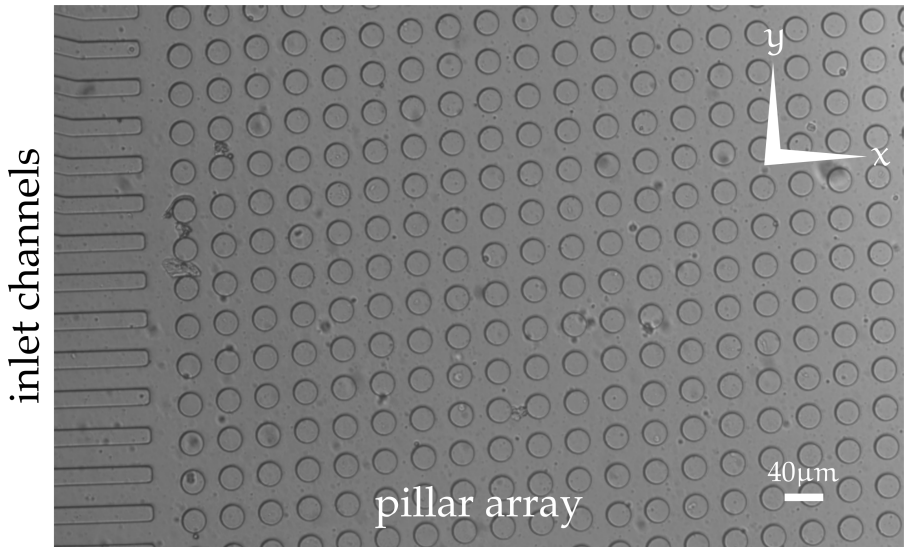

Figure 3.1: Microscopic image of an example DLD device. Multiple inlet channels, guiding fluid and suspended particles into the device (from left to right), are seen on the left. The obstacle array, with cylindrical micro-pillars is to occupy the rest of the image. Here, the obstacle array parameters (see figure 3.4) are: pillar diameter $D = 12\mu m$, the array gap $G = 28\mu m$, array pitch $\lambda = 40\mu m$ in both x and y directions and the lateral row shift $\Delta\lambda = 3\mu m$. The inclination of the array to the flow-wise x direction is clearly discerned from the image. Image taken at Helen Bridle's lab, *Heriot-Watt University*, Edinburgh.

to be extremely influential in the field of microfluidic bio-particle separations (Carey et al., 2018; Wyatt Shields IV, Ohiri et al., 2017; Yan et al., 2016).

The group had been working on separation of DNA molecules in microfluidic diffusion ratchets, exploring asymmetric DNA diffusion modes (Duke and Austin, 1998). For these diffusion ratchets to work, fluid flow needed to be correctly aligned with an array of asymmetric obstacles, which meant precise control of boundary conditions at the inlet and outlet of the device. However, due to a few blocked inlet channels, Richard Huang had the flow moving at an angle to the obstacle array on an average, in one of his devices. Contrary to expectations, this error seemed to enhance flow separation rather than diminish it (Sturm et al., 2014)! As a result of this misaligned fluid flow 'accident', the DLD was born (Huang et al., 2004). The top view of a typical DLD device is shown in figure 3.1.

In the DLD, the flow inclination to the obstacle array (see figure 3.1) creates an asymmetry in the forces experienced by particles when interacting with array obstacles. Particles experience an additional non-hydrodynamic 'push' lateral to the average flow direction. For particles larger than a certain critical size, this lateral push results in trajectories that are laterally displaced with respected to the average flow direction. Particles below this critical size are not laterally displaced, making size-based particle separation possible. 'Large' and 'small' particle separation is illustrated in figure 3.2 and the physics explained in detail in the next section 3.2. The role of particle diffusion is com-

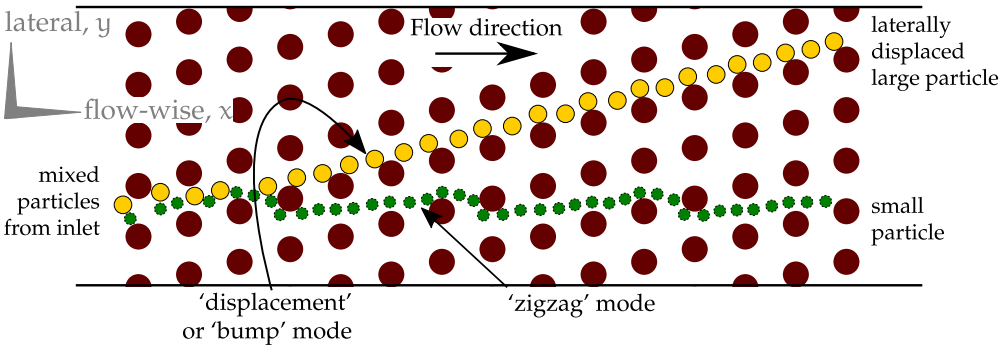

Figure 3.2: Illustration for size-based particle separation in the DLD device. The obstacle pillars are circular in cross section (dark red). The flow is from left to right, along the x axis. Two differently sized particles are let in through the same array lateral gap. The smaller particle (dark green) 'zig-zags' around obstacles, and flows along the average flow direction. The larger particle (light yellow) gets laterally displaced (along $+y$ direction) when interacting with an obstacle pillar, and follows the array inclination. Particles get separated and can be collected at different lateral (y) positions.

pletely absent in this mechanism. In fact, separation is enhanced at higher *Péclet numbers* (Pe). When $Pe \gg 1$, the paths followed by the particles are deterministic, without any Brownian stochastic noise. This gives the device an unprecedented size-resolution and selectivity. Hence the name; *deterministic lateral displacement* or 'DLD' for short.

Péclet number
The ratio of characteristic time for diffusion to that for convection, over a given length

3.2 DLD OPERATION PHYSICS

A typical DLD device consists of an array of micro-meter scale obstacles in a microfluidic channel. A microscopic image of a DLD with cylindrical pillar obstacles is shown in figure 3.1. The DLD 'works' by creating an asymmetric bifurcation pattern of fluid flowing through the gaps between these obstacles, as shown in figure 3.3. This flow bifurcation pattern results from the inclination of the obstacle array to the average fluid flow direction. Size-based particle separation is achieved by having the 'larger' particle cross the bifurcating stagnation streamlines, after interacting with the pillars and flowing through the gaps. In the following, we have a look at the DLD geometry, the underlying flow pattern and then the particle-pillar interaction, in order to understand this simple DLD principle.

We refer to figure 3.4 for the following discussion. Consider a DLD device with an array of circular obstacle pillars, each having diameter D. The obstacle pillar array has a pitch (or pillar centre-to-centre distance) of λ, in both the flow-wise (x) as well as the lateral-to-flow (y) directions. Thus, the gap between obstacles is given by $G = \lambda - D$, in both the x and y directions. In order to break the flow symmetry and create flow bifurcations, each downstream row of obstacles is shifted by a certain distance $\Delta\lambda$, in the y direction. Thus, the obstacle array makes an inclination of $\alpha = \tan^{-1}\frac{\Delta\lambda}{\lambda}$ to the average

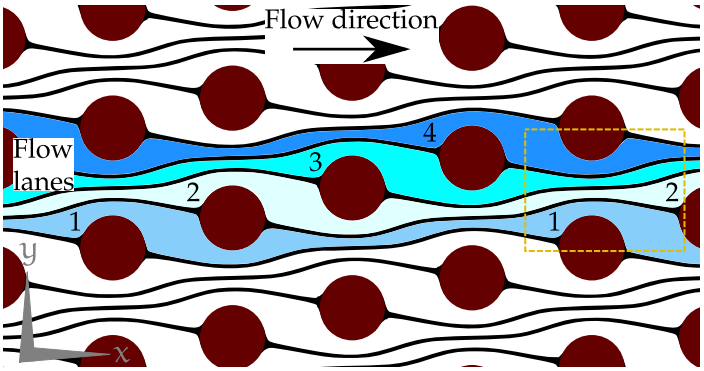

Figure 3.3: Illustration for flow division through a DLD obstacle array. The image shows stagnation (or dividing) streamlines (curved lines, black) obtained using a particle-free 2D simulation. These stagnation streamlines divide the flow into distinct flow-lanes. The number of these flow-lanes through a lateral array gap depends on the array inclination to the flow direction. The rectangular box (dashed line, yellow) marks one such array gap. In our simulation we obtain 4 distinct flow-lanes through each gap. The flow-lanes through the marked gap are numbered 1–4, and coloured (various shades, blue). Due to the periodicity of the array, notice that the 4 lanes cycle though, and return to their original configuration after crossing 4 obstacle rows. The labels 1–4 for each flow-lane are placed next to the array gap at which the lane appears as the 'first' in terms of the lateral y position. Therefore, each lane flows adjacent to a pillar, becoming the 'first' flow-lane through an array gap, every 4 rows.

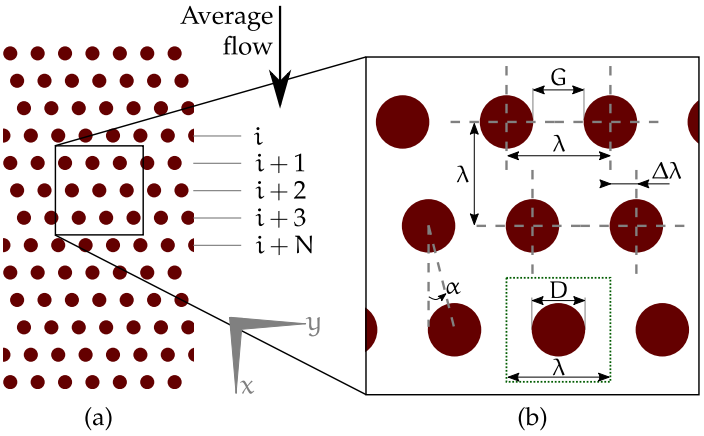

Figure 3.4: Diagram showing geometric details for an example DLD obstacle array. The flow is from top to bottom, along x axis. The left panel (a) shows an array with a flow-wise periodicity of $N = 4$. This means that obstacles in every i^{th} row of the array (in the x direction) have the same lateral arrangement (y positions) as those in the $(i+N)^{th}$ row. The right panel (b) shows a zoomed-in region of the obstacle array. All important DLD parameters such as the array pitch (or pillar centre-to-centre distance) λ, the array gap G, the obstacle pillar diameter D and the row shift $\Delta\lambda$ are indicated. In this example, since $N = 4$, the row shift fraction (RSF) is $\varepsilon = \lambda/\Delta\lambda = 1/N = 0.25$. The array inclination is computed as $\alpha = \tan^{-1}(\varepsilon) \approx 14.04°$.

flow direction (x axis), as seen in figure 3.4b. The ratio, $\Delta\lambda/\lambda$, that sets the array inclination to flow is known as the row shift fraction (RSF) ε. Clearly, the inverse of this ratio $1/\varepsilon = \lambda/\Delta\lambda$, tells us the number of rows after which the obstacles would repeat their lateral (y positional) arrangement. Therefore, the inverse of RSF gives the flow-wise array periodicity $N = 1/\varepsilon$. Periodicity N is usually selected to be an integer value in order to avoid effects which we shall talk about in section 3.2.2.

In our example arrays in figures 3.3 and 3.4, we have chosen an array periodicity of $N = 4$. Therefore, the array inclination is $\alpha = \tan^{-1} = 1/4 \approx 14.04°$. Due to this inclination, the flow through each array gap is forced to bifurcate, with the major flow fraction flowing over, while the rest flowing under the upcoming downstream pillar. The bifurcation can be identified by a 'stagnation' streamline that originates from the downstream pillars, and passes through the respective upstream gaps, as seen in figure 3.3. Now, such bifurcations occur through all array gaps, leading to a large number of distinct flow lanes being formed (see figure 3.3). If the array period N is an integer value, the number of distinct flow lanes equals N. In figure 3.3, $N = 4$, and hence four distinct flow lanes pass through each array gap. Here, the flow periodicity matches that of the array. This regular flow patter is independent of the flow-rate or fluid velocity in the Stokes flow regime, wherein most of the DLD devices are operated (McGrath, Jimenez and Bridle, 2014).

We now introduce simple spherical particles in this laminar flow pattern, as shown in figure 3.5. In the Stokes flow regime, a sufficiently small (relative to flow features) particle is expected to simply follow flow streamlines, and therefore remain within its flow-lane. All Flow-lanes assume the lowest lateral position through array gaps every N rows, and flow adjacent to a pillar, due to array periodicity (see figure 3.3). For a given array gap, we call this the 'first' lane, shown in figure 3.5a. Hence, in the DLD, a particle would have to interact with a pillar every N rows, regardless of its starting flow-lane.

The particle-pillar contact adds extra non-hydrodynamic force terms to the motion of the particle, thus breaking the symmetry and reversibility of Stokes flow. The consequence of this particle-pillar interaction on the particle trajectory is decided by the relative particle size. As illustrated in figure 3.5b, if the particle radius is sufficiently small, the particle mass-centre remains within its flow lane during the particle-pillar contact, and the particle flows under the downstream pillar. In this 'small' particle case, the particle always remains in its starting flow-lane. This trajectory mode for the small particle is termed as the 'zigzag' mode since the particle appears to zig-zag through obstacles, while flowing downstream through the microfluidic channel (see figure 3.2).

However, if the particle is large enough, its mass-centre will not remain in its starting flow lane as it flows past a pillar. The particle-pillar contact 'bumps' the particle into the adjacent flow lane due to the volume exclusion effect, as seen in figure 3.5b. This process repeats at every downstream gap for the 'large' particle. As a result, the particle follows a trajectory set by the array inclination to flow. This trajectory mode for the 'large' particle is termed as the 'bump' or 'displacement' mode. Here, the particle is laterally displaced

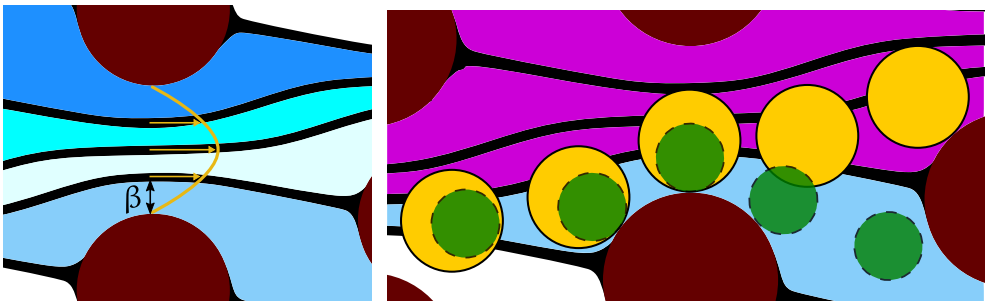

(a) 'First' flow-lane (b) Particle-pillar interaction

Figure 3.5: Sketch illustrating flow division though an array gap and the size-dependent outcome for a particle traversing the gap. In the left panel (a), flow-lanes flowing through a representative DLD array gap (previously marked in figure 3.3) are illustrated. For the gap shown, the foremost flow-lane in terms of increasing lateral y position, flowing adjacent to the pillar, is termed the 'first' flow-lane. The width β of this flow-lane at the narrowest section of the gap is shown. β can be estimated by assuming an equal volume flux between all flow-lanes and a parabolic velocity profile through the gap. The right panel (b) shows the idealised outcome for differently sized spherical particles, flowing through the aforementioned gap, after interacting with the DLD pillar. The flow-lanes are now coloured as per the flow bifurcation over the downstream pillar; with the 'first' flow-lane (lighter, blue) flowing under, and the remaining three flow-lanes (darker, magenta) flowing over the downstream pillar. Both particles start out in the 'first' flow-lane and collide with the pillar after flowing towards the gap. This pillar interaction imposes an additional non-hydrodynamic (volume exclusion) force on both the particles, leading to their lateral (y-directional) motion. Due to its radius being larger than β, the larger particle (lighter, yellow) is 'bumped' into the adjacent flow-lane (darker, magenta) by the pillar. However, the smaller particle (darker, green) manages to keep its mass centre within the 'first' flow-lane (lighter, blue), despite the pillar push. After every pillar interaction, the smaller particle remains within its flow-lane while the larger particle switches into a flow-lane flowing above the downstream pillar. This asymmetry in particle-pillar interaction leads to size-based particle separation (see figure 3.2).

by a distance equal to the row shift $\Delta\lambda$, after travelling a distance of λ in the flow-wise (x) direction. This simple principle was shown to achieve size-based bi-modal separation between 'large' and 'small' spherical polystyrene micro-beads, with an unprecedented size resolution of 10 nm (in micro-meter sized array gaps) (Huang et al., 2004).

3.2.1 *Critical separation size*

In the DLD, the size at which the particle transitions from the zigzag to the displacement mode is called as the 'critical' particle/separation size d_c^p for the device. Naturally, predicting this critical separation size is crucial for DLD applications. From figure 3.5a, it should be apparent that the width of the

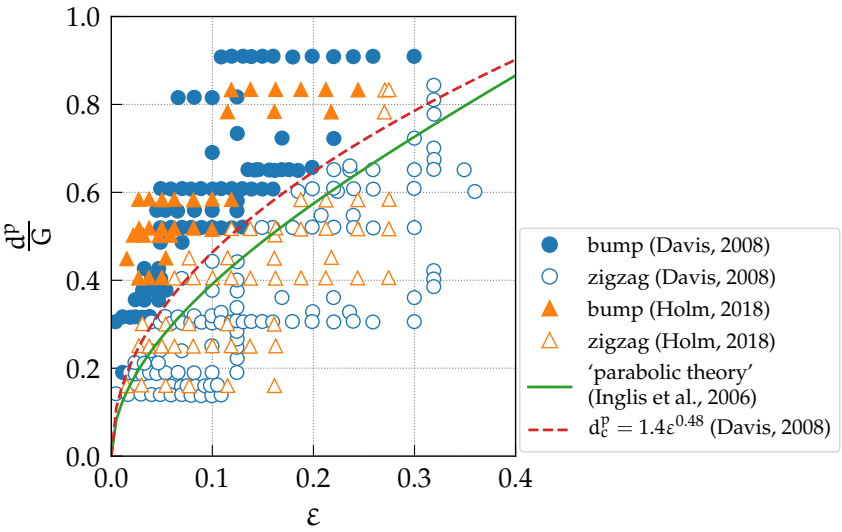

Figure 3.6: Plot of the trajectory mode as a function of the normalised particle diameter d^p/G and the row shift fraction ε, measured using polystyrene micro-beads, from the two experimental theses authored by Holm and Davis (Davis, 2008; Holm, 2018). Filled markers indicate particle 'bump' mode, while the empty markers indicate 'zigzag' mode. The 'parabolic' theory (taking $d_c^p = 2\beta$, for the correct root of the equation 3.1) prediction and the Davis empirical law (equation 3.2) estimates for the critical separation diameter are also shown. Note that all experimental data points from the original sources have not been shown. The focus here is on data points closer to the critical bifurcation region.

'first' flow-lane β, measured through the narrowest section of each array gap, would decide the critical particle size. Since flow-lanes cyclically switch roles through array gaps, the volume flux through each of them should be exactly equal. Using this idea, Inglis, Davis, Austin et al. have taken the first step towards a theoretical estimation of the critical separation size in the DLD. Based on particle-free 2D flow simulations through the DLD geometry, they assume a parabolic flow velocity profile through the narrowest section of each array gap, and compute the width, β, of the 'first' flow-lane (Inglis, Davis, Austin et al., 2006) (see figure 3.5a). They obtain the cubic relationship,

$$\left(\frac{\beta}{G}\right)^3 - \frac{3}{2}\left(\frac{\beta}{G}\right)^2 + \frac{\varepsilon}{2} = 0. \tag{3.1}$$

Assuming that particles have a negligible effect on flow-lanes, the authors approximate the critical particle diameter as $d_c^p \approx 2\beta$. Here, β is computed as the root of the equation 3.1, such that $0 < \beta < G/2$, for $\varepsilon \in [0, 0.5]$.

Experimental results show that this 'parabolic' theory consistently underpredicts the critical size for the DLD (Inglis, Davis, Austin et al., 2006). Figure 3.6 shows a comparison of the experimentally observed trajectory modes in the DLD (obtained using polystyrene beads), from two extensive experimental theses (Davis, 2008; Holm, 2018). These are compared with the 'parabolic' theory prediction. It is clear that the parabolic theory does not provide

a satisfactory understanding of the experimentally observed particle trajectories. In the absence of a clear understanding of the particle trajectory bifurcation behaviour, an empirically derived equation from (Davis, 2008) is used by most experimentalists for predicting critical particle size in the DLD, given as,

$$d_c^p = 1.4\varepsilon^{0.48}, \tag{3.2}$$

and is also plotted in the figure 3.6.

The physical reasons for the mismatch between theory and experiments are still not well understood. It has often been speculated that these differences arise due to particle presence modifying the fluid flow through array gaps (Holm, 2018; Krüger, Holmes and Coveney, 2014). This argument is further buttressed by the fact that the critical diameter d_c^p measured numerically (as $d_c^p = 2\beta$) from 2D flow simulations (in (Holm, 2018) as well as our own), in the absence of particles, agrees well with the parabolic theory predictions. This discrepancy highlights the significance of numerical simulations, wherein the simulated particles affect and are affected by the surrounding fluid flow, for predicting correct particle trajectories in the DLD.

3.2.2 *Mixed modes*

The physics described up till now should always result in a bi-modal distribution of the particle trajectories; one along the average flow direction (zigzag mode) and the other set by the array inclination (displacement mode). From simple theoretical considerations Long et al. point out that this does not hold true when non-integer array periodicities (where $\lambda/\Delta\lambda = N$ is a rational fraction) are used, and results in multi-directional particle trajectory modes in the DLD (Long et al., 2008). In such cases, particles with diameters $d^p < d_c^p$ can display intermediate (in-between zigzag and displacement) as well as negative migration angles. Furthermore, such trajectories were experimentally observed even when N was set to an integer value (Kulrattanarak, van der Sman, Lubbersen et al., 2011; Kulrattanarak, van der Sman, Schroën et al., 2010). Kulrattanarak, van der Sman, Lubbersen et al. (2011) classed these intermediate migration trajectories as 'mixed' modes, since the trajectories displayed characteristics of both displacement and zigzag modes.

anisotropic permeability *The resistance to flow (or flow permeability) through the array depends on direction*

The authors hypothesised that these mixed modes arose from *anisotropic permeability* of the obstacle array. They suggest that anisotropy of permeability is brought about by breaking the rotational symmetry of flow, either due to the pillar shape asymmetry or the obstacle array arrangement (Kulrattanarak, van der Sman, Lubbersen et al., 2011). In section 3.3.1, we look at the two ways of arranging the obstacle arrays. The authors show that using anisotropic arrays results in asymmetric flow-lane width distribution through the array gaps. Recall that in section 3.2.1, we assumed symmetric and equal fluid flow through all the flow-lanes. This assumption breaks down, resulting in

particles smaller than the critical size ($d^p < d_c^p$) displaying mixed trajectory modes.

Still, for the various kinds of obstacle shapes and array layouts used, there is ample DLD literature where such mixed modes are not observed (Inglis, 2009; Inglis, Lord and Nordon, 2011; McGrath, Jimenez and Bridle, 2014). The nature of this puzzle is rather subtle, and manifests as an interplay between the applied pressure gradient direction and the resulting average flow direction, which do not remain parallel in anisotropic arrays. The chapter 8 in this work answers this puzzle, and provides design guidelines to avoid or exploit such anisotropic flow effects in the DLD.

3.2.3 *Diffusion effects*

The DLD technique was born from diffusion based microfluidic separation devices. Therefore, it is important to understand the role of particle diffusion in the DLD, especially when the application deals with nano-meter scale particles, such as in (Huang et al., 2004; Wunsch et al., 2016). In general, particle diffusion serves to destroy deterministic separation achieved by the obstacle arrays in the DLD. The reason is quite simple; diffusion is a stochastic process, that has (in the absence of obstacles) no preferential direction. If significant, diffusion leads to greater mixing of particles in the DLD.

For particle diffusion in the DLD, two length scales are important; the array pitch in the flow-wise direction λ_x and the overall length of the array. Over these two length scales, diffusion competes with convective transport of particles. The relative importance of these two transport phenomena is given by the Péclet number (Pe). If diffusion remains sufficiently small compared to convective particle transport, it can be *rectified* over the shorter length scale of the array pitch by the array row-shift. However, particle diffusion over the entire array length is always detrimental to particle separation (Davis et al., 2006), since it leads to the spreading of particle distributions at device outlets.

rectification
Reduction of multi-directional behaviour to selected directions

A detailed analysis of diffusion and its consequences in the DLD is carried out in (Heller and Bruus, 2008) and we do not repeat the details here. Such stochastic Brownian motion for particles is absent from our simulations. This is justified since we simulate only micro-meter scale DLD devices, operated at sufficiently high flow rates. Here, particle transport by convection dominates their diffusive motion ($Pe \gg 1$), and particle migration due to diffusion is entirely negligible.

3.3 DLD PARAMETERS AND THEIR IMPLICATIONS

In the section 3.2, we saw the simple physical principle leading to particle separation in the DLD. In this section, we elaborate on the various DLD parameters of importance, and their consequences on particle separation. The parameters of importance for a microfluidic separation device can broadly be categorised as flow parameters, geometric (device) parameters and particle parameters. As mentioned previously in section 1.3.1, the DLD is operated

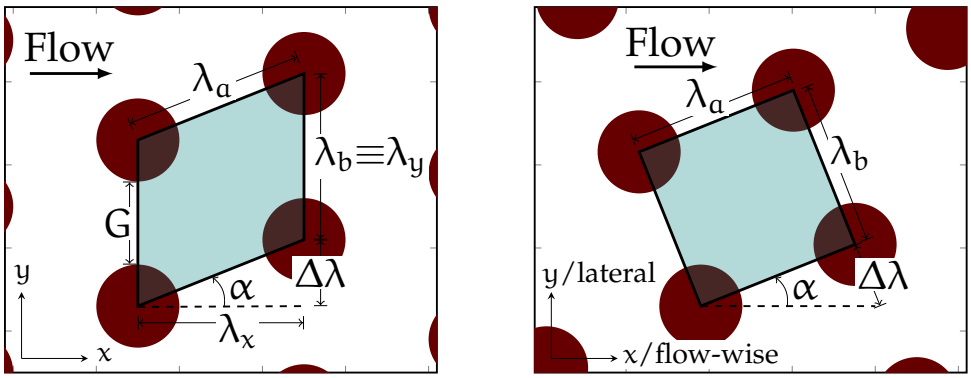

(a) Parallelogram layout (b) Rotated-square layout

Figure 3.7: The two types of obstacle array layouts; (a) the parallelogram layout and (b) the rotated-square layout. The parallelogram layout is obtained by shifting the downstream obstacle rows by $\Delta\lambda$ in the $+y$ direction. The rotated-square layout is obtained by inclining a Cartesian square arrangement of pillars to the flow direction by angle α. Note the differences in the 'unit cells' (with sides λ_a and λ_b) in the two layouts.

in the Stokes flow regime, and there are no inertial effects causing particle migration. This flow regime constraint has been violated in certain experiments, where the DLD has been tested at moderate *Reynolds numbers* (Dincau, Aghilinejad, Kim et al., 2017; Lubbersen, Dijkshoorn et al., 2013; Lubbersen, Schutyser and Boom, 2012). However, this is certainly not the norm. Therefore, in all our simulations we assume the Stokes flow regime to be satisfied in the DLD. The flow (or particle) Reynolds number (or, the parameters characterising flow) is therefore not relevant. Accordingly, we focus attention on the device geometry and the particle parameters.

Reynolds number, Re
Ratio of characteristic inertial to viscous forces in fluid flow

3.3.1 *Obstacle array layout*

Setting the array inclination to average flow direction is critical for DLD operation, as explained in section 3.2. There are two alternative ways of aligning obstacle arrays to flow, shown in figure 3.7; the parallelogram layout (figure 3.7a)[2] and the rotated-square layout (figure 3.7b). The obstacle array discussed previously in section 3.2 was laid in the parallelogram layout. In this layout, each downstream row of obstacles is laterally shifted by a certain distance $\Delta\lambda$. This creates an array inclination to flow given by $\alpha = \tan^{-1}(\Delta\lambda/\lambda_x)$, where λ_x is the centre-to-centre pillar distance along the flow-wise x direction (also see figure 3.4 and detailed description in section 3.2). This array layout is so named because the array 'unit cell' forms a parallelogram (with sides, $\lambda_a > \lambda_b$), as seen in figure 3.7a.

2 In DLD literature the term 'rhombic layout' is a popular alternative designation for the parallelogram layout (Holm, Beech et al., 2011; McGrath, Jimenez and Bridle, 2014; Zeming, Salafi et al., 2016). I favour the latter, for the sake of descriptive correctness and clarity.

The obstacle array can also be inclined to the flow by employing rotated-square layout, as was done in the original DLD paper (Huang et al., 2004). Here, the obstacles are laid out with their centres forming a square Cartesian grid, and the entire grid is then rotated with respect to the average flow direction, to give the inclination α. The array 'unit cell' in this case forms a square (with sides, $\lambda_a = \lambda_b$), inclined to the flow direction, as seen in figure 3.7b. If the array inclination and gap size are set equal in both the layouts, the two are ideally expected to produce equivalent particle separation outcomes. However, in reality, the flow in certain DLD devices with the parallelogram layout is afflicted by anisotropic permeability and particle mixed modes (see section 3.2.2), while no such mixed modes have been reported with the rotated-square layout (Kulrattanarak, van der Sman, Lubbersen et al., 2011).

In all our previous discussions on the DLD obstacle arrays, we have considered the array pitch to be equal in the lateral to the flow-wise directions, i. e. $\lambda_x/\lambda_y = 1$. In most DLD devices, this ratio remains unity (McGrath, Jimenez and Bridle, 2014). Changing the ratio λ_x/λ_y adds another free parameter to the DLD geometry considerations. As seen in figure 3.7, this would also change the array 'unit cell' sides ratio λ_a/λ_b, and therefore the size of the lateral to flow-wise obstacle gaps in the DLD. The ratio λ_x/λ_y influences flow anisotropy (Kulrattanarak, van der Sman, Lubbersen et al., 2011), as well as particle trajectories (Zeming, Salafi et al., 2016) in the DLD. We devote the chapter 8 to study the effect of the DLD array layout and the associated geometric parameters on anisotropic permeability and consequently on particle trajectories.

3.3.2 *Pillar shape and device depth*

The symmetric cylindrical pillar shape has come to be the standard design for DLD array obstacles (McGrath, Jimenez and Bridle, 2014). It is natural to expect that moving away from the cylindrical pillar shape would influence the flow pattern, the critical particle size and consequently the separation behaviour. Loutherback, Puchalla et al. have used these ideas to design arrays with asymmetrical triangular pillars to break the flow symmetry and produce true irreversible ratcheting effect (Loutherback, Puchalla et al., 2009). Also, the authors have demonstrated reduction in the critical separation size in the DLD, with these triangular pillars (Loutherback, Chou et al., 2010).

Recently, array post shape engineering was shown to significantly enhance red blood cell (RBC) lateral displacement in the DLD (Zeming, Ranjan and Zhang, 2013). Here, Zeming, Ranjan and Zhang produced an obstacle shape to exploit RBC tumbling dynamics in the DLD. Concurrent with our work, post shape engineering is emerging as a major branch within DLD research (Kabacaoglu and Biros, 2018; Ranjan et al., 2014). This is especially true for separation of complex bio-particles such as RBCs (Au et al., 2017; Beech, Ho et al., 2018; Henry, 2017; Zhang, Henry et al., 2015). Numerical investigations,

such as the present, are expected to feature prominently in these studies in the future.

DLD device depth H (along the z direction in figure 3.7) is another geometric parameter that has not received much attention in the literature. The ratio of the device depth to the array gap (H/G) governs whether the flow field can be treated as essentially 2D, or consideration needs to be given to the presence of top and bottom device walls. So far, device depth has been used as a means to constrain the degrees of freedom (of motion) for asymmetrical particles such as the RBCs (Beech, Holm et al., 2012; Krüger, Holmes and Coveney, 2014). Changing the device depth is seen to have considerable effect on the dynamics of RBCs, influencing their trajectories in the DLD (Henry et al., 2016). In the present work, we have utilised both, the pillar shape design as well as the device depth, to exploit RBC orientation and deformable behaviour (chapters 9 and 10).

3.3.3 *Particle effect*

The theory for predicting particle separation is developed solely on particle-free fluid flow through obstacle arrays (section 3.2), even though running DLD devices without particles is rather pointless. This has often been cited as the source of the discrepancy between parabolic theory predictions and the experimentally observed particle trajectories in the DLD (Davis, 2008; Holm, 2018; Krüger, Holmes and Coveney, 2014). A particle traversing through a DLD device is expected to modify the ambient flow field, which could potentially explain the observed discrepancies (see figure 3.6). Furthermore, it has been experimentally observed that the critical size in the DLD is limited to $d_c \approx G/5$ (Davis et al., 2006). Below this limit particle separation is not possible, since all particles display the zigzag mode, howsoever small the array inclination.

In the absence of clear theory that captures such experimental variations, simulation studies become crucial. Simulation work based on passive advection of finite-sized particles by the fluid flow (Dincau, Aghilinejad, Hammersley et al., 2018) would inherit the aforementioned mismatch in predicted and observed particle trajectories. In the simulations in this thesis, the motion of particles is bi-directionally coupled to the fluid flowing through the DLD. Hence, my simulations are fundamentally better suited to correctly capture the subtle particle effects on flow-lanes, and consequently on particle trajectories in the DLD.

Additionally, the DLD principle is geared towards highly dilute systems (Huang et al., 2004). The lateral displacement of particles relies on isolated particle-pillar interactions. In reality, experiments always use a suspension of particles through the DLD, usually diluted with buffer streams (Davis et al., 2006). However, processing higher particle concentrations can be crucial in certain cases, such as for rapid isolation of rare cells/bacteria from blood (Wyatt Shields IV, Reyes and López, 2015). This problem has not received much attention, but experimental observations suggest that particle separa-

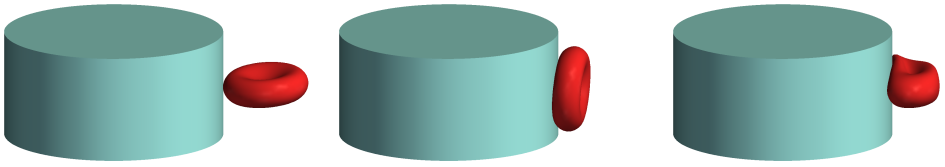

(a) 'in-plane' (b) 'upright' (c) deformed

Figure 3.8: Schematic for visualising the effect of the instantaneous orientation and deformation of an RBC on the location of its mass-centre as it traverses past a DLD pillar. The right panel (a) shows an RBC crossing a cylindrical DLD pillar gap by presenting its largest radius (r_{RBC}) to the pillar. This RBC orientation is referred to as 'in-plane'. The middle panel (b) shows the RBC crossing the same pillar gap, oriented to present its thickness to the pillar. This RBC orientation is 'upright' relative to the DLD, and thus presents a much smaller cross section flowing through the gap. The left panel (c) shows a highly deformed RBC flowing past a pillar. In spite of its 'in-plane' orientation, the deformed RBC to appears smaller in cross section, and its mass-centre is closer to the pillar wall than r_{RBC}.

tion at higher volume fractions becomes increasingly difficult in the DLD (Davis et al., 2006; Lubbersen, Schutyser and Boom, 2012). We investigate this effect in chapter 10, and establish the mechanism for separation failure at limiting particle concentrations.

3.3.3.1 *Particle morphology*

As seen in figure 3.5b, particle trajectory mode in the DLD depends on whether the particle mass centre switches flow lanes when colliding with an obstacle pillar. For non-spherical bio-particles like the RBCs, this interaction depends on their instantaneous orientation in the microfluidic device. And, if the particles deform significantly, their trajectories would further depend on their deformability. These points are illustrated in figure 3.8, for an RBC interaction with a single DLD pillar. Since most bio-particles are deformable and possess complex shapes, their DLD trajectory modes would results from a combination of these effects. At this level of complexity, simple theoretical models such as those from Inglis, Davis, Austin et al. (2006) become ineffectual.

As seen in the previous chapter 2, RBCs possess complex anisotropic shapes and are highly deformable under physiological conditions. In DLD arrays, RBC shape and orientation plays a deciding role in selecting its trajectory (Beech, Holm et al., 2012; Henry et al., 2016; Holm, Beech et al., 2011). Depending on the device geometry and flow conditions, RBCs can orient to present their larger diameter or their smaller thickness to the flow through the array gaps, as seen in figures 3.8a and 3.8b respectively. Thus, RBCs can undergo zigzag or displacement modes in same DLD geometry. RBCs are also highly deformable and this adds another degree of freedom to their dynamics influencing RBC trajectory mode in the DLD, as seen in figure 3.8c. The RBC can display a rich variety of dynamic behaviour in confined shear flows (see chapter 2).

Such dynamic effects have recently been shown to have significant influence on RBC trajectories in the DLD (Henry et al., 2016).

Therefore, in addition to size, particle shape and dynamic behaviour can be exploited towards segregating particle populations. As seen in chapter 1, such sorting, of say RBC populations, has the potential to be an early indicator of an individual's health (Beech, Holm et al., 2012). Our simulations can reproduce the rich dynamic behaviour of the RBCs in DLD arrays. Hence, we explore RBC dynamics in the DLD, leading to innovative DLD pillar designs for deformability sensitive separation (chapter 9).

3.4 OVERVIEW OF APPLICATIONS

The DLD has been successful over a broad range of applications for size-based particle sorting. This section aims to highlight the wide range of DLD applications, paying special attention to bio-particle separations. The references provided here do not exhaustively cover all DLD applications till date, and these can be gleaned from recent review articles in (Antfolk and Laurell, 2017; McGrath, Jimenez and Bridle, 2014).

3.4.1 *Size-based cellular separations*

The DLD was established to be a high-resolution separation technique, with the first paper demonstrating the sorting of micro-meter scale polystyrene beads down to a resolution of 10 nm (Huang et al., 2004). Interest immediately turned to blood cell separations; with Zheng et al. showing separation of larger white blood cells (WBCs) from smaller RBCs (Zheng et al., 2005). Subsequently, in what has proven to be an influential paper for DLD designs, the inventing group at Princeton demonstrated blood cell fractionation as well as artificial *plasma skimming* from freshly drawn human whole blood with two separate DLD devices (Davis et al., 2006).

plasma skimming
The process of obtaining clear blood plasma, free from cellular matter

Since then the DLD has been used for multiple applications involving biomaterials, such as separation of epithelial cells from fibroblast cells (Green, Radisic and Murthy, 2009), isolation of parasites from human blood (Holm, Beech et al., 2011), fungal spore purification (Inglis, Herman and Vesey, 2010) and sorting and enrichment of circulating tumor cells (CTCs) from blood (Liu, Zhang et al., 2013; Loutherback, D'Silva et al., 2012). In fact, the DLD has proven to be a popular choice for cellular enrichment or depletion, as as a pre-step for other other microfluidic routines (Jiang et al., 2017; Zhang, Green et al., 2012). Being a label-free and passive technique, the DLD has been shown to maintain viability of cell populations post separation (Campos-González et al., 2018; Loutherback, D'Silva et al., 2012; Zhang, Green et al., 2012). The success of the DLD is not just limited to beads and bio-particles; size-based droplet sorting with and without cellular encapsulation has been demonstrated (Jing et al., 2015; Joensson, Uhlén and Svahn, 2011; Tottori and Nisisako, 2018). Such encapsulation combined with separation can enable cellular assays and other single cell studies.

In recent years, the DLD design has been tweaked for high particle throughput (Loutherback, D'Silva et al., 2012), and the bottleneck of slow flow rates has been overcome with the help of device parallelisation (Fachin et al., 2017; Inglis, Lord and Nordon, 2011). This makes the technique apt for sample preparatory protocols (Karabacak et al., 2014). Being a continuous flow method and requiring tiny sample volumes, the technique can be readily integrated as a preparatory step for cytometry (Civin et al., 2016). Already, preparatory operations such as cellular labelling, washing, lysis, and subsequent organelle extraction have all been successfully demonstrated with the DLD (Chen, D'Silva et al., 2015; Morton et al., 2008). Additionally, cytometric analytic operations for detecting morphological changes, which manifest as cell size alterations, have also been demonstrated with the DLD (Inglis, Davis, Zieziulewicz et al., 2008; Inglis, Morton et al., 2008).

3.4.2 *Sub-cellular separations*

In their paper original paper, Huang et al. also demonstrated *Escherichia coli* chromosomal separation in the DLD (Huang et al., 2004). Passive separation of such cellular constituents would mean progress towards on-chip cellular biopsies. The cellular organelles are generally in the sub-micron range, and present a greater challenge for separation in the DLD. In this range, the separation of cancer cell derived micro-vesicles from heterogeneously shed vesicle population has been demonstrated (Santana et al., 2014). Recently, fabrication of nano-meter scale DLD devices has allowed for the separation of cellular exosomes and colloids in the DLD (Wunsch et al., 2016). However, nano-scale DLD devices have not gained as much popularity as their micron-scale counterparts (Salafi, Kwek Zeming and Zhang, 2017). At the nano-meter scale the operating Péclet numbers cannot be made very large, and diffusion tends to ruin separation efficiency (Kim, Wunsch et al., 2017). In the present work, we limit ourselves to micro-meter scale devices without particle diffusion, and therefore always operate in the large Péclet number regime ($Pe \gg 1$).

3.4.3 *Beyond size — particle deformation and rotation*

Despite the added complexity in predicting cellular trajectories (as seen in section 3.3.3), cell deformability and complex morphology could come in handy for diagnostic applications. Using morphologically altered RBCs, Beech, Holm et al. have shown that the outlet distribution of RBCs, processed through the DLD, could potentially provide a 'fingerprint' of the health state of an individual (Beech, Holm et al., 2012). This microfluidic mapping of RBC outlet distributions in the DLD relies on their altered deformability leading to differing RBC trajectory modes, where stiffer particles tend to move on the displacement mode (Holmes et al., 2014; Krüger, Holmes and Coveney, 2014). Here, the deformed RBC cross section acts as the effective particle size, when traversing the array gap (Krüger, Holmes and Coveney, 2014).

In addition to deformation, dynamic motion of particles has significant effect on their trajectory modes in the DLD. Recently, Rotation or tumbling of discoid-shaped RBCs and rod-shaped bacteria was shown to enhance their lateral displacement in the DLD (Zeming, Ranjan and Zhang, 2013). The authors used post shapes engineered to induce such rotational motion (Ranjan et al., 2014; Zeming, Ranjan and Zhang, 2013), which has led others to employ similar approaches to exploit anisotropies in the shape of target bio-particles (Au et al., 2017; Beech, Ho et al., 2018). Furthermore, Henry et al. demonstrated that RBC dynamic motion could also induce a change in its trajectory. The authors used higher fluid viscosities in order to achieve tank-treading induced pillar-wall repulsion for the RBCs (Henry et al., 2016). Separations based on complex RBC dynamics and deformability in the DLD is a nascent fast-evolving field, which could potentially be exploited for blood diagnostics and assays, especially for diseases that tend to alter RBC membrane stiffness (Tomaiuolo, 2014).

3.4.4 *From bench-top to bedside...*

Over the last decade, the DLD technique has seen many successes. The use of the DLD for depletion of RBCs from blood for CTC enrichment has now been well established (Karabacak et al., 2014). In fact, plastic disposable DLD devices that can pre-process blood samples, and speed up cytometric rare cell analysis have been fabricated (Civin et al., 2016). Holm, Beech et al. have recently showcased a DLD microfluidic chip that can be operated with a hand-held syringe, making the system portable and easy-to-use (Holm, Beech et al., 2016). Indeed, the success of the DLD is leading to the adoption of the technology for cellular separations, enrichment and processing by many commercial microfluidic enterprises (Campos-González et al., 2018; *GPB Scientific* 2018; Karabacak et al., 2014; Wyatt Shields IV, Ohiri et al., 2017). However, it would be premature to call the DLD an "established" method yet as many unanswered questions still remain.

3.5 OPEN QUESTIONS

Over the last few years, the DLD has grown into one of the most popular techniques for passive label-free microfluidic separation of bio-particles. However, despite the successes, many open questions still remain, mostly concerning the presence and dynamics of particles in the DLD. In the following, we list all the research questions that this thesis answers, along with brief notes on the previously known literature and our subsequent findings. These open questions have all been previously discussed in this chapter (in sections 3.2 and 3.3). The research presented in this thesis brings out knowledge crucial for the maturation of the DLD technology.

1. In the first study, the issue of array anisotropy leading to mixed trajectory modes is investigated. As mentioned in section 3.2.2, mixed

modes have been observed in certain the DLD devices while not in others. Kulrattanarak, van der Sman, Lubbersen et al. hypothesise that these mixed modes arise due to array anisotropy of the parallelogram layout (Kulrattanarak, van der Sman, Lubbersen et al., 2011). However, an investigation into the nature of the problem is missing. Current understanding is based on non-integer flow periodicities caused by asymmetric flow-lane distribution through array gaps (Kulrattanarak, van der Sman, Schroën et al., 2010; Long et al., 2008). Still, it is not know why particles in other DLD devices employing the parallelogram layout remain unaffected by anisotropic mixed modes. In chapter 8, we thoroughly investigate the anisotropy effect in the two types of DLD layouts, and find that the parallelogram layout suffers from anisotropic permeability. We give a clear phenomenological understanding of the inherent parallelogram array anisotropy and identify the design features causing anisotropic flow effects. These should help device manufacturers avoid or exploit particle mixed modes in anisotropic arrays.

Independently and almost at the same time as us, Kim, Wunsch et al. have also studied DLD anisotropy, mapping asymmetry between the flow-field periodicity and the geometric array periodicity, in the parallelogram layout (Kim, Wunsch et al., 2017). However, they did not look at the rotated-square layout, or the effect of non-cylindrical pillar shapes. Their findings are in excellent agreement with ours, and provide an alternative perspective on the problem. It is indeed curious how science has the uncanny habit of arriving at the same finding through independent researchers, yet at almost the same time.

2. The motion of deformable objects through the DLD is a highly challenging problem for both experimental as well as numerical researchers. In particular, the motion of deformable RBCs through the DLD is a compelling problem, as discussed in section 3.4.3. Unsurprisingly, this has drawn the attention of several investigators in the last few years (Henry, 2017; Holm, 2018; Kabacaoglu and Biros, 2017). The motivation for these studies come from the desire to exploit the DLD device for blood cell separations and diagnostics, potentially leading to Lab-on-Chip and point-of-care medical devices.

   The dynamics of RBC motion through the DLD is rich and complex (Henry et al., 2016). Our full 3D DLD simulations, with two-way coupling of deformable RBC motion with the flow-field, are well suited to resolve such complexity. Building on the work in (Henry, 2017; Zeming, Ranjan and Zhang, 2013), we investigate RBC dynamics in DLDs with complex pillar shapes, with an eye on engineering shapes that are sensitive to RBC deformability. Exploiting RBC dynamics and wall induced cross streamline migration, we engineer devices that can reverse RBC trajectory modes, solely by altering the pillar shape. The numerical results of this work are presented in chapter 9.

3. Finally, we investigate the effect of high particle volume fraction on the DLD technique. Experimental results for particle suspension separation in the DLD have been reported previously in (Lubbersen, Boom and Schutyser, 2014; Lubbersen, Schutyser and Boom, 2012). Though, a systematic investigation of the physical mechanisms involved has not been done. Again, RBCs are our particles of choice in this study, due to sizeable experimental interest and practicality. The choice of RBCs as particles lets us change the effective particle size in the DLD simply by changing RBC membrane deformability (Krüger, Holmes and Coveney, 2014).

   I find that the displacement mode is highly susceptible to a breakdown, when the particle volume fraction is moderately increased. The zigzag mode on the other hand remains robust even at high particle concentrations. The reason for this behaviour stems from the increased particle-particle collisions at higher particle concentrations. These collisions affect zigzag and displacement modes asymmetrically, highlighting the inherent differences in the two trajectory modes. Our findings are in good agreement[3] with the experimental work in (Lubbersen, Schutyser and Boom, 2012). The findings of this study are presented in chapter 10. These results are important for the design and realisation of DLD systems operating at high particle volume fractions, such as lab-on-chip systems using undiluted blood.

The task of designing, optimising, and understanding particle modes in the DLD has so far been dominated by experimental endeavours. This work, is one of the few in this field that have been lead by theoretical and numerical investigations. Nonetheless, I have worked closely with experimental collaborators to understand and design DLD arrays. In particular, the research undertaken in answering the questions 1,2 and 3 has been supported by experimental collaborations and evidence. However, I shall not report these experimental findings in this thesis, unless absolutely necessary. The reader is requested to refer to my recent publications on this topic for details on the same.

This chapter concludes the introduction to the work in this thesis. Next, I shall give the reader a detailed look at the mathematical and numerical models that have enabled this work.

3 The simulated and experimental systems are not exactly comparable. The experimental results in (Lubbersen, Schutyser and Boom, 2012) are obtained at moderate Reynolds numbers ($2 < \mathrm{Re} < 34$), while our work is confined entirely to the Stokes flow regime ($\mathrm{Re} \leqslant 1$).

Part II

METHODS

In the lattice Boltzmann method, "non-linearity is local, non-locality is linear" ...

— Sauro Succi (attribution stated in-quotes)

4

MATHEMATICAL MODEL

In this chapter we review the mathematics necessary to describe the twin foundations of this thesis; microfluidic flow and particle deformation. The deterministic lateral displacement (DLD) microfluidic device as well as the particle types under investigation have been introduced previously, in chapter 3. *Continuum* equations are deployed to detail both the phenomena of fluid flow as well as particle membrane deformation. For fluid flow through the device, we have the famous continuum *Navier-Stokes* (NS) equations. And in the case of the particle, we use energy models in order to obtain the deformation state. Both these phenomena are strongly coupled to each other though their "mutual" boundary conditions.

continuum
Physical description that considers matter to possess continuously varying properties, ignoring molecular scale discontinuities

Each particle in the DLD is represented as a 2D deformable solid membrane, completely enclosing a fluid volume. The membrane deformation strain-energy model used here, was originally proposed for the deformation of a healthy red blood cell (RBC) (Skalak, Tozeren et al., 1973). However, the model adapts well for polystyrene micro-beads, which are rigid and spherical. Here, a closed spherical membrane with a high value of stiffness is used, such that the particle deformation scale becomes negligible.

The mathematical model presented here makes no assumptions about the type of device employed (DLD), and is general enough to be applicable to any applications involving fluid flow and deformable particles. In this chapter we are intentionally succinct, and the reader is referred to detailed texts such as (Batchelor, 2000; Chakraborty and Mitra, 2011; Gompper and Schick, 2008; Temam and Miranville, 2005) for the fundamentals, origins and theory of the equations contained herein. That being said, the reader should find this chapter a useful starting point for all the "numerical methods" chapters (5, 6 and 7) that follow.

The current chapter serves as a repository for all the mathematical equations that we shall tackle numerically. Thus, the present chapter sets the bounds on the physics contained in this thesis. The first section 4.1 in the chapter deals with the mathematical notation employed, the second section 4.2 is a refresher on the fundamental equations of fluid flow and the third section 4.3 presents the equations governing particle membrane deformation.

4.1 MATHEMATICAL NOTATION AND PRELIMINARIES

In this section we briefly outline mathematical symbols and conventions used in this chapter, as well as in the rest of this thesis. Tensors and vectors are indicated by using bold font letters, mainly when written in-line with the text (e. g. the stress tensor $\boldsymbol{\sigma}$ or the velocity vector $\mathbf{u}$). For numbered equations however, the *index notation* for representing tensors of any rank is preferred.

The index notation is a useful way to denote vectors and tensors in mathematics. In this work, a general tensor component is written subscripted (or indexed) with Greek letters (e. g. $\sigma_{\alpha\beta}$ or u_α). Since we are in 3D Cartesian space with the the axial coordinates given by (x, y, z), a tensor component along a specific direction is obtained by replacing these in place of the Greek letters (e. g. y-directional stress $\sigma_{\beta y}$, x-directional velocity u_x). Any letter (or symbol) with non-Greek subscripts other than the letters x, y or z, is not deemed as a tensor object.

4.1.0.1 *Einstein summation convention*

An important advantage of using the index notation is its use with the "Einstein summation convention". Under the Einstein summation convention, if an index appears twice in a term (and is not otherwise defined), that term has to be summed over all possible values for the repeated index (e. g. $u_\beta \sigma_{\alpha\beta} = u_x\sigma_{\alpha x} + u_y\sigma_{\alpha y} + u_z\sigma_{\alpha z}$). Expressing general tensor operations such as dot product, full tensor contraction, pre/post transpose multiplication etc., becomes unambiguous and straightforward with this rule.

4.2 EQUATIONS OF FLUID FLOW

In this section, we look at the equations governing fluid flow in general and the DLD specifically. Due to the micro-meter length scales and (relatively) small pressure gradients involved, liquid flow through microfluidic devices (such as the DLD) is generally incompressible and laminar (Chakraborty and Mitra, 2011, Chapter 5). Hence, the incompressible mass and momentum conservation equations can sufficiently describe the physics of fluid flow through the DLD. In numerical works, these two equations are generally referred to as the Navier-Stokes equations (Batchelor, 2000).

Needless to say, in devices employing magneto-electric fields or heat transfer, additional equations describing the relevant physics (electromagnetism, energy conservation) are required in the flow model (Chakraborty and Mitra, 2011; Pamme, 2006). DLD devices employing external electromagnetic forces or heat transfer are rare, as discussed in section 3.4. Also, DLD operation is practically *isothermal*; i. e. frictional heat exchange between the fluid and device walls is negligible. The flow through a DLD is driven with a pressure gradient (chapter 3) and this negligible frictional heating has next to no impact on the fluid flow field. Therefore, we do not need the energy conservation equation.

isothermal
A process in which the system temperature remains constant

The mass conservation equation is given as,

$$\frac{\partial \rho}{\partial t} + \frac{\partial \rho u_\beta}{\partial x_\beta} = 0, \tag{4.1}$$

where, $\mathbf{u}$ is the fluid velocity at at position $\mathbf{x}$ in the flow.

The momentum conservation equation for a *Newtonian fluid*, at the position $\mathbf{x}$ is,

$$\frac{\partial \rho u_\alpha}{\partial t} + u_\beta \frac{\partial \rho u_\alpha}{\partial x_\beta} = -\frac{\partial p}{\partial x_\alpha} + \mu \frac{\partial^2 u_\alpha}{\partial u_\beta \partial u_\beta} + f_\alpha, \tag{4.2}$$

where ρ is the fluid density, p is the hydrostatic pressure, μ is the dynamic viscosity of the fluid and $\mathbf{f}$ is the volumetric body force density acting on the fluid (with *SI units* N/m^3). The NS equation 4.2 is written in its general compressible form without the bulk viscosity term. Since we have assumed the fluid to be Newtonian and isothermal, the dynamic viscosity μ appears outside the double derivative in the equation 4.2.

For solving an incompressible system with constant density ρ, which is the case for flow through the DLD, the NS equations above are all we need. However, as we shall see in the chapter 5, the lattice Boltzmann method used for solving the NS equations is in fact mildly compressible, and ρ varies slightly. We therefore need an equation relating ρ to either p or $\mathbf{u}$, to obtain a closed system of equations. In our *isentropic* and isothermal case, this closure relation is,

$$p = c_s^2 \rho, \tag{4.3}$$

where, c_s^2 is the speed of sound in the fluid medium. Equation 4.3 is called an *equation of state* for the fluid (Batchelor, 2000).

Newtonian fluid
Class of fluids which, when stressed, deform at a rate (or flow) that is linearly proportional to the applied stresses i. e. their viscosity is constant

SI units
short for "International System of Units", a metric unit system built on seven base units

isentropic
A process in which the system entropy remains constant

4.2.1 *Boundary conditions*

Before moving on to the boundary conditions needed to solve the NS equations above, we briefly remark upon the equivalence of the pressure gradient term $(-\partial p/\partial x_\alpha)$, and the force density term f_α in the momentum equation 4.2. For a purely pressure driven flow without any external body force, the pressure gradient at any position, can be split into an average term taken over the fluid domain, and a local variation term. Considering pressure driven flow through a straight micro-channel, the average pressure gradient times channel length should equal the imposed pressure drop across the channel. The average pressure gradient can therefore be seen as a body force that drives the flow along the direction of decreasing pressure, in pure pressure driven flows. Conversely, a flow driven solely by a volumetric body force $\mathbf{f}$ (such as gravity) can be mimicked by one which is driven by an equivalent average pressure gradient imposed *via* inlet-outlet boundaries.

We take advantage of this equivalence for simulating pressure driven fluid flow through the DLD. Most experiments use syringe pumps to push fluid through the DLD channel. The resulting fluid flow is due to the pressure drop generated across the channel. We mimic this pressure driven flow in the DLD with an external constant body force density $\mathbf{f}$.

We use the periodic boundary condition for simulating relevant DLD sections, since, in the DLD, particle separation is achieved with flow over periodic obstacles. This condition can be written as $\mathbf{u}(x_\alpha) = \mathbf{u}(x_\beta)$, where the inlet boundary is at x_α and the outlet boundary is at position x_β. Hence, unlike in experiments, we do not need to specify pressure values at the inlet and outlet boundaries of a DLD device.

This leaves us with the DLD side-channel walls and the particle-fluid interface. The *no-slip* velocity boundary condition is needed for both the stationary DLD channel side walls as well as the particle-fluid interface moving within the fluid. This boundary condition can be written as $\mathbf{u} = \mathbf{u}_w$, where the subscript '$w$' indicates a solid wall or interface.

no-slip
Fluid velocity at any fluid-solid interface equals the interface velocity

4.3 PARTICLE DEFORMATION MODEL

In this thesis, the type of particles simulated are limited to two choices; human red blood cells (RBCs) and polystyrene micro-beads. Both these particles are modelled as fluid-filled capsules, enclosed by a 2D deformable membrane. In the adopted mathematical model, the 2D membranes can undergo finite shear, area dilation and bending deformation. The membrane model also allows for conservation of the total membrane surface area and enclosed volume.

The mathematical model for membrane deformation is primarily devised for simulating RBCs, which have complex shape mechanics in confined flows (Noguchi and Gompper, 2005). Additionally, since experimentalists extensively employ spherical (polystyrene) micro-beads for DLD devices characterisation, we also simulate these using the same model. The micro-beads are modelled as spherical capsules enclosed by a 2D deformable membrane, but with membrane material parameters chosen such that particle deformation is negligible.

In the deformation model, the internal membrane stresses are linked to the membrane energy state (Gompper and Schick, 2008). Separate energies are defined for shear, local area dilation, bending, total surface area deviation and total enclosed volume deviation. The total membrane energy is assumed to have reached a minimum, with no internal membrane stresses when the particle reaches its undeformed (equilibrium) shape. This equilibrium shape is pre-defined (for both particles types), and provided as an input condition. Membrane deformation leads to change in its energy state. Consequently shape (equilibrium) restoring internal (shear and normal) stresses emerge within the membrane. Since our particle model is designed to replicate RBC deformation mechanics, it is instructive to take a brief look at RBC biology previously discussed in section 2.1.1.

4.3.1 *RBC membrane equilibrium shape*

Our membrane energetic model requires a pre-defined equilibrium shape as input condition, in order to compute deformation stresses. In reality, for a

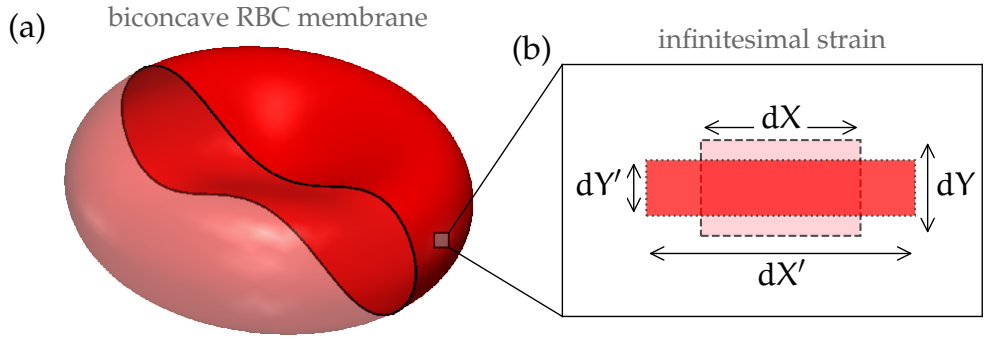

Figure 4.1: The left panel (a) displays a computer generated image of an undeformed equilibrium RBC membrane. Half the RBC is made transparent in order to highlight its biconcave cross section (seen in black). The right panel (b) illustrates elastic strain deformation of an infinitesimal membrane area element. The undeformed sides dX and dY of an infinitesimal rectangular membrane patch (dashed line, light pink) change to dX' and dY' (dotted line, red), when the RBC undergoes elastic strain deformation. Stresses generated from this deformation are tangential to the deformed membrane element.

given *osmolarity* of the suspeding solution, this equilibrium RBC shape manifests such that the membrane energy reaches a minimum (Lim, Wortis and Mukhopadhyay, 2002). Under normal physiological conditions, the equilibrium shape is (mainly) seen to be biconcave discoid. We assume that the fluid flowing through the DLD has the physiological osmolarity condition at all times, and therefore the RBCs assume the equilibrium biconcave shape shown in figure 4.1(a), when undeformed. This axisymmetric biconcave shape was measured by Evans and Fung using interference microscopy, and is given as (Evans and Fung, 1972),

osmolarity
Referring to the total number (concentration) of solute particles in a litre of solution

$$z(r_\phi) = \pm\frac{1}{2}\sqrt{1-\left(\frac{r_\phi}{R_0}\right)^2}\left(c_0 + c_2\left(\frac{r_\phi}{R_0}\right)^2 + c_4\left(\frac{r_\phi}{R_0}\right)^4\right) \tag{4.4}$$

where the RBC profile in the z direction is given as a function of the azimuthal radius $r_\phi = \sqrt{x^2+y^2}$. The RBC is azimuthally symmetric, with $z(r_\phi)$ as the axis of rotational symmetry. Since the RBC is discoid in shape (see figure 4.1), the (x, y) directions are the in-plane directions, while the z direction is along the thickness of the RBC. For an in-plane maximum RBC radius of $R_0 = 3.91\ \mu m$, the constants in the equation 4.4 are given as $c_0 = 0.81\ \mu m$, $c_2 = 7.83\ \mu m$ and $c_4 = -4.39\ \mu m$. These parameters set a maximum RBC thickness of $2.56\ \mu m$ and a minimum thickness in the centre of $0.81\ \mu m$. In this work, this equilibrium shape is assumed without any internal pre-stresses.

The total thickness of the RBC membrane is of the order of $\mathcal{O}(10^{-8})$ meters, while the diameter of the RBC is of the order of $\mathcal{O}(10^{-5})$ meters. Therefore, the RBC membrane can be safely assumed 2D. The structure of the polymer proteins that make up the cytoskeleton as well as the lipid proteins that make up the bi-layer is of the order of $\mathcal{O}(10^{-8})$. Therefore, at the micron

scale the RBC membrane can be simulated with an isotropic smooth continuous 2D material (Gompper and Schick, 2008). The 2D membrane material properties should reflect both the fluid bilayer (incompressibility and bending resistance) and elastic cytoskeletal (stretch and shear elasticity) characters, described in the continuum limit. A scaling comparison of the relative importance of the membrane shear and bending resistances gives an "elastic length scale" for the RBC membrane as $\sim 0.3\ \mu m$ (Gompper and Schick, 2008). This means that at length scales above $\approx 0.3\ \mu m$, the membrane elastic stresses (if present) dominate those from bending, and tend to decide the (local) membrane shape. We shall discuss both of these in detail, in the following sections.

4.3.2 *Membrane strain deformation*

The elastic strain behaviour of RBC membrane material is modelled with a *hyperelastic* deformation law. A hyperelastic material is one whose stress-strain relationship is defined based on an elastic energy density functional (Temam and Miranville, 2005, Chapter 5). The elastic energy functional, ϵ^s, describes the change in local energy density of the material due to the local strain in the material. An energy based relationship between stress and strain allows for easy description of non-linear deformation behaviour, such as those of biological membranes. Of course, the chosen functional form of the elastic energy density should be able to correctly reproduce experimentally observed material behaviour under strain.

The strain (or the stretching and shearing) of material points on a 2D membrane can be captured mathematically by the deformation gradient tensor. In general, if material body points at initial coordinates $\mathbf{X}$ get deformed to a coordinate space $\mathbf{X}'$, we can write the displacement vector space for all material point of the body as $\mathbf{S} = \mathbf{X}' - \mathbf{X}$. Thus, the material deformation gradient tensor $\mathbf{D}$, is,

$$D_{\alpha\beta} = \frac{\partial X'_\alpha}{\partial X_\beta} = \frac{\partial S_\alpha}{\partial X_\beta} + \delta_{\alpha\beta}, \tag{4.5}$$

Kronecker delta
A unit tensor defined as

$$\delta_{\alpha\beta} = \begin{cases} 1 & ;\alpha = \beta \\ 0 & ;otherwise \end{cases}$$

where $\delta_{\alpha\beta}$ is the *Kronecker delta*.

The tensor $\mathbf{D}$ contains information about the deformation state of the membrane, this information comes contaminated with rigid body rotations of the material points. Neither is the tensor $\mathbf{D}$ guaranteed to be symmetric, a shortcoming for defining the stress-strain energy density relationship.

For an isotropic material, the stress-strain relationship should be independent of coordinate rotations or shifts in the origin. Therefore, the eigenvalues $\{\lambda_1, \lambda_2\}$ (2 for the 2D membrane) of the deformation gradient tensor $\mathbf{D}$ are the true indicators of the strain in the membrane. The eigenvalues are equal to the principal stretch ratios for 2D planar deformation of the RBC membrane, as shown in figure 4.1(b). These are written as,

$$\lambda_1 = \frac{dX'}{dX} \quad \text{and} \quad \lambda_2 = \frac{dY'}{dY}, \tag{4.6}$$

where, dX and dY are the sides of an infinitesimal rectangular patch on the undeformed RBC membrane, and dX' and dY' are the corresponding sides of the rectangle after deformation.

4.3.2.1 *The Skalak law*

For deformable bio-membranes, the stress-strain relationship remains linear only in the small deformation regime. But, for the RBC membrane, the ratios $\{\lambda_1, \lambda_2\}$ could scale as high as ~ 2 (Gompper and Schick, 2008). Thus, the use of linear stress-strain relations cannot be justified, and the large strain (or finite deformation) theory comes into the picture (Temam and Miranville, 2005, Chapter 17). The standard approach in such cases is to make use of the *Green's strain tensor* $\mathbf{E}$, defined as,

$$E_{\alpha\beta} = \frac{1}{2}(D_{\gamma\alpha}D_{\gamma\beta} - \delta_{\alpha\beta}), \tag{4.7}$$

such that, in the small strain limit, we get results similar to those from the (linear) Engineering strain definition. The (first) term $\mathbf{G} = \mathbf{D}^T\mathbf{D}$ in equation 4.7 decides the amount of strain in the material. Also, it is G (also termed the right Green-Cauchy strain tensor) that makes the strain tensor rotationally invariant and symmetric.

Like eigenvalues, the *invariants of the tensor* $\mathbf{E}$ also remain invariant under coordinate transformation (rotation and/or translation). These invariants, say $\{I_1', I_2'\}$, could be used instead of the eigenvalues of $\mathbf{D}$, to indicate the state of strain in the membrane. Therefore, the strain energy functional can be defined as a function of these invariants $\epsilon^s(I_1', I_2')$.

invariants of a tensor
Coefficients of the equation whose roots are the corresponding eigenvalues for that tensor

Starting from a similar argument, Skalak, Tozeren et al. first redefine these invariants as $I_1 = 2I_1'$ and $I_2 = 2I_1' + 4I_2'$. This is done in order to directly relate the *area dilation* strain $\lambda_1^2\lambda_2^2 = dA'/dA$, to the second invariant, such that when there is no local area dilation, the second invariant $I_2 = 0$. Here, the $dA' = dX'dY'$, and $dA = dXdY$ are the infinitesimal post and pre deformation areas, respectively (see figure 4.1(b)).

area dilation strain
Ratio of deformed surface area to the undeformed surface area in the infinitesimal limit

With these transformations, it is easy to obtain the relations (Skalak, Tozeren et al., 1973),

$$I_1 = \lambda_1^2 + \lambda_2^2 - 2 \qquad \text{and} \tag{4.8}$$

$$I_2 = \lambda_1^2\lambda_2^2 - 1. \tag{4.9}$$

The transformed first invariant I_1 relates to the hydrostatic component (or mean strain) of the strain tensor, while the second invariant I_2 relates to the local area dilation.

With the intent to strongly penalise local area dilation strains (as the RBC membrane is practically incompressible), Skalak, Tozeren et al. proposed the non-linear relationship (Skalak, Tozeren et al., 1973),

$$\epsilon^s = \frac{\kappa^s}{12}(I_2^2 + 2I_1 - 2I_2) + \frac{\kappa^\alpha}{12}I_2^2, \tag{4.10}$$

for the RBC membrane strain energy functional ϵ^s. Here, κ^s is the elastic strain (covering normal and shearing deformation) modulus and κ^α is the (local) area dilation modulus, for the membrane.

Thus, both the membrane cytoskeletal shear resistance as well as the area dilation strain resistance of the membrane bilayer are taken into account. This form for the strain functional is usually (but not officially!) called the "Skalak law". We shall not go into the other strain energy constitutive models in use for modelling the membrane of the RBC such as (Navot, 1998; Ramanujan and Pozrikidis, 1998). Notably, it has been shown that the Skalak law is the most appropriate hyperelastic constitutive relationship for describing the deformation of a RBC membrane (Dimitrakopoulos, 2012).

4.3.3 *Membrane bending deformation*

The initial ideas on the bending resistance of RBC membranes were proposed by Helfrich in the year 1973. In fact, this was a first of its kind (and remarkable for the time!) attempt to explain the experimentally observed equilibrium RBC shapes, based solely on membrane bending energetics (Deuling and Helfrich, 1976; Helfrich, 1973). Helfrich used an elastic bending energy formulation with a "spontaneous" curvature term.

When all points on the RBC membrane attain their spontaneous curvatures, the bending energy is at its minimum. Since we are only interested in the variation of the bending energy, this minimum value can be arbitrarily defined. Computations are simplified if we choose this value to be zero. Thus, the total bending energy E_B can be written in the (harmonic) form as (Gompper and Schick, 2008),

$$E_B = \frac{\kappa^b}{2} \iint \left(H(r_\alpha) - H^0\right)^2 dA, \tag{4.11}$$

where, κ^b is the membrane bending modulus. Here, H^0 gives the spontaneous curvature, a local invariant property of the RBC membrane. $H(\mathbf{r})$ is mean curvature of the membrane surface at position $\mathbf{r}$ defined with respect to the centroid of the membrane. The mean curvature can be computed as the trace (or the first invariant) of the curvature tensor as, $\frac{\mathrm{tr}(\mathbf{C})}{2} = 1/2(C_1(\mathbf{r}) + C_2(\mathbf{r}))$. Here, $\{C_1(\mathbf{r}), C_2(\mathbf{r})\}$ are the principal values of curvature. These are related to the principal radii of curvature, $\{R_1, R_2\}$, as $C_i = 1/R_i(\mathbf{r})$ for $i = \{1, 2\}$, at membrane position $\mathbf{r}$.

Though this form of bending energy is popular in numerical works for quantifying the bending resistance of the RBC membrane, it neglects two other contributing terms. The first of these is the Gaussian curvature contribution to the bending energy given as $\kappa_G \int K(\mathbf{r}) dA$. $K(\mathbf{r})$ is the Gaussian surface curvature and is given by the determinant (or the second invariant) of the curvature tensor as, $K(\mathbf{r}) = \mathrm{Det}(\mathbf{C}) = C_1 C_2$. Fortunately for us, this contributing term remains invariant in cases where the surface is smooth and the surface topology does not change (Gompper and Schick, 2008). In this

work, the closed RBC membrane always remains closed (topology invariant). Thus, the contribution from the Gaussian curvature term to membrane bending energetics is zero.

The other significant term that enters the calculation for the bending energy comes from a difference in areas between the two leaflets of the membrane bilayer. This area difference is a result of differences in the number of lipid molecules between the outer and inner leaflets. The form of this energy contribution turns out to be non-local, and is not captured by an equation of the form 4.11.

Since the bending contribution from arising from the bilayer area difference is ignored in our formulation, we shall not discuss it further. The reader is referred to (Gompper and Schick, 2008, Chapter 2) for an extensive discussion on the same. Neglecting this contribution adds a systematic error to the bending energy computations in our simulations. However, as seen earlier, the equilibrium RBC shape is pre-defined by equation 4.4, and for non-equilibrium shapes, the elastic shear stresses should dominate the bending stresses at membrane length scales greater than $\sim 0.3\ \mu m$. Therefore, this simplification is not a major concern. Indeed, a similar approach has been taken by many researchers for reasons of computational simplicity and efficiency (Doddi and Bagchi, 2009; Ghosh et al., 2006; Kraus et al., 1996; Pozrikidis, 2001; Pozrikidis, 2003).

4.3.4 *Area and volume conservation*

This section is concerned with the energy equations governing the variation of total membrane surface area and enclosed volume. At this point, the reader might be slightly surprised to find yet another section on area conservation. The membrane area conservation should ideally be handled by the local area dilation term (term with κ^{α}) in the equation 4.10. However, in order to hold the total surface area nearly constant (as needed for the RBC membrane), we would have to use a large value for the area dilation modulus κ^{α}. Though such a value can be motivated from physiological considerations, it leads to numerical difficulties in explicit solution algorithms such those employed here. Therefore, we can define a global area conservation energy E_A with a form similar to the bending energy as (Gompper and Schick, 2008),

$$E_A = \frac{\kappa_A}{2} \frac{(A - A^0)^2}{A^0}, \tag{4.12}$$

where, A^0 is the total surface area of the underformed membrane, and A is the total area after membrane deformation. κ_A is the area modulus for the RBC membrane, whose value can be measured from RBC deformation experiments ($k_A \approx 0.5\ J/m^2$).

As mentioned in section 4.3.1, changes in the shape and volume of the RBC are driven by changes in the osmolarity of the suspending solution (Yawata, 2003, Chapter 2). Therefore, the RBC volume is strongly conserved under normal physiological conditions, with constant osmolarity. By normal physiolo-

isotonic
The RBC cytosol and the suspending fluid have the same osmotic pressure

gical conditions, we mean that the cell is suspended in an *isotonic* fluid, when used in the DLD. I have not yet come across any DLD devices using RBCs and employing non-isotonic solutions with concentration gradients. Therefore, I have not incorporated such gradients in the fluid model.

However, as we shall see in chapter 7, the numerical scheme for coupling the membrane-fluid motions does not guarantee fluid volume conservation. This shortcoming can lead to particle volume drift; a gradual change in the volume of the particle over time, purely due to numerical artefacts. We overcome this issue by defining a harmonic energy potential for global particle volume conservation as (Krüger, 2012),

$$E_V = \frac{\kappa_V}{2}\frac{(V - V^0)^2}{V^0}, \tag{4.13}$$

where, V^0 is the total volume of the undeformed particle and V is the particle volume after deformation. κ_V is the volume modulus, whose true physical value can be motivated from osmotic pressure driven RBC volume change. However, in our model κ_V is artificial, and set purely based on numerical considerations. In fact, for the sake of numerical stability, the values of κ_A and κ_V are set to ≈ 1000 times lower than their physiologically correct counterparts. Still, we make sure that the total area and volume of the RBC (and micro-beads) does not vary by more than 1% (Krüger, 2012).

This concludes our discussion on the various energies computed from membrane deformation. We can write all energy contributions towards the total membrane energy E_M as,

$$E_M = E_S + E_B + E_A + E_V, \tag{4.14}$$

where, the total elastic strain energy E_S is computed by integrating over the entire membrane surface, i. e., $E_S = \oint \epsilon^s \, dA$.

4.3.5 *Principle of virtual work*

In this final section, we turn to the method for obtaining the local stresses (or forces) generated due to membrane deformation. We employ the *principle of virtual work* to compute the local membrane forces from each of the corresponding energy modes in equation 4.14 (Temam and Miranville, 2005, Chapter 15). This principle can be written as,

principle of virtual work
The (virtual) work done by a physical force through all virtual displacements for a system in static equilibrium is zero

$$F_\alpha^{\{S,B,A,V\}}(r_\alpha) = \frac{\partial E_{\{S,B,A,V\}}}{\partial r_\alpha}, \tag{4.15}$$

where, $\partial/\partial r$ indicates taking a gradient over a small virtual displacement, and $\mathbf{F}(\mathbf{r})$ is the local force, at membrane location $\mathbf{r}$. The superscripts $\{S, B, A, V\}$ differentiate between membrane force components arising separately from membrane strain, bending, total area and volume energies, receptively.

5

FLUID FLOW – LATTICE BOLTZMANN METHOD

In this chapter we shall go over the fluid flow solver employed in this thesis. We use the lattice Boltzmann method (LBM) for obtaining a fluid flow solution in microfluidic devices. Unlike most conventional computational fluid dynamics (CFD) solvers, the LBM does not directly solve the well known mass and momentum balance equations of *continuum* fluid dynamics; i. e. the Navier-Stokes (NS) equations. Instead the LBM solves the discretised Boltzmann equation, which has origins in the kinetic theory of gases. The *macroscopic* fluid variables that satisfy the NS continuum equations are subsequently obtained from the LBM solution.

macroscopic
Properties that are tangible to human senses such as density, velocity of a fluid

In chapter 4, we have seen that we would need a capable NS solver in order to numerically analyse the deterministic lateral displacement (DLD). The aim of this chapter is for the reader to get a "feel" for the LB method for obtaining flow solutions in the DLD devices and serves as a brief introduction to the LBM for fluid flow. Towards this end, we shall emphasise the modelled fluid dynamics, rather than rigorous mathematical or numerical intricacies of the LBM. The code employed for this thesis is entirely derived from the LBM implementation by Krüger (2012), and the finer details of the implementation can be found therein. This gives us a validated and streamlined LBM code. At the end of this chapter the reader should have gained an understanding of the basics of the LBM and the reasons for its choice.

This chapter begins with an overview of the LBM in section 5.1. Some ideas from the kinetic theory useful for understanding the LBM, are discussed in section 5.2. The core of the numerical LB scheme is discussed in section 5.3, and the initial and boundary conditions are presented in section 5.4. The implementation of external forces is described in section 5.5. The methods used to recover the NS solution from the LBM are briefly discussed in section 5.6. We conclude the chapter with a few remarks in section 5.7.

5.1 OVERVIEW

Though the LBM has been around for a while, it is not as old as most of the conventional CFD methods that discretise the NS equations directly. The LBM was born in the late 1980s, out of *lattice gas cellular automata* (LGCA) methods (Wolf-Gladrow, 2000), constructed for solving fluid flow problems. In subsequent years, the LBM has matured; tackling a wide variety of problems, as seen in (Chen and Doolen, 1998). For example, LBM has been employed for problems as far afield as those in biological flows (Ouared and Chopard, 2005), porous media flows (Spaid and Phelan, 1997), multiphase and multicomponent flows (He, Chen and Zhang, 1999; Martys and Chen, 1996), heat transfer modes (Dixit and Babu, 2006; Vernekar and Mishra, 2014; Wang,

LGCA
Particle based fluid simulation algorithm that relies on simultaneous update rules for discrete particle velocities

Wang and Li, 2007), turbulent flows (Yu, Girimaji and Luo, 2005), acoustics (Viggen, 2014) well as relativistic hydrodynamics (Mendoza et al., 2010).

Reynolds number
Ratio of time scales for momentum transport by diffusion to that by convection in fluid flow

Adapting the LBM to solve such a wide spectrum of applications has meant that some added complexity is incorporated into the base LB scheme. However, even the simplest implementation of the LBM performs admirably at low *Reynolds numbers* and can handle complex geometries with greater ease than conventional CFD techniques. Therefore, the LBM has gained popularity for investigations of bio-suspension and microfluidic flows (Aidun and Clausen, 2010; Zhang, 2011). In this thesis, we employ what is probably the simplest *isothermal* LBM implementation for effectively solving the incompressible NS equations.

asymptotic
Approaching a certain value as a limit, i. e. as a limiting case

As the name suggests, the LBM does not discretise the NS equations directly. In the LBM, an *asymptotic* solution to the NS equations is obtained by discretely solving the Boltzmann equation with a simplified collision operator. The discretisation is carried out with the sole intent of recovering the macroscopic variables of the NS equation. The Boltzmann equation is capable of describing matter at both the molecular and macroscopic scales. When the *Knudsen number* is small, the Boltzmann equation can be used to describe macroscopic continuum fluid behaviour. These ideas have roots in the Kinetic theory, which gives a statistical *meso*-scale description for fluids (Jeans, 1940). It should be noted that though the LBM solves the Boltzmann equation discretely, it does not solve for the evolution of the Boltzmann equation; i. e. information at the molecular level is lost in this discretisation, and only the NS equations are solved correctly.

Knudsen number
Ratio between the molecular mean free path (length) between collision and the length scale representative of the flow

meso
from Greek; meaning "in-between" or "middle"

In the case of dense particle suspension flows such as those investigated in this thesis, the LBM computation time scales linearly with the number of particles. Another major advantage for the LBM is the intrinsic parallelisability of its algorithm. This is because, in the LBM, most of the "heavy" computations are done locally at every discrete node, and do not need information from the neighbour nodes in the fluid domain. The only non-local step in the LB algorithm is linear, and computationally "light".

Additionally, the LBM bypasses the need to solve a Poisson equation for pressure, the main culprit for numerical difficulties in conventional CFD. The LBM remains mildly compressible, even when solving for the incompressible NS equations, and the pressure is obtained from an equation of state.

5.2 IDEAS FROM KINETIC THEORY

In this section we shall familiarise ourselves with some basic ideas from the kinetic theory of mono-atomic gases (Chapman, 1952). Kinetic theory is a statistical description of gas motion, linking the macroscopic continuum fluid properties to the discrete molecular picture of a fluid. The variables discretised and solved for in the LBM, are grounded in the kinetic theory description of matter. Macroscopic variables such as fluid velocity $\mathbf{u}$ and density ρ are then "recovered" (or computed) from the LBM solution, using the kinetic theory. In order to understand the LBM solution algorithm, it is therefore

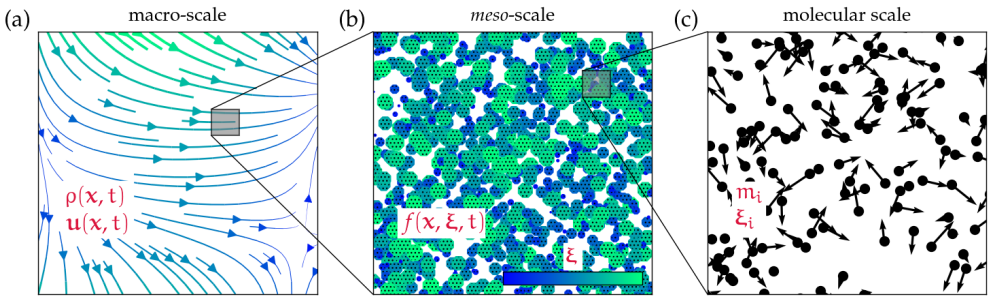

Figure 5.1: Visualisation of (a) macro, (b) *meso* and (c) molecular scales. In the left panel (a) an arbitrary flow at the macroscopic level of detail is shown. Here, fluid properties such as velocity $\mathbf{u}$ and density ρ can be perceived by the human senses. If we zoom-in sufficiently into this flow, we shall eventually see individual molecular motions. This is shown in the right panel (c), with the molecular mass m_i and velocity $\boldsymbol{\xi}_i$ for a molecule with index i. The middle panel (b) represents a description of the flow somewhere in between the macro and molecular scales; the *meso*-scale. Here, the flow properties are described by a *meso*-scale variable f, which incorporates information about the molecular velocities $\boldsymbol{\xi}$ along with that from the macroscopic mass density ρ. Variable f is the generalisation of mass density ρ, and represents the distribution of matter with molecular velocities in the neighbourhood of $\boldsymbol{\xi}$ at a given spatial location.

very important to grasp these concepts rooted in the kinetic theory. Hence, we digress from the LBM to spend some time over these ideas and the variables brought along.

5.2.1 *Macroscopic, meso-scopic and molecular worlds*

In our everyday experience, we are intuitively familiar with the macroscopic description of fluids. We can define properties such as fluid velocity $\mathbf{u}$ and fluid density ρ that are tangible to the human senses (as in figure 5.1(a)). Furthermore, we could also correctly describe the same fluid as a collection of a large number of individual molecules with mass m_i and corresponding molecular velocities $\boldsymbol{\xi}_i$ (i indicating molecular id). This is the molecular picture of a fluid as seen in figure 5.1(c).

The kinetic theory takes a somewhat middle path between these two extreme views. The fluid is described in terms of a new variable called the density distribution function (or particle population) f. Instead of tracking the mass and velocity of each and every molecule, we now record the probability distribution of the fluid mass density, as a function of the molecular velocity $\boldsymbol{\xi}$ and the position $\mathbf{x}$, and define the function $f(\mathbf{x}, \boldsymbol{\xi}, t)$. Variable t indicates the time dependence for f. Since this description lies somewhere in between the macroscopic and molecular descriptions, it is often termed as a *meso*-scopic description of fluids (illustrated as a coarse grained molecular velocity contour-scatter plot in figure 5.1(b) for visualisation purposes only).

Before looking at the connection between f and the macroscopic variables, we shall first understand the physical meaning of the quantity represented by

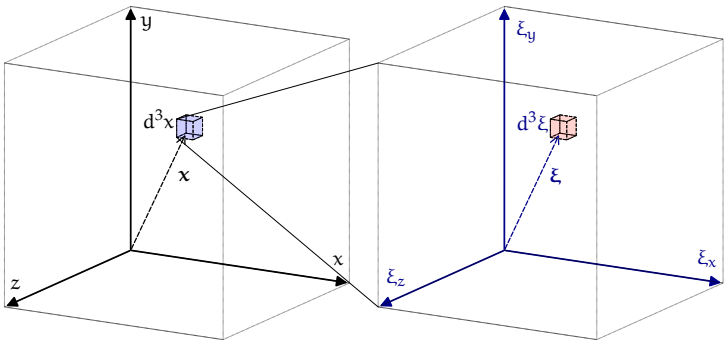

Figure 5.2: Cartesian axes of the physical and velocity sub-spaces used for defining the *meso*-scale particle populations f. The 3D physical space dimensions are shown on the left. At any location $\mathbf{x}$ in the physical space, we can open an imaginary infinitesimal window and observe the molecular motions. The 3D velocity space dimensions used to plot the molecular mass against their velocities $\boldsymbol{\xi}$ are shown on the right. The molecular mass distribution mapped in this 6D space (termed the *phase-space*) determines the particle populations f, at any given time t.

infinitesimal
Extremely small; tending but not equal to zero

f. We refer to the figure 5.2 for the following discussion. Consider a fluid with density $\rho(\mathbf{x}, t)$ and velocity $\mathbf{u}(\mathbf{x}, t)$ marked with Cartesian axes. Let us say that we are at position $\mathbf{x}$ in the fluid, sitting inside an *infinitesimal* physical volume d^3x, in the Cartesian physical space shown on the left in figure 5.2. Now, let us give ourselves a special (imaginary) probe, that lets us "see" the velocity of each and every molecule inside the volume d^3x. With the help of this probe we can map a Cartesian velocity sub-space (ξ_x, ξ_y, ξ_z) at $\mathbf{x}$ (shown on the right in figure 5.2), and plot all the observed molecular velocities $\boldsymbol{\xi}$ against the number of molecules possessing them. Soon, a plot of the distribution of molecular mass, for every possible molecular velocity direction builds up in the 3D velocity space at $\mathbf{x}$. The infinitesimal velocity volume $d^3\xi$ now contains the fraction of molecular mass at physical location $\mathbf{x}$ (inside an infinitesimal physical volume d^3x) that possesses the velocity $\boldsymbol{\xi}$ (strictly a velocity between $\boldsymbol{\xi}$ and $\boldsymbol{\xi} + d\boldsymbol{\xi}$). This mapping is now termed as our distribution function $f(\mathbf{x}, \boldsymbol{\xi}, t)$; defined as the mass density of fluid particles at position $\mathbf{x}$ with molecular velocity $\boldsymbol{\xi}$ at time t. Thus, we have obtain a *meso*-scopic picture of the fluid.

5.2.2 *Macroscopic variables and the distribution function*

In this section we state some "rules" that help us go from the distribution function description to the macroscopic variables. These rules follow naturally from the definition of the distribution function in the previous section 5.2.1.

For the first rule, we have,

$$\rho(x_\alpha, t) = \int f(x_\alpha, \xi_\alpha, t) d^3\xi. \tag{5.1}$$

The equation 5.1 simply states that we would obtain the physical mass density if we sum over all of the possible velocities for the density distribution function, at any physical location $\mathbf{x}$. Referring to the figure 5.2, this operation amounts to computing the total mass distribution in the entire velocity space inside the infinitesimal physical volume d^3x, to get the mass density at $\mathbf{x}$.

As above, we can also sum the total molecular momentum distribution, given by $(f\boldsymbol{\xi})$, over the entire velocity space at any location $\mathbf{x}$. This should now give us the *momentum density* at position $\mathbf{x}$ as,

momentum density
Ratio of the momentum possessed by an infinitesimal fluid element to its volume

$$\rho(x_\alpha, t) u_\beta(x_\alpha, t) = \int \xi_\beta f(x_\alpha, \xi_\alpha, t) d^3\xi. \tag{5.2}$$

Combining the equations 5.1 and 5.2, we can obtain the macroscopic fluid velocity $\mathbf{u}$ at location $\mathbf{x}$.

Similarly, the macroscopic total energy density of the fluid can be computed as,

$$\rho(x_\alpha, t) E(x_\alpha, t) = \frac{1}{2} \int \xi_\beta \xi_\beta f(x_\alpha, \xi_\alpha, t) d^3\xi, \tag{5.3}$$

where, E is the total energy per unit mass. Here, the total molecular energy equals the translational molecular energy ($\xi \cdot \xi/2$), and we neglect contributions from the vibrational and rotational energies of the molecule.

It can also be shown that the *specific internal energy* $e(\mathbf{x}, t)$ (per unit mass) can be computed as (Viggen, 2014),

specific internal energy
energy of a system due to the molecular motions

$$\rho(x_\alpha, t) e(x_\alpha, t) = \frac{1}{2} \int v_\beta v_\beta f(x_\alpha, \xi_\alpha, t) d^3\xi. \tag{5.4}$$

Here, the molecular velocity $\boldsymbol{\xi}$ has been decomposed as $\boldsymbol{\xi} = \mathbf{u} + \boldsymbol{v}$. The velocity $\boldsymbol{v}$ is deviation of the molecular velocity $\boldsymbol{\xi}$ from the macroscopic flow velocity $\mathbf{u}$, at any position $\mathbf{x}$. $\boldsymbol{v}$ is called the "peculiar" velocity of the fluid molecules.

The equations 5.1–5.4 link the *meso*-scopic distribution function to the macroscopic variables and are called the moments of the distribution function f. These moments are distinguished by their "order", given by the number of velocity terms multiplied with f inside the integral.

5.2.3 *The equilibrium distribution function*

In this section we look at the value of the distribution function when the fluid is in equilibrium. We know from dynamics that molecular collisions would tend to distribute the molecular energy evenly. For example, a fluid held in

a container and left to itself, eventually reaches equilibrium because of local molecular collision driven re-distribution of energy. Based on our earlier assumption that we consider only the translational energy of molecules (section 5.2.2), collision would therefore tend to distribute molecular velocities evenly in all directions about their mean.

Hence, when a fluid reaches equilibrium, we can assume that all peculiar velocity directions are equally probable due to the isotropic collision process. That is, the peculiar velocity $\boldsymbol{v}$ is distributed with spherical symmetry about the mean velocity $\boldsymbol{u}$. At equilibrium, we can assume that the distribution function is a function solely of the peculiar velocity v. This equilibrium distribution function was first found by Maxwell for a mono-atomic gas (Maxwell, 1867) and can be written as,

$$f^{eq}(\boldsymbol{x}, |\boldsymbol{v}|, t) = \rho \left(\frac{1}{2\pi R T} \right)^{3/2} e^{-|v|^2/2RT}, \tag{5.5}$$

where, the superscript '^{eq}' denotes equilibrium, R is the gas constant, T the absolute temperature of the gas and ρ the density of the gas. Later, Boltzmann derived the same *via* statistical mechanics, and showed it to be unique. Therefore equation 5.5 is also known as the *Maxwell-Boltzmann distribution*. In the LBM, the equilibrium distribution function comes in handy for modelling the process of molecular collisions.

5.2.4 *The Boltzmann equation*

Boltzmann also proposed an equation describing the evolution of the distribution function (or particle populations) with time. This equation is the cornerstone for the LBM; the Boltzmann equation. It is written as,

$$\frac{df}{dt} = \frac{\partial f}{\partial t} + \xi_\beta \frac{\partial f}{\partial x_\beta} + \frac{f_\beta}{\rho} \frac{\partial f}{\partial \xi_\beta} = \Omega(f), \tag{5.6}$$

where, $\mathbf{f}$ is the body force density (defined per unit volume of the fluid). Here, $\Omega(f)$ is called the collision operator, governing the change in f due to molecular collisions. This change should takes f towards equilibrium (f^{eq}). $\Omega(f)$ can be seen as a source term in the equation 5.6, causing f to evolve over time.

It can be easily shown that by taking the zeroth, first and second order moments of the equation 5.6 (i. e. using equations 5.1– 5.4), we can obtain the macroscopic mass, momentum and energy conservation equations, respectively. The zeroth moment of equation 5.6 gives the required NS mass conservation equation 4.1. Taking the first moment of equation 5.6 gives the momentum conservation equation. However, this equation is in the general *Cauchy momentum* form (and not the NS equation 4.2 we need), where the viscous stress tensor depends on the form of the distribution function. We shall tie this loose end after discretising the Boltzmann equation, and "recover" the required incompressible NS momentum equation 4.2.

Cauchy momentum equation
General momentum balance equation valid for any continuum material, including solids

5.3 THE DISCRETISED LB EQUATION

In order to solve the Boltzmann equation numerically, we must first discretise it; i. e. we want to obtain the values of f at discrete set of points in time and space. We know (from the discussion in 5.2) that f is defined over a 7D space $\{x, y, z, \xi_x, \xi_y, \xi_z, t\}$. This means that in addition to the temporal and physical dimensions, the discretisation of the equation 5.6 needs to be also carried out over the velocity dimensions (unlike conventional CFD methods).

Historically, discretisation of the velocity space in the LBM followed naturally from that in the LGCA methods (Wolf-Gladrow, 2000). This can also be done through a mathematically rigorous route, using Hermite polynomial series expansion as well as Gauss-Hermite quadrature rule to obtain the discrete velocity set $\boldsymbol{\xi}_i$ (Shan, Yuan and Chen, 2006). Here, 'i' indicates the index for a finite set of velocities that discretise the velocity space. After discretising the velocity sub-space, we then discretise the physical and temporal space using the method of characteristics. In the following discussion on the discretisation of the Boltzmann equation we shall assume that there are no external forces ($\mathbf{f} = 0$) or mass sources present. We handle forces separately (section 5.5).

5.3.1 *Discretisation of velocity space*

The route to discretise the velocity space starts with the known analytical form of the equilibrium distribution function (equation 5.5). The procedure in short is; express f^{eq} as a Hermite polynomial series expansion in $\boldsymbol{\xi}$. The coefficients of this series appear as integrals over the velocity space and can be evaluated using Gauss-Hermite quadrature rule. Application of Gauss-Hermite quadrature rule for integral evaluation gives us the discrete velocities $\boldsymbol{\xi}_i$ and corresponding integration weights w_i, such that the algebraic weighted summations remain exactly equal to the analytical integrations[1].

The first three of the series coefficients turn out to be very similar in form to the moments of the distribution function. Hence the Hermite polynomial expansion for f^{eq} is truncated after the first three coefficients. The truncated equilibrium distribution f^{eq} can now reproduce the macroscopic moments (equations 5.1– 5.4) exactly when evaluated at the discrete velocities $\boldsymbol{\xi}_i$ with weights w_i (as a consequence of the exact coefficient evaluation). A similar procedure is followed for the distribution function f to get the same set of discrete velocity and weights pairs, that also satisfy the first three moments of f. The complete and mathematically heavy discretisation procedure is presented explicitly in (Krüger, Kusumaatmaja et al., 2017, Chapter 3).

The discretised velocities and corresponding weights obtained from the above procedure are termed as a velocity set $\{\boldsymbol{\xi}_i, w_i\}$. This set depends on the total number of discrete velocities chosen and the dimensional constraints on these velocities. In LBM parlance, a velocity set and the resulting velocity

1 Note that here we talking about integrals in the coefficient terms for the Hermite polynomial expansion (not shown in this chapter), and not the moment integrals in equations 5.1–5.4!

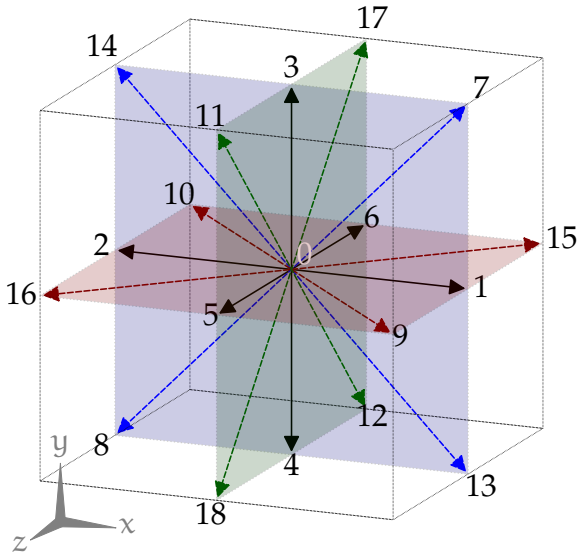

Figure 5.3: Visual representation of the D3Q19 velocity set. The D3Q19 uses 19 distinct velocity directions in 3D to discretise the velocity space. Velocity directions along the three majoy axes (in grey, bottom left) are shown as (black) solid-line arrows. The non-axial velocity directions are shown as dashed (coloured) arrows. The D3Q19 possesses 3 groups of co-planar velocities, with 6 velocities in each group. Theses 3 orthogonal (mutually and to the axes) planes are shown in the same colour as the in-plane non-axial velocity components. The velocity directions are labelled with their respective indices. The "rest" velocity with zero velocity magnitude, solely indicated by the index 0.

space discretisation is almost always denoted as DdQq, where d and q are placeholders for the number of physical dimensions and total number of discrete velocities chosen, respectively.

We employ the D3Q19 velocity set (with 19 velocities, in 3D) shown in figure 5.3. It turns out that for the D3Q19 velocity set (as well as for a few other frequently used sets) we get an unwieldy factor of $\sqrt{3}$ for the velocities ξ_i. Here, we go for another simplification, and absorb this factor into the definition of the molecular velocity, scaling all velocities as $\mathbf{c}_i = c_s \xi_i$, where $c_s = \Delta x/\sqrt{3}\Delta t$. The new re-scaled velocity set $\mathbf{c}_i$ is entirely in terms integer velocities, adapting nicely to boolean programming. The complete D3Q19 velocity set employed in this thesis is given explicitly in table 5.1. Interestingly, it can be shown that $c_s = \Delta x/\sqrt{3}\Delta t$ gives the speed of sound in the D3Q19 velocity discretisation (Viggen, 2014).

The equilibrium distribution function (equation 5.5) along the velocity direction $\mathbf{c}_i$ for isothermal flows can now be approximated in terms of Hermite polynomial expansion (truncated) as,

$$f_i^{eq} \approx w_i \rho \left(1 + \frac{c_{i,\alpha} u_\alpha}{c_s^2} + \frac{u_\alpha u_\beta (c_{i,\alpha} c_{i,\beta} - c_s^2 \delta_{\alpha\beta})}{2c_s^4} \right), \tag{5.7}$$

where $\delta_{\alpha\beta}$ is the Kronecker delta. Following the syntax of equation 5.7 for the velocity direction indicated by index i, the discrete distribution function can be written as f_i and the collision operator as Ω_i.

So far, we have seen that the discretisation of the velocity space was carried out such that the macroscopic variables would be recovered exactly by taking the moments of the distribution function over all discrete velocities of D3Q19. Thus we compute the macroscopic quantities as,

$$\rho = \sum_i f_i = \sum_i f_i^{eq} \qquad \text{and} \tag{5.8}$$

$$\rho u_\alpha = \sum_i f_i c_{i,\alpha} = \sum_i f_i^{eq} c_{i,\alpha}. \tag{5.9}$$

5.3.2 *Discretisation of time and physical space*

The discretisation of the physical space is carried out with the help of the method of characteristics (or the method of trajectories). The procedure for this discretisation is detailed in (Krüger, Kusumaatmaja et al., 2017, Chapter 3), and is not repeated here. The discretised Boltzmann equation is written as,

$$f_i(x_\alpha + c_{i,\alpha}\Delta t, t + \Delta t) - f_i(x_\alpha, t) = \Delta t \Omega_i. \tag{5.10}$$

This is a second order discretisation in physical space and time (Krüger, Kusumaatmaja et al., 2017, Chapter 4). Here, Δt is the discrete time step and the discrete physical distance is given by $\Delta x = c_{i,\alpha}\Delta t$. Δx defines a discrete set of point locations in the physical domain, which are termed as *lattice nodes*. The equation 5.10 is called the *lattice Boltzmann equation* (LBE).

We can see that the discretisation in the physical space and the temporal space are tightly linked in the LBM. This close connection between the two arises because we want the discrete particle populations f_i to always end up at a neighbouring lattice node after travelling a distance of Δx in each time increment Δt. In this discretised *Cartesian mesh*, a single lattice node taken along with the associated velocity set can be termed as a *unit lattice cell*. Now, it only remains to figure out an appropriate form of the discrete collision operator Ω_i.

Cartesian mesh
Mesh with square or cubic unit elements and all vertices separated by integer values

5.3.3 *BGK collision operator*

The original form of the collision operator Ω proposed by Boltzmann was a double integral, that accounted for particle collisions over all possible velocity directions. Around 80 years after Boltzmann, a much simpler, linearised collision operator was proposed by Bhatnagar, Gross and Krook (Bhatnagar,

Gross and Krook, 1954). This is the famous 'BGK' collision operator written as,

$$\Omega_i = -\frac{1}{\tau}(f_i - f_i^{eq}), \tag{5.11}$$

where, τ is a characteristic time, called the *relaxation time*.

τ represents the time scale needed for f_i to relax (change) to f_i^{eq}. Instead of modelling all the collision processes explicitly, the BGK operator simply models the "relaxation" (or the evolution) of the particle populations f_i towards their equilibrium state f_i^{eq}. The BGK assumes that this change is linear during the simulation time step Δt. When we state that the collision process takes f towards f^{eq}, this only indicates the process of local equilibration of the fluid. Globally, the fluid still remains in non-equilibrium.

Even with such a simplification of the collision process (equation 5.11), the LBM is able to reproduce macroscopic fluid behaviour. From the equations 5.8, 5.9 and 5.11, we can easily deduce that the zeroth and first moments of the BGK collision operator are zero. This is an important constraint for any collision operator to satisfy, in order to conserve mass and momentum during the collision process. There are other more advanced collision operators in the literature that improve the stability the solution, but we exclusively use the BGK in this thesis because of its simplicity, computational efficiency and correct reproduction of low Reynolds number flow physics.

5.3.4 *Lattice BGK algorithm*

We can now plug the BGK operator into the discrete LB equation 5.10. A simple rearrangement of the terms gives,

$$f_i(x_\alpha + c_{i,\alpha}\Delta t, t + \Delta t) = \left(1 - \frac{\Delta t}{\tau}\right) f_i(x_\alpha, t) + \frac{\Delta t}{\tau} f_i^{eq}. \tag{5.12}$$

The equation 5.12 is often termed as the lattice BGK equation (or LBGK for short). We can deduce (both mathematically and intuitively) that when $\tau/\Delta t < 1/2$, the equation 5.12 would become unstable, with f_i oscillating around f_i^{eq} with an increasing amplitude. Therefore, $\tau/\Delta t \geqslant 0.5$ is a necessary condition for stability when using the BGK collision operator for the LBM.

Most algorithms employing the LBGK split the equation into two distinct steps; *collision* and *streaming*. The equation 5.12 is split into,

$$f_i^\star(x_\alpha, t) = \left(1 - \frac{\Delta t}{\tau}\right) f_i(x_\alpha, t) + \frac{\Delta t}{\tau} f_i^{eq} \quad \text{; the collision step, and} \tag{5.13}$$

$$f_i(x_\alpha + c_{i,\alpha}\Delta t, t + \Delta t) = f_i^\star(x_\alpha, t) \quad \text{; the streaming step.} \tag{5.14}$$

This 2-step split of the particle population evolution equation, as well as the terms used for their description, are a legacy from the LGCA. But there is

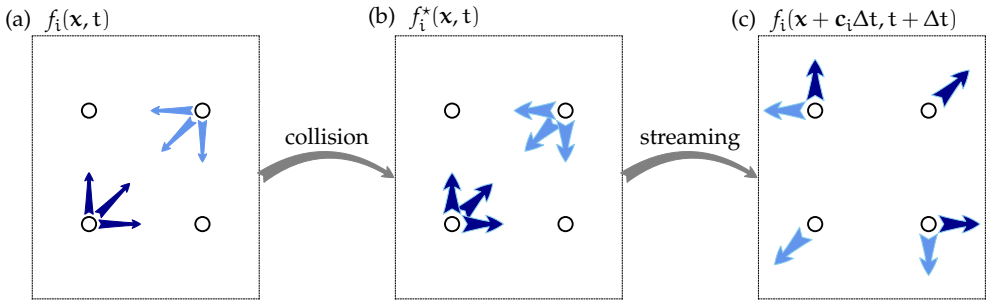

Figure 5.4: The process of *collision* and *streaming* illustrated for one time step in the LBM. The left panel (a) shows 4 lattice node neighbours with particle populations f (shown for 2 of them), along few representative discrete velocity directions, at time t. These populations undergo a process of *collision* locally at each node, and the populations are modified to $f^\star$ as shown in panel (b). Thereafter, the post-collision populations $f^\star$ *stream* towards their neighbour nodes with velocities given by the D3Q19 velocity set. They arrive at their respective neighbour nodes at time $t + \Delta t$ as shown in the right panel (c), completing one time step in the LBM. These are now the pre-collision populations f at their new nodes and the process repeats over the next time step, until end time.

a very good reason for keeping this structure for the LBM; the collision step in equation 5.13 is completely local at a lattice node. This lends very well for parallelisation and scalability of the simulation algorithm. The streaming is non-local and needs neighbour node information. However, it only involves an exchange of particle populations amongst neighbouring nodes, which is a computationally "light" process. The collision and streaming steps are visualised in figure 5.4. Note that both these operations take place in a single LBM time step (with an increment Δt).

The minimal LBM simulation algorithm is as follows.

1. Start at time $t = t_0$ with initialised particle populations at every node in the simulation domain.
2. From the particle populations, compute the macroscopic variables ρ and $\mathbf{u}$ using equations 5.8 and 5.9.
3. Then, using these values of ρ and $\mathbf{u}$, compute the equilibrium distribution function from equation 5.7.
4. The collision step: Modify particle populations at every lattice node using the equation 5.13.
5. The streaming step: Move (or stream) the post-collision populations to their neighbour lattice nodes (equation 5.14) with velocities according to the D3Q19 velocity set.
6. Increment the time counter by $+\Delta t$. This completes one time step for the LBM.

7. Return to step (2), and repeat the loop until the desired final time-step is reached.

This completes our discussion on the discretisation of the Boltzmann equation, leading to the LBM with the BGK collision operator. We now turn our attention to the handling of initial and boundary conditions in the LBM.

5.4 INITIAL AND BOUNDARY CONDITIONS

In this section we shall first deal with the boundary conditions, and then look at the initial conditions employed with the LBM in this work. In general, boundary conditions prescribe fixed scalar values or the gradients of scalar values or both, at the boundary of the simulation domain (section 4.2.1). For a microfluidic system these are defined in terms of the macroscopic variables. However, since the LBM works at the *meso*-scale, we have to prescribe the boundary conditions in terms of the unknown particle populations entering the domain at the boundaries. This needs to be done in a way such that the intended macroscopic boundary effect would be correctly reproduced.

The same argument holds true for prescribing the initial condition for the simulation; unknown particle populations at all lattice nodes have to be prescribed, such that they reproduce the corresponding macroscopic initial values correctly ($\rho = \rho_0$ and $\mathbf{u} = \mathbf{u}_0$ at initial time $t = t_0$). Fortunately, in our case the procedures for obtaining the unknown populations turn out to be quite simple.

As explained in section 4.2.1, we need two types of general fluid boundary conditions; the wall boundary and the periodic boundary. The wall boundary condition can be categorised as deformable (in the case of the surface of a deformable particle moving in the fluid) or fixed (the walls confining the fluid). The wall boundary condition for a deformable particle is handled using the immersed boundary method (IBM). The IBM is a specialised scheme for treating deformable fluid-solid coupled interactions. In the IBM, the presence of the moving wall is impressed upon the ambient fluid using an external body force density added to the LBE (and not through direct assignment of particle populations). Therefore, this method is not considered to be a LB-style boundary condition and the IBM is treated separately in chapter 7.

5.4.1 *Fixed wall boundaries*

We are now left with fixed boundaries that form the confining walls of the deterministic lateral displacement (DLD) device. These walls impose the no-slip velocity boundary condition. For stationary walls (as in the case of the DLD) this means the macroscopic fluid velocity at the wall $\mathbf{u}_w$ equals 0. The simplest way to impose the zero velocity no-slip wall boundary condition in the LBM is called the *bounce-back* scheme. In this work, we use a variation of this scheme called the *half-way bounce-back*, illustrated in figure 5.5.

We briefly discuss the idea of the half-way bounce-back scheme for zero wall velocity $\mathbf{u}_w = 0$. This scheme modifies the streaming step of the LBGK

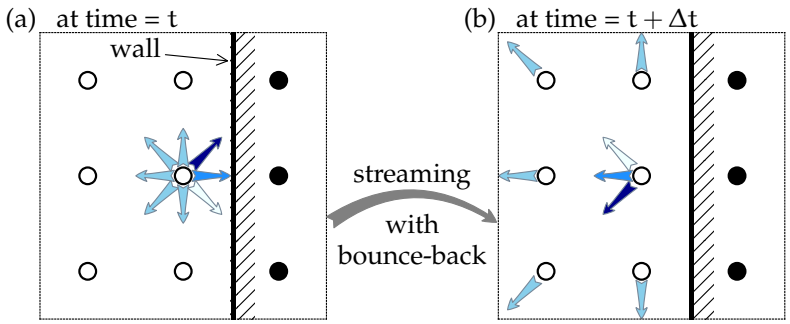

Figure 5.5: Illustration for the half-way bounce-back scheme for a stationary no-slip wall. This scheme modifies the *streaming* step. Wall boundary is created by adding "solid" lattice nodes (filled circles) that do not take part in the flow solution. The lattice nodes participating in the flow solution are termed "fluid" nodes (empty circles). Post collision particle populations streaming towards a solid node $f^{\star,\bullet}$ meet the wall mid-way between the solid and fluid nodes at time $t + \Delta t/2$. Velocities of these populations are reversed by 180°, and the populations end up at the original node after time $t + \Delta t$.

solution algorithm. In order to implement this scheme we define extra lattice nodes that do not participate in the fluid flow solution. These extra nodes are positioned right next to, but outside the solution domain wall. These are referred to as "obstacle" or "solid" nodes, identifying the solid wall material (see figure 5.5). While the lattice nodes that participate in the fluid flow solution are termed as "fluid" nodes. The solid nodes become neighbours of the fluid nodes that are right next to the domain wall boundary. Strictly speaking, these solid nodes are not necessary for the implementation of the bounce-back scheme, but they greatly simplify its implementation.

The half-way bounce-back scheme modifies the streaming step (5) of the LBGK algorithm. Recalling equation 5.14, we know that the streaming step replaces older particle populations at a fluid node with populations from the neighbour nodes according to the D3Q19 velocity set (table 5.1). But what would happen at lattice nodes next to a wall boundary? Along certain velocity directions, these fluid nodes have solid node neighbours, which cannot supply the unknown particle populations since they do not participate in the LBGK solution algorithm. Along these velocity directions, the half-way bounce-back rule come into play. This rule can be written as,

$$f_{i-}(x_\alpha, t + \Delta t) = f_i^{\star,\bullet}(x_\alpha, t), \tag{5.15}$$

where, the superscript '$\bullet$' indicates post-collision populations that would cross the wall and move towards solid lattice nodes and the index '$i-$' indicates a velocity set direction such that $\mathbf{c}_{i-} = -\mathbf{c}_i$.

The streaming step (5) modified due to the half-way bounce-back rule can be interpreted as follows. The post-collision particle populations leave the boundary fluid node at time t. Out of these, the set of particle populations that would cross the wall and move into the solid domain $f_i^{\star,\bullet}$ meet the wall

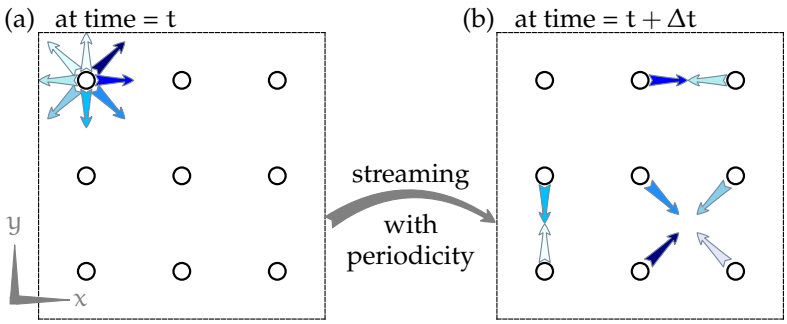

Figure 5.6: Illustration for periodic boundary condition along both x and y directions. The streaming step for fluid nodes (in a 3×3 domain) that lie next to periodic boundary pairs is modified. At these nodes, certain post collision populations leave the fluid domain based on their velocity direction $f^{\star,\circ}$, through one periodic boundary. These populations re-enter the domain through the second periodic boundary belonging to the same pair. For simplicity, periodic boundary pairs are considered mid-way between lattice nodes.

(located midway between the fluid and solid nodes) at time $t + {}^{\Delta t}/_{2}$. They are reflected by 180° at the boundary wall, and travel back in the opposite direction with velocity $-\mathbf{c}_i$. They arrive at the original fluid node at time $t + \Delta t$.

The bounce-back scheme conserves mass, since effectively none of the particle populations leave the domain at the wall boundaries. For a stationary wall modelled with the half-way bounce-back scheme, the momentum computed halfway between the solid and fluid nodes is zero. This scheme therefore reproduces a no-slip wall approximately mid-way between a solid node and a neighbouring fluid node shown in figure 5.5. The exact location of the wall, however, depends on τ and is an advanced topic of discussion in the LBM (Krüger, Kusumaatmaja et al., 2017, Chapter 5).

The half-way bounce-back rule is second order accurate in space for a planar wall with a unit normal that right-aligns with the Cartesian lattice node mesh. However, in cases where the wall has an arbitrary shape (e. g. cylinder), it is found that the scheme reduces to first order accuracy (Ginzbourg and d'Humières, 1996). This is because the bounce-back scheme when used with a curved wall on a Cartesian mesh, reproduces it inexactly as straight lines connected by step changes. This is referred to as the "staircase" approximation for a curved wall boundary.

5.4.2 *Periodic boundaries*

In comparison to the wall boundary condition, periodic boundaries have an even simpler implementation in the LBM. The periodic boundary condition also modifies the streaming step (5) of the LBGK algorithm. Boundaries periodic in the x and y directions for a 3×3 lattice node domain are shown in figure 5.6. Lattice nodes that lie next to a matched pair of periodic boundar-

ies, become lattice nodes neighbours. For example, in figure 5.6, the first and third vertical (node) columns are periodic node neighbours (similarly, first and third node rows). If fluid node at any location $\mathbf{x}_\alpha$ is the periodic neighbour for the fluid node at position $\mathbf{x}_\beta$, we can write the modified streaming step as,

$$f_i(\mathbf{x}_\alpha, t + \Delta t) = f_i^{\star,\circ}(\mathbf{x}_\beta, t), \tag{5.16}$$

where, the superscript '$\circ$' indicates particle populations that would leave the fluid domain through a periodic boundary during streaming. Here, the post collision particle populations are streamed to their corresponding periodic neighbour nodes, without modifying the original velocity direction.

Since an identical set of particle populations leaves and re-enters the fluid domain in every time step Δt, periodic boundaries also conserve mass and momentum globally. Of course, the periodic mapping of lattice nodes ($\mathbf{x}_\alpha \rightleftharpoons \mathbf{x}_\beta$) needs to be pre-defined based on the physical geometry. This is usually done with the help of "ghost" lattice nodes (similar to the obstacle nodes with the bounce-back scheme) or directly with the help of a periodicity mapping function. We have now seen both the boundary handling schemes for the LBM employed in this thesis.

5.4.3 *Initialisation*

At the start of a fresh LBM simulation ($t = t_0$), we would not have any particle population values at any of the lattice nodes in the domain. Before proceeding with the step (2) of the LBGK algorithm, we need to set these values. This needs to be carried out in such a way that the moments of the initial particle populations reproduce the correct ρ and $\mathbf{u}$ distribution over the physical domain. Hence, we use the equilibrium particle populations (obtained from equation 5.7) to initialise values at all nodes in the simulation.

The initialisation of a simulation is important only for unsteady flows where the final state of interest depends on the initial state. The initial state is not very important in the case of flows where the memory of the initial state is lost after a number time steps such time-periodic, steady or dense suspension flows. The simulations in this thesis fall in the second category. Therefore, the values for our initial macroscopic variables $\mathbf{u}(\mathbf{x}_\alpha, t = t_0)$ and $\rho(\mathbf{x}_\alpha, t = t_0)$ (in the equation 5.7) can be arbitrary but physical; we generally set $\mathbf{u}_0 = \mathbf{u}(\mathbf{x}_\alpha, t = t_0) = 0$ and $\rho_0 = \rho(\mathbf{x}_\alpha, t = t_0) = 1$.

5.5 FORCING

As discussed in chapter 4, a constant fluid body force density (per unit volume) is used to mimic the average pressure drop that drives flow through a DLD device. Unlike conventional CFD methods, we cannot simply add a force density term to the discretised LB equation 5.10. Adding a force density to the LBE is non-trivial for two reasons; The force term in the Boltzmann

equation 5.6 appears paired with the gradient of f in the velocity space. And, if incorrectly included, the force density can bring in spurious terms into the momentum balance equation (Krüger, Kusumaatmaja et al., 2017, Chapter 6).

The discretisation of the term containing the external force density (in the equation 5.6) is carried out similarly to that for f^{eq}. The velocity space discretisation follows the Hermite polynomial series expansion and the use of Gauss-Hermite quadrature mentioned in section 5.3. The detailed velocity space discretisation for the body force term is given in (Krüger, Kusumaatmaja et al., 2017, Chapter 6). This discretisation gives us the discrete velocity form of the LB equation with an external force, written as,

$$\frac{\partial f}{\partial t} + c_{i,\alpha}\frac{\partial f}{\partial x_\alpha} = \Omega_i + f_i, \tag{5.17}$$

where, f_i represents the discretised force term, along the i^{th} direction for D3Q19.

Similar to equation 5.7, f_i can also be expressed as a truncated Hermite polynomial series. However, rather than going down this route of explicitly defining the force for each velocity direction, the f_i in equation 5.17 can be absorbed into the collision operator Ω_i. In the LBM, this approach is known as the *Shan-Chen forcing* scheme (Shan and Chen, 1993).

Hence, Ω_i needs to reproduce both the relaxation process as well as (implicitely) the effect of the imposed body force on the populations. This is done by modifying equilibrium distribution function f_i^{eq} in the collision operator. Normally, f_i^{eq} would be computed from the local ρ and $\mathbf{u}$ at the lattice node. However, when a body force density $\mathbf{f}$ imposed on the fluid, the velocity entering the calculation of f_i^{eq} is modified as,

$$u_\alpha^{eq} = \frac{1}{\rho}\sum_i f_i c_{i,\alpha} + \tau\frac{\Delta t}{\rho} f_\alpha, \tag{5.18}$$

where, the superscript '^{eq}' simply recognises that the velocity in equation 5.18 is not the macroscopic velocity of flow $\mathbf{u}$. It is the modified velocity entering in the calculation of f_i^{eq} in order to implicitly introduce a body force $\mathbf{f}$ into the BGK collision operator.

In the presence of a body force, the macroscopic velocity of flow also needs a correction in order to stay second order space-time accurate (Guo, Zheng and Shi, 2002) and is given as,

$$u_\alpha = \frac{1}{\rho}\sum_i f_i c_{i,\alpha} + \frac{\Delta t}{2\rho} f_\alpha. \tag{5.19}$$

Equation 5.19 is a correction for the first moment of the particle populations in the presence of forces. This corrected equation replaces the one in 5.9 given earlier. With this, we complete our discussion on the discretisation of the Boltzmann equation for obtaining the LB equations needed in this thesis.

5.6 RECOVERING NAVIER-STOKES FROM THE LBM

In this section we shall address the question (left open in section 5.2); How does one get a solution for the incompressible NS equation 4.2 from the Boltzmann equation solved by the LBM? The mass conservation NS equation 4.1 is obtained exactly by taking the zeroth moment of the LBE. However, taking the first moment of the LBE leads us only to the general Cauchy momentum balance equation.

This link was first established in the 1910s, independently by Chapman and Enskog, using a perturbation analysis for the Boltzmann equation. Here, the distribution function f is expanded as a perturbation series about its equilibrium f^{eq} in decreasing orders of the Knudsen number. This multi-scale perturbation analysis is therefore called the *Chapman-Enskog analysis* (Chapman, 1952) and can be applied to the discrete LBE (Krüger, Kusumaatmaja et al., 2017, Chapter 4). This analysis shows us that the viscous stress term in NS equations is related to the non-equilibrium part of the distribution function $f^{neq} = f - f^{eq}$. From this, we can compute the viscous stress tensor as,

$$\sigma_{\alpha\beta} \approx -\left(1 - \frac{\Delta t}{2\tau}\right) \sum_i c_{i,\alpha} c_{i,\beta} f_i^{neq}. \tag{5.20}$$

The computation of the viscous stress tensor in equation 5.20 is completely local to the lattice node and no spatial derivatives need to be computed. This calculation is not necessary for the LBGK algorithm, and is carried out only when the fluid viscous stress state needs to be evaluated.

Furthermore, the *Chapman-Enskog analysis* of the LBE gives us the following relations in order to correctly reproduce the NS momentum equation with the BGK collision approximation. The pressure variation is obtained from,

$$p - p_0 = c_s^2(\rho - \rho_0), \tag{5.21}$$

where, $c_s = \Delta x/\sqrt{3}\Delta t$ is the sound speed for the D3Q19 velocity set, ρ_0 is the initial density of the fluid and p_0 is an arbitrary datum pressure corresponding to the initial density ρ_0. The equation 5.21 is therefore equivalent to the equation of state 4.3 for the *meso*-scopic LB system.

Importantly, we also obtain the relations for fluid viscosity,

$$\mu = c_s^2 \rho \left(\tau - \frac{\Delta t}{2}\right), \tag{5.22}$$

$$\mu_B = \frac{2}{3}\mu, \tag{5.23}$$

where, μ is the dynamic viscosity and μ_B is the bulk viscosity of the fluid.

Hence, we see that the free parameter τ defines the viscosity for a simulation with the LBM. This result should not come as a surprise. The relaxation time τ is contained within the collision process and is defined as the time

scale needed for f to go to f^{eq}. In other words, τ represents a molecular time scale of the order of the time between molecular collisions. This time scale therefore decides the value of macroscopic transport coefficients such as the dynamic viscosity μ (or momentum diffusion coefficient).

5.7 REMARKS

The LBM evolved in the late 1980s from modifications to the LGCA (McNamara and Zanetti, 1988). The idea behind these modifications was to get rid of some major shortcomings of the LGCA such as statistical noise (Wolf-Gladrow, 2000, Chapter 5) in fluid flow simulations. As a result, some of the terminology employed in the LBM is a legacy from the LGCA methods. Some of these names are quite informative, and give an intuitive meaning to the method. The noun "lattice" in the name of the method, for example, indicates that the mesh in this method is unlike that in the conventional CFD methods. Indeed, the Cartesian fluid mesh employed in this thesis, with regularly spaced nodes with links inter-connecting D3Q19 velocity links them, looks like latticework.

It may seem surprising and counter-intuitive to some that in the LBM, the incompressible pressure field is obtained from density variation (equation 5.21). If truth be told, the LBM outlined above solves the compressible NS equations with an inexact bulk viscosity μ_B, given in equation 5.23. Therefore, the degree of compressibility in our LBM simulations is an important factor, and needs to be kept close to the incompressible limit. Hence, with the LBM, we end up solving for a mildly compressible fluid flow (which is closer to the physical picture), to get a solution for incompressible NS equations.

The compressibility error in flow solutions come from the inexact estimation of the bulk viscosity μ_B in the LBM. The compressibility effect is given by the local Mach number. Hence, the Mach number must be kept sufficiently low so that the μ_B does not play a role in the solution. Generally, if the Mach number $Ma < 0.2$, the flow can be considered incompressible.

Another drawbacks of the LBM has to do with setting the simulation flow viscosity. Since the viscosity is linked to the relaxation time (equation 5.22) in the BGK collision operator, the choice of μ is strongly restricted by stability and accuracy constraints in the LBGK scheme (Krüger, Kusumaatmaja et al., 2017, Chapter 4). Also, being an inherently time dependent method, the LBM is not particularly well suited for obtaining steady flow solutions.

Furthermore, representing curved boundaries accurately in the LBM is a non-trivial task, and requires interpolations of particle populations. The case for moving curved boundaries is even more complicated. However, we note that both these cases are probably not as complicated and computationally intensive as body fitted meshing and mesh regeneration employed in conventional CFD. Unlike bounce-back, other type of LBM boundaries such as the pressure or velocity inlet/outlet are also not straightforward to implement.

The LBM is formally second order accurate in space and time. However, as discussed in section 5.4, the bounce-back wall boundary condition (for

curved boundaries employed in this thesis) limited to first order accuracy in space-time. The IBM is also a first order space-time accurate (see section 7.4) coupling method. This causes the fluid solution to degenerate to a first order space-time accuracy in the present work. As we are mostly concerned with predicting particle trajectories in the DLD, this fact does not pose much of a problem. Our purpose is served by increasing the mesh resolution sufficiently in order to suppress discretisation errors.

The LBM by itself is a fascinating and constantly advancing research topic. For those wanting gain deeper understanding of the LBM and use it for solving the myriad of hydrodynamic problems, (Krüger, Kusumaatmaja et al., 2017) and (Viggen, 2014) are both insightful reads.

Table 5.1: The Gauss-Hermite quadrature weights w_i and the velocities $\mathbf{c}_i$ for the D3Q19 velocity set listed explicitly for all 19 indices.

i	0	1	2	3	4	5	6	7	8	9	10	11	12	13	14	15	16	17	18
w_i	$1/3$	$1/18$	$1/18$	$1/18$	$1/18$	$1/18$	$1/18$	$1/36$	$1/36$	$1/36$	$1/36$	$1/36$	$1/36$	$1/36$	$1/36$	$1/36$	$1/36$	$1/36$	$1/36$
$c_{i,x}$	0	+1	-1	0	0	0	0	+1	-1	+1	-1	0	0	+1	-1	+1	-1	0	0
$c_{i,y}$	0	0	0	+1	-1	0	0	+1	-1	0	0	+1	-1	-1	+1	0	0	+1	-1
$c_{i,z}$	0	0	0	0	0	+1	-1	0	0	+1	-1	+1	-1	0	0	-1	+1	-1	+1

6

PARTICLE DEFORMATION – FINITE ELEMENT ENERGY MODEL

In this chapter we outline the computation of the particle membrane deformation forces employing surface discretisation, finite element method (FEM) and membrane energetics. Using the FEM approach, the 2D membrane of each particle is sub-divided into a finite set of "elements". The internal forces generated in each discrete element are then computed from the elastic energy stored in the element during its deformation. Additionally, we compute "penalty" forces due to change in the membranes curvature, area and enclosed volume. These forces tend to drive the deformed particle membrane back to its equilibrium shape. For the sake of brevity, we term this combined numerical approach for membrane deformation mechanics as finite element energy model (FEEM).

The ideas on continuum deformation energy model, and the resulting forces were presented previously in the chapter 4, for a 2D closed membrane. The aim of this chapter is to provide the discretised equations for this deformation energy model. Hence, we recommend the reader go through the section 4.3 before continuing. At the end of this chapter the reader will have gained an understanding of the FEM discretisation of the membrane, and using this FEM mesh to compute the deformation forces as described in section 4.3. The code employed for the computations outlined in this chapter was directly ported from that used in (Krüger, 2012). The reader can find further details on discrete membrane energetics, force derivations and benchmark tests there.

We start the chapter by looking at membrane discretisation in section 6.1. We then discuss the strain energy and force computation in section 6.2. The bending energy and force contributions are discussed in section 6.3. The discretised penalty force computations for conserving the total surface area and the enclosed membrane volume are provided in section 6.4. We conclude the chapter with a few short observations in section 6.5.

6.1 MEMBRANE DISCRETISATION

In this section, we look at the particle membrane discretisation needed for the FEM calculations of membrane strain deformation. We use 2D planar triangular elements to discretise the surface of the particle membrane. The triangular elements are interconnected, forming the unstructured particle mesh.

Each triangular element of the mesh possesses two attributes; "nodes" and "faces". The face of a triangular element is defined by its area normal. While the elemental nodes lie at the vertices of the triangular faces. Each node is shared between many connected triangular elements (upto 6 in figure 6.1), while each face is exclusive to a single element.

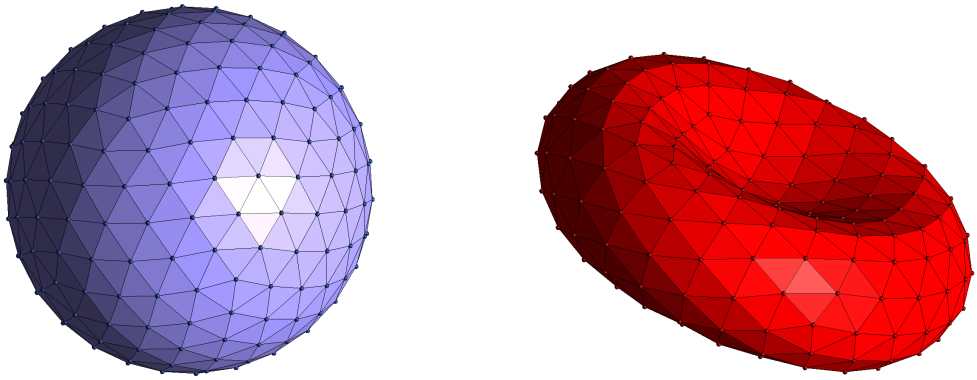

(a) Unit spherical mesh (b) Unit red blood cell mesh

Figure 6.1: The two types of particle meshes employed; (a) the spherical mesh and (b) the red blood cell (RBC) mesh. Both the meshes shown here have 500 triangular elements each (500 faces and 252 nodes). The nodes at the vertices of the element are shown as spherical glyphs. The spherical mesh is generated starting from a *regular icosahedron*, and performing repeated subdivisions of its elements. The RBC mesh is generated from the spherical mesh by translating the mesh nodes along the axis of rotational symmetry for the resulting RBC mesh. The transformation equation used here has been obtained from well established experimental measurements of the physiological RBC geometry by Evans and Fung.

This tells us that shared nodes decide the interconnectivity of the mesh elements. The connecting line between any two nodes forms the "edge" of a face. Each edge is shared by exactly 2 faces, if the membrane mesh has no free edges (the case for cellular membranes). We term two elements as neighbours if they have an edge (or two nodes) in common. Example meshes for a red blood cell (RBC) and a spherical polystyrene bead are shown in figure 6.1.

6.1.1 *Mesh generation*

The degree of homogeneity and spatial isotropy of membrane surface discretisation can play an important role in deciding the success or failure of particle laden flow simulation (Krüger, Varnik and Raabe, 2011). Towards this end, the procedure adopted to generate the particle mesh becomes important. To obtain the particle mesh, we start from a *regular icosahedron*, circumscribed inside a sphere of unit radius. Following the procedure given in Krüger, Varnik and Raabe (2011), new nodes are generated by bisecting the edges of the regular icosahedron. These nodes are then radially moved on to the circumscribing unit sphere. The newly generated edges are again bisected and the new nodes moved, until a spherical mesh (with unit radius) of sufficient resolution is obtained.

regular icosahedron
One of five Platonic solids; with 20 equilateral triangles as faces, 12 vertices and 30 edges of equal length

This unit spherical mesh can be scaled to the necessary radius quite easily, and is used to simulate spherical particles, such as rigid polystyrene beads, in this thesis. An additional step is needed in order obtain the mesh for an RBC. All nodes of the (previously generated) unit spherical mesh are "squashed"

or re-mapped along an axis (of symmetry) of the original icosahedron, such that the nodes satisfy the equilibrium RBC profile equation 4.4. This chosen direction becomes the new axis of rotational symmetry for the RBC mesh. As before, the mesh for a given RBC radius can be obtained by simply scaling this unit RBC mesh.

This procedure gives a high quality spherical mesh in terms of element homogeneity (edge lengths, face areas, angle distribution) as seen in figure 6.1a. Also, the sub-divided mesh remains symmetric about the original icosahedron symmetry axes. Mesh homogeneity is retained to a large degree, even after the nodal re-mapping to obtain the RBC mesh, as seen in figure 6.1b. Krüger, Varnik and Raabe show that this procedure gives improved results for suspended deformable particles when compared with other meshing techniques, such as the tool `gmsh` (Geuzaine and Remacle, 2009). Further details on particle meshing, and interfacing with the LBM solver are found in Chapter 8, Krüger (2012).

6.2 FEM FOR STRAIN DEFORMATION

In this section, we go over the main ideas from the FEM. These are used for computing the membrane strains and the resulting deformation forces. In the FEM, a material is discretised into a finite number of elements. A solution for the stress-strain state of the material is then obtained discretely over each element (Sadd, 2014, Chapter 16). In our case, the material is a hyperelastic closed 2D membrane, whose deformation is governed by Skalak's constitutive law, as discussed previously in section 4.3.2.1. All further discussion on the FEM in this section keeps this specific context in mind.

As outlined in section 6.1, we use 2D planar triangular elements for membrane discretisation. One such triangular element is shown in figure 6.2. We now make the important assumption that the material displacement vector $\mathbf{S}$, (recall section 4.3.2) varies linearly over each triangular mesh element. This is written as

$$S_\alpha(X,Y) = d_1 + d_2 X + d_3 Y, \tag{6.1}$$

where d_i for $\{i = 1,2,3\}$ are some constant coefficients, and (X,Y) are the planar Cartesian coordinates for the triangular geometry.

In order to obtain $\mathbf{S}$ over the triangular element, the (boundary) nodal displacements $\mathbf{S}_n$ for the three nodes $n = \{1,2,3\}$ are used. Substituting $\mathbf{S}_n$ into equation 6.1, a relation for $\mathbf{S}(X,Y)$ can then be obtained as

$$S_\alpha(X,Y) = \phi_1 S_{1,\alpha} + \phi_2 S_{2,\alpha} + \phi_3 S_{3,\alpha} = \sum_{n=1}^{3} S_{n,\alpha}\phi_n(X,Y), \tag{6.2}$$

where $\mathbf{S}(X,Y)$ is formulated as a linear combination of the individual displacements at the three nodes $\mathbf{S}_n = \{\mathbf{S}_1, \mathbf{S}_2, \mathbf{S}_3\}$. From here on we always

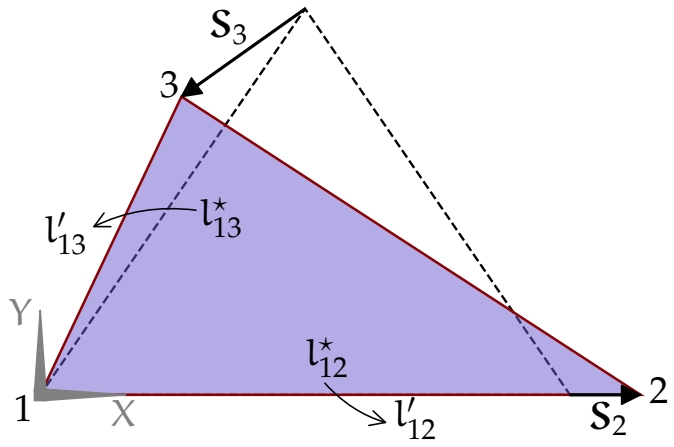

Figure 6.2: Sketch for the deformation of a single triangular element of the membrane mesh. The undeformed (equilibrium) shape of the element is shown as an unfilled triangle with dashed edges. The deformed shape for the element is shown with a filled (purple) triangle with continuous (brown) edges. The deformed triangular shape has been transformed (rotated and translated) onto the undeformed configuration. The transformation is carried out such that the node 1 coincides, and the edge connecting nodes 1 and 2 overlaps, so as to simplify the nodal displacements to $\{\mathbf{S}_1 = 0, \mathbf{S}_2 = S_{2,X}, \mathbf{S}_3\}$. The triangle sides get deformed from $\{l^\star_{12}, l^\star_{13}\}$, to $\{l'_{12}, l'_{13}\}$, respectively. The force due elastic deformation of the triangular element is computed, solely from the three nodal displacements, in the rotated reference frame. The force is then transformed back to the original coordinate frame.

use 'n' as the index for elemental nodes. Here, $\phi_n(X, Y)$, $n = \{1, 2, 3\}$ are called "shape functions" that provide the interpolation weights for deformation within a triangular element. The shape functions also inherit a linear form (due to the assumed linearity in equation 6.1) and can be written as

$$\phi_n(X, Y) = a_n + b_n X + c_n Y, \tag{6.3}$$

where the coefficient set $\{a_n, b_n, c_n\}$, for each node n, depends solely on the initial undeformed triangular element configuration. These are determined by evaluating the shape functions ϕ_n at their corresponding nodal positions $\mathbf{X}_n$. That is, the interpolation weights provided by ϕ_n need to be constrained such that, when $\mathbf{X} = \mathbf{X}_n$, the nodal displacements $\mathbf{S} = \mathbf{S}_n$. This constraint can be written as, $\phi_n(\mathbf{X}_m) = \delta_{nm}$, with $\{n, m\} = \{1, 2, 3\}$, where δ is the Kronecker delta.

Now, if we take the gradient of the equation 6.2 the result would be a constant value, independent of coordinates X and Y. Recall from section 4.3.2 that the deformation gradient tensor $\mathbf{D}$ is computed in a similar fashion. Thus, the tensor $\mathbf{D}$ is constant over the face of an element. $\mathbf{D}$ depends only on the shape function coefficients $\{a_n, b_n, c_n\}$, and nodal displacements $\mathbf{S}_n$. We need to find $\mathbf{D}$, in order to compute Skalak, Tozeren et al.'s strain energy

density functional for each element, obtained from the modified invariants of Green's tensor $\mathbf{D}^T\mathbf{D}$.

We can further simplify our calculations for $\mathbf{D}$, since we know that $\mathbf{D}^T\mathbf{D}$ is invariant under coordinate transformation (recall section 4.3.2.1). Thus, we rotate and translate each deformed triangular membrane element onto the plane containing its undeformed state, in the coordinates space (X, Y). This is always done such that the one vertex (node $n = 1$) of the deformed triangle coincides with that from its undeformed state. And, one face edge (between nodes $n = 1$ and $n = 2$) of the deformed and undeformed triangles overlaps, as shown in figure 6.2. In the rotated frame, The nodal displacements are now reduced to $\{\mathbf{S}_1 = 0, \mathbf{S}_2 = S_{2,X}, \mathbf{S}_3\}$, which greatly simplifies calculations.

Referring to figure 6.2, we name undeformed element edge lengths $l^\star_{12}$ and $l^\star_{13}$, as measured between nodes 1–2 and 1–3, respectively. The corresponding deformed lengths are l'_{12} and l'_{13}, with the elemental displaced state given as $\mathbf{X}' = \mathbf{X} + \mathbf{S}$. Let the undeformed and deformed angles subtended by these edges, l_{12} and l_{13} be $\varphi^\star$ and φ', respectively. Using these notations in the rotated coordinates, the deformation gradient tensor $\mathbf{D}$, is found to be (Gompper and Schick, 2008),

$$D_{\alpha\beta} = \begin{bmatrix} \frac{l'_{12}}{l^\star_{12}} & \frac{1}{\sin\varphi^\star}\left(\frac{l'_{13}}{l^\star_{13}}\cos\varphi' - \frac{l'_{12}}{l^\star_{12}}\cos\varphi^\star\right) \\ 0 & \frac{l'_{13}}{l^\star_{13}}\frac{\sin\varphi'}{\sin\varphi^\star} \end{bmatrix}. \tag{6.4}$$

Once the deformation gradient is known, we compute the principal invariants for each triangular element as,

$$I_1 = \mathrm{tr}\big(D_{\gamma\alpha}D_{\gamma\beta}\big) - 2 \qquad \text{and} \tag{6.5}$$

$$I_2 = \det\big(D_{\gamma\alpha}D_{\gamma\beta}\big) - 1, \tag{6.6}$$

where, tr() and det() indicate the trace and determinant operations over tensor components.

From $\{I_1, I_2\}$, we now obtain the elastic energy density ϵ^s for the element by using the Skalak's law (see equation 4.10). The total elastic deformation energy E_S of the membrane is then obtained by integrating over the total membrane surface area as $E_S = \oint \epsilon^s \, dA$, In the discrete form, this becomes $E_S = \sum_f a^\star_f \epsilon^s_f$. Here, $a^\star_f$ is the undeformed area of the elemental face with index 'f', which runs over all mesh faces.

The forces generated due to strain deformation in the element are obtained from the principle of virtual work as,

$$F^S_{n,\beta} = -\frac{\partial E_S(\{X'_{n,\beta}\})}{\partial X'_{n,\beta}}. \tag{6.7}$$

The strain force $\mathbf{F}^S_n$ is computed at the nodal position n of the triangular element. Infinitesimal virtual displacements of the nodes in equation 6.7 are

considered post-deformation, hence the use of $\mathbf{X}'_n$ here. Here, the strain force $\mathbf{F}^S_n$, lies in the plane of the triangular element, i. e., the component $F^S_{n,Z} = 0$. After completing above calculations, the force vector $\mathbf{F}^S_n$ is rotated back to the original coordinate space, and the force contributions from all faces attached to each node n summed up. The translational and rotational invariance of the underlying energy model ensures that the computed linear and angular momenta of all the elements is conserved.

6.3 DISCRETE BENDING ENERGETICS

In order to obtain a discrete form for the bending energy, we revisit the section 4.3.3, and inspect the equation 4.11. Here, the difference between deformed and spontaneous local curvatures $(H(\mathbf{r}) - H^0)$ sets the bending energy (at position $\mathbf{r}$ on the membrane). For our triangulated mesh, an efficient way to quantify membrane local curvature deviations is by making use of the difference in angle between surface normals of two neighbouring triangular faces (Kantor and Nelson, 1987). A pair of triangular elements (faces) are considered neighbours if and only if they share an edge (or 2 nodes). With this in mind, we can start without the spontaneous curvature term and write the bending energy E^b, with the form,

$$E^b = \frac{\tilde{\kappa}^b}{2} \sum_{\langle i,j \rangle} (\hat{n}_{\alpha,i} - \hat{n}_{\alpha,j})^2 = \tilde{\kappa}^b \sum_{\langle i,j \rangle} (1 - \hat{n}_{\alpha,i} \hat{n}_{\alpha,j}), \tag{6.8}$$

where the index pair $\langle i, j \rangle$ runs over all neighbouring faces of the discretised membrane mesh, and $\hat{\mathbf{n}}$ represents the unit normal for an elemental face. Here, $\tilde{\kappa}^b$ is the modified bending modulus. $\tilde{\kappa}^b$ needs to be rescaled correctly in order to obtain results consistent with those from equation 4.11, for small bending deformation angles (Gompper and Kroll, 1996). If θ_{ij} is the angle between a pair of neighbouring triangular faces with indices $\langle i, j \rangle$, we can write $\hat{\mathbf{n}}_i \cdot \hat{\mathbf{n}}_j = \cos\theta_{ij}$ in the equation 6.8.

Now, expanding $(1 - \cos\theta)$ in θ and assuming small angular deflections, we obtain the relation,

$$E^b \approx \frac{\tilde{\kappa}^b}{2} \sum_{\langle i,j \rangle} \theta^2_{ij}, \tag{6.9}$$

by dropping the higher order terms ($> \mathcal{O}(\theta^3)$) in the expansion, and substituting the same in equation 6.8. Equation 6.9, describes a membrane bending energy that varies as a function of the angular configuration of the membrane mesh elements.

As clarified in section 4.3.1, equilibrium RBC shapes manifest due to minimisation of the membrane bending energy, subject to surface area and enclosed volume constrains (Gompper and Schick, 2008). However, my work assumes this equilibrium shape as the biconcave discoid, parametrised by

Evans and Fung (1972) and approximated by the discretised mesh shown in figure 6.1b. This equilibrium shape is an input to the simulation and any deviation from this shape should be penalised by an increase in the membrane bending energy. This idea can be incorporated into equation 6.9 as

$$E_B = \frac{\tilde{\kappa}^b}{2} \sum_{\langle i,j \rangle} (\theta_{ij} - \theta^\star_{ij})^2 = \tilde{\kappa}^b \sum_{\langle i,j>i \rangle} (\theta_{ij} - \theta^\star_{ij})^2, \tag{6.10}$$

where $\theta^\star_{ij}$ is the angle between a pair of neighbour faces indexed by $\langle i, j \rangle$, computed from the undeformed RBC shape. Equation 6.10 gives the final form of the discretised bending energy.

The set of equilibrium angles $\{\theta^\star_{ij}\}$ for a given mesh are computed only once, from the initial undeformed mesh. These angles are "remembered" by the deforming RBC mesh at each subsequent time step. We can think of this idea as an alternative realisation of the shape memory of the RBC membranes (Fischer, 2004). By computing bending energy from equation 6.10, we avoid a direct discretisation of the membrane curvature, thus simplifying and speeding up the numerics needed for the membrane bending energy.

Equation 6.10 can be seen as describing a membrane mesh bending energy that possesses a minimum when $\{\theta_{ij}\} = \{\theta^\star_{ij}\}$, for all neighbouring face pairs $\langle i, j \rangle$ in the particle mesh. When the membrane configuration deviates from its "remembered" equilibrium angles $\{\theta^\star_{ij}\}$, E_B is finite and larger than zero. A discrete "penalty" force $\mathbf{F}^B_n$ can now be computed at each element nodes. This force is directed such that it tends to restore the original configuration. Using virtual work principle as before, this force is computed as

$$F^B_{n,\beta} = -\frac{\partial E_B(\{X'_{n,\beta}\})}{\partial X'_{n,\beta}}. \tag{6.11}$$

6.4 AREA AND VOLUME ENERGETICS

Previously in section 4.3.4, we saw the (harmonic) energy functions defined for total membrane surface area and enclosed volume. It is reasonably straightforward to obtain the discrete counterparts for these energy potentials (Seifert, 1997). The total membrane area energy is computed from the discretised mesh faces by using the relations,

$$A = \sum_j a_j \qquad \text{and} \qquad A^0 = \sum_j a^\star_j, \tag{6.12}$$

where A and A^0 are the total surface areas for the deformed and undeformed membrane meshes, respectively. Similarly, a_j and $a^\star_j$ are the elemental face areas (with the face index j) for an deformed and undeformed mesh element, respectively.

The discrete terms in the volume energy equation 4.13 are computed as

$$V = \frac{1}{3}\sum_j a_j \hat{n}_{\alpha,j} r_{\alpha,j} \qquad \text{and} \qquad V^0 = \frac{1}{3}\sum_j a^\star_j \hat{n}_{\alpha,j} r_{\alpha,j}. \tag{6.13}$$

Here, the V and V^0 are the total volumes enclosed[1] by the undeformed and deformed particle meshes, respectively. And, $\mathbf{r}_j$ is the position vector to the mesh face centroid (with the index j) with origin at the centroid of the entire membrane mesh.

Using the principle of virtual work, the area force $\mathbf{F}^A$ and volume force $\mathbf{F}^V$, at each mesh node are calculated as,

$$F^A_{n,\beta} = -\frac{\partial E_A(\{X'_{n,\beta}\})}{\partial X'_{n,\beta}} \qquad \text{and} \qquad F^V_{n,\beta} = -\frac{\partial E_V(\{X'_{n,\beta}\})}{\partial X'_{n,\beta}}, \tag{6.14}$$

where the symbols have their usual meaning.

6.5 REMARKS

We note that obtaining an arbitrarily sized (arbitrary number of faces and nodes) particle mesh is not possible in the present work. This is because, subdividing the icosahedron with the procedure outline in section 6.1.1 leads to meshes with the total number of faces N_f that increase as $N_f = 20 \times i^2$. Here, i is the number of (integer) steps taken in the subdivision of the icosahedron (Krüger, Varnik and Raabe, 2011). We cope well with this shortcoming since we employ the immersed boundary method (IBM) for fluid-solid interface coupling. We shall learn more about the IBM in the following chapter 7. In the unavoidable case that an intermediate mesh size is needed, we can commence the meshing from a regular octahedron instead, and obtain meshes with total number of faces that grow as $N_f = 8 \times i^2$ (Ramanujan and Pozrikidis, 1998).

Furthermore, in order to compute the membrane forces at each mesh node by evaluating the local derivative (equations 6.7, 6.11 and 6.14), we should have functional forms for the energies $\{E_S, E_B, E_A, E_V\}$, dependent on $\mathbf{X}$. However, these are not readily available. Therefore, we first substitute in for the respective energies, and evaluate the derivatives (by using the chain rule, for example), simplifying wherever possible. Though this approach results in some rather lengthy expressions, it turns out that using these evaluated expressions is computationally efficient than direct numerical evaluation of the energy derivatives. The rather lengthy but complete derivations for obtaining the force terms, are published in (Krüger, 2012, Appendix C), and are not repeated in this thesis.

1 The volume associated with a face with index j can become negative when $\mathbf{r}_j \cdot \hat{\mathbf{n}}_j < 0$. However, this does not alter the validity of the volume energy computations.

7

FLUID-SOLID COUPLING – *IMMERSED BOUNDARY METHOD*

In this chapter we shall have a brief look at the coupling mechanism between the particle membrane and the ambient fluid. We use the immersed boundary method (IBM) to achieve *bi-directional coupling* at every time step of the simulation. At its essence the immersed boundary method is an interpolation mechanism between the particle membrane and the ambient fluid. The basic idea for the method derives from the *no-slip* condition and Newton's third law of motion. After an overview of the immersed boundary method in section 7.1, we shall go over the governing equations and their discrete forms in sections 7.2 and 7.3, respectively. Some concluding remarks are given in section 7.4.

bi-directional coupling
Fluid moves the particle membrane and the membrane "pushes back" on the fluid

no-slip
Fluid velocity at the fluid-solid interface equals the interface velocity

7.1 OVERVIEW

The immersed boundary method (IBM) was born in 1972 from Peskin's numerical study on the motion of heart valves (Peskin, 1972). Here, heart valves were modelled as deformable immersed surfaces in a fluid. The original IBM proposed by Peskin is a simple and elegant method to couple fluid-structure boundary interactions, especially when the immersed boundary surface is inherently deformable. Therefore, the IBM lends itself very well to problems involving biological membranes interacting with fluids. The method has since been adapted and used for a variety of fluid-structure interaction problems, both with rigid and deformable boundaries (Mittal and Iaccarino, 2005; Sotiropoulos and Yang, 2014).

The IBM relies on two separate grids or meshes for solving fluid-structure interactions; an *Eulerian mesh* that is used for obtaining the fluid flow solution and a *Lagrangian mesh* that tracks the immersed solid boundary. See figure 7.1 for an illustration of the two types of meshes. In the case of a rigid boundary, the Lagrangian mesh points do not move relative to one another and are anchored to predetermined (stationary or moving) positions. When deformability is desired, the Lagrangian mesh is additionally used for solution of relative deformation of the surface and the mesh points move relative to each other. These two meshes "talk" to each other *via* the IBM at every time step. For the sake of brevity as well as to avoid confusion, henceforth we shall reserve the term "markers" to refer to the Lagrangian mesh points and "nodes" to refer to the Eulerian mesh points.

Eulerian mesh
A mesh with time invariant positions for each mesh point or node

Lagrangian mesh
A mesh where the mesh points or marker positions can evolve with time

The "talking" bit done by IBM is primarily an interpolation mechanism that imposes the no-slip boundary condition on the immersed surface. Eulerian fluid velocity is interpolated onto the marker points and force is interpolated back (or "spread") from the markers onto the Eulerian grid nodes. The idea

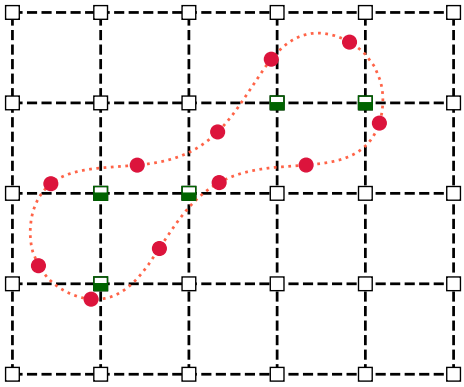

Figure 7.1: Illustration for a Lagrangian immersed boundary mesh in an Eulerian (Cartesian) fluid mesh. The immersed boundary surface shown as (red) dotted line mimics the 2D profile of a red blood cell. The Lagrangian mesh markers are shown as filled (red) circles. The Eulerian fluid mesh nodes outside the immersed surface are shown as squares. The fluid nodes enclosed by the solid surface are shown as half-filled (green) squares. The fluid mesh nodal connections are shown as (black) dashed lines.

for enforcing the no-slip velocity condition differs slightly in the case of rigid and deformable boundaries. In the case of a deformable boundary, the markers move with the interpolated velocity thus ensuring the no-slip condition. Elastic forces generated due to the deformation of the boundary are then spread onto the fluid mesh nodes. This can be interpreted as the principle of "action-reaction" embodied in Newton's third law. When the boundary is rigid, the force spreading is essentially done in order to bring the velocity of the ambient fluid equal to the local boundary velocity. In the case of stationary rigid boundaries, the markers cannot move due to fluid flow, and the boundary velocity is zero. While for moving rigid boundaries, the markers can move due to imposed fluid stresses, however their relative motion is constrained by the body's rigidity.

The IBM has many advantages for complex fluid-structure interaction problems. The main advantage of the IBM is that the boundary shape is not restricted by the structure of the fluid mesh, and arbitrarily complex shapes can be used. The IBM is simple to implement even for complex boundary conditions, and the numerical costs are relatively low. The method can be paired with any Navier-Stokes (NS) fluid solver that supports external forcing. The constitutive model defining deformation behaviour can also be selected independent of the solid immersed elastic surface.

The applications of the IBM include; simulation of heart valves and cardiovascular flows (Peskin, 1972; Peskin, 1973; Peskin, 1977), flow in blood vasculature (Arthurs et al., 1998; Kim, Lim et al., 2009), flapping filament dynamics (Zhu and Peskin, 2002), suspensions (Fogelson and Peskin, 1988), bio-films (Dillon et al., 1996)and red blood cells (Eggleton and Popel, 1998).

7.2 GOVERNING EQUATIONS

In this section we shall go over the governing equations for the IBM. The purpose here is not to go down the mathematically rigorous route in deriving these and associated equations, but rather to gain a physical understanding of the IBM coupling between the fluid and the solid surface. Therefore, we shall look only at the governing coupling equations and their physical interpretations. The detailed mathematical formalism for the IBM, along with the advantages, limitations and the research outlook is presented by Peskin in (Peskin, 2002) for those interested in reading up on the method.

Before moving onto the equations, we state the assumptions in the IB method used in this thesis:

1. The no-slip condition is assumed correct.
2. The immersed solid surface is assumed to be a 2D *closed membrane* immersed inside a 3D fluid domain.
3. The mass density of the immersed surface is considered equal to that of the ambient fluid. In other words, the immersed membrane is neutrally buoyant.

closed membrane *Membrane made up of a 2D surface that is compact and without boundary*

A representation of the "moving" immersed surface mesh and the "fixed" Eulerian mesh are shown in figure 7.1. The immersed surface is represented by dotted (red) line, which forms the profile of a red blood cell (RBC). The Lagrangian mesh markers are generated on this dotted line as solid (red) circles. The fluid flow (i. e. the NS equations) is solved on the Cartesian Eulerian mesh whose nodes are shown as squares. Note that some of the fluid nodes, shown as half-filled (green) squares, are completely enclosed by the solid immersed surface. These nodes can be treated differently by the flow solver (such as receive a different fluid viscosity e. g. when studying RBC dynamics under shear seen in section 2.2), if needed.

Since we have two meshes, we define two coordinate systems to describe variables in each of them separately. We shall reserve the upper case letters for the Lagrangian coordinate system and use the lower case letters for the Eulerian coordinate system. Let the position vector of a fluid element in the Eulerian system be given by $\mathbf{x}$, and that for a point on the solid surface be given by $\mathbf{X}$. Both of the above are Cartesian coordinates. However, it is instructive to define additional 2D curvilinear coordinates (r, s) for the Lagrangian immersed surface such that $\mathbf{X} = \mathbf{X}(r, s, t)$. Here t is the time variable.

The IBM coupling equations are written as,

$$\frac{\partial \mathbf{X}}{\partial t} = \mathbf{u}(\mathbf{X}(r, s, t), t) = \int \mathbf{u}(\mathbf{x}, t)\delta(\mathbf{x} - \mathbf{X}(r, s, t))\,d\mathbf{x}, \tag{7.1}$$

$$\mathbf{f}(\mathbf{x}, t) = \int \mathbf{F}(r, s, t)\delta(\mathbf{x} - \mathbf{X}(r, s, t))\,dr\,ds. \tag{7.2}$$

Here, $\delta(\mathbf{x} - \mathbf{X}(r,s,t))$ is Dirac delta function, and $\mathbf{f}(\mathbf{x},t)$ and $\mathbf{F}(r,s,t)$ are the force densities in the Eulerian and Lagrangian coordinates, respectively. It is important to distinguish that the fluid force density ($\mathbf{f}(\mathbf{x},t)$) is force per unit volume while the surface force density ($\mathbf{F}(r,s,t)$) is force per unit area. We see that equation 7.1 takes Eulerian input and gives Lagrangian output, while equation 7.2 takes Lagrangian input and converts it to Eulerian output. This to-and-fro mapping happens through the definition of the delta function. The delta function is 3D and chosen to be the same in both the equations.

The equation 7.1 can be seen as enforcing no-slip condition on the boundary, whereas the equation 7.2 is the transfer of force from the Lagrangian surface into the Eulerian fluid domain. The two equations together are interpreted as the "action-reaction" equations realised from Newton's third law. The fluid "acts" on the immersed surface by moving the surface with the ambient fluid velocity (thus imposing no-slip). The immersed boundary "reacts" to this flow-driven motion by pushing or spreading forces into the fluid. Naturally, Peskin refers to the equation 7.1 as (velocity) *interpolation* and to the equation 7.2 as (force) *spreading*.

interpolation
Velocity mapping from fluid to the surface, to satisfy no-slip

spreading
Force distribution by the immersed surface into the ambient fluid

It is important to note that though the above equations have similar form, they behave rather differently. In equation 7.1 the numerical value of the velocity in the Lagrangian frame $\dot{\mathbf{X}} = \dfrac{\partial \mathbf{X}}{\partial t}$ is the same as that in the Eulerian frame $\mathbf{u}(\mathbf{x},t)$, at corresponding points (as stated explicitly). In equation 7.2 however, the numerical value of force in Eulerian ($\mathbf{f}(\mathbf{x},t)$) and Lagrangian frames ($\mathbf{F}(r,s,t)$) is not equal at corresponding locations. This difference arises because the integral in equation 7.1 is 3D while that in equation 7.2 is 2D. Therefore, the force $\mathbf{f}(\mathbf{x},t)$ becomes singular (like a 1D Dirac delta function) while the velocity $\dot{\mathbf{X}}$ remains finite. Though $\mathbf{f}(\mathbf{x},t)$ becomes infinite on the immersed boundary, its integral over any finite volume containing the boundary, remains finite.

7.3 DISCRETISATION OF THE IB EQUATIONS

In this section we shall examine the spatial and temporal discretisation for the immersed boundary method. In their discrete forms the integral equations 7.1 and 7.2 are replaced by finite sums. These summations are carried out over immersed boundary markers and their ambient fluid neighbour nodes.

The discrete IBM equations can be written written as

$$\dot{\mathbf{X}}(r,s,t) = \sum_{\mathbf{x}} \mathbf{u}(\mathbf{x},t)\delta_{\Delta}(\mathbf{x} - \mathbf{X}(r,s,t))\Delta x^3, \tag{7.3}$$

$$\mathbf{f}(\mathbf{x},t) = \sum_{r,s} \mathbf{F}(r,s,t)\delta_{\Delta}(\mathbf{x} - \mathbf{X}(r,s,t))\Delta r \Delta s. \tag{7.4}$$

Here, $\delta_{\Delta}(\mathbf{x} - \mathbf{X}(r,s,t))$ is the discrete counterpart of the continuous Dirac delta function. Δx is the discrete distance between fluid nodes and $(\Delta r \Delta s)$ is

the discrete area assigned to a surface marker. In our case, the fluid solver is the lattice Boltzmann method (LBM) and the Eulerian mesh is the lattice with $\Delta x = 1$ (see chapter 5).

Spatial discretisation now effectively boils down to finding a suitable discrete form for the Dirac delta function. Such a discrete delta function determines the linear combination of weights for mapping properties (velocity and force) between the fluid nodes and surface markers. Peskin (2002) has enumerated a number of postulates in that the discretised delta function should satisfy and stated their mathematical significance. The purpose of these postulates is to reduce the imprint of the discrete Eulerian grid on the immersed surface as well as to ensure that the computational cost remains reasonable.

The first postulate is to assume that the 3D delta function can be separated into a product of three 1D functions, that scale with the fluid mesh width Δx, along the three coordinate directions. That is, the discrete delta function can be written as

$$\delta_\Delta(\mathbf{y}) = \frac{1}{\Delta x^3}\phi(\frac{y_1}{\Delta x})\phi(\frac{y_2}{\Delta x})\phi(\frac{y_3}{\Delta x}), \tag{7.5}$$

where y_1, y_2, y_3 are the Cartesian components of the distance vector $\mathbf{y} = (\mathbf{x} - \mathbf{X})$. Though this assumption (equation 7.5) is not necessary, it greatly simplifies computations. The 1D discrete delta function, $\phi(r) = \phi(\frac{y_\alpha}{\Delta x})$, is often referred to as the interpolation kernel or stencil.

Another postulate of importance relates to the interpolation range or *bounded support* for the discrete delta function. This postulate reads,

bounded support *The extent that the discretised finite delta function spreads over the fluid mesh, when centred on a surface marker*

$$\phi(r) = 0 \quad \text{for} \quad |r| \geqslant 2. \tag{7.6}$$

This postulate is limits the interpolation range between the Eulerian and Lagrangian meshes and is therefore important from the standpoint of computational efficiency for the method.

Working through all the postulates, it turns out that the minimum number of fluid nodes necessary to satisfy all of them is indeed 4; or in other words the minimum support for the delta function needs to be $4\Delta x$. This agrees well with the postulate in equation 7.6, that limits $(-2 \leqslant r \leqslant 2)$. The final form as well as the derivation for this 4-point stencil is given in (Peskin, 2002) and we shall not state it here.

Another of the postulates constraints the minimum support to an even number, in order to work well with the central difference operator employed in Peskin's flow solver for gradient computations. Fortunately for us, the LBM does not rely on such a discretisation for the local solution of the NS equations, and this postulate is no longer needed. In the absence of this postulate, the minimum bounded support needed for the interpolation stencil reduces to 3 fluid mesh nodes (or $3\Delta x$).

7.3.0.1 *The interpolation stencils*

The 3-point stencil used in our simulations reads,

$$\phi_3(r) = \begin{cases} \frac{1}{3}(1+\sqrt{1-3r^2}) & \text{for} \quad 0 \leqslant |r| \leqslant \frac{1}{2}, \\ \frac{1}{6}(5-3|r|-\sqrt{-2+6|r|-3r^2}) & \text{for} \quad \frac{1}{2} \leqslant |r| \leqslant \frac{3}{2}, \\ 0 & \text{for} \quad \frac{3}{2} \leqslant |r|. \end{cases} \tag{7.7}$$

smooth
The first derivative exists and is continuous

The 3-point stencil is continuous and smooth, and is constructed similar to the 4-point stencil, *via* Peskin's other remaining postulates. Use of the 3-point stencil results in significant savings in computational costs, especially for 3D simulations where the interpolation and spreading operations for a surface marker reduce from 64 fluid nodes to 27 fluid nodes.

Going against Peskin's advise, we also deploy a 2-point stencil whenever needed (simulations in chapter 10). This stencil is often used in literature and is defined as,

$$\phi_2(r) = \begin{cases} 1-|r| & \text{for} \quad 0 \leqslant |r| \leqslant 1, \\ 0 & \text{for} \quad 1 \leqslant |r|. \end{cases} \tag{7.8}$$

The reasons for using the compact 2-point stencil are:

1. The computational costs are drastically reduced in 3D simulations, where the support for the delta function is reduced to just 8 fluid nodes.
2. The compact 2-point stencil reduces the numerical "blurring" of the immersed boundary surface to the size of the fluid mesh resolution Δx.

The first point above comes in handy especially when simulating dense particles suspensions, whose macro-physics is under scrutiny (Krüger, Gross et al., 2013). As regards to the second point, it has been observed that the surfaces modelled with IBM appear to be "blurred", resulting in larger apparent size for immersed particles (Feng and Michaelides, 2009; Krüger, Varnik and Raabe, 2011). This increased apparent size scales with the support of the stencil used for the discrete delta function. The 2-point stencil minimises this footprint to the order of the fluid mesh width. Obviously the use of the 2-point stencil also brings some issues with it. The fluid mesh becomes much more visible to the immersed boundary and the solution may no longer be smooth. That is, there can be a jumps in the velocity and force as the surface markers cross the Eulerian grid planes, since ϕ_2 is not *smooth*.

With the intention to plug our interpolation stencil in the IBM equations, we now refer to figure 7.2. Here, we make use of the indices i and m to indicate discrete fluid node and surface marker positions, respectively. In figure 7.2, the fluid neighbourhood for a surface marker with index m, for the

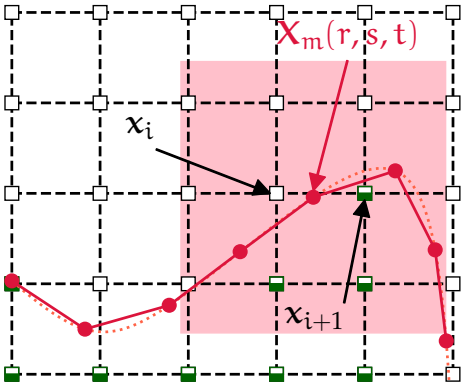

Figure 7.2: A zoomed-in section of the immersed boundary showing the fluid node neighbourhood for some Lagrangian surface markers. The surface markers are indexed as m and the fluid mesh nodes are indexed as i. The colourised (red) square region indicates the extent of the interpolation neighbourhood or support for the 3-point stencil for the marker at position $\mathbf{X}_m$. If the 3-point stencil is employed, the marker at $\mathbf{X}_m$ receives velocity contributions from all nodes covered by the (red) square region. Conversely, the force from the marker at $\mathbf{X}_m$ is spread to all nodes in the same square region, with the same weights as that for the interpolation step. The nodes in this region can receive force contributions from other markers at $\mathbf{X}_{m--}$ or $\mathbf{X}_{m++}$. Other fluid nodes outside this (red) region, do not contribute velocity or receive force from the marker at $\mathbf{X}_m$, though they may be coupled with other neighbouring surface markers.

3-point stencil, is indicated as an overlaid (red) square region with side $3\Delta x$. Since this is a 2D fluid domain, we see that the fluid node neighbourhood for the m^{th} marker encompasses 9 fluid nodes. Out of interest, a 2-point stencil here would spread over the four closest fluid nodes for the m^{th} marker, and the corresponding discrete delta function would be perform a bi-linear interpolation from these nodes to the marker point. Also, note that the interpolation stencil works over inner (empty squares) and outer (striped-green squares) fluid nodes without any distinction.

We now recast the equations 7.3 and 7.4 in a more usable form as

$$\dot{\mathbf{X}}_m(m,t) = \sum_i \mathbf{u}_i(x_i,t)\left(\frac{1}{\Delta x^3}\phi^3(r_1)\phi^3(r_2)\phi^3(r_3)\right)\Delta x^3, \tag{7.9}$$

$$\mathbf{f}_i(\mathbf{x}_i,t) = \sum_m \mathbf{F}_m(m,t)\left(\frac{1}{\Delta x^3}\phi^3(r_1)\phi^3(r_2)\phi^3(r_3)\right)\Delta r\Delta s. \tag{7.10}$$

Finally, looking at figures 7.1 and 7.2, the discerning reader would have wondered as to the relationship between the discretisation for the immersed surface (Δr and Δs) and that for the fluid domain (Δx). Krüger, Varnik and Raabe (2011) have pointed out that the ratio of nominal marker spacing to fluid node spacing should be $\frac{\sqrt{\Delta s^2 + \Delta r^2}}{\Delta x} < 1.5$, in order to maintain the

impermeability of the immersed surface and prevent cross boundary flow. In this thesis we have set the marker spacing to node spacing ratio as close to unity as possible.

For temporal discretisation of the IBM, we use an explicit time step scheme, or the so-called forward Euler method. This simply means that we compute the positions of the markers at time $t + \Delta t$ from the marker velocities computed at time t. The equation for this update can be written as

$$\mathbf{X}(t + \Delta t) = \mathbf{X}(t) + \Delta t \dot{\mathbf{X}}(t), \tag{7.11}$$

where Δt is the discrete time step and $\dot{\mathbf{X}}(t)$ the velocity of a marker at time t. The recipe for the IBM as we use it, is now complete.

7.4 REMARKS

The IBM is an elegant and simple approach to handling complex, arbitrary boundary conditions. With the IBM, the presence of the immersed boundary enters the flow solution only *via* body forces. But this simplicity comes at a cost. For sharp interface boundaries, such as those caused by cell membranes, the IBM is only first order accurate in space. As Peskin aptly puts it; 'the IB method smears out sharp interfaces to a thickness which is of the order of the meshwidth' (Peskin, 2002). Otherwise, the method is formally second order accurate in space for 3D bulk bodies immersed in fluid.

Another important shortcoming of the IBM is that the velocity interpolations in the IBM are not *divergence-free*, even when the chosen underlying fluid solver is (in general, the LBM is not divergence-free). As a consequence, a common problem with the IBM is that the volume enclosed within a *dilation-free* closed surface can change over several time steps.

divergence-free
There can be no point sources or sinks for the velocity field

dilation-free
The surface cannot be stretched or compressed, and the total surface area is conserved

The Dirac delta function that appears in the IBM equations is responsible for the translation of properties between the two coordinate systems. The moments of Dirac delta function must obey the rules, $\int \delta(\mathbf{x} - \mathbf{X}) d\mathbf{x} = 1$ and $\int (\mathbf{x} - \mathbf{X}) \delta(\mathbf{x} - \mathbf{X}) d\mathbf{x} = 0$. Moreover, the delta functions used for spreading and interpolation operations need to be exactly equal. These rules ensure that the force, torque and power evaluated on the Lagrangian and Eulerian coordinates are equal; meaning that there is no spurious generation of momentum, angular momentum or energy at the immersed interface during the coupling. For a case like ours, with a neutrally buoyant immersed surface, these constraints also give us conservation of momentum and energy at the immersed interface (Peskin, 2002).

Though we stated the assumptions and limitations of the IBM earlier, we have not justified our continued use of the IBM for this work. We do so now. This work is primarily concerned with the numerical investigation of the deterministic lateral displacement (DLD) particle separation technique. The particles are either cells or polystyrene micro-beads. The membranes of cells and micro-organisms are of the order of nano-meters. The IBM assumption that the immersed membranes are 2D surfaces is therefore quite natural.

The approximation of the rigid micro-beads as fluid filled (highly) stiff membranes is rather deficient, but we find that for our DLD model, it produces a good match with the experiments.

DLD is a size-based separation technique. Therefore, the use of compact support with the 2-point IBM stencil, in order to reduce the hydrodynamic footprint of the particle, is also well qualified. We are concerned more about predicting the correct particle behaviour in the DLD rather than the smoothness of the flow solution. The buoyancy of the cells is also not an issue since the experimental time scales for the density difference to manifest are much greater than those for the particle to transverse the DLD device. In other words, sedimentation is undesired in the DLD and the assumption of neutral buoyancy is safe.

The IBM employed in this study couples the flow solution from the LBM (chapter 5) to the surface deformation solution from the finite element energy method (FEEM) (chapter 6). The first use of IB-LBM for deformable RBCs was in 2007 in various studies (Bagchi, 2007; Dupin et al., 2007; Zhang, Johnson and Popel, 2007). This methodology for mesoscale simulation of cells has proven to be very popular, and detailed discussion of the numerical aspects of the IB-LBM-MEM can be found in (Krüger, Varnik and Raabe, 2011; Mountrakis, Lorenz and Hoekstra, 2017). We recommend (Krüger, Kusumaatmaja et al., 2017) for a quick read on the use of the IBM with the LBM as well as an exhaustive pool of references. This chapter was primarily intended as a refresher to understand the modelled physics, advantages and limitations of IBM in the context of our application. For a deeper dive (into the interpolation stencils, viscous coupling etc.) the curious reader is directed towards (Krüger, 2012), where the IBM employed is identical to the one in this thesis.

Part III

RESEARCH

It is nice to know that the computer understands the problem. But I would like to understand it too.

— Eugene Wigner

8

ANISOTROPY IN DETERMINISTIC LATERAL DISPLACEMENT ARRAYS

Few years after the invention of deterministic lateral displacement (DLD), anisotropic flow permeability was hypothesised to cause *mixed* mode particle behaviour in these microfluidic arrays (Kulrattanarak, van der Sman, Lubbersen et al., 2011; Sturm, 2007). However, the underlying reasons for such anisotropic flow to manifest and cause mixed mode particle motion, are not clear. In this chapter, we study the phenomenon of anisotropic permeability in the DLD arrays. As seen in chapter 3, correct device operation dictates that on an average the flow should remain at a fixed inclination to the obstacle array. We find that this condition is violated when anisotropic arrays, with certain specific design features, are used in the DLD. The flow starts deviating from the direction of the applied pressure gradient, leading to unpredictable particle trajectories in the DLD.

mixed mode
Particle shows characteristics of being in zigzag as well as in displacement mode, in the same array geometry

Fluid-only 2D simulations are used to uncover DLD array anisotropy. These simulations are guided by detailed experimental observations collected by collaborators on this project. In order to illustrate the consequences of using anisotropic DLD arrays, these external experimental observations are also presented in this chapter and precede the corresponding simulation results and discussions. The simulations show that the parallelogram layout possesses intrinsic anisotropic permeability, whereas the rotated-square layout is anisotropy-free. Furthermore, it is found that array anisotropy becomes severe when highly asymmetric post shapes or unequal lateral to flow-wise array pitch is used. From the study, a set of design principles are recommended to avoid anisotropic flow effects in the DLD. The results detailed in this chapter have previously been published in Vernekar, Krüger et al. (2017).

The fist section 8.1 introduces the problem. The experimental observations on flow and particle behaviour in the two obstacle array layouts is detailed in section 8.3. In sections 8.2 and 8.4, we then understand the nature of intrinsic array anisotropy, manifestation of anisotropic flow deviations and DLD design "enablers" that help such deviations. Causes leading to severe anisotropy in DLD arrays are discussed in section 8.5. Section 8.6 lists some relatively simple design guidelines for suppressing anisotropic flow deviations, and therefore avoiding unintended particle behaviour. A short summary and concluding remarks are given in section 8.7.

8.1 INTRODUCTION AND PROBLEM STATEMENT

A few years after the advent of the DLD by Huang et al. (2004), the experimental microfluidics community started noticing that particles could traverse through the DLD with migration angles that were somewhere in-between

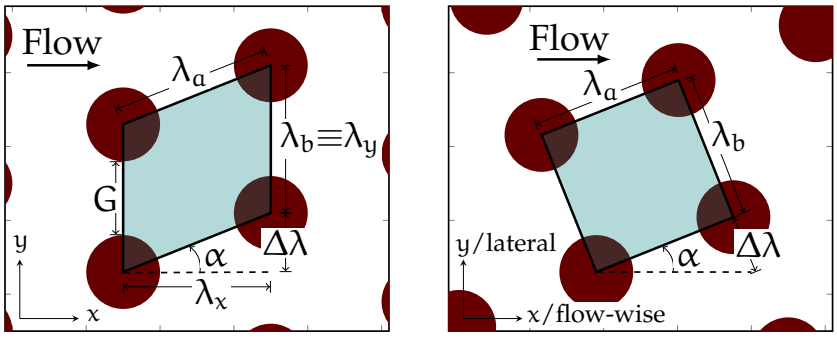

(a) Parallelogram layout (b) Rotated-square layout

Figure 8.1: (a) Row shifted parallelogram layout and (b) rotated-square layout geometries used in DLD arrays. Note the lateral (y) and flow-wise (x) directions. Figure reproduced from chapter 3.

those for zigzag and displacement modes (Kulrattanarak, van der Sman, Lubbersen et al., 2011). Such modes were theoretically possible if the array periodicity $N = 1/\varepsilon = \lambda_x/\Delta\lambda$ (and therefore the flow periodicity) turned out to be a non-integer value (Long et al., 2008). Here, λ_x is the array pitch in the flow-wise (x) direction, $\Delta\lambda$ the row shift along the lateral y direction and ε is the row shift fraction (RSF). See figure 8.1a reproduced from the introductory chapter 3. Interestingly, intermediate migration angles have also been observed in experimental DLD devices designed with integer periodicity (N) values (Kulrattanarak, van der Sman, Lubbersen et al., 2011). However, such mixed modes have not been universally observed in all DLD devices.

It has been hypothesised that anisotropic permeability of flow through the DLD arrays could cause the flow periodicity to vary away from N, and thus cause unintended particle motion (Kulrattanarak, van der Sman, Lubbersen et al., 2011; Sturm, 2007). Anisotropic permeability to flow means that the average flow direction does not remain parallel to the imposed driving pressure gradient in the device. This anisotropic deviation in the flow direction arises from the geometry of the obstacle array (Rice et al., 1970). This intrinsic array anisotropy to flow was attributed to cause an asymmetric distribution of flow lane widths through the array gaps. The asymmetric flow lane distribution is further correlated to intermediate particle migration (between zigzag and displacement) angles, for small particle trajectories in the DLD (Kulrattanarak, van der Sman, Lubbersen et al., 2011; Kulrattanarak, van der Sman, Schroën et al., 2010). However, there has not been deeper clarity on the matter.

This leaves many important questions unanswered. Such as, what are the sources of anisotropic flow permeability, if present at all, and how does it affect particle trajectories? And further, why do numerous DLD devices report successful operation (as discussed in section 3.4), without observed mixed modes?

I answer these questions with 2D, fluid-only numerical simulations. The investigations are centred around and follow from the experimental observations provided by the co-authors in (Vernekar, Krüger et al., 2017). These

experimental observations vividly illustrate the consequences of array anisotropy on particle trajectories. The experiments presented here were not conducted as a part of my PhD research, but are reported for the sake of comprehension and completeness.

The main research question answered in this chapter concerns the sources and variation of array anisotropy in the DLD. Using numerical simulations considering only the periodic unit cell of an array, we map array anisotropy in both parallelogram and rotated-square array layouts, employing the standard cylindrical pillar. These two layouts are generally used interchangeably, without accounting for the consequences of subtle differences between the two. With multiple-pillar large-domain simulations, we then study the design conditions when array anisotropy leads to flow deviation and particle mixed modes. Such mixed modes are usually undesirable and lead to particle separation failure. We show that it is possible to prevent such consequences by avoiding anisotropic flow "enabler" design features in the DLD. Different DLD array parameters, as well as non-cylindrical pillar shapes are also examined for their contributions to anisotropic permeability of the array.

8.2 NATURE OF ARRAY-INDUCED ANISOTROPY

An anisotropic array can be seen as one possessing the tendency to induce a lateral-to-flow pressure gradient along the y axis, when a driving pressure is applied along the flow-wise (x) direction (see figure 8.1). This pressure gradient becomes problematic in the DLD only when it induces a flow component in the lateral direction (Kulrattanarak, van der Sman, Lubbersen et al., 2011). The flow anisotropy for a specific array layout can therefore be quantified as the ratio of lateral-to-flow pressure drop to the flow-wise pressure drop in the unit cell of the array (see figure 8.5a). This flow anisotropy should not be confused with the geometric anisotropy/asymmetry of the DLD array, which is conveyed by the row shift fraction, ε.

Experiments described in the following section 8.3 (see figures 8.2 and 8.3) are examples of such anisotropic flow tilts, and the resulting consequences on particle trajectories. In these experiments, the flow tilts along the prevalent array inclination, thus reducing the effective array inclination to flow. This decreases effective ε, and therefore also reduces the critical separation diameter d_c, locally. Spatially varying d_c causes unexpected particle bumping for small particles that are expected to be in the zigzag mode, and induces experimentally observed mixed modes. To avoid spatially dependent d_c and unintended particle trajectories, it is necessary to understand and control the sources of anisotropic flow permeability in the DLD.

In fact, that the parallelogram layout would display a greater anisotropy than the rotated-square arrangement was first hypothesised (as far as I know) by Sturm (2007). This hypothesis was based on the understanding of optical transmission in crystals. Specifically, a phenomenon caused by anisotropic optical transmission known as optical birefringence, as observed in materials such as calcite. In calcite, this is caused by the non-cubic (parallelepiped)

unit cell of the crystal structure. In contrast, optical materials with cubic unit cells show no birefringence, and therefore no anisotropic transmission. This analogy (and the hypothesis by Sturm) has served as an inspiration for the detailed investigations into flow anisotropy in DLD for both the array layouts, which are generally treated as equivalent for a given inclination, $\alpha = \tan^{-1}(\varepsilon)$.

8.3 EXPERIMENTAL OBSERVATIONS OF ARRAY ANISOTROPY

In this section, we present the experimental evidence demonstrating the contrasting fluid and particle behaviour in the two array layouts employed in the DLD; parallelogram and rotated-square. The flow in the parallelogram layout deviates from the horizontal causing unintended particle behaviour. Surprisingly, particles in the rotated-square layout do not show such behaviour. The results in this section are external to the research in this thesis, and are intended to provide insight into the experimentally observed differences between the two layouts.

8.3.1 *Parallelogram layout*

cascaded arrays
DLD devices with multiple array sections, generally with varying inclinations (α) or gap sizes (G), placed serially one after the other

Figure 8.2 shows an experiment intended for particle separation and particle crossing in a DLD device with multiple *cascaded arrays*. The fluid flow through this device shows significant deviation away from the horizontal near the interface between two array inclinations. The parallelogram layout is used in all the cascaded sections of the device, without any interfacing structures. We focus on the first two sections schematically illustrated in figure 8.2(A). The two array sections have equal but opposing inclinations of $\alpha \approx \pm 11.3°$ ($\varepsilon = 1/5$). Placing counter inclined arrays next to one another does not mean that particle separation would be reversed. Afer separating out the larger particles will continue move along the prevalent array inclination in subsequent array sections. Such oppositely inclined arrays can be used for separating out larger particles in the first section and then running them through required chemical streams in the second section for operations[1] such as cell lysis, labelling and washing. The vertical and horizontal array pitch in both sections is 11 μm. The other array parameters are stated in the caption of figure 8.2. The full device is shown in figure 8.2(B) and the fabrication details are given in (Vernekar, Krüger et al., 2017).

CCD camera
A camera using a highly sensitive "charged coupled device" (CCD) photon detector

Figure 8.2(D) is a time sequence overlay of a series of images captured from a colour *CCD camera*, that show the overall trajectory of the beads and the dye from the sample inlet through the first two sections of the device. A jet of red 2.7 μm beads mixed with green fluorescent dye is injected through the inlet of the device. The 2.7 μm beads (red), clearly follow the bump mode and trace out the array inclination. However, we can observe that the (green)

1 Strictly speaking these counter inclined arrays are not necessary for such operations, but they offer the possibility of having the larger particles flow back across inlet flow streams post de-mixing.

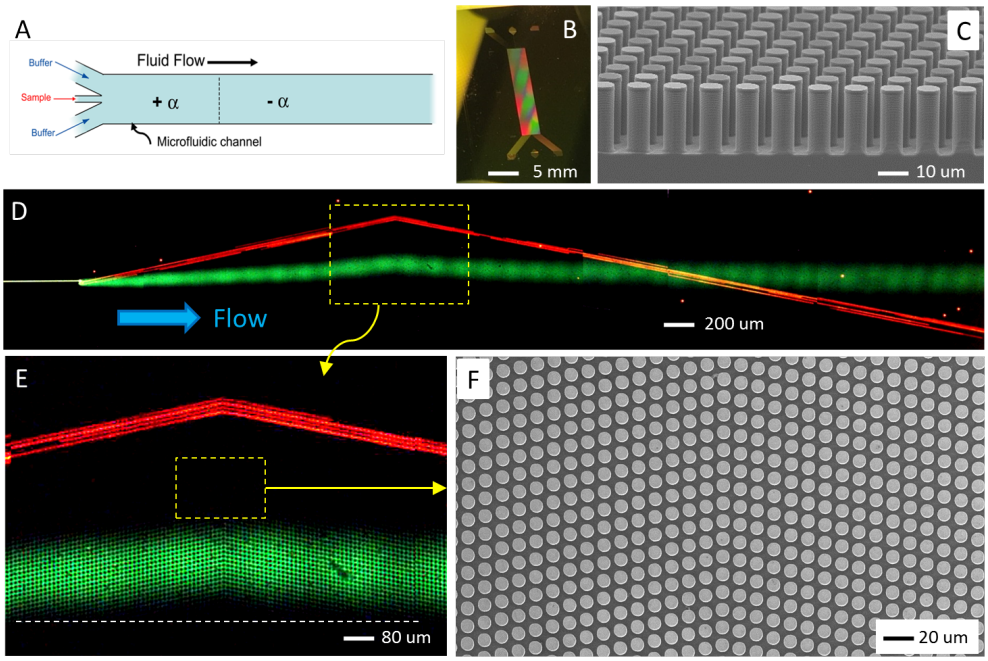

Figure 8.2: Device for demonstrating anisotropic flow tilt in the parallelogram layout. (A) Schematic of the device with two counter-inclined array sections having equal positive and negative inclinations $\pm\alpha$. (B) Photo of the DLD device, as etched into a silicon substrate. (C) Cross sectional SEM image of the DLD array showing cylindrical posts arranged in the parallelogram layout, with array pitch $\lambda = 11$ µm, array gap $G = 3.7$ µm and array inclination of $\alpha = \pm 11.3°$. (D) Time exposure overlay demonstrating the flow separation of a mixed jet of fluorescent dye (green) and 2.7 µm diameter (red) beads, through the DLD array. The blue arrow indicates the direction of average flow. (E) Zoomed-in image highlighting the deviation of the fluorescent dye close to the interface between positively and negatively inclined array sections. Dashed white line indicates the direction (horizontal) of applied pressure gradient. (F) Top view SEM image showing the region near the interface junction between the counter-inclined array sections. The image is reproduced from (Vernekar, Krüger et al., 2017) (©CC BY).

fluorescent dye deviates significantly from the horizontal, especially in the region around the interface between the array sections. From the zoomed-in image in figure 8.2(E), we see that the fluorescent dye shows a preferential tilt along the prevalent array inclination. This tilt is especially noticeable as the dye flows across the interface between the counter-inclined array sections. The details of this junction are shown in the top view scanning electron microscope (SEM) image in figure 8.2(F).

This experiment captures the phenomenon of anisotropic flow tilt in the parallelogram DLD array. In this experiment, the trajectory of the particle in the bump mode remains unaffected since the bead diameter of 2.7 µm is greater than the critical particle size $d_c = 2.4$ µm for the two array sections. However, such a tilt adversely influences the trajectories of small particles travelling in the zigzag mode through the device. We see this effect in a

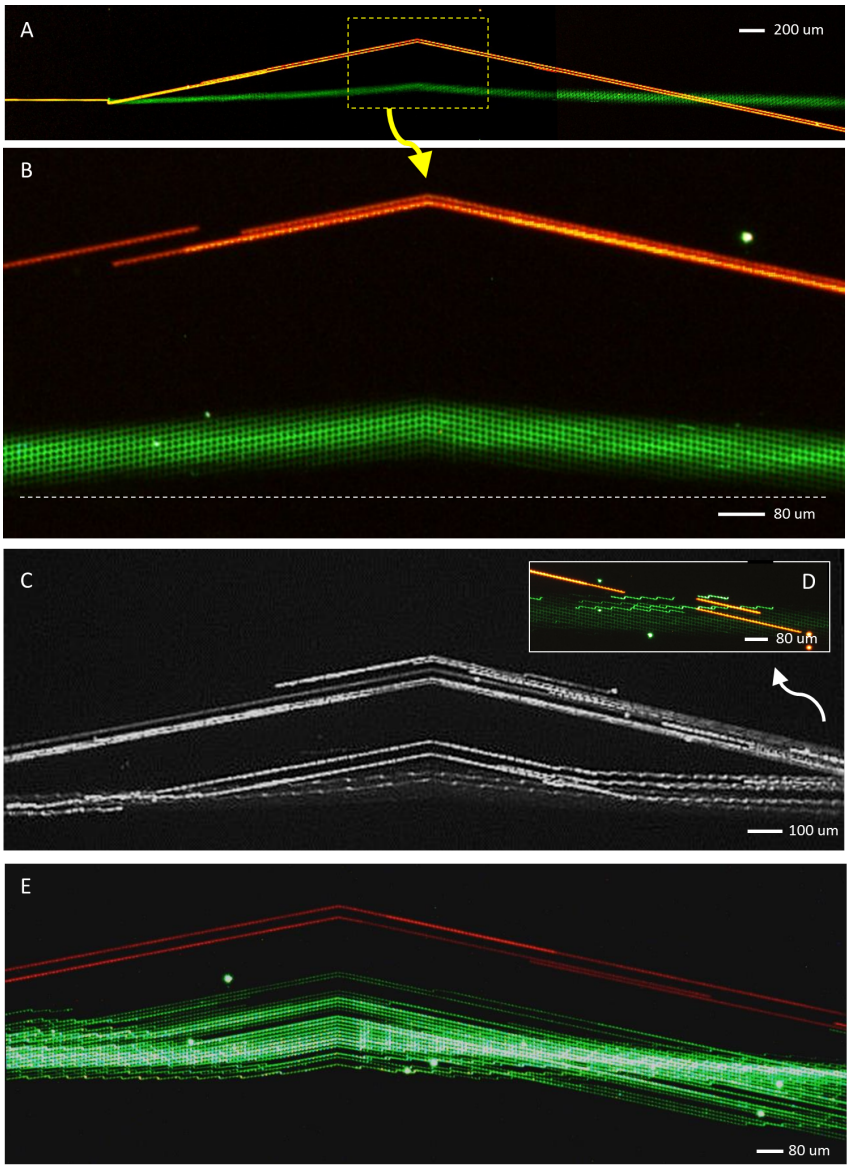

Figure 8.3: Device for demonstrating consequences of array anisotropy on particle trajectories. (A) Time exposure overlay of a mixed jet of 0.5 μm (green) and 2.7 μm (red) beads injected into the same DLD device shown in figure 8.2 ($\alpha = \pm 11.3°$ and $G = 3.7$ μm). (B) Zoomed-in image (colour camera, time exposure) of the 2.7 μm bead in the bump mode (top stream) and the 0.5 μm following the zigzag mode (bottom stream). The deviation of the 0.5 μm beads near the interface between array sections is clearly seen. The dashed (white) line near the bottom indicates horizontal. (C) Video frame sum (monochrome camera) of beads passing through the interface between sections. The image now includes the trajectories of 1.9 μm diameter fluorescent beads (bright, bottom stream), along with the other two as before. Here, the 1.9 μm beads are expected to be in the zigzag mode in both sections ($d_c = 2.4$ μm), but undergo anisotropic "bump" mode near the interface between arrays. The inset (D) records their trajectories (bright green) at the crossover region, further beyond the interface in the negatively inclined array section. Here, the 1.9 μm beads (bright green) return to their expected zigzag mode, far away from the interface. (E) Time exposure (colour) showing the addition of 2.3 μm beads (also green), which are close to the critical particle size d_c. Here, the top stream is still that for the 2.7 μm (red) beads. Note that the intermediate 2.3 μm beads appear to be locked into an anisotropic "bump" mode well beyond the array interface (bottom right). The image is reproduced from (Vernekar, Krüger et al., 2017) (©CC BY).

second experiment shown in figure 8.3, using the same device. Here, an input jet of beads with different sizes was used. Figure 8.3(A) is a time-lapse overlay of images showing the separation of 0.5 μm and 2.7 μm beads in the first two array sections. Here, the smaller beads are well below the critical size for the arrays, i.e. $d_c > 0.5$ μm, and these beads travel in the zigzag mode. These beads simply follow the fluid flow and are perturbed away from the horizontal as they approach and leave the interface between the two array sections. Figure 8.3 shows a zoomed-in view of this lateral deviation.

To further illustrate the impact of the anisotropic flow deviation on intermediate bead sizes, 1.9 μm green fluorescent beads were added to the input bead jet mixture. A monochrome CCD video frame sum of the particle motion is shown in figure 8.3(C). The inset in this figure shows the time-lapse overlay from the color CCD camera, placed over the second array section well beyond the array interface region. We clearly see from the figure 8.3(C) that the 1.9 μm beads show a transition from zigzag to bump-type motion as they approach the array interface region (bottom jet stream), while the 2.7 μm beads are in the bump mode (top jet stream). Well beyond the array section interface, the 2.7 μm beads (red) remain in bump mode, as seen in the inset. Here, we also see that the bright green 1.9 μm beads have now reverted back to the zigzag mode, travelling horizontally. The zigzag path traced by the faded green 0.5 μm beads is also just visible in the colour inset.

Normally, a bead with diameter smaller than the critical diameter (d_c) for the array is expected to track horizontally throughout the device, along the direction of flow driving pressure drop. As we can see from the experiment shown in figure 8.3, while the 1.9 μm bead initially tracks horizontally, it alters its trajectory mode in the region near the interface between the array sections. The bead moves in the bump mode tracing the local array inclination. The particles start to bump upwards at the end of the first array section, and then immediately downwards at the start of the second array section. Sufficiently away from the interface, the particles then return to the zigzag mode in the middle region of the second array section.

The experiment in figure 8.3 plainly shows the 2.7 μm bead in the bump mode, the 0.5 μm bead in the zigzag mode and the 1.9 μm bead in the mixed mode in the same DLD device. We suspect that the unintended mixed mode motion of the bead is caused by anisotropic permeability leading to the lateral flow acting on the particles near the array interface. As we shall see later with the help of simulations (section 8.4), the flow no longer remains horizontal in the parallelogram layout due to its intrinsic anisotropic permeability. The flow tilts, especially in regions close to the interface between array sections, thus reducing the effective array inclination,. Such unintended particle motion could prove undesirable for particle separation, especially for high-resolution applications.

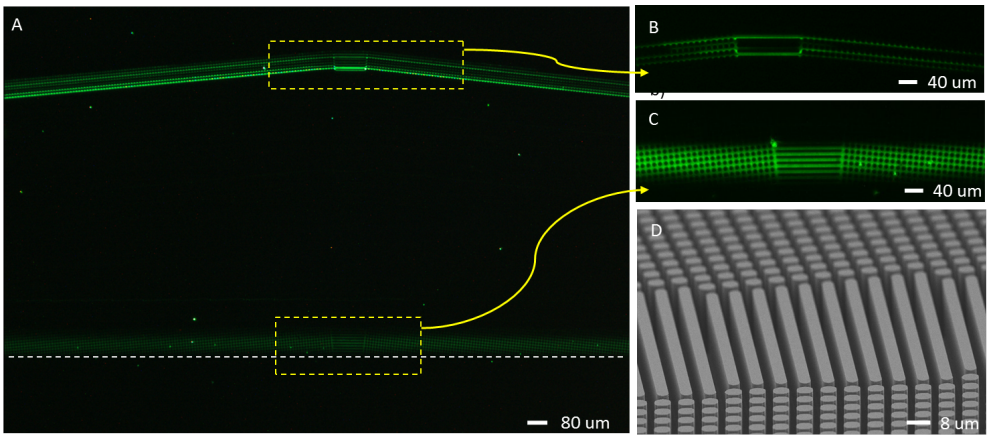

Figure 8.4: Bead trajectories in a DLD device with the rotated-square layout. (A) Time exposure overlay (colour) of 1.9 μm (green) and 0.5 μm (green) fluorescent beads in the DLD device, with rotated-square arrays. Similar to the device in figure 8.2, here we have two adjacent counter-inclined array sections with inclination of $\alpha = \pm 5.71°$ (or $\varepsilon = 1/10$). Both array sections have $\lambda = 8$ μm, $G = 2.4$ μm and a design critical size of $d_c = 1.1$ μm. Zoomed-in insets of regions near the array section interface, showing (B) the 1.9 μm bead in the bump mode and (C) the 0.5 μm bead in the zigzag mode, respectively. For the 0.5 μm tracer beads in the zigzag mode, no significant deviation from the horizontal (dashed white line) is observed. (D) An SEM image of the rectangular connectors used to match adjacent rotated-square array sections. The image is reproduced from (Vernekar, Krüger et al., 2017) (©CC BY).

8.3.2 *Rotated-square layout*

When the rotated-square layout is used, there is no significant flow deviation from the horizontal, neither near nor away from array interface regions in cascaded arrays. The experiment shown in figure 8.4 employs two arrays in the rotated-square layout with a positively inclined first array section followed by a negatively inclined second section. The arrangement is similar to that shown in figure 8.2(A). The counter-inclined arrays have an inclination angle of $\alpha = \pm 5.71°$ (or $\varepsilon = 1/10$). The two arrays have a shorter 8 μm array pitch, compared to the device discussed earlier. Unlike the parallelogram arrays in figure 8.2(F) (which have matching interface boundaries), a set of rounded rectangular "connector" structures are used to match the boundaries of the two adjacent array sections in the rotated-square layout. These structures (of varying length) are seen in the SEM image shown in figure 8.4(D). Other parametric details about the device are provided in the caption of the figure 8.4, and the device manufacturing details can be found in Vernekar, Krüger et al. (2017). The critical diameter for this device is expected to be $d_c = 1$ μm.

Figure 8.4(A) shows the time-lapse image overlay of 1.9 μm and 0.5 μm (green) fluorescent bead trajectories through the device, near the interface region between the counter-inclined array sections. We see that the beads have already undergone lateral separation, after injection as a narrow stream

of bead mixture through the device sample inlet. The 1.9 μm beads (top jet stream) are larger than the device critical size and follow the bump mode while the smaller 0.5 μm beads follow the zigzag mode (bottom jet stream), acting as fluid flow tracers, as expected. The zoomed-in image in figure 8.4(B) highlights the particle paths in the bump mode as they transit the interface. Note the switch between a bumping motion along the upper side of the posts in the positively inclined array, compared to a bumping action on the underside of the posts in the negatively inclined second array section. Figure 8.4(C) similarly shows a zoomed-in image of the path of the 0.5 μm particles across the array section interface. These tracer beads span all available flow lanes in the zigzag mode, clearly marking out the rotated-square geometry and the interface connectors.

No observable deviation of the zigzagging tracers, and therefore of the flow is seen near the interface (or in other array regions). The overall path of the 0.5 μm beads remains horizontal, along the applied pressure gradient as seen in figure 8.4(A). This suggests an absence of anisotropic permeability for the rotated-square layout. Therefore, unlike the parallelogram layout, the rotated-square layout should be averse to unintended particle motions and mixed modes.

8.4 MAPPING ANISOTROPIC PERMEABILITY

We put Sturm's hypothesis (of non-cubic array layouts inducing flow anisotropy) to the test using high-resolution 2D simulations. The simulations carried out here can be divided into two classes; single-pillar and large-domain. In the first 'single-pillar' simulation set, as the name suggests, we simulate flow over a single obstacle pillar (with 400×400 lattice nodes) with periodic boundaries along x and y directions. The flow is driven by a prescribed body force along the pressure drop direction through the DLD (see section 4.2.1). A feedback body force component normal to the pressure drop direction is dynamically computed to ensure zero net lateral fluid flux in the single pillar domain. This approach simulates flow over an individual post of an infinite array, with (far away) lateral side walls that prevent net accumulation of fluid at large distances from the post. We also model multiple pillars in large-domains similar to the above experiments, where entire array sections are simulated. Here, arrays with as many as 150×120 posts have been modelled in order to investigate the flow tilt due to array anisotropy. All simulations are in the Stokes flow regime with the typical Reynolds number (computed based on the maximum velocity and array gap G) $Re < 0.8$ in the single pillar simulation and $Re < 1 \times 10^{-4}$ in the large-domain simulations.

8.4.1 *Anisotropic lateral pressure drop*

For the sake of simplicity, we start with a symmetric circular post shape with post-to-gap ratio of unity ($G/D = 1$). The simulated array gap and post diameter are $G = D = 10$ μm, and therefore the array pitch is $\lambda = 20$ μm. With

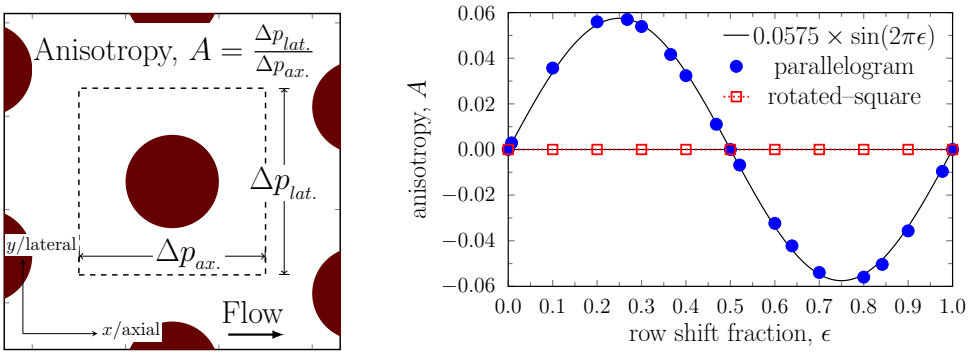

(a) Anisotropy definition

(b) Anisotropy for cylindrical pillar array

Figure 8.5: (a) An illustration defining anisotropy as quantified in our simulations. Δp is the average pressure drop over the array pitch λ, measured over a single periodic domain (dashed box). (b) Variation of anisotropy A in the parallelogram and rotated-square layouts (for circular posts) with changing array inclination given by ε.

these two variables held constant, single pillar simulations in the parallelogram and rotated-square layouts are carried out over a range of RSF values ($\varepsilon = 0.0$ to 1.0, with increments of $+0.1$ or smaller).

When using periodic boundary conditions in the x and y directions, flow simulation over a single pillar of an anisotropic array would result in a non-zero average velocity component in the lateral (y) direction. That is, an anisotropic array shows a mismatch between average pressure gradient direction and the average flow direction. In reality, this lateral flow component is restricted by the presence of side walls of the microfluidic channel. Hence, we can use the average lateral pressure drop required to achieve zero mean flow along the y direction in order to quantify array anisotropy. We define array anisotropy A as the dimensionless ratio of the induced lateral pressure drop (along the y direction) to the applied pressure gradient (along the x direction) required to drive the flow. This definition is neatly illustrated for a unit cell of a the obstacle array in figure 8.5a.

Using this definition, we compute the anisotropy at steady state and in Stokes flow, over the range of ε. Both the parallelogram and rotated-square geometries are tested. Figure 8.5b plots the variation of anisotropy for different array inclinations written in terms of the RSF (ε). The sign of A indicates the direction of the lateral pressure drop, with a positive sign indicating that the induced lateral pressure drop has the same direction as the array inclination and *vice versa*[2].

As seen from figure 8.5b, anisotropy in the parallelogram array shows a sinusoidal dependence on ε. Furthermore, the absolute anisotropy values for ε and $1 - \varepsilon$ are equal. This symmetry comes from the geometry of the array, where a parallelogram array with inclination $0.5 < \varepsilon < 1.0$ is equivalent to one with $1 - \varepsilon$, but with a row shift in the $-y$ direction. From the simulations,

2 This fact is deduced from the numerous simulations carried out in this chapter

we obtain a maximum absolute anisotropy of $\approx 5.6\%$, at $\varepsilon = 0.25$ and 0.75 in the parallelogram geometry.

Conversely, the rotated-square layout returns vanishing anisotropy for all tested values of ε. This conveys that no lateral pressure drop is induced when fluid flows through the rotated-square layout. This identically zero anisotropy for the rotated-square layout hints at geometric and time-reversal symmetry of Stokes flow around the periodic obstacles. Such symmetries would indicate that Stokes flow is time independent in the rotated-square layout and the flow-field does not change upon a reversal of the applied pressure drop direction. These results corroborate Sturm's hypothesis of the rotated-square array having an advantage over the parallelogram layout in avoiding anisotropic effects.

8.4.2 *Anisotropic flow tilt*

When array anisotropy manifests solely as a pressure drop, particle trajectory modes remain unaffected, because the fluid flow stays horizontal and at a fixed inclination to the array. Array anisotropy is only problematic when it induces a tilt in the flow direction. For the parallelogram arrays with symmetric circular posts, the anisotropy direction is the same as that of the row shift, as seen in figure 8.5b. Hence, flow deviation occurs in the direction of the array incline (or the array row shift) in anisotropic parallelogram array. This causes a decrease in the effective array inclination, and thus a reduction in the critical separation diameter d_c, locally.

To test this reduction in effective array inclination and understand the flow tilt behaviour, we simulate two DLD devices, as shown in figure 8.6. The first device employs the parallelogram layout (see figure 8.6(B)) and the second has the rotated-square layout (see figure 8.6(C)). Each simulated DLD device has two array sections with a total of 152×120 circular posts along the flow-wise and lateral directions, respectively. The post diameters are $10\ \mu m$ and the array gap size is $G = 10\ \mu m$, similar to the single pillar simulations. These device simulations are similar to the experiments presented in section 8.3, except that the simulation arrays can be considered infinitely long without well defined inlets/outlets.

The simulated domain is $3.2mm \times 2.4mm$ (3200×2400 lattice nodes in the x and y directions). See figure 8.6(A) for an illustration of the simulation setup. Periodic boundaries are used in the x direction, while no-slip side walls are present at the boundaries along the y direction. The flow is driven by a pressure gradient along the x direction. Each device has two counter-inclined array sections, with inclination angle $\pm\alpha$ for the left and right sections, respectively. The array inclination is set at $\varepsilon = \pm 0.2$. In each device, the two array sections are separated by an interface gap of $\approx 4\lambda$ ($80\ \mu m$), similar to the ones employed in the experimental devices in figures 8.3 and 8.4.

The figures 8.6(B) and (C) show zoomed-in regions capturing the right device side wall, and the interface gap between array sections, for both simulated devices. Here, the flow streamlines (blue lines) are plotted at arbitrary

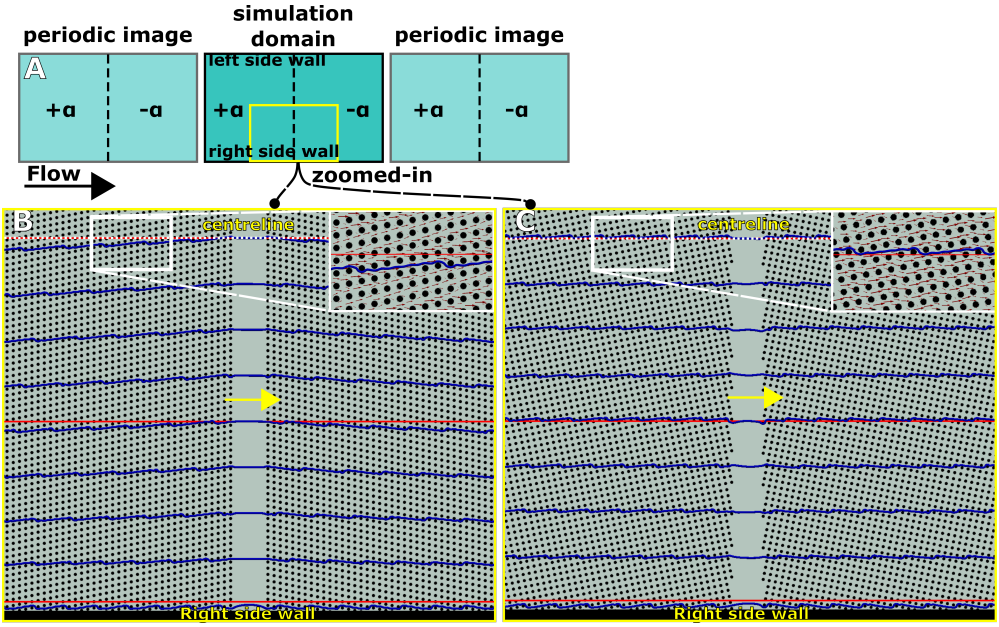

Figure 8.6: Results for anisotropic flow tilt in the parallelogram and rotated-square arrays. (A) The large-domain simulation setup for both parallelogram and rotated square DLD devices. Each device has two counter-inclined array sections with $\varepsilon = \pm 0.2$. Both devices have periodic inlet and outlet boundaries along x direction and no-slip side walls along the y direction. Fluid streamlines (blue lines) in region near the right side wall, for (A) the parallelogram layout device and (B) the rotated-square layout device. Reference horizontal lines (red) indicate the direction of applied pressure gradient (parallel to side walls). (B) As we move away from the right side wall, the streamlines tilt in the direction of prevalent array inclination in the parallelogram layout device. (C) In the rotated-square device, no such flow deviation is seen and the streamlines remain parallel to the side walls throughout. The small deviations from the horizontal are due to streamlines navigating around posts, tracing the ideal zigzag trajectory. The arrows in the zoomed-in insets indicate the local velocity field. The dashed (white) line indicates the device centreline.

fixed equal intervals from each other, for both the devices. In the parallelogram device (figure 8.6(B)), the streamline closest to the right side wall remains horizontal throughout. As we move away from the right side wall and towards the device centre, the streamlines show a marked tilt along the prevalent array inclination. At ≈ 10 posts away from the right side wall, a visible flow tilt can be observed, and this flow tilt continues to increase as we move further away from the right side wall. Along the centre of the device, the flow is no longer parallel to the side walls. A similar behaviour is observed at the other (left) side wall (plot not shown).

In the region around the centreline, the effective array inclination is reduced from $\varepsilon = 1/5$ to $\approx 1/7$, as a result of the flow tilt. Typically, DLD devices target this zone for particle separation. This change in ε occurs gradually as we move from the side wall to the centre. Therefore, the periodicity $N = 1/\varepsilon$ would rarely equal an integer value. It is known that non-integer N

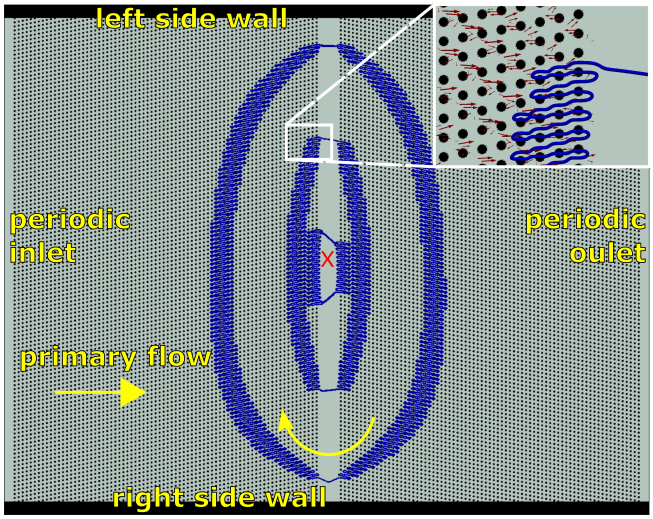

Figure 8.7: Background secondary recirculation flow pattern visualised *via* streamlines (blue lines) in the parallelogram layout device from figure 8.6(B). Here, both the right and left side walls for the simulated device are shown. The two counter-inclined array sections are inclined with $\varepsilon = \pm 0.2$, respectively. The secondary flow field is obtained by subtracting the primary x velocity component, measured at the device centre (shown as X), from the overall primary flow field. The arrows in the zoomed-in inset show the local secondary flow field.

values can lead to mixed modes, as well as negative migration angles (Long et al., 2008). Such effects are highly undesirable for predictable bi-modal particle sorting in the DLD. Furthermore, factors such as the distance of the particle from the side walls, now influence the critical separation size d_c in the device.

Figure 8.6(C) shows a similar streamline plot for the rotated-square device. Here, the streamlines (blue lines) remain horizontal and parallel to the side walls, throughout. The streamlines appear to zigzag around the array obstacles with unchanging periodicity N, set by the array geometry. The lack of flow deviation can be attributed to the absence of anisotropy. Here, unlike in the parallelogram layout, the critical separation size d_c is well defined and spatially invariant, making separation much more predictable. Therefore the rotated-square layout should be preferred over the parallelogram layout for particle separation applications.

8.4.3 *Background secondary recirculation*

In section 8.4.2 we have seen that inherent anisotropic permeability of the parallelogram array could tilt the fluid flow along the prevalent array inclination. However, this need not always be the case. If the anisotropic lateral pressure gradient is balanced by normal stresses at the no-slip wall boundaries, no lateral flow will arise in the array. In such a case, the streamlines stay parallel to the walls, and are not tilted. In fact, this the reason the streamline closest to the right side wall stays horizontal in figure 8.6(B). However, certain

common design features found in DLD devices, allow the anisotropic lateral pressure gradient to induce secondary flows. These secondary flows perturb the primary streamlines away from the horizontal, and along the prevalent array inclination.

We take a deeper look at the flow field in simulated parallelogram device shown in figure 8.6(B). We discover that the anisotropic lateral pressure gradient starts to be released near the interface between the two counter-inclined array sections. This results in a "ladder-like" background secondary recirculation pattern near the interface, as seen in figure 8.7. This secondary flow-field is obtained by subtracting the x directional velocity component at the centre of the device (marked 'X' in figure 8.7), from the primary velocity field everywhere. In the present simulation, this background flow is clockwise, meandering around obstacles in the array. Note that the streamlines shown in figure 8.7, close in on themselves and are therefore stagnation (or separation) streamlines.

This recirculatory flow causes the tilt in the primary flow and is responsible for locally altering the critical separation diameter d_c of the device. Such background recirculation is absent from the rotated-square layout. As we shall see next, certain device features allow this background recirculation to manifest in anisotropic arrays. We term these features as anisotropic flow "enablers".

8.4.4 *Anisotropic flow tilt "enablers"*

Design features that allow the induced lateral anisotropic pressure gradient to drive secondary recirculation have unknowingly been employed in many DLD devices (see chapter 3). In general, we find that placing sections with large differences in their intrinsic anisotropy values adjacent to one another leads to background recirculatory flow. An example of such anisotropic flow effect is seen in the experiment in figures 8.2 and 8.3, where array sections with opposing anisotropy values are placed next to each other. Additionally, the presence of low-impedance isotropic regions, such as an obstacle-free interface gap between array sections, also leads to anisotropic flow deviations in the DLD.

In order to substantiate the claim that the presence of an interface gap between array sections leads to anisotropic flow tilt, we run two large domain simulations. Two very similar DLD devices are simulated; one device has an interface gap between two similarly inclined array sections (figure 8.8a), while the gap is absent in the other (figure 8.8b). Here, the parallelogram array layout is used for both array sections in the device. The inclination in both the array sections is equal and positive, $\alpha \approx +14.0°$ (or $\varepsilon = 0.25$), as seen in figures 8.8a and b.

In the first device seen in figure 8.8a, the interface gap acts as an enabler for anisotropic flow deviation by allowing the fluid flux to compensate for its upward tilt within the array sections. The large isotropic obstacle-free gap is unable to impose a lateral pressure to keep the flow along the horizontal, and

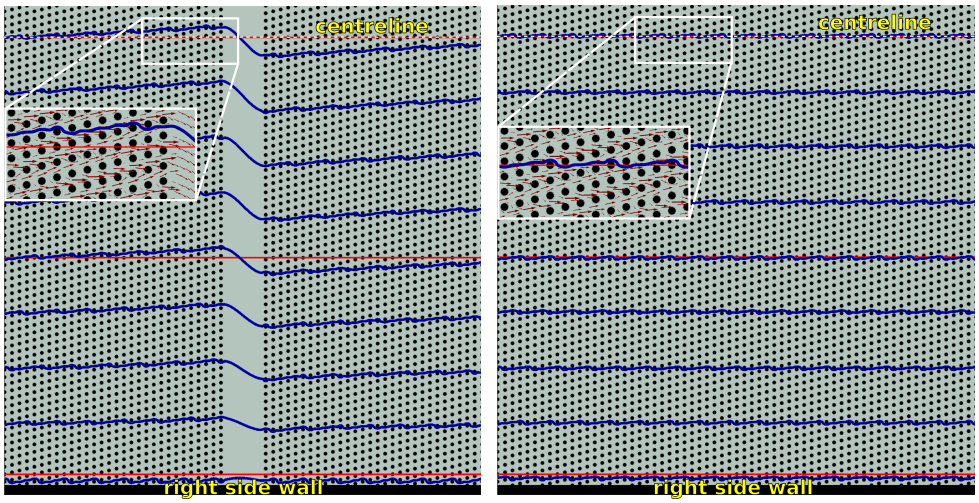

(a) Interface gap present

(b) Interface gap absent

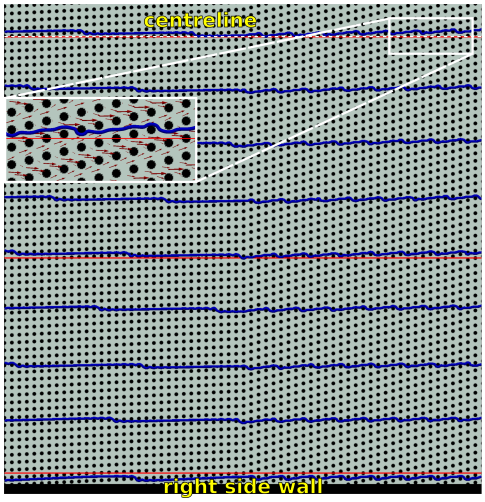

(c) Cascaded without interface gap

Figure 8.8: Flow streamlines demonstrating the effect of anisotropic flow "enabler" designs in the DLD. Simulated DLD device with (a) an interface gap between positively (similarly) inclined array sections, and (b) a device without an array section interface gap. Both devices have two array sections in the parallelogram layout with circular pillars and an inclination of $\varepsilon = +0.25$. The fluid streamlines are plotted for both simulations (blue lines). These show significant flow tilt in (a) the device with the interface gap, while no flow tilt in (b) the device without an interface gap. (b) Here, flow remains horizontal and parallel to the side walls. (c) Streamlines in a cascaded DLD device with two array sections. The left section has inclination of $\varepsilon = 0.05$ and the right section has an inclination of $\varepsilon = 0.25$. The flow tilts upwards in the right section, and to compensate this tilts, deviates downwards in the left section. Horizontal lines (red) indicate the direction for the applied average pressure gradient. All panels are zoomed-in views of larger DLD devices in regions near the right side wall. Arrows in the insets indicate the local velocity field.

allows the anisotropic pressure to be released resulting in a secondary recirculation. This allows the flow to tilt within the arrays along their prevalent inclination.

As seen in figure 8.8b, the absence of the gap in the second device forces the flow to stay along the horizontal throughout, confirming interface gaps as enablers of anisotropic flow tilt. Additional simulations with rectangular connectors in the interface gap, such as those seen in figure 8.4(D) were carried out to see if the compensatory lateral fluid flux in the interface gap could be choked (plots not shown). No flow tilt is observed in the array when the lateral gap between these connectors is kept the same as the array gap G. The connector elements simply mimic the no gap situation, as seen in figure 8.8b. However, when the spacing between these connectors was increased to $> 4\lambda$, the flow tilt is seen to reappear again.

Even without the gap, anisotropic flow deviation can occur in cascaded arrays. Flow tilt can manifest whenever arrays with large differences in their intrinsic anisotropic permeability are placed next to each other. This need not be the case only when array sections with opposing inclinations are placed next to one another, as done in the experimental devices shown in figure 8.2 and 8.4. To illustrate this point I carried out large-domain simulation of a cascaded parallelogram layout device with two sections at inclinations $\varepsilon = 0.05$ and 0.25, respectively. All other array parameters are the same, and the device sections lack an interface gap in between. The resulting streamlines (in the region near the right side wall) are plotted in figure 8.8c.

Here, the array with the higher intrinsic anisotropy dominates, tilting the flow along its preferential inclination. This causes a complimentary fluid flow tilt in the adjacent array. We see from figure 8.8c that, away from the side walls, the flow deviates slightly upwards in the right array section ($\varepsilon = 0.25$), and slightly downwards in the left array section ($\varepsilon = 0.05$). Here, the effective array inclinations (measured near the device centreline) reaches $\varepsilon = 0.231$ and 0.068 in the right and left array sections, respectively. Hence, we postulate that DLD devices using cascaded arrays of the form in figure 8.8c may generally have a locally varying critical separation diameter d_c.

From simulations (and experiments) it is observed that, for cascaded DLD devices with similarly inclined array sections, anisotropic flow tilt occurs at the entrance and exit regions of the arrays. When the interface gap is no more than 6λ (the case for many experimental devices), the flow-wise length of the array section affected by anisotropic flow tilt scales with the strength of anisotropy and y directional width of the array section. For cylindrical post parallelogram arrays, it is seen that the extent of the anisotropic zone protruding into the entrance and exit regions of the array section does not exceed the lateral array width. Therefore, a zone free from anisotropic flow deviation can be attained at the centre of an array by having more than twice the number of obstacle pillars in the x direction than in the y direction. Cascaded DLD devices with "long and narrow" array sections, possessing sufficient number of pillars in the centre zone of each section unaffected by anisotropic flow tilt,

and therefore with an invariant d_c, are therefore recommended for particle separation applications.

In simulations, it is simple to confine all lateral force in the DLD geometry with the addition of a lateral pressure drop. However, as we have seen, the presence of side walls in a real device does not guarantee that the flow would remains horizontal everywhere. The presence of "enabler" design features leads to lateral flow deviations in anisotropic arrays, as we move away from the side walls. An interface gap is one such common "enabler" feature used at the beginning and end of arrays in the DLD, to relieve clogging. Therefore "enablers" features like interface gaps should be identified and removed. When the cascaded arrangement of different array sections is used in a DLD device, the anisotropy-free rotated-square layout, rather than the parallelogram layout, should be the preferred design option.

8.5 CAUSES OF EXCESSIVE ANISOTROPY

In recent years, the DLD technique has seen an increasing use of non-circular post shapes, and use of non-standard array parameters, such as non-unity array unit cell aspect ratios (λ_a/λ_b) and post size to array gap ratios (G/D). In this section we look at the intrinsic anisotropic permeability of such non-standard DLD array designs. Similar to the simulations reported in section 8.4, single post simulations are carried out to map array anisotropy for different array parameters and post shapes, and large-domain simulations carried out to visualise anisotropic flow tilt.

8.5.1 *Unequal axial-to-lateral array pitch*

DLD devices with unequal lateral to flow-wise array pitch have shown to give enhanced separation results in specific applications (Zeming, Salafi et al., 2016). We shall see here that using such non-unity aspect ratios (λ_a/λ_b) for the array unit cell has advantages, but comes at the cost of elevated array anisotropy. With single post simulations, the effect of axial to lateral array pitch ratio on anisotropic permeability of the array is studied. This aspect ratio can be quantified as $\Lambda = \lambda_a/\lambda_b$ or as λ_x/λ_y, as illustrated in figure 8.1. In the simulations, the flow-wise pitch λ_a is varied, keeping the lateral pitch fixed at $\lambda_b = 2G = 2D$. All other parameters for the periodic simulation domain are the same as before.

Figure 8.9a plots the variation of anisotropy with varying unit cell aspect ratio in the parallelogram layout, for the array inclinations $\varepsilon = \{0.1, 0.3, 0.5\}$. The anisotropy A for inclinations of $\varepsilon > 0.5$ is equal and negative ($-A$) to those for a negatively inclined array with inclination $1 - \varepsilon$ and are not plotted. For $\varepsilon = 0.5$ the anisotropy is zero for all Λ due to the symmetry of the geometry.

Interestingly, for the parallelogram array, anisotropy steadily decreases and converges to zero as the aspect ratio Λ is increased. This is a significant observation for reducing anisotropic permeability in the parallelogram arrays,

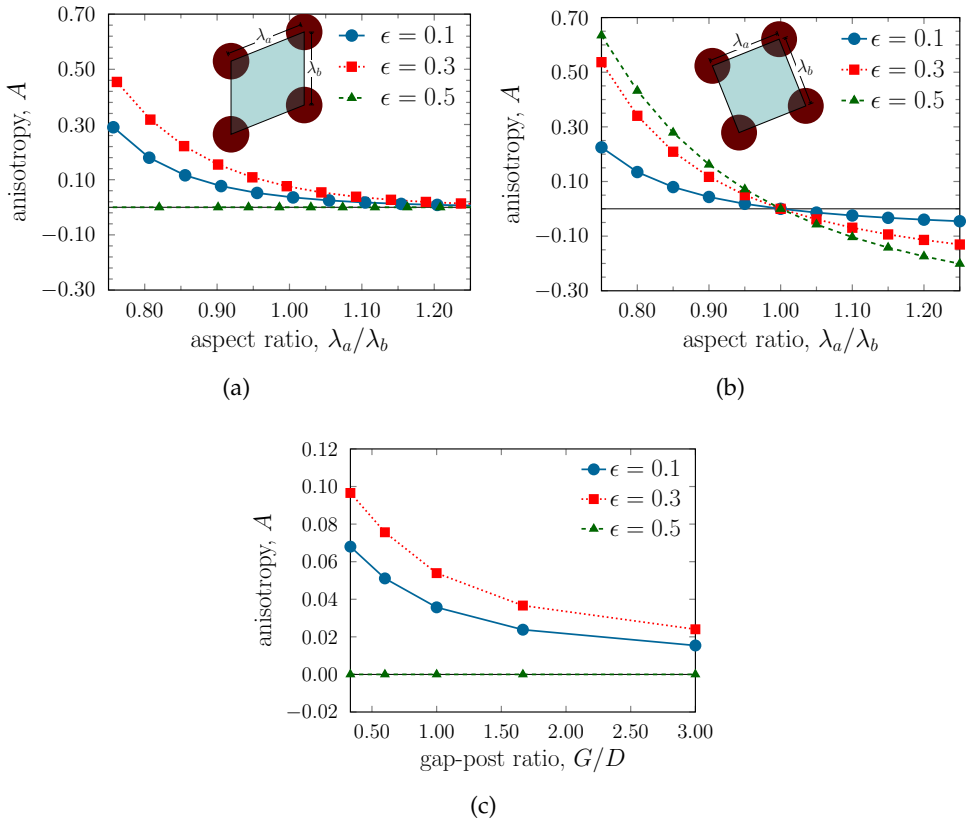

Figure 8.9: Variation of anisotropy (A) with the unit cell aspect ratio ($\Lambda = \lambda_a/\lambda_b$) for (a) the parallelogram layout and (b) the rotated-square layout, with circular pillars. The corresponding array unit cells are indicated as insets in the respective plots. (c) Variation of anisotropy with increase in the gap-to-post diameter ratio (G/D) for the parallelogram layout with circular pillars. In an equivalent rotated-square layout, the anisotropy is identically zero for a circular pillar and G/D has no effect.

especially since the critical radius of the device is independent of the aspect ratio, when G and ε are held constant. Note that α does not remain the same. For example, the simulations predict $r_c = d_c/2 = 1.8$ µm for the $\varepsilon = 0.1$ simulations, and $r_c = 3.6$ µm for the $\varepsilon = 0.3$ simulations, independent of the parallelogram array unit cell aspect ratio Λ. Still, employing $\Lambda > 1$ has a clear disadvantage; larger aspect ratios means longer arrays for the same net lateral displacement. This further means a longer device footprint and a higher resistance to fluid flow. Therefore, such arrays are normally not used.

Figure 8.9b shows the variation of anisotropy with aspect ratio for the rotated-square layout, for RSF $\varepsilon = \{0.1, 0.3, 0.5\}$. Here, we observe that the sign of anisotropy changes when Λ crosses the value of unity. For $\Lambda < 1$ anisotropy is positive and for $\Lambda > 1$ it is negative, while for $\Lambda = 1$ the anisotropy is zero. Hence, unless necessarily required, $\Lambda = 1$ should be chosen for the rotated-square layout to avoid unintended anisotropic flow effects.

8.5.2 *Unequal array gap-to-post size ratio*

Unequal array gap G to post diameter D ratios ($G/D \neq 1$) are commonplace in the DLD arrays, since reducing G is an effective way to decrease the critical separation size d_c for a device. Figure 8.9c plots the variation of anisotropy with the change in G/D ratio for the parallelogram array. Here, anisotropy increases as the size of array gap relative to the the post decreases. However, we can see that the highest anisotropy value is lower than that induced when changing Λ. These results indicate that having larger array gap sizes compared to post sizes reduces the anisotropy in the parallelogram array. Also, for $G/D > 2.0$, the rate of decrease of anisotropy A appears to drop significantly, indicating that this may not be a very good strategy for eliminating anisotropy in DLD arrays, and that a parallelogram layout with point obstacles would still exhibit finite anisotropy. For the rotated-square layout, the array gap-to-post size ratio does not have any effect and the anisotropy remains zero.

8.5.3 *Post shape induced anisotropy*

In this section, we take a look at the effect of using asymmetric post shapes on anisotropic permeability. Here, we start with an experiment with right triangular posts, which shows severe anisotropic flow tilt, and unintended particle behaviour. Again, this experimental work is not a part of the present thesis research, and has been reproduced here from (Vernekar, Krüger et al., 2017) for explanatory purposes. The experiment is shown in figure 8.10(A)-(C). The DLD device used here has two array sections, both with a negative inclination given by $\varepsilon = -0.1$, in the rotated-square layout. The post shape used for the arrays is the right triangle. The two sections are placed alongside each other with an interface gap as seen in figure 8.10(A). The cylindrical pillars seen in the gap are roof supports for the device. All array parameters are the same in the two sections and are are listed in the caption of figure 8.10. The sole difference between the sections is that in the right array section the triangular posts are rotated about their positions by 90° counter-clockwise, relative to those in the left array section, as seen in figure 8.10(A).

Figure 8.10(B) shows the trajectories of fluorescent 3.1 µm diameter beads through the array sections. The bead size is greater than the design critical separation radius in both the sections ($r_c = 1.1$ µm on the vertex side and $r_c = 1.5$ µm on the flat side of the triangle) and the beads are therefore expected to be in the displacement mode, tracing the negative array incline in both array sections. Instead, as we can see from the figure 8.10(B), the beads are in an abnormal zigzag mode in the left section and are in the displacement mode in the right section. Careful examination shows that in the right section, close to the interface gap, the beads are bumping on the flat side of the triangle, rather than on the vertex side as intended.

This anomalous particle behaviour is due to flow tilt induced in the rotated-square device as a result of the highly anisotropic right-triangular pillar

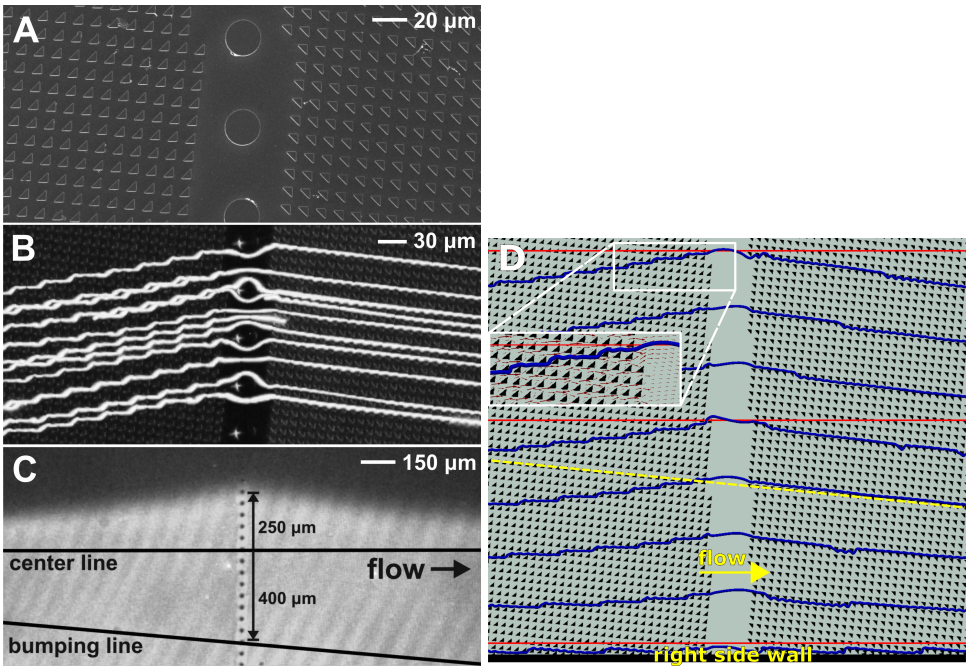

Figure 8.10: Anisotropy of a device with right triangular posts in the rotated square arrangement. (A) SEM of the interface gap between two array sections of the experimental device. The array inclinations are identical on either side with $\varepsilon = -0.1$. The triangular posts are rotated by 90° counter-clockwise in the left section, relative to those in the right. The array parameters $\lambda = 10$ µm and $G = 4$ µm are equal in both sections. (B) Epifluorescence micrograph showing trajectories (white lines) of 3.1 µm beads, expected to be in the displacement mode in both sections. In the left section, the beads are in an abnormal zigzag mode,while in the right section they travel in an inverted displacement mode. (C) The deviation of fluorescent dye, injected along the right side wall of the device, as it crosses the interface gap. The array inclination, device centreline and maximum deviation of the dye region are marked. (D) Flow streamlines (blue lines) from a simulated device with triangular posts, mimicking the experimental device. Significant tilting of the streamlines along the triangle hypotenuse is seen, even a short distance away from the right side wall. The dashed yellow line traces the negative array inclination of both array sections. Arrows in the inset indicate the local flow field. The experimental images (A)-(C) are reproduced from (Vernekar, Krüger et al., 2017) (©CC BY).

shape. The flow pattern in both sections tilts along the hypotenuse of the right-triangle rather than the prevalent array incline. This causes an increase in the effective inclination of the array in the left section and a decrease in the effective inclination in the right array section. In fact, beads bumping on the flat side of the triangles in the right array section hint that the flow tilts beyond the array incline ($\alpha = \tan^{-1}(\varepsilon) \approx -5.7°$), effectively creating a positively inclined array zone close to the interface gap. This flow tilt is visualised by introducing fluorescent dye in the bottom section of the device, as seen in figure 8.10(C). The strong local flow deviation can be gauged from the inclin-

Table 8.1: Anisotropy for different post shapes in the rotated-square layout, with an inclination of $\epsilon = 0.1$. The finite anisotropy when using the circular post ($O(10^{-7})$) is caused by numerical approximations and is treated as zero. Note that for circular posts in the parallelogram layout inclined at $\epsilon = 0.1$, the anisotropy is $A = 3.6 \times 10^{-2}$.

Post shape		Anisotropy, A
Circular		3.1×10^{-7}
Square		2.1×10^{-6}
Equilateral triangle		3.2×10^{-3}
Right triangle		1.8×10^{-1}
I-shape		5.2×10^{-3}

ation of the interface between dye and non-dye regions, demonstrating that the flow tilts along the hypotenuse of the triangular pillars.

To substantiate this claim, large-domain simulation of a device mimicking the experimental device was carried out. The simulation has 160×120 posts in the flow-wise and transverse directions, respectively. The simulated device has two array sections, both in the rotated-square layout, with the same boundary conditions as shown in figure 8.6(A). The triangular posts in the second section are rotated by 90° counter-clockwise, relative to those in the left section. All other device parameters match those in the experiment, except the fact that we do not simulate the cylindrical roof supports located in the interface gap.

Figure 8.10(D) shows the streamlines (blue lines) for a subset of the device close to the right side wall. Already 10 posts away from the side wall, we see that the flow tilt away from the horizontal becomes large and significant. The flow tilt increases to a maximum as we move towards the centre of the device. In the central zone, the flow tilts by $\approx 11.3°$ in the left section, while in the right section, the flow tilts by $\approx -11.9°$ to the horizontal. This means that the effective array inclination in the left section is $\varepsilon \approx -0.31$, leading to an critical diameter of $d_c \approx 3.19$ μm. And an effective inclination of $\varepsilon \approx +0.11$ in the right array section, resulting in an critical diameter of $d_c \approx 1.94$ μm. These results help explain the experimental observations of having the 3.1 μm diameter bead in the abnormal zigzag mode in the left section, and in the bump mode in the right array section. Such large flow deviations from the horizontal caused by the anisotropic triangular post demonstrate that anisotropy can dramatically reverse particle behaviour, even for large particles expected to be in the bump mode in the DLD.

Alternative post shapes

In order to study the role of the post shape induced anisotropy, single post simulations are carried out, and the anisotropy measured. These simulations are similar to those in section 8.4.1. Four different non-cylindrical post shapes,

previously used in the DLD literature, are tested; namely the right triangle, equilateral triangle, square and the I-shape. All the posts are defined such that they can be circumscribed inside a circle of 10 μm. The rotated-square layout is used at an inclination of $\varepsilon = 0.1$, and other array parameters are kept the same as in section 8.4.1. Each post is rotated counter-clockwise to align with the array inclination.

The results for the anisotropy of asymmetric post shapes are collected in table 8.1, alongside that for the circular post in the rotated square array. We can see that highly asymmetric posts such as the right triangle display anisotropy an order of magnitude larger than the maximum value caused by the parallelogram layout with circular posts (at $\varepsilon = 0.25$). However, for the other post shapes, the anisotropy value is nearly zero, and importantly lower than that for the parallelogram layout with circular posts. Therefore, unless highly flow symmetry breaking post shapes (such as the right triangle) are used, anisotropy arising from the obstacle layout can be more important than that induced by the post shape.

Furthermore, these highly asymmetric post shapes can be used to cancel out the anisotropy arising from the parallelogram layout. Post shape induced anisotropy can be varied by rotating them relative to the flow direction. Using this idea, asymmetric post shapes could be used for cancelling the net effect of anisotropy, even in an anisotropic DLD layout.

8.6 SUPPRESSING ANISOTROPIC FLOW TILT

We have established the presence of anisotropy, and the factors leading to anisotropic flow tilt in DLD arrays. We also know that anisotropy is a problem only when it leads to a flow deviation, causing unintended particle trajectories and mixed mode behaviour. Avoiding such problems, and ensuring that the critical separation diameter does not vary locally within the device, is important for predictable bi-modal particle separation in the DLD. Below a number of design pointers, informed from both simulations and experiments, are suggested for suppressing the manifestation of the anisotropic lateral flow tilt.

1. Prefer the rotated-square layout instead of the parallelogram layout for DLD design.
2. "Enabler" design features such as interface gaps and counter-inclined adjacent array sections to be avoided.
3. Reduce anisotropy in the parallelogram layout by increasing the flow-wise to the lateral array gap.
4. Rotate asymmetric non-circular post shapes to counter array anisotropy.
5. Use "long and narrow" array designs with a greater ratio of posts in flow-wise to lateral direction ($\gg 2$) to obtain a central zone free from anisotropic flow tilt, and therefore having an invariant critical separation size d_c.

8.7 SUMMARY AND CONCLUDING REMARKS

In this chapter anisotropic permeability in the DLD arrays has been thoroughly investigated. These numerical investigations have followed naturally from the experimentally observed phenomenon of unintended and mixed mode particle motion in the DLD. Anisotropic obstacle arrays induce a pressure gradient perpendicular to the average flow direction. This induced anisotropic pressure can drive flow in the lateral direction, unless balanced by normal stresses at the no-slip wall boundaries of the device. Anisotropic flow can induce a "ladder-like" localised background recirculatory flow pattern, that impacts the primary flow streamlines. Background recirculation causes the imposed flow to deviate in the direction of the anisotropic pressure drop, which in turn leads to locally varying critical separation size d_c, and unintended mixed mode particle trajectories in the DLD.

We find that the parallelogram layout displays inherent anisotropy, which shows a sinusoidal dependence on the RSF ε. In contrast, arrays with circular posts in the rotated-square layout show no anisotropy and therefore no flow tilt. In the rotated-square layout with circular posts, the flow remains parallel to the device side walls throughout, and thus d_c remains predictable. Therefore, for particle separation applications, the rotated-square layout is recommended over the parallelogram layout.

Moreover, multiple causes of elevated anisotropy in DLD arrays have been identified. Unequal flow-wise and lateral post gaps, larger gap to post diameter ratio and non-circular post cross sections can all lead to a severe increase in anisotropy. Such parameter changes can make even the rotated-square layout highly anisotropic. Furthermore, asymmetric post shapes can induce anisotropic flow on their own. Using a highly asymmetric right triangular post leads to a highly anisotropic device, while the square, equilateral triangle and I-shape lead to relatively negligible anisotropic effects. However, changing the array gap to post size ratio in the rotated-square layout does not lead to anisotropy.

If anisotropic geometries such as the parallelogram layout or right triangular posts are used, one should avoid design features we term as "enablers". The presence of enabler features allows anisotropic pressure to cause background recirculation leading to off-axis lateral flows. One typical enabler feature is the interface gap between array sections, often seen in cascaded DLD devices, or at the beginning or end of arrays. The flow modifications induced by anisotropic permeability plays an important role in the success or failure of a DLD devices, needs to be take care of at the device design stage. Additionally, this study is relevant to a large class of low Reynolds number flows through microfluidic channels and porous media, where the fluid flows past an ordered set of periodic obstacles, similar to those in used in the DLD.

9

TRAJECTORY MODE BIFURCATION REVERSAL DUE TO HYDRODYNAMIC 'LIFT'

Several previous studies have looked at motion of deformable red blood cells (RBCs) through deterministic lateral displacement (DLD) arrays. These have mostly been studies on the effects of RBC deformability and orientation, on their motion through cylindrical post arrays (Beech, Holm et al., 2012; Krüger, Holmes and Coveney, 2014). A year ahead of the start of my PhD research, Zeming, Ranjan and Zhang (2013) introduced a special non-cylindrical pillar shape, which produced remarkable lateral displacement results for RBCs. The enhanced displacement modes appears to result from the dynamical rotation or tumbling of RBCs, induced by the shape of the pillar. Furthermore, a recent study by Henry et al. (2016) also showed enhanced lateral displacement, when the RBCs were induced to tank-tread through an cylindrical post DLD array. In this chapter, the dynamics and motion of deformable RBCs through DLD arrays with special pillar shapes is studied. The purpose of this study is aimed at understanding the role of RBC dynamics towards trajectory mode selection, when flowing past DLD pillars that aid such motions.

In this work, we take the same base pillar shape as the one by Zeming, Ranjan and Zhang (2013), and obtain two other derivative shapes in order to study the effect of RBC deformability and dynamics on trajectory modes. The motion and dynamics of deformable RBCs are analysed with the help of 3D fluid-structure coupled simulations, for three pillar shape geometries. Simulation results of RBC motion over multiple pillars are used to categorise the RBC trajectory modes and build a phase-map, for increasing inclinations of the pillar array to flow. Contrary to expectations, it is found that increasing RBC membrane deformability can lead to a mode bifurcation reversal when the modified pillar shapes are used. The interplay of RBC dynamic modes with the special pillar shapes is seen to be a key component in driving this reversal. Furthermore, the hydrodynamic 'lift'[1] and tumbling orbits are observed and analysed in order to explain the trajectory mode reversal.

Section 9.1 takes a look at the problem statement in the context of recent advances motivating this study. Details on the 3D simulations are provided in section 9.2. Section 9.3 contains short description of solver validation for predicting the trajectory modes for rigid spherical micro-beads in the present DLD geometries. Section 9.4 maps the trajectory mode bifurcation behaviour for all array designs. Sections 9.6 and 9.7 detail the physical mechanisms postulated to govern the mode-bifurcation behaviours in selected arrays. Lastly, the summary and conclusions are given in section 9.8.

1 In this chapter, 'lift' is used to indicate cross streamline repulsive migration of a deformable cell, and does not mean that there is a net force acting on the cell.

9.1 INTRODUCTION AND PROBLEM STATEMENT

The motion of rigid beads through DLD arrays is well described by the volume exclusion effect (steric interaction between particles and pillars), and the critical separation size can be modelled by a simple (empirical equation 3.2) power law. However, the motion of RBCs through DLD arrays shows a much more complex behaviour, which depends on their deformability, fluid viscosity contrast and dynamic motion. Previously, using shallow DLD devices (< 5 μm deep) to confine orientation, it was found that RBCs with greater membrane deformability would tend towards the zigzag mode (Beech, Holm et al., 2012; Krüger, Holmes and Coveney, 2014). In such devices, the deformed (prolate ellipsoid-like) RBCs present a smaller cross sectional area to the flow when passing through DLD array gaps, and thus appear smaller to flow. However, this simple idea shows shortcomings when the RBCs are allowed greater degrees of freedom, and are allowed to undergo characteristic dynamic motions in the DLD (see section 3.3).

Following the pioneering work of Huang et al. (2004), most DLD applications till date have used a standard cylindrical pillar array with equal pitch in flow-wise and lateral directions. Naturally, a number of researchers have since attempted array design with non-cylindrical pillar shapes, mostly aimed at optimisation of the critical separation diameter d_c and improved particle throughput, with varying degrees of success. In 2013, Zeming, Ranjan and Zhang obtained bumping of RBCs at higher than empirically predicted array inclinations (termed as "enhanced bumping"), in experiments where the RBCs displayed tumbling dynamics when flowing through the DLD. Their pillars were shaped in such a way so as to aid RBC rotation when crossing the lateral gaps between the pillars. Further to this study, Henry et al. (2016) observed that the lateral displacement could also be enhanced when the RBCs were induced to tank-tread through the lateral array gaps. Here, the authors decreased the viscosity contrast between *cytosolic* and outer suspending fluid to achieve RBC tank-treading in a DLD with cylindrical pillars. These two studies opened the door for exploiting dynamic RBC motions in the DLD as additional mechanisms for trajectory mode selection.

cytosolic
Belonging to the (inner) cellular fluid, enclosed by the cell membrane

In addition to RBC size, and the principle of volume exclusion described in section 3.2, the mechanisms introduced by complex RBC dynamics in shear are seen to strongly influence RBC trajectories in the DLD. No light has yet been shed on what these mechanisms are. The aforementioned researchers speculated that inertial effects from particle rotation/tumbling, and wall induced hydrodynamic 'lift' due to a tank-treading RBC could explain the enhanced 'bumping', leading to greater lateral displacement of RBCs in their respective studies. However, it is unclear whether such effects are indeed present. These questions are investigated here.

In this chapter, I examine the dynamic motion of RBCs through arrays with three special pillar shapes. Importantly, the hydrodynamic migration velocities and the RBC orientation is computed in order to understand the observed trajectories. Finding the physical mechanisms influencing the RBC trajectory

modes in these arrays is significant for innovating deformability sensitive DLD devices. Detecting RBC deformability changes in blood with the DLD holds considerable potential towards disease diagnostics. For instance, in the case malaria, the infected RBCs express altered deformability within a day of being infected (see chapter 1). Altered RBC membrane deformability presents an opportunity as an early stage diagnostic marker for Lab-on-Chip devices to exploit.

The objective of this study is to discover the mechanisms for RBC migrations in DLDs, taking into account their dynamic motions when non-cylindrical complex pillar shapes are used. These pillar shapes are (empirically) designed to favour one RBC dynamic mode over the other. Towards this end, I explore the motion of RBCs through three sets of parallelogram arrays (with different pillar shapes), described in section 9.2.1. My motivation for simulating these specific pillar shapes is inspired from the work of Zeming, Ranjan and Zhang (2013).

The three pillar shapes are all derived from a base square shape. The first shape is generated by "subtracting" a U-shaped groove from the square shape, the second shape is generated by "adding" a C-shaped ridge to the base square shape and the third shape is the unchanged square shape, acting as the control. The purpose for constructing these shapes is to investigate the effect of a groove and a ridge on RBC dynamics through the DLD. In fact, the exact dimensions for these shapes are obtained from experimental devices fabricated by collaborators. The simulations are carried out to complement experimental testing of these shapes, which are seen to induce distinct RBC dynamics than that seen in devices with cylindrical pillars.

9.2 SIMULATIONS

In this section, we look at the geometric details of the special pillar shapes used in the simulations. We shall also take a look at the important numerical details and the parameter space explored in this study.

9.2.1 *Geometry and RBCs*

DLD GEOMETRY: Three new pillar shapes are employed in this study. These are, the Square, the U-groove and the C-ridge shape, and are illustrated in figure 9.1, along with their respective dimensions. The U-groove and C-ridge shapes are derivatives of the Square pillar shape (shown in figure 9.1a). The general idea for constructing these special shapes follows from the experiments of Zeming, Ranjan and Zhang (2013) (see section 9.1). In these experiments an 'I-shape' pillar, similarly derived from the Square shape, was able to induce rotation (or tumbling) when RBCs crossed the lateral pillar gaps.

This idea of inducing RBC tumbling gives rise to the construction of the U-groove shape in this study, which is obtained by cutting out a U shaped portion (with a semicircular bottom arc with radius $R = 5$ μm) from the Square base pillar shape. An array with the U-groove shape is shown in fig-

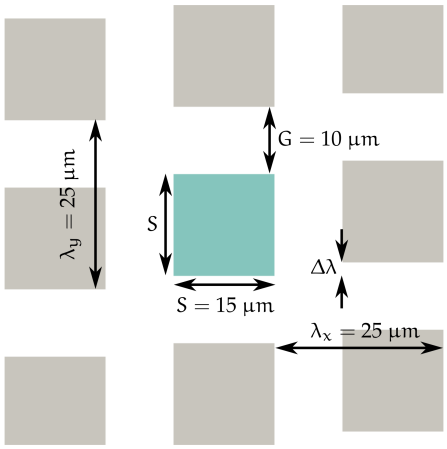

(a) Square pillar array

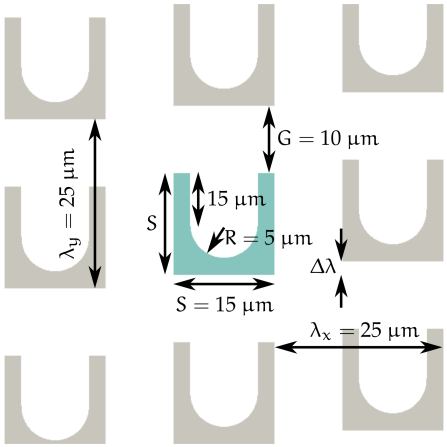

(b) U-groove pillar array

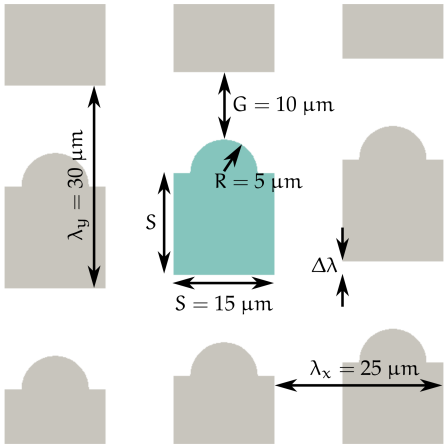

(c) C-ridge pillar array

Figure 9.1: Sections of obstacle arrays with the (a) Square, (b) U-groove and (c) C-ridge shapes. The Square shape pillar shape and array dimensions are adopted from those in Zeming, Ranjan and Zhang (2013). The U-groove shape is derived from the square shape by subtracting a square and semi-cylindrical portion, from the original square shape as shown. The C-ridge pillar shape is also derived from the square shape with the addition of a semi-cylindrical potion at the top of the square. The simulations are carried out over a single pillar (coloured pillar) of the array with periodic boundary conditions that mimic the rest of the array (grey pillars).

ure 9.1b. The C-ridge shape, on the other hand can be seen as a 'negative' of the U-groove shape. For pressure driven flow, the fluid streamlines contract (and then expand) as they flow through the C-ridge array gaps, while those through arrays U-groove shape expand (and then contract). The C-ridge shape is derived from the Square base shape by adding a semicircular ridge (with radius $R = 5$ μm) on top of the square. With the addition of the semicircular top ridge, the flow induced by this shape is (to a certain degree) similar to that by the standard cylindrical pillar shape. Thus, the RBCs are expected to show similar dynamical behaviour here.

In our study, the base Square shape dimensions are the same as that in the experimental work of Zeming, Ranjan and Zhang (2013) with sides of $S = 15$ μm. For the arrays employing either of the three pillar shapes, the axial (flow-wise) array pitch $\lambda_x = 25$ μm, and the array gaps (in both directions) $G = 10$ μm, are also exactly identical to those used in the experimental work. The only major departure in terms of the array dimensions, is the lateral array pitch λ_y. While for the Square and U-groove pillar shapes the lateral array pitch is the same as the flow-wise array pitch $\lambda_y = \lambda_x = 25$ μm, that employed for the C-ridge pillar shape has to be increased to $\lambda_y = 30$ μm in order to accommodate for the addition of the ridge feature. The depth for all three array sets is chosen as $H = 15$ μm. It is anticipated that such consistency in terms of dimensions would help in future comparisons with experiments. The remaining dimensional array details are given in the caption of figure 9.1.

RED BLOOD CELLS: The red blood cells are modelled as elastic biconcave membranes, with a shape defined by the equation 4.4. For this study, we set the in-plane radius (along the major axis) for the RBC to $R_0 = 3.91$ μm. This results in a maximum thickness of $t_0 = 2.4$ μm for the undeformed cells. These RBC dimensions are held constant in all the simulations. The deformability of the RBC membrane is governed by its bending κ^b, strain κ^s and local area dilation (or areal dilation) κ^α moduli. For a healthy RBC, the generally accepted values for bending and strain moduli obtained from experiments are $\kappa^b = 1.8 \times 10^{-19}$ Nm and $\kappa^s = 4.2$ to 5 μN/m, respectively (Evans, 1983; Skalak, Tozeren et al., 1973; Skalak, Ozkaya and Skalak, 1989). Therefore the non-dimensional ratio of bending to strain is calculated as $\frac{\kappa^b}{\kappa^s R_0^2} \approx 2.5 \times 10^{-3}$. The non-dimensional value for the local area dilation modulus is set to $\kappa^\alpha = 1.0$. In reality, κ^α needs to be orders of magnitude larger than κ^s since the RBC membrane is effectively incompressible. However, in my simulations I have set $\kappa^\alpha <= 1.0$ for numerical stability reasons, and hence the computations allow for some local membrane area deviations. When changing cell deformability in different simulations, the non-dimensional ratio of bending to strain modulii, and κ^α are kept constant.

The two additional cell membrane moduli, for enclosed volume conservation κ_V, and global area conservation κ_A, are both set to unity. Furthermore, the ratio of inner (enclosed fluid) to outer fluid viscosities (the viscosity contrast) for the simulations is set to $\Gamma = 5$, which is approximately the physiolo-

gical value measured for human RBCs *in vivo*. These values are also held constant in all simulations.

9.2.2 *Numerical details*

In the present study, the simulations are carried out over a single pillar of the DLD array with periodic boundary conditions in the flow-wise (x) and lateral-to-flow (y) directions. The simulation domain uses $50 \times 50 \times 32$ lattice nodes for simulations with the Square and U-groove pillars, and $50 \times 60 \times 32$ lattice nodes for simulations with the C-ridge pillar, in the x, y and z directions respectively. The periodic boundary mapping along the x direction is shifted by $\pm\Delta\lambda$ to account for the lateral shift between successive rows of pillars. In the z direction, stationary top and bottom walls are modelled with the help of half-way bounce back scheme.

Clearly, $\lambda_x = 25\ \mu m = 50$ lattice nodes in all simulated domains, which gives the lattice (mesh resolution) length scale of $\Delta x = 0.5\ \mu m$. By taking the lattice length scale as a unit of distance, the simulation density $\rho = 1$ for density (mass) and the simulation time step $\Delta t = 1$ as a unit of time, all relevant terms can be written with respect to 'lattice units' (or simulation units). The undeformed RBC radius can be written as $R_0 = 7.82\Delta x$ in terms of the lattice length scale, or implicitly as $R_0^* = 7.82$, where the superscript * indicates that the variable value is measured with respect to lattice units. We switch to lattice units whenever appropriate in this chapter, especially since it is convenient to use them in order to compute the non-dimensional numbers of relevance to the study. Obviously, these non-dimensional numbers (or ratios), being independent of the set of units chosen, are universal and can be used for interpreting the results in terms of physical units of convenience.

The flow is driven by a pressure gradient, mimicked with the help of a body force $\mathbf{f}$ (per unit volume) that acts on all the fluid nodes in the simulation domain. The imposed body force is $\mathbf{f}^* = (0.5, 0.0, 0.0) \times 10^{-5}$, acting along the x direction, in all simulations. Since the parallelogram array modelled here is anisotropic, a lateral component for the body force f_y is computed at runtime, such the mean fluid flux in the y direction equals zero. This lateral body force is necessary to model the presence of channel side walls for the DLD array. This approach places the side walls at large but finite $\pm Y_w$ distance from the simulated single pillar. This lateral body force is added at all fluid lattice nodes for all simulations carried out over a unit pillar of an array, in this thesis.

Using lattice units, the Reynolds number for the flow is computed as

$$Re = \frac{u_m^* G^*}{\nu^*} \approx 0.218, \tag{9.1}$$

where u_m is the typical maximum velocity magnitude measured for all simulations, and ν is the kinematic viscosity. $Re < 0.5$ means we can assume that inertial effects are negligible and the simulations are dominated by viscous dissipation (Stokes flow regime).

For all simulations in this study the same RBC mesh, with 1280 triangular elements, is employed. The deformation of the RBC membrane is quantified in terms of the capillary number as

$$Ca = \frac{p' G R_0}{\kappa^s} = \frac{f_x^* G^* R_0^*}{\kappa^{*,s}}, \tag{9.2}$$

where p' is the average pressure drop across λ_x. Here, we have taken the array gap G as the characteristic length scale for viscous fluid stress in the DLD geometry, consistent with the definition of Reynolds number in equation 9.1. We shall use the capillary number Ca to quantify RBC membrane deformability. The Reynolds number $Re \approx 0.2$ is held constant for all simulations with the same pillar shape.

Generally, the row shift fraction (RSF) is defined as $\varepsilon = \Delta\lambda/\lambda_y$, where λ_y is the array pitch in the lateral direction. However, λ_y is not equal for the Square/U-groove and C-ridge geometries, whereas we have a constant λ_x for all simulated pillars. Therefore, it is suitable to redefine RSF as $\varepsilon' = \Delta\lambda/\lambda_x$. This definition of ε' also gives the correct array inclination with $\alpha = tan^{-1}(\Delta\lambda/\lambda_x)$.

9.2.3 *Study parameters*

DEFORMABLE RBC SIMULATIONS: For an array with a given pillar shape, multiple, single-RBC simulations are carried out at varying row shifts given by ε'. The membrane deformability is held constant for simulations at different ε'. The RBC deformability is characterised by the capillary number Ca. Such a set of simulations mimic experimental tests where RBCs are flowed through a *cascaded DLD* setup with an step-wise increase in the row shift, at a constant flow rate. These simulations are carried out for all three pillar shapes at 5 distinct values for cell deformability given by the capillary numbers $Ca = \{0.00598, 0.01975, 0.0598, 0.1975, 0.598\}$. These values are rewritten as $Ca' = \{0.1, 0.33, 1.0, 3.3, 10.0\}$ for convenience, where $Ca' = 16.71355Ca$. In the simulations, these changes in Ca are achieved by varying the membrane strain $\kappa^{*,s}$ and bending $\kappa^{*,b}$ moduli, such that their non-dimensional ratio is held constant (see section 9.2.1). Physically, these step changes in Ca can be seen as a ramping up of the driving flow rate through the DLD system. The Reynolds number Re is held constant in our simulations. In reality, Re would vary with a change in the flow rate. However, in the Stokes flow regime, flow-rate changes have a negligible effect on the nature of the flow field, and Re can be assumed constant. For a given Ca, the maximum RSF variation is between $\varepsilon' = 1/50$ and $8/50$.

cascaded DLD
DLD arrays placed one after the other in series, mostly when varying the array inclination or inter-pillar gap

Each simulated case, with parameters (pillar shape, Ca, ε'), lets us identify a trajectory mode for the deformable RBC through the DLD setup. The critical row shift fraction ε'_c, that defines the critical array inclination at which the cells would transit from perfect bump (or displacement) mode to the horizontal zigzag mode, is then identified by running simulations at increasing RSF values and analysing cell trajectories. Now, this bifurcation zone in most

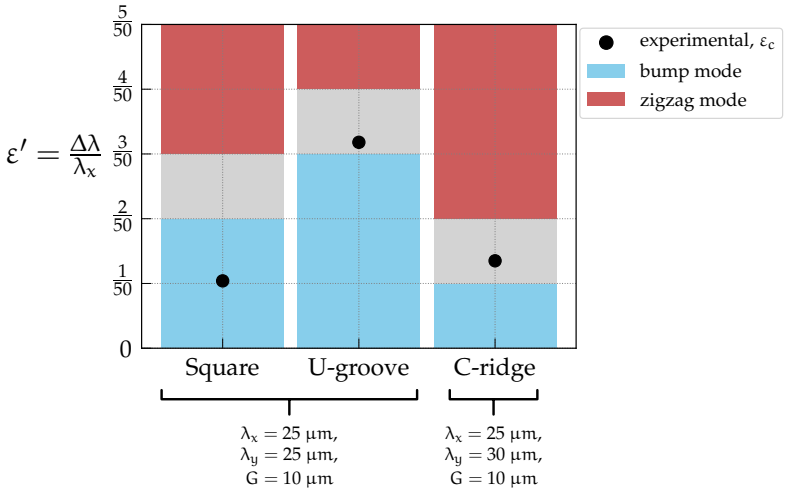

Figure 9.2: Trajectory mode-bifurcation plot for a rigid 3 μm bead in the simulated DLD arrays. The coloured bars plot the trajectory modes identified from rigid bead simulations, for all three pillar shapes. The simulations predict that the critical row shift fraction ε'_c, at which the bead transitions from zigzag to bump mode, would lie in the grey region. The corresponding experimental estimate is indicated with a (black) marker points.

simulated cases is not sharp, and is defined by large transitional ε' values, where the cell trajectories exhibit mixed mode. The RBC trajectories in the mixed mode motion show characteristics of being in both displacement and zigzag modes. With this procedure we can build a mode bifurcation map for the RBC trajectory modes, identifying the critical transition region which would enable RBC separation based on membrane deformability. The reader should note that in order to identify this critical transition zone for each pillar shape and Ca, we do not scan all the ε' values, but only those that lie in-between clearly identifiable displacement and zigzag mode trajectories. As such, an *ad-hoc* search is conducted for mapping the bifurcation region in the (Ca, ε') space for each pillar shape, without running over the entire parameter space.

The initial positions of the cells in all the simulations are kept the same and lie in the device depth mid-plane. Off-mid plane initialisations are also done, in a few simulations to test 3D dynamics for the rigid RBC at $Ca' = 0.1$ with the U-groove pillar shape. All simulations are carried out till the RBCs cross greater than $3\lambda_x/\Delta\lambda$ pillars along the flow-wise direction, allowing for the correct identification of the cell/particle trajectory modes independent of the bias introduced by the initial conditions.

9.3 SOLVER VALIDATION

Since the pillar shapes used in this study are non-cylindrical, the standard method (using equation 3.2) for estimating the critical separation diameter d_c no longer holds. It is therefore necessary to recalibrate the simulation setup, and validate the same against experimental results. The validation of

the code, for the three new pillar shapes, is carried out against the experimental results from my collaborators on the project. In these experiments the motion of a 3 μm rigid spherical bead is tracked through cascaded DLD devices. Devices were fabricated for the U-groove, C-ridge and Square pillar shapes, with cascaded arrays at varying row shifts. The experimental array dimensions are the same as those simulated here (given in section 9.2.1). Multiple 3 μm bead trajectories, tracked through these cascaded devices, are used to determine an average critical RSF value from the experiments.

RIGID BEAD SIMULATIONS: Rigid spherical beads are simulated for the purpose of solver validation. In these simulations a spherical membrane mesh with a radius of 3.0 μm is used. The membrane mesh has 320 triangular elements. Here, the values for bending and strain moduli as set as high as numerically stable for each simulation. The objective here is to minimise all deformability effects, and set the capillary number $Ca \approx 0$. Therefore, the capillary number no longer has any physical meaning. The trajectory modes and the critical separation RSF ε_c' are determined in a similar way to that described earlier in section 9.2.3, except I do not identify mixed mode particle behaviour for validation as this was not considered in the experiments.

The validation results are plotted in figure 9.2. The bar plots cover simulation cases for discrete RSF values marked on the y axis and are coloured according to the observed trajectory mode of the simulated bead. Here, all non-displacement mode trajectory motions are classified as zigzag mode, which is consistent with the experimental classification. The grey regions in figure 9.2 indicate the predicted range for RSF values where the mode transition occurs.

For the two complex derivative pillar shapes (C-ridge and U-groove), we see that the experimental results are in excellent agreement with the simulation predictions. However, a modest mismatch occurs for the Square pillar shape, where simulations over-predict the region of critical transition, by at least one unit row shift $\Delta\lambda = \Delta x$. A probable cause for this discrepancy could be the fact that in the simulations the Square shape has sharp well-defined corners, whereas in the experimental device these are more rounded. Since the mesh resolution would have to be more than doubled in order to capture such rounded corners, this point remains un-tested. This error could also come from the numerical limitations of the cell-pillar contact model, or the membrane-fluid diffuse interface due to the immersed boundary method. Since this study deals with uncovering the physics underlying trajectory mode transition for deformable RBCs, the agreement as seen in figure 9.2 is considered satisfactory. With these code calibrations, we move on to the results of this study, which is detailed in the following sections.

9.4 DEFORMABILITY-BASED MODE BIFURCATION REVERSAL

The trajectories, orientations and velocities of RBCs through simulations with different pillar shapes are tracked. In these simulations, the cells are initial-

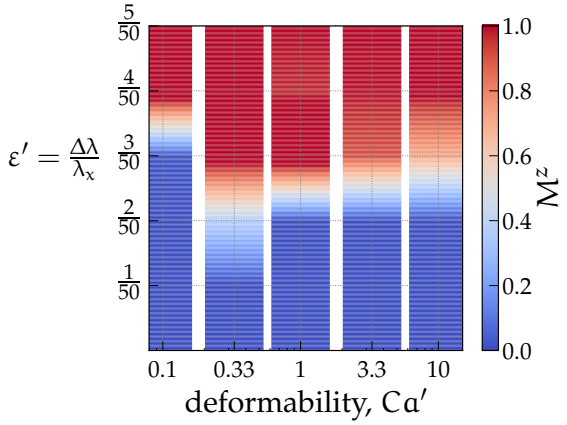

(a) U-groove pillar

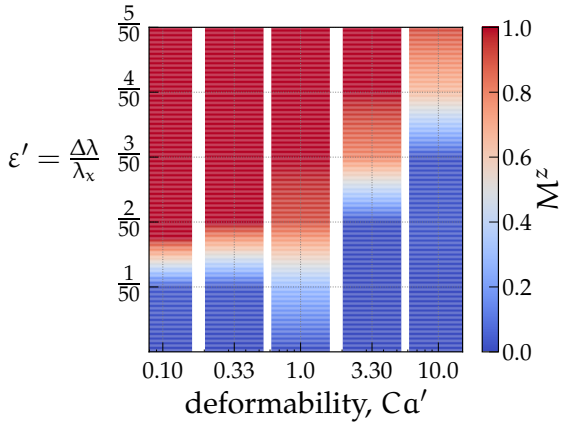

(b) C-ridge pillar

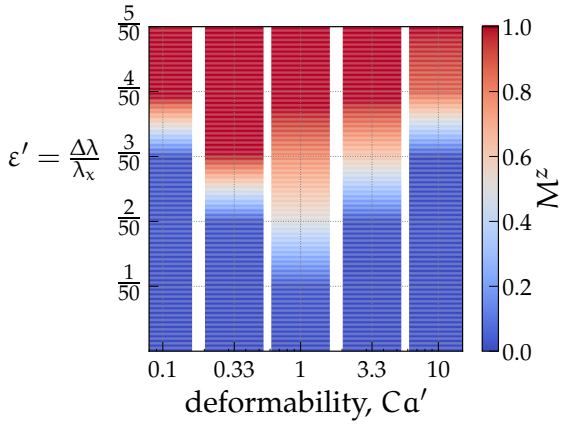

(c) Square pillar

Figure 9.3: Phase-bifurcation maps for RBC trajectory modes in arrays with (a) the U-groove pillar, (b) the C-ridge pillar and (c) the Square pillar. The x axis in all three maps gives the cell deformability, plotted at five discrete values of capillary number Ca'. Here, $Ca' \approx 16.71Ca$ is the adjusted capillary number. The y axis gives the row shift fraction (RSF). The contours show the variation of M^z, which is a positive, real valued measure of the cell trajectory modes. $M^z = 1$ indicates perfect zigzag (darkest red) and $M^z = 0$ indicates perfect bump mode (darkest blue). The critical RSF ε'_c can be noted from the (white) transition zone from blue to red, which also indicates mixed mode trajectories with $0 < M^z < 1$.

ised with their centres in the depth mid-plane (at a depth of $z = 7.5\ \mu m$ from both, top and bottom walls) of the device. The cell trajectories need to be classified into zigzag or displacement mode, so that we can understand trajectory mode-bifurcation as a function of cell deformability and array RSF (Ca, ε'). This requires identifying the trajectory mode from cellular paths. The task is problematic because of the emergence of a large variety of transitional mixed mode behaviour of the cell trajectories in the DLD. These mixed modes arise mainly because of the anisotropic shape of the RBCs combined with the use of complex pillar shapes, and less so because of the non-integer array periodicity N employed. It is clear that a discrete classification of the modes, as zigzag, mixed and displacement, would loose the complexity observed in the RBC trajectories.

This difficulty can be overcome by defining a real-valued measure of the cells "zigzagginess", or in other words, its deviation from from perfect displacement path through the array. We know that in perfect horizontal zigzag mode, a cell should undergo exactly $N = 1/\varepsilon = \lambda_y/\Delta\lambda$ zigzag events, whereas in perfect displacement this number is zero. Therefore, if the number of pillars crossed by the cell through the simulated domain is n, I can write the number of expected zigzag events for the cells path as n/N. Comparing this number to the actual number of zigzag events can be used to obtain a non-negative real number that indicates the cells trajectory mode.

This real valued measure for the cell trajectory deviation away from the array inclination (or the cells zigzagginess) is defined as

$$M^z = \frac{m}{n} N, \tag{9.3}$$

where m is the number of observed zigzag events and n is the number of pillars crossed by the cell in the flow-wise (x) direction. m and n are also computed as a real-valued numbers as,

$$m = \frac{1}{\lambda_y}\left|\frac{X}{\lambda_x}\Delta\lambda - Y + Y_0\right| \qquad \text{and} \qquad n = \frac{X}{\lambda_x}, \tag{9.4}$$

where (X, Y, Z) and (X_0, Y_0, Z_0) are the final and initial positions of the cell along the flow-wise, lateral-to-flow and depth-wise directions, respectively.

This simple definition returns $M^z = 0$ for a pure displacement mode, and $M^z = 1$ for perfect zigzag. Any value such that $0 < M^z < 1$ indicates a cellular trajectory with an average inclination in-between the array inclination α and the horizontal. If the computed value of $M^z > 1$, this indicates that the cell trajectories are negative, and the cells migrate below the horizontal line.

Continuously varying phase-bifurcation maps for the RBC trajectory modes with the new parameter M^z are plotted for all three pillar shapes in figure 9.3. Here, the M^z values are plotted as contour bars at five discrete values of deformability Ca against increasing ε' values. The darkest blue zones indicate perfect displacement, while the darkest red zones indicate perfect zigzag. The white region of separation between the red and the blue indicates the likely

critical mode-bifurcation region, where the critical RSF ε' value is located. The white zones, along with zones of lighter shades of red and blue hold information from the mixed mode cell trajectories. Note that when $M^z > 1$, the maps in figure 9.3 treat the trajectories as perfect zigzag and therefore the contours are coloured as equal to $M^z = 1$. The maps do not take into account negative migration angles. These phase-bifurcation maps help identify the behaviour of the critical separation RSF value ε'_c as a function of the RBC membrane deformability (Ca) for each pillar shape.

In the first of these maps for the U-groove pillar in figure 9.3a, we observe that the highest critical RSF ε'_c is seen at the highest tested RBC rigidity at $Ca' = 0.1$. With increase in the cell deformability to $Ca' = 0.33$ the critical RSF value falls by a couple of row-shifts. Upon further step increase of the cell deformability ($1 < Ca' < 10$), ε'_c appears to remain nearly constant, but the spread of the mixed mode zone is seen to increase. Such a behaviour is along expected lines, as an increase in membrane deformability means a decrease in the RBC apparent size in the device due to prolate-like deformation of RBC, as it flows through the array gaps (Krüger, Holmes and Coveney, 2014). This makes the deformed RBCs prone to the zigzag mode than when they are rigid, explaining the decrease in ε'_c. The trends seen here however do not explain the elevated bumping seen in the experiments of Zeming, Ranjan and Zhang (2013). We shall see later that full 3D dynamics of the rigid RBC in the U-groove pillar array is responsible for this elevated bumping.

The phase-bifurcation map for trajectory modes with the C-ridge pillar shape is seen in figure 9.3b. Remarkably, the phase-bifurcation trend sees a reversal when the cellular deformability is increased. Here, as the cellular deformability increases, so does the transitional mixed mode region, ultimately leading to an elevated ε'_c at the highest softness of $Ca' = 10.0$. This phase-reversal is non-intuitive since it suggests that an increase in cellular deformability does not have a detrimental effect on RBC bumping.

The phase-bifurcation map for the square pillar is plotted in figure 9.3c. Here, an interesting non-monotonic trend is seen for ε'_c. The transitional zone shows a sharp bifurcation for the rigid RBC case at $Ca' = 0.1$. With increase in deformability till $Ca <= 1$, the critical RSF decreases, showing a greater mixed mode spread at $Ca = 1$. Beyond this critical deformability ($Ca > 1$) the critical RSF ε'_c increases. As with the C-ridge shape, these trends for the Square shape suggest the presence of additional mechanisms that reverse the effect of increased cell deformability on the effective size of cells in the DLD.

Though these phase-maps only cover five discrete deformability values, the trends seen here show that with changed pillar shape, completely opposing phase-bifurcation behaviours are observed for RBCs in the DLD. This hints at an additional physical effect other than cell size playing an important role in deciding the critical RSF in arrays. The behaviour seen in figure 9.3c hints that the dominant physics leading to trajectory mode selection changes with increasing cell deformability. These additional dominant physical effects that strongly influence mode-bifurcation are seen to depend the nature of the pillar shape used. In order to find what these effects are, I take a look at

the deformability dependent changing kinematics of the RBCs through the arrays in the next section.

9.5 RBC MOTION

In this section we take a look at the kinematics of the RBC as it move through the different arrays in the displacement mode ($M^z \approx 0$). The RSF values selected for these plots are just below the critical RSF values ($\varepsilon' < \varepsilon'_c$) for each of the pillar shape arrays examined. The cell are initialised such that they are symmetric about the device depth mid-plane at (with centroid at $z = 7.5$ μm). The RBC motion is examined over three successive pillars, after the cell has crossed more than $2\lambda_x/\Delta\lambda$ pillars along the flow-wise direction in the simulation. This eliminates initialization biases introduced to the periodic simulations. However, in the absence of dynamic perturbations to RBC motion, the bias introduced by the symmetric initialisation about the depth mid-plane can persist throughout the simulations, and out-of-mid-plane cell dynamics suppressed. The analysis here is based on images from full-3D simulations, projected onto the depth plane (z-direction) of the devices.

The phase-bifurcation maps (figure 9.3) seen previously hint at two different physical mechanisms at play for the rigid and soft RBC motion through DLD arrays. Therefore , this section focuses attention on the RBC kinematics observed for the limits of the $C\alpha'$ values tested in my simulations.

9.5.1 *Rigid RBC motion*

A time-lapse sample of the kinematics of RBC motion over three consecutive pillars in arrays with the three different shapes is shown in figure 9.4. The RBC kinematics seen in the figure are representative of rigid RBC motion in the displacement mode through all the three arrays. Here the RBCs with rigidity is set at $C\alpha' = 0.1$, display characteristic tumbling motion through the arrays. The row shifts seen in the figure are just below the critical row shifts (given by $\varepsilon'_c \times \lambda_x$) where clear displacement mode motion can be observed. Comparing the three tumbling motions seen in figures 9.4a, 9.4b and 9.4c, the effect of pillar shape on tumbling becomes clear. Though the cell tumbles in all three geometries, the spatial degrees of freedom provided by each are different.

In the U-groove pillar in figure 9.4a, the cell assumes a near-vertical profile within the groove of the pillar, or just before climbing over the first prong of the pillar (see RBC just before going over the first pillar and while crossing the second pillar in figure 9.4a). Looking at the figure 9.4b, it is seen that the cell flips over the trailing edge of the ridge in each instance. This means that while climbing over the next C-ridge pillar, the cell does not do a flip, but rather goes over the pillar at a relatively fixed 'attack' angle. In the case of the Square pillar array seen in figure 9.4c, the cell climbs over the pillar by doing a flip (similar to the motion over U-groove pillar), but due to the constraint of geometry remains horizontal when passing over the pillar.

(a) "U-groove" pillar, $Ca' = 0.1$ and $\varepsilon' = 3/50$

(b) "C-ridge" pillar, $Ca' = 0.1$ and $\varepsilon' = 1/50$

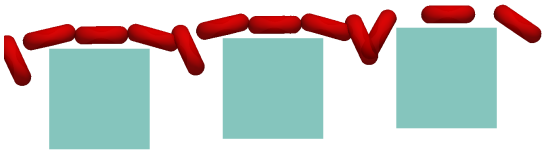

(c) "Square" pillar, $Ca' = 0.1$ and $\varepsilon' = 3/50$

Figure 9.4: Simulation time-lapse overlay of a single rigid RBC ($Ca' = 0.1$), as it crosses three consecutive pillars. Typical RBC tumbling motion over (a) the U-groove pillar, (b) the C-ridge pillar and (c) the Square pillar array is seen. All three cases shown are in displacement mode ($M^z \approx 0$) for row shift fractions captioned in the respective panels.

Correlating these observations to the mode-bifurcation seen for the rigid red blood cell in figure 9.3, I hypothesise that the approach angle that the RBC takes when climbing over a pillar array plays an important role in deciding its trajectory mode selection. This approach angle is determined by the geometry as well as the resulting flow-field. Another remarkable observation is that the tumbling remains in the shear plane and the tumbling RBC centres of mass do not leave the device depth mid-plane. As we shall see later in section 9.6, this proves to be a significant issue. This quasi-2D nature of the RBC tumbling dynamics in these simulations could explain why the phase-bifurcation maps in figure 9.3a fail to reproduce elevated bumping seen in the experiments for pillars similar to the U-groove (Zeming, Ranjan and Zhang, 2013).

9.5.2 *Soft RBC motion*

Sample time-lapse image overlays of soft RBCs over the three consecutive pillars of the three different array shapes are seen in figure 9.5. The RBCs are highly deformable with a membrane rigidity characterised by $Ca' = 10$, in

(a) "U-groove" pillar, $Ca' = 0.1$ and $\varepsilon' = 2/50$

(b) "C-ridge" pillar, $Ca' = 0.1$ and $\varepsilon' = 3/50$

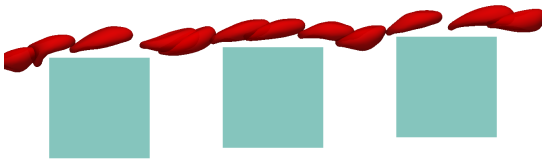

(c) "Square" pillar, $Ca' = 0.1$ and $\varepsilon' = 3/50$

Figure 9.5: Simulation time-lapse overlay of a single soft RBC ($Ca' = 10$), as it crosses three consecutive pillars. Typical RBC tank-tread like motion over (a) the U-groove pillar, (b) the C-ridge pillar and (c) the Square pillar array is seen. All three cases shown are in displacement mode ($M^z \approx 0$) for row shift fractions captioned in the respective panels.

all three simulations. The row shift fractions chosen for the figures 9.5a, 9.5b and 9.5c are the maximum values for which RBCs are seen to undergo pure displacement mode ($M^z \approx 0$) in the arrays. The motions seen in the figure are characteristic of tank-tread like RBC dynamics. Comparing this motion of the RBCs in the three array geometries in figures 9.5a, 9.5b and 9.5c, their kinematics appear very similar. The cell membrane undergoes periodic tank-treading as the RBC passes through the arrays in all three cases examined. In displacement mode motion, at the high deformability of $Ca' = 10$, similar RBC kinematics is seen in all tested simulations irrespective of the pillar shape or RSF ε'.

In figure 9.5a the RBC is seen to rotate out of plane while moving over the U-groove pillar, exposing the concave dimple at its centre (seen as the RBC moves over the second prong of the second pillar in the figure 9.5a). This shows that the tank tread motion achieves true-3D dynamics and the initialisation symmetry is broken. Examining the trajectory of the tank treading particle (not shown) it is clear that the soft RBC leaves the depth mid-plane of the DLD when moving in the displacement mode. This off mid-plane

($z = 7.5$ μm) tank-tread dynamics is also true for the RBC motion through C-ridge and Square pillar arrays, seen in figures 9.5b and 9.5c.

From figures 9.5b and 9.5c it is seen that the RBC kinematics appear alike[2]. The deformations of the cells before climbing over a pillar, over the pillar, and after leaving the pillar, in the two cases show great similarity. This suggests that the trajectory mode-bifurcation reversal effect seen in the phase-maps 9.3b and 9.3c arise from physical effects driven by shape changes of the soft RBCs as they move over the array pillars. Contrasting with RBC kinematics in figure 9.5a, it is seen that unlike RBC motion in the C-ridge and Square cases, the RBC here widens when crossing over the pillar through the lateral gap. Such deformation is encouraged by the flow-field over the U-groove pillar, which expands downstream of the first prong and contract upstream of the second.

Another significant observation seen in figures 9.5b and 9.5c, contrasting with figure 9.5a, is that the RBCs maintain a large liquid film layer between their membrane and the pillar. For the C-ridge and Square pillar shapes, the soft RBCs barely come in physical contact with the pillar walls when moving over them, while the soft RBC is seen to periodically bump into the U-groove pillar prongs without exception. This contrasting motion indicates that wall induced soft cell cross streamline migration could have a significant impact on the cell trajectories through the C-ridge and Square pillar arrays. This hypothesis is further supported by the fact that no mode-bifurcation reversal is seen for the U-groove pillar with increasing deformability (figure 9.3a). Here such wall induced migration could be inhibited by the diverging-converging streamlines over the U-groove pillar (due to the presence of the groove and the lack of a no-slip wall boundary). In order to gauge whether soft particle cross streamline migration is physically significant, I compute sample migration velocities for the RBC motion through the C-ridge pillar array in section 9.7.

9.6 FULL-3D RBC TUMBLING DYNAMICS

Since the tumbling dynamics seen for the rigid RBC ($Ca' = 0.1$) in figure 9.4 (section 9.5.1) turn out to be quasi-2D in nature, this section investigates the effect of perturbed rigid RBC initialization that breaks the depth mid-plane symmetry. These simulations are carried out for the U-groove pillar array at various RSF (ε') values with the rigid RBC at $Ca' = 0.1$, and the results are plotted in figure 9.6. In all the simulations shown here, the cell is initialised at depth $z = 6.75$ μm. Such an initialization is seen to break the symmetry of tumbling motion (about the shearing depth mid-plane) for the RBC. In real devices, it is expected that the RBCs would be pushed out of depth mid-plane due to suspension effects, perturbations due to device manufacturing defects and flow-field perturbations introduced by the syringe pumps used to drive the flow.

2 more alike than that seen in figure 9.5a

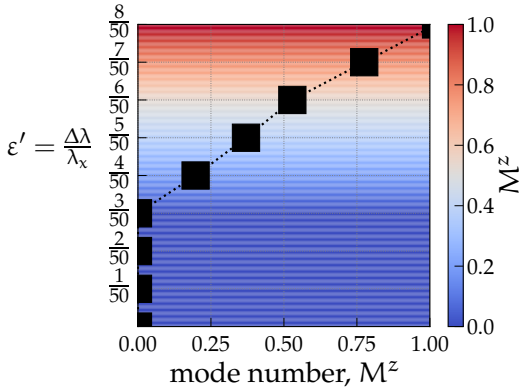

(a) mode-bifurcation for "C-ridge" pillar, $Ca' = 0.1$

(b) "C-ridge" pillar, $Ca' = 0.1$ and $\varepsilon' = 3/50$

Figure 9.6: Simulation results for asymmetric (off device mid-plane) RBC initialization at depth $z = 6.75$ μm. (a) The line plot (and the mode-bifurcation contour) shows a linear increase in the mode number M^z indicating greater spread of mixed mode behaviour between $3/50 \leqslant \varepsilon' \leqslant 8/50$. This increases effective critical RSF value ε'_c and would lead to greater lateral displacement. (b) Simulation time-lapse overlay of the full-3D tumbling motion of the RBC superimposed over the quasi-2D tumbling (background, faint red) observed in figure 9.4a (for depth mid-plane initialization at $z = 7.5$ μm). The rigid RBC at $Ca' = 0.1$ with the asymmetric initialization shows qualitative increase in effective size as it crosses the two prongs of the U-groove pillar shape.

An out-of-plane initialization leads to greater mixed modes behaviour as well as higher overall lateral displacement for the RBC. These results are seen in the trajectory mode-bifurcation map in figure 9.6a, where the "zig-zagginess" mode number M^z is plotted with square markers (as well as with bar-contour to facilitate comparison with figure 9.3). It can be seen that though the threshold for pure bump mode remains at the same RSF value $\varepsilon' = 3/50$ in these newer simulations, the effective lateral displacement of the RBC would be increased due to an elevated limit for pure zig-zag at $\varepsilon' = 8/50$ (increased spread of mixed mode behaviour). At RSF values between $3/50 \leqslant \varepsilon' \leqslant 8/50$, the mode number M^z shows near-linear variation.

In figure 9.6b, I record the kinematic motion (time-lapse) for the rigid RBC in this simulation, and compare it with that seen earlier in figure 9.4a (reproduced in figure 9.6b with faded red). Although the differences in the motions

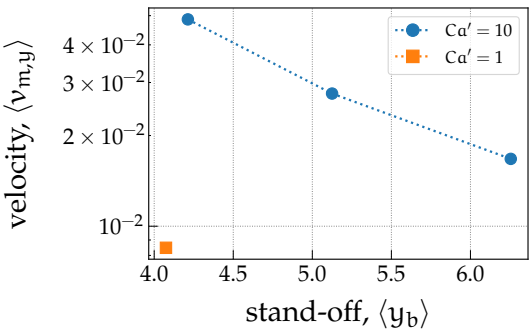

Figure 9.7: Plot for average cell migration velocity (y component) against the average stand-off distance for the cell centroid for two different cell deformabilities in the C-ridge pillar. All cases plotted are for displacement mode motion. The average cell migration velocity is the velocity "lag" for the cells centroid relative to the cell-free flow in the same geometry. The average migration velocity is scaled with the (approximate) average particle-free fluid velocity in C-ridge pillar geometry. The average stand-off distance gives the average y-position of the cell centroid above the C-ridge pillar ledge (y distance from the bottom of the semicircular ridge feature), indicating how close the cell passes to the pillar in the displacement mode.

are not striking, the 3D orientation of the RBC in the new simulation is clearly seen. This 3D tumbling motion leads to the RBC presenting a greater cross-section to flow as it flows over the two prongs of the U-groove pillar. However, this is not always true and appears to happen periodically, leading to bumping in some instances. The linear trend for M^z seen in figure 9.6a appears to indicate that the probability for bumping induced by the 3D RBC tumbling decays linearly with increase in the row shift of the array. It would take a considerable amount of further research on the orientation dynamics of the RBC in flow-fields generated by the U-groove pillar shape to prove or disprove the above idea. The scope for such research is beyond the ambit of the time and funding for my PhD and therefore would not be investigated further in this chapter.

9.7 MIGRATION VELOCITY

In this section I compute the average migration velocity for the soft RBC moving in displacement mode through the C-ridge pillar array. The cell migration velocity ($\boldsymbol{v}_m$) is calculated as the difference between the velocity of the cell centroid ($\boldsymbol{v}_c$) and the steady-state particle-free velocity in the DLD C-ridge geometry ($\mathbf{u}^\infty$) at the same location, at every time step, i. e. $\boldsymbol{v}_m(\mathbf{x}, t) = \boldsymbol{v}_c(\mathbf{x}, t) - \mathbf{u}^\infty(\mathbf{x})$. These calculations are done for four simulations at two different Ca values, as seen in figure 9.7. The reason for choosing these four simulation datasets is that the motion of the RBC here is hydrodynamically fully resolved with no "contact" between the cell and the pillar walls. Particle-wall "contact" is modelled as a force penalty imposed on the RBC membrane nodes, preventing them from crossing into the lattice wall nodes.

This force is unphysical but numerically necessary, and results in misleading migration velocity calculations.

The average of y-component of the migration velocity $\langle v_{m,y} \rangle$ is computed by taking a path-integrated average of $\boldsymbol{v_m}$ over the trajectory of the cell in the C-ridge DLD device. The migration velocity is normalised by the scale of average x-directional fluid velocity u_x^∞ from particle free simulation at $\varepsilon' = 1/50$. Another important observable is cell distance from the pillar walls in the displacement mode (see figure 9.5b). An indicative stand-off distance $\langle y_b \rangle$ is computed by taking path-integrated average of the lateral y position of the cell centroid through the C-ridge DLD. This distance is measured from the bottom of the ridge feature (the part of the C-ridge pillar that forms a flat ledge). This average distance $\langle y_b \rangle$ turns out to be similar for transitional RSF $< \varepsilon'_c$ at $Ca' = 1$ and $Ca' = 10$ in the C-ridge pillar.

The figure 9.7 plots the y-component of the average migration velocity $\langle v_{m,y} \rangle$ against the average stand-off distance $\langle y_b \rangle$. Note that the transition to zigzag mode is observed to occur after the distance $\langle y_b \rangle$ drops below ≈ 4. The average migration velocities decrease with increase in $\langle y_b \rangle$, and this can be attributed to the well known hydrodynamic wall repulsion effect for soft particles (Geislinger and Franke, 2014). What is also not surprising is that the average migration velocity seen for the highest softness ($Ca' = 10$) is an order of magnitude higher than that for the cell with one order lower softness (at $Ca' = 1$). Though not conclusive, the velocities seen in figure 9.7 indicate that hydrodynamic cross streamline migration of soft particles is the most likely physical ingredient responsible for the mode-bifurcation reversal seen with the C-ridge and Square pillar DLD arrays. As such, this calls for a deeper and systematic analysis of this physical effect in the DLD. This finding shows that the design based on rigid bead motion would fail when soft particles are used in the DLD.

9.8 SUMMARY AND CONCLUSIONS

As seen in chapter 1, the microfluidic sorting and manipulation of RBCs based on their membrane properties holds great potential for lab-on-chip disease diagnostics. The work of Zeming, Ranjan and Zhang (2013), and later that of Henry et al. (2016) demonstrated that the DLD could be exploited for the sorting of RBCs, based on their dynamics *via* the use of clever post shapes, or a change in the suspending medium viscosity. Their findings mainly centred around the idea that RBC dynamics lead to 'enhanced' bumping or lateral displacement. This meant displacement mode at higher array inclinations (or larger values of row shifts), than the array inclination that would be naively expected based on standard theory (see section 3.2.1). Exploiting such effects would open the door for RBC manipulations based on morphological criteria other than the RBC size.

In this chapter I explore the causes that enable such enhanced bumping at higher-than-expected row shifts fractions in the DLD arrays. Simulations of a single RBC (dilute limit) flowing through a single-pillar periodic simula-

tion domain are carried out to record the trajectories of cells crossing arrays at various inclinations. The pillars comprising these obstacle arrays are non-cylindrical, and have one out of three special shapes, namely Square, C-ridge and U-groove. These special pillars are designed to trigger differing RBC dynamic motions when crossing array gaps. For all three pillar shape DLDs, the single cell paths are simulated at increasing RSF values ($1/50 \leqslant \varepsilon' \leqslant 8/50$), at 5 different deformabilities quantified by the RBC membrane capillary number Ca.

Since the trajectories of the cells show complex modal behaviour and cannot be easily classed as either displacement or zigzag, a new trajectory mode parameter $M^z \geqslant 0$ is defined to quantify the modal behaviours. Mode number M^z indicates the relative cellular trajectory deviations in the mixed and zigzag modes, away from the path of perfect displacement along the array inclination. With this new parameter, I build a continuously varying phase-bifurcation map for the RBC trajectory modes, for all three pillar shape simulations. Furthermore, I take a detailed look at the RBC motions induced by the individual pillars at array RSF values just below the critical RSF ε'_c. The analysis of these kinematics presents critical insight into the observed trajectory modes, the resulting phase-bifurcation behaviour and the physical mechanisms involved.

My main findings are that there are additional physical effects (than apparent particle size) that dominate RBC dynamics in the DLD. These effects differ depending on the deformability of the cell. The first of these findings is that if perturbed, the rigid RBC prefers to move away from the depth mid-plane of the device and shows a highly complex 3D tumbling behaviour. This means that 2D simulations of such systems (Kabacaoglu and Biros, 2017; Quek, Le and Chiam, 2011; Ye et al., 2014; Zhang, Henry et al., 2015) do not capture the full particle dynamics and therefore could prove to be misleading. Such 3D dynamics is seen to lead to greater spread of the mixed mode behaviour at higher RSF, which results in overall greater lateral displacement. I therefore postulate that the 3D tumbling dynamics of RBCs in the U-groove pillar shape DLD is the likely cause for the elevated critical RSF obtained in the experimental device by Zeming, Ranjan and Zhang (2013). Proving such a claim would require substantial amount of further research work and is well beyond the scope of my PhD.

The second major finding is the observation of an interesting reversal of the critical RSF zone in the phase-bifurcation maps for the C-ridge and Square pillar arrays, with increasing cellular deformability. Preliminary analysis reveals that soft cell cross-streamline migration is the most likely physical mechanism responsible for this reversal of the mode-bifurcation trend. The interplay between the flow-field, no-slip pillar walls and the periodic deformation of the soft cell leads to sustained particle displacement mode at elevated RSFs in the C-ridge and Square pillar arrays. From the findings it is seen that the Square pillar array would serve very well for a deformability sensitive DLD device. Nevertheless, this migration effect for soft cells needs to be studied in greater detail.

The findings of this chapter bring us closer to understanding the full-3D tumbling dynamics driven enhanced lateral displacement in grooved pillar DLDs. In addition a new physical phenomenon that dominates lateral displacement for soft cells under certain conditions with special pillar shapes is uncovered. The physical mechanisms found by this study can lead to new pillar shapes that exploit tumbling of RBCs when they are rigid, or cross streamline particle migration when the RBCs are soft, for deformability-sensitive RBC manipulation.

10

BREAKDOWN OF DETERMINISTIC LATERAL DISPLACEMENT

In many particle separation applications that use the deterministic lateral displacement (DLD) microfluidic device, high operating particle volume fractions are desirable (e. g. blood tests). From the DLD operating principle seen in section 3.2, we know that the separation depends on isolated interactions between particles and obstacle pillars, i. e. the technique has been designed with dilute suspensions in mind. In this final chapter, we look at high particle volume fractions in the DLD, and its consequences.

Full 3D red blood cell suspension (in aqueous plasma) simulations are used to study the effect of cell volume fraction (also called haematocrit, Ht) on the DLD performance. The performance of the DLD depends on the performance of its two trajectory modes; displacement and zigzag. In this chapter, the performance of both modes at higher volume fractions (Ht) is analysed by defining appropriate statistical measures (called *failure rates*). I observe that the displacement mode breaks down at high particle volume fractions, while the zigzag mode remains robust. This leads to the postulate that it would be difficult to separate a dense large-particle suspension from a few smaller particles (e. g. RBCs from platelets), without dilution in the DLD. The opposite case, of separating a few larger particles from a dense background of smaller particles (such as white blood cells from RBCs) would be relatively easy. The results presented in this chapter have previously appeared in Vernekar and Krüger (2015).

The chapter starts by stating the problem in section 10.1. The simulation setup is given in section 10.2. In section 10.3, we follow the cell trajectories in all the simulated devices. We then take a look at the outlet cell distributions, in fictitious device outlets placed downstream, in section 10.4. In section 10.5, appropriate "failure" probabilities are computed to understand and quantify trajectory mode performance with increasing Ht. Section 10.6 ends the chapter with a short summary and conclusions.

10.1 INTRODUCTION AND PROBLEM STATEMENT

As seen in chapter 3, size-based particle separation in the DLD relies on the outcomes of individual particle-pillar interactions. As a result, the DLD works very well when dilute particle suspensions are used, as practised in nearly all experiments. Dilution is achieved in most DLD devices through pretreatment of the sample (e. g. blood dilution) or by using buffer inlet streams that reduce the effective volume fraction of the suspension as it flows through the DLD.

Higher particle/cell volume fractions are rarely employed in experimental benchmarking of the DLD for separation applications. And when high volume fractions have been tested in the DLD, a reduction in the efficiency of the device was observed (Inglis, Lord and Nordon, 2011; Lubbersen, Schutyser and Boom, 2012). Attempts at using blood at higher haematocrit in the DLD has led to issues with cell stiction to device walls and device clogging, resulting in separation failure (Davis et al., 2006; Zheng et al., 2005). However, the use of higher volume fractions is highly desirable. This not only increases the device throughput, but also avoids additional steps for dilution, promising simpler operational procedures.

In this study we investigate the effect of RBC volume fraction (Ht) on DLD performance. Under physiological conditions, the blood haematocrit is usually measured at $Ht \approx 40\text{-}45\%$. Use of undiluted blood would simplify blood processing and bring the DLD technique one step closer to their use in point-of-care (POC) microfluidic chips. Eliminating dilution is also a major advantage when the bio-particles targeted for separation and extraction are rare (e. g. circulating tumour cells), and any dilution decreases the probability of isolating such particles.

We study the volume fraction effect with 3D numerical simulations of RBC suspension flow through the DLD and various $Ht < 46\%$. The suspending medium is aqueous plasma. Our investigations are two-fold; firstly to simply observe and map the effect of increased Ht on cell trajectories, and secondly to understand the underlying mechanisms involved. In order to narrow the focus on the effect of the blood haematocrit Ht, the DLD device setup previously (numerically) investigated by Krüger, Holmes and Coveney (2014) is chosen. The authors have thoroughly mapped this setup for deformable RBCs, where greater deformability decreases the effective RBC size. Choosing a well mapped pre-existing setup allows us to probe for the effect of Ht in DLD devices, where the cell trajectories in the dilute limit are known *a priori*.

10.2 SIMULATIONS

In this section we shall look at the physical and simulation parameters involved in the present study. As mentioned previously, the simulation parameter set is "borrowed" from the study by Krüger, Holmes and Coveney (2014), except for the number of cells simulated.

10.2.1 *Geometry and RBCs*

DLD GEOMETRY: Firstly, let us take a look at the geometric construction for the simulated DLD devices. Recall figures 3.4 and 3.7a for the following geometric description. We choose the parallelogram layout for the DLD in this study, and take the flow-wise, lateral and depth-wise directions as x, y and z, respectively. A shallow device is chosen for this study, with a height of $H = 4.8\ \mu m$ in the z direction. This is done so that the RBC orientation in the device is locked solely to one degree of freedom, about its axis of symmetry.

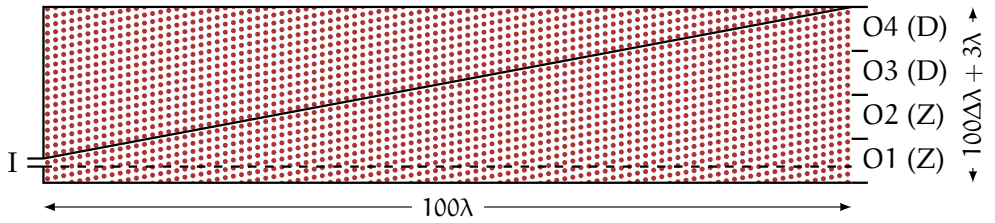

Figure 10.1: Illustration indicating the placement and definition of the four imaginary outlets. The four equisized outlets, O1-O4, are placed at flow-wise position $100\lambda < x \leqslant 101\lambda$. The outlets O1 and O2 are designated to collect particles in the zigzag mode, while the outlets O3 and O4 are designated for collecting displacement mode particles. The width of all outlets put together is $100\Delta + 3\lambda$, with an additional 2λ width considered below the horizontal (dashed line), since a few cells tend to be negatively displaced. For the representative geometry, we have taken $\varepsilon = 0.1875$. The solid diagonal line traces the array inclination that would be followed by a single cell on ideal displacement entering at the inlet (I).

This means that the RBCs always lie with their major axes in the x-y plane, and cannot rotate about their centre. The RBC are confined and this prevents orientation dependent trajectory selection for the RBCs.

In accordance with most experimental work involving blood cells in the DLD, we employ the symmetrical cylindrical shape for the array pillars. The pillar diameter is chosen as $D = 20$ μm, and the obstacle array pitch set to $\lambda_x = \lambda_y = \lambda = 32$ μm, in both the x and y directions. This gives us an inter-pillar gap of $G = 12$ μm. These device dimensions held constant in all simulations. The critical diameter d_c is varied by changing the row shift fraction for the device (RSF) $\varepsilon = {}^{\Delta\lambda}/_{\lambda}$, where $\Delta\lambda$ is the array row shift in μm. Thus, $\Delta\lambda$ is the sole geometric DLD parameter that decides changes to the device setup in this study.

Furthermore, four imaginary outlet bins are defined, as shown in figure 10.1. The four outlets are equal in size (O1-O4), and are placed at distance of 100λ downstream (in the x direction) of the inlet. In other words, the RBCs are expected to cross at least 100 periodic pillars along the x direction. This gives the total DLD device length, which corresponds to ≈1.3mm. This number is chosen as an amenable compromise between computational costs and obtaining sufficiently large number of pillar-particle interactions through each device. The outlet bins allow us to see where the RBCs end up.

The four outlets are designated based on the particles mode they are expected to collect, in the dilute limit. Hence, the lower outlets O1 and O2 are designated as zigzag outlets and are expected to collect particles that travel horizontally in the zigzag mode. The upper outlets O3 and O4 are designated as displacement outlets, since particles that are expected to be in the displacement mode would end up into these outlets. In other words, we simply divide the outlet region, designating the lower half for zigzag and the upper half for displacement particles. Note that, as shown in figure 10.1, a small additional region of size 3λ (in the negative y direction) is added to the outlet region. Here, 1λ accounts for the width of the inlet and 2λ for potential negative

lateral migration of particles. This additional length is equally distributed amongst all outlets, i. e. $100\Delta\lambda + 3\lambda$ is the total width of all four outlets put together.

RED BLOOD CELLS: As explained in chapter 4, the RBCs are modelled as elastic biconcave membranes, whose shape is defined by the equation 4.4. The membrane deformation is determined by its bending κ^b, strain κ^s and area dilation κ^α moduli. In this study, we set the in-plane RBC radius (along the major axis) as $R_0 = 3.9$ μm, and the RBC maximum thickness as 2.4 μm, for all the simulations. From experimentally measured elastic properties for a healthy RBC, we have $\kappa^b = 1.8 \times 10^{-19}$ Nm and $\kappa^s = 5 \times 10^{-6}$ N/m (Evans, 1983; Skalak, Tozeren et al., 1973). Therefore, the non-dimensional ratio of bending to strain for a healthy RBC is held equal to $\kappa^b/(\kappa^s R_0^2) \approx 2.4 \times 10^{-3}$ when varying cell deformability, in all simulations. The non-dimensional area dilation modulus is set equal to $\kappa^\alpha = 0.5$ for numerical stability reasons, which allows some non-physical local area dilations of the RBC membrane, while the non-dimensional moduli for total area and volume conservation are both set equal to unity, $\kappa_A = \kappa_V = 1$. The ratio of inner and outer fluid viscosities is set to 5, which is close to the physiological value. The above values are kept invariant for all the simulations in this study.

10.2.2 *Numerical details*

In order to reduce the computational costs, a periodic domain containing a single array cylindrical obstacle is used for all the simulations. The domain boundaries have shifted periodic mapping in the x direction by $\pm\Delta\lambda$, to incorporate the effect of the array row shift. There is no shift in the y directional periodicity. The number of fluid lattice nodes in the x, y and z directions are $80 \times 80 \times 12$. This sets a lattice length scale of $\Delta x = 0.4$ μm, and therefore gives an undeformed RBC diameter of $19.6\Delta x$. In the z direction, top and bottom walls are simulated with the half-way bounce-back scheme. The flow is driven by an imposed body force $|\mathbf{f}| = f_x$ (per unit volume) along the x-direction. A feedback lateral body force component f_y is computed in order to set the average y directional momentum flux to zero. This suppresses anisotropic net flow in the y direction induced by the array geometry, and mimics the effect of side walls at a large ($\pm y$) distance from the pillar. The Reynolds number in all simulations is $Re < 0.7$, ensuring that inertial effects are negligible.

All RBC membranes are meshed with 2000 triangular surface elements. Here, we quantify RBC deformation in terms of the non-dimensional *capillary number* defined as,

capillary number *The ratio of the characteristic deforming viscous stress to the characteristic restoring elastic stress, felt over the RBC membrane*

$$Ca = \frac{p' l_c R_0}{\kappa^s} = \frac{f_x^* l_c^* R_0^*}{\kappa^{*,s}}, \tag{10.1}$$

where p' is the average pressure gradient in the x direction and l_c is the characteristic length scale for viscous stress in the DLD geometry. In the sim-

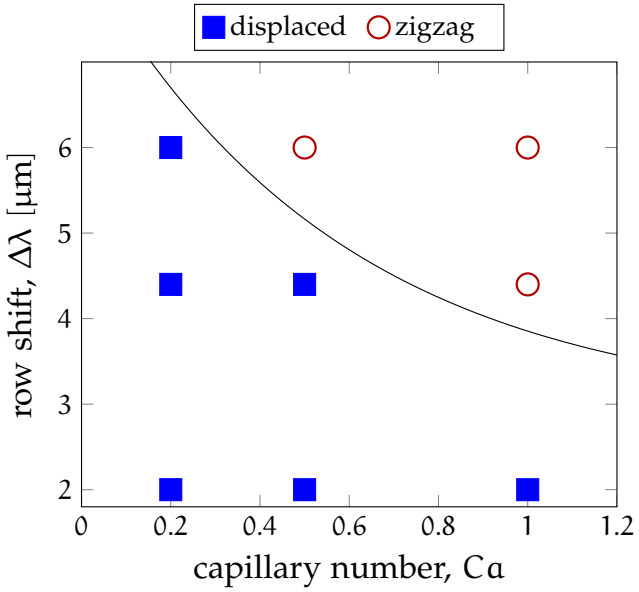

Figure 10.2: The zigzag-displacement bifurcation phase diagram for the parameters space considered. Nine data points $(Ca, \Delta\lambda)$ are simulated, and these are shown with markers. At these nine points, the expected cell trajectory modes in the dilute limit are identified from (Krüger, Holmes and Coveney, 2014). Empty circles (red) indicate zigzag mode and solid squares (blue) indicate the displacement mode, for single cell simulations ($Ht < 2.8\%$). The solid line is the critical separation curve for the zigzag-displacement bifurcation, as resolved by Krüger, Holmes and Coveney with a greater number of simulations.

ulations, we use the geometric mean of the array gap as the characteristic length, $l_c = \sqrt{G \times H}$. The corresponding calculation of Ca in lattice units is also shown in equation 10.1. The superscript * is used to indicate terms measured in lattice units.

10.2.3 *Study parameters*

The trajectory mode for a given capillary number Ca, in a device with a set row-shift $\Delta\lambda$, is already known for the geometry from the previous study by Krüger, Holmes and Coveney (2014). These trajectories were determined in the dilute limit ($Ht \approx 2.7\%$), and can be considered as the expected or predicted modes when a single RBC traverses such a device. The phase diagram for zigzag-displacement trajectory mode bifurcation, for various $(Ca, \Delta\lambda)$, is given in figure 7 in (Krüger, Holmes and Coveney, 2014). From here, we have selected three capillary numbers $Ca = \{0.2, 0.5, 1.0\}$ and three RSF values $\varepsilon = \{ {}^{5}/_{80}, {}^{11}/_{80}, {}^{15}/_{80}\}$, in order to investigate the effect of Ht on DLD performance. The trajectory mode phase diagram for these three sets of values (extracted from (Krüger, Holmes and Coveney, 2014)) is shown in figure 10.2. We have three points in the zigzag mode (red, circles), while the rest are in the displacement mode (blue, squares). Also, the critical (hydrodynamic)

radii, measured as the width of the dividing streamline β (see section 3.2.1) for selected RSF values, are listed in the table 10.1.

Since a periodic domain is used, the number of cells simulated in each domain decides the total RBC haematocrit in the device. That is, in a periodic setup the device is always full of RBCs everywhere, even when single cell simulations are carried out. Therefore, RBC haematocrit Ht is the appropriate parameter to gauge device saturation and test performance. We shall test all DLD devices at the haematocrit values $Ht = \{8.0, 16.1, 32.2, 40.2, 45.6\}\%$, which corresponds to simulating $\{3, 6, 12, 15, 17\}$ cells respectively in the periodic domain. Note that the approximate physiological value of haematocrit in humans is $Ht \leqslant 45\%$.

The above Ht values are tested in devices with row-shifts $\Delta\lambda = \varepsilon\lambda = \{2.0, 4.4, 6.0\}$ μm, with deformable RBCs characterised the Ca values given in figure 10.2. Therefore, $5 \times 3 \times 3 = 45$ simulations have been carried out for this study. Furthermore, initial RBC positions are chosen arbitrarily, only taking care to avoid obstacles and cell overlap. For simulations with identical number of cells simulated, the initial cell positions in the domain are also kept identical when varying Ca and ε. In a given simulation, all simulated RBCs are mono-disperse in terms of size and membrane elastic behaviour.

10.3 CELL TRAJECTORIES

For all cases described above, the periodic domain simulations are run till all cells go past the pillar over 100 times (i. e. cross a distance of 100λ in the x direction). Some sample cell trajectories through a few devices are plotted in figures 10.3 and 10.4, for Ht = 8% (3 cells) and 45.6% (17 cells), respectively. Both the x and y axes in the plots are normalised by the array pitch λ. Therefore, the x axis in each plot gives the number of pillars crossed by the cells in the flow-wise direction. The solid line in each plot indicates the idealised displacement trajectory and the dashed line (in figure 10.4) indicates the ideal zigzag trajectory for the device, in both figures. An overview of both the figures quickly tells us that an increase in cell haematocrit has significant consequences for the cell migration angles as well as cell scatter.

Table 10.1: The stagnation streamline widths for the three sets of simulated row shifts obtained from particle-free 3D simulations. The stagnation streamline width is measured at the central plane of the DLD.

Row shift, $\Delta\lambda$ [μm]	Row shift fraction, ε	Stagnation streamline width, β [μm]
2.0	5/80	1.2
4.4	11/80	2.1
6.0	15/80	2.7

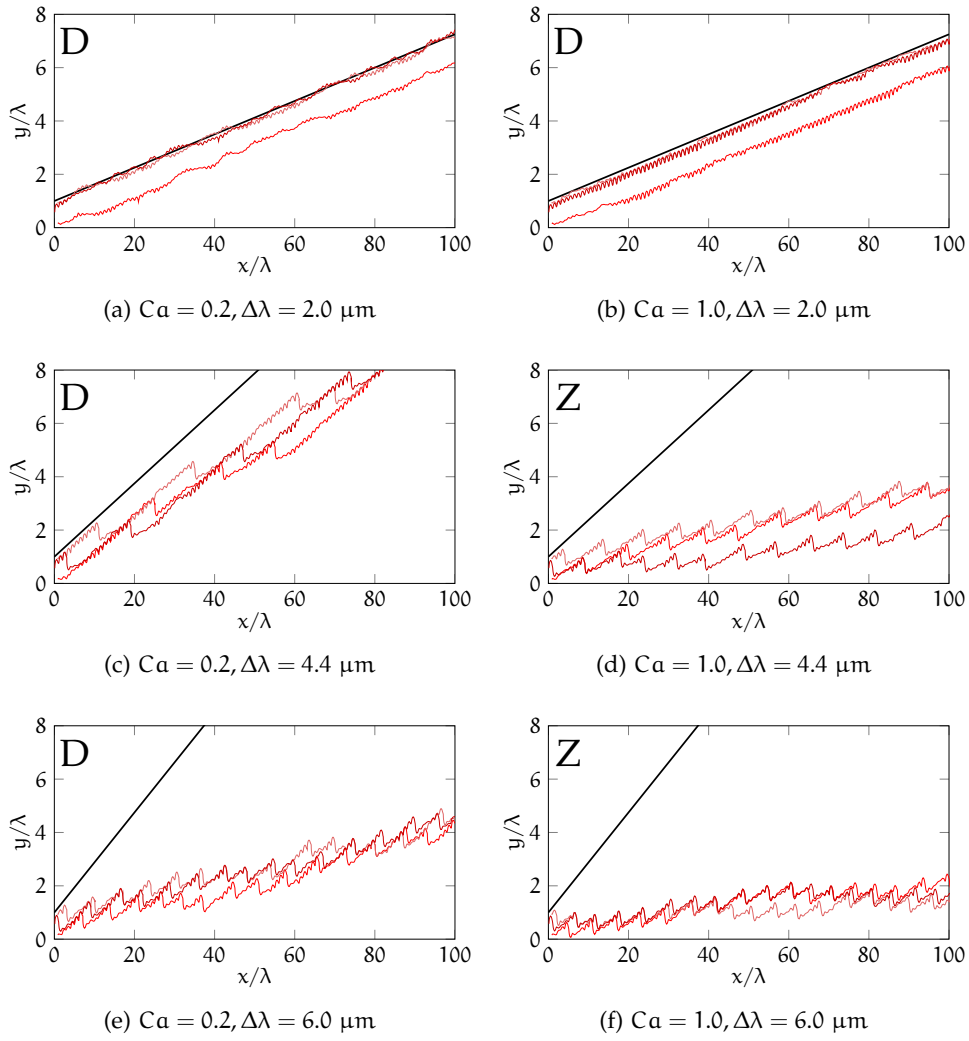

(a) $Ca = 0.2, \Delta\lambda = 2.0\ \mu m$ (b) $Ca = 1.0, \Delta\lambda = 2.0\ \mu m$

(c) $Ca = 0.2, \Delta\lambda = 4.4\ \mu m$ (d) $Ca = 1.0, \Delta\lambda = 4.4\ \mu m$

(e) $Ca = 0.2, \Delta\lambda = 6.0\ \mu m$ (f) $Ca = 1.0, \Delta\lambda = 6.0\ \mu m$

Figure 10.3: Cell trajectories for simulations at $Ht = 8.0\%$. Individual cell trajectories (with identical membrane properties) are marked in different shades of red. The diagonal solid line (black) indicates the inclination of the pillar array, marking a single array path. The expected cell trajectory modes are indicated as "D" for displacement and "Z" for zigzag, in the top-left corner of the panels. These are obtained from the phase-map in figure 10.2. The x and y axes are normalised by the array pitch λ. Note that the two axes are not scaled equally, for clarity. Panels along a given row have the same row shift $\Delta\lambda$, while those in the same column have the same Ca, both in increasing order.

The figures 10.3 and 10.4 are made up of 6 panels each. In each figure, these panels are arranged such that we have simulated devices with increasing row shift of $\Delta\lambda = 2.0$, 4.4 and 6.0 in the row-wise order. The columns have increasing capillary numbers, with Ca taking the values 0.2 and 1.0, in the left and right columns, respectively. All sub-plots are marked with the letters "Z" or "D" to indicate whether the RBCs would undergo zigzag or displacement

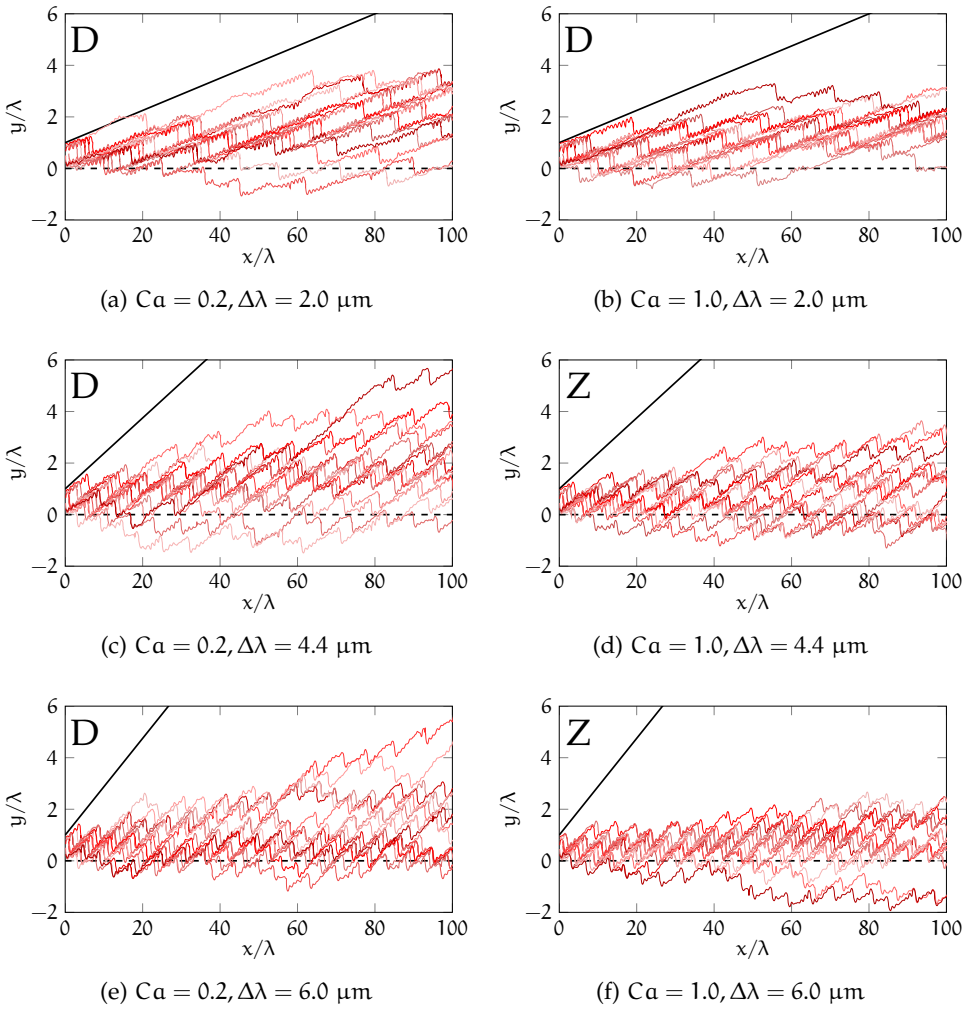

(a) $Ca = 0.2, \Delta\lambda = 2.0\ \mu m$ (b) $Ca = 1.0, \Delta\lambda = 2.0\ \mu m$

(c) $Ca = 0.2, \Delta\lambda = 4.4\ \mu m$ (d) $Ca = 1.0, \Delta\lambda = 4.4\ \mu m$

(e) $Ca = 0.2, \Delta\lambda = 6.0\ \mu m$ (f) $Ca = 1.0, \Delta\lambda = 6.0\ \mu m$

Figure 10.4: Cell trajectories for simulations at $Ht = 45.6\%$. Individual cell trajectories (with identical membrane properties) are marked in different shades of red. The dashed horizontal line indicates direction of average flow, and is drawn from the inlet. The simulations sets $(Ca, \Delta\lambda)$ shown here are equivalent to those in figure 10.3, but with a higher Ht. See figure 10.3 for an equivalent description of the panels. Note that the two axes are not scaled equally, for clarity.

modes, when a single cell is simulated. In these plots a sharp periodic y directional dip indicates a pass below a pillar by the cell, in the zigzag mode.

We first discuss cell trajectories at $Ht = 8\%$ (3 cells), and refer to the figure 10.3 for the following discussion. When, $\Delta\lambda = 2.0$ (in figures 10.3a and 10.3b) the cell trajectories are seen to follow the ideal displacement migration angles. Here, one out of the three cells follows a different ideal displacement path, due to its different starting location. Such ideal displacement paths can be termed 'array paths'. Cell trajectories on these array paths are parallel to one another, at an inclination α set by the array. An array path defines the displacement mode, and can be contrasted with fluid 'flow lanes'

(see section 3.2) that define the ideal zigzag trajectory. We make use of this terminology (of 'array paths' and 'flow lanes') in the discussions that follows.

Returning to the figure 10.3, we see that for $Ca = 0.2$ and all row shifts $\Delta\lambda$ in left column of panels, the displacement mode is expected. Already at $Ht = 8\%$ (3 cells), we can see that the displacement mode increasingly suffers when the row shift is increased, and we move towards the critical bifurcation curve seen in figure 10.2. The zigzag mode on the other hand (in figures 10.3d and 10.3f in the second column) remains relatively unharmed. The cells appear to periodically swap array paths to stay within their flow lanes, and this period is nearly equal for all three cells. Here, the trajectories for the three cells appear to be on a slightly positive incline, instead of purely horizontal motion. Such behaviour in the zigzag mode has previously been explained, and results from the non-integer array periodicities $N = 1/\varepsilon$ that are used here (Long et al., 2008).

Now referring to the figure 10.4 for the subsequent discussion on cell trajectories at $Ht = 45.6\%$. We see that none of the trajectories are in pure displacement mode. Even for the simulation point furthest away from the critical separation curve ($Ca = 0.2, \Delta\lambda = 2.0$) (in figure 10.2), the cell paths in figure 10.4a fail to be sufficiently displaced. We can also see that the cell trajectories suffer a large scatter at the highest haematocrit of $Ht = 45.6\%$, relative to that seen previously in figure 10.3 at $Ht = 8\%$. Here, at $Ht = 45.6\%$, the cell scatter is seen to be as large as $\approx 7\lambda$ in the lateral direction, while that for previous case at $Ht = 8.0\%$ is $\approx 1\lambda$. For cases expected to be in the displacement mode (figures 10.4a, 10.4b, 10.4c and 10.4e) the cell trajectories appear no different than for those in the zigzag mode (in figures 10.4d and 10.4f). However, the array path swapping events are not regular for the cells here, and the cell scatter appears qualitatively larger for the cases expected to be in the displacement mode compared to those in the zigzag devices. This suggests that there is an underlying stochastic mechanism in addition to simple zigzag mode physics, governing these cell trajectories.

Based on these trajectories we can make the following observations. When the zigzag mode is expected, the mean outlet cell position does not vary more than $\approx 3\lambda$ from the initial cell position, even at the highest $Ht = 45.6\%$. On an average, these cells tend to follow a near horizontal trajectory, and can therefore be collected at outlets placed at similar lateral (y) positions as the device inlet. Therefore, device outlets placed at higher lateral (y) positions are left free for collecting displaced cells. This suggests that, even at high haematocrit, it would still be possible to separate a few larger particles from a dense suspension of RBCs.

However, in simulations where the cells are expected in the displacement mode, the mean cell lateral positions fall significantly short and end up far from expected, as the Ht is increased. Here, the mean cell lateral outlet position appears to depend on the row shift $\Delta\lambda$ and cell deformability Ca. In fact, at $Ht = 45.6\%$, the mean cell trajectories are close to the horizontal, and these cells would end up in the same outlets as the zigzagging particles. This indicates a breakdown of the displacement mode since these cells were ex-

pected to laterally displace, like those in the dilute limit. Therefore, it can be postulated that it would be difficult to separate smaller particles from a dense background RBC suspension in the DLD.

10.4 CELL OUTLET DISTRIBUTIONS

In the previous section, we saw how an increase in Ht results in cells deviating from their expected mean trajectories (from single cell simulations) in a DLD device at a given flow rate, which decides the simulated data point $(Ca, \Delta\lambda)$. This Ht increase results in many of the cells designated for the displacement outlets, ending up in the zigzag outlets. We can term a DLD trajectory mode as "robust" based on the whether a majority of the cells would end up in their designated outlets, when the particle volume fraction is increased. A robust mode would still make it possible to separate out particles from the cellular suspension.

We can call the zigzag mode robust, if a majority of the cells end up in the outlets O1 and O2 in simulations where zigzag mode is expected. Similarly, the displacement mode can be termed robust in a given device if a majority of the cells reach outlets O3 and O4, in simulations where RBCs are expected to laterally bump. This definition would still allow for separation of either larger or smaller cells in the spare outlets, in the respective cases. Note that the device row shift and the RBC deformability characterised by $(Ca, \Delta\lambda)$ already set the designated outlets for the cells, in each simulation (from the bifurcation map in figure 10.2).

In this section, we plot the number of cells collected in each of the four imaginary outlets defined at a distance of 100λ from the inlet (figure 10.1). Outlet cell distributions from selected simulations are plotted in figure 10.5. The outlet cell distributions are presented for $Ht = 16.1\%$ and 45.6%, in the left and right columns respectively while each row has the same set of $(Ca, \Delta\lambda)$ values. The rows are split into two blocks based on the expected trajectory mode. In the sub-plots, the row shifts take the values $\Delta\lambda = 0.2, 4.4, 6.0\ \mu m$, and the capillary number $Ca = 0.2$ and 1.0. The rows are arranged such that the higher row numbers have $(Ca, \Delta\lambda)$ data points closer to the critical separation curve, plotted in figure 10.2. Here, both the size of the outlet bins as well as the number of cells in each bin have been normalised by their respective maximum values to enable easy comparison. Bars are coloured green if the cells are in their designated outlets and red if they end up in the wrong outlet bins. From these, we can discern the robustness of the two expected trajectory modes, at increased haematocrit.

The expected zigzag mode cell distributions are plotted in figures 10.5a, 10.5b, 10.5c and 10.5d. At lower $Ht = 16.1\%$ (left column), we see that all the cells end up in the designated zigzag outlets 1 and 2 (figures 10.5a and 10.5c). When using the highest tested volume fraction at $Ht = 45.6\%$, all the cells are still collected in their designated outlets, as before. This demonstrates that when the dense RBC suspension is in the zigzag mode, it would still be

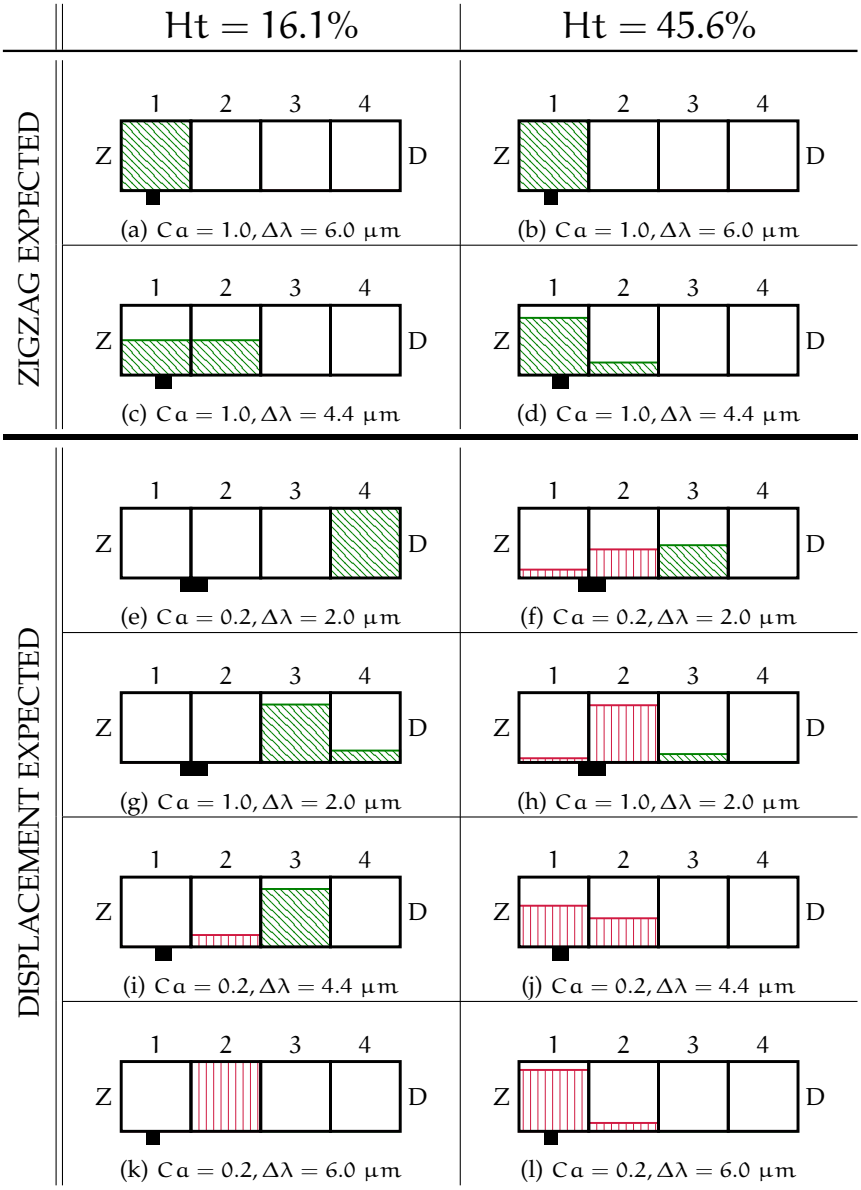

Figure 10.5: Histograms of RBC outlet distributions for selected simulations at Ht = 16.1% and 45.6% arranged as panels in two columns, respectively. The first two rows are for simulations where the zigzag particle mode is expected, while the displacement mode is expected for the simulation histograms in the last four rows. The panels have the same simulation parameter set (Ca, Δλ) in each row, with only the haematocrit increasing from the left column to the right column. The panel rows are arranged in increasing order such that the distance of the simulation data point (Ca, Δλ) from the critical separation curve plotted in figure 10.2, decreases monotonically in both the expected modes. The panel histograms have three different row shift values Δλ = {2.0, 4.4 and 6.0} μm, and two capillary numbers Ca = 0.2 and 1.0. All four outlet bin widths, as well as the cell histograms are normalised for ease of comparison. The position of the inlet relative to the outlets is indicated by a black rectangular box at the bottom of all panels. The outlet bin numbers (1-4) are marked atop the respective bins, with outlets 1-2 designated to collect zigzag RBCs, and outlets 3-4 designated to collect displaced RBCs. Slanted hatching (green) indicates successful and vertical hatching (red) indicates faulty collection of cells in these designated outlets.

possible to separate and collect larger particle (e. g. white blood cells) in the displacement mode in the empty outlets 3 and 4.

The cell outlet distributions for the cases where displacement is expected are shown in figures 10.5e, 10.5g, 10.5i and 10.5k, for $Ht = 16.1\%$. Here, nearly all RBCs are collected in the designated displacement outlets 3 and 4, for all but one of the cases shown. The exception arises for $(Ca = 0.2, \Delta\lambda = 6.0\ \mu m)$, which is the case closest to the critical separation curve (see figure 10.2). Here, all RBCs end up in the second zigzag outlet O2. For the higher haematocrit $Ht = 45.6\%$, the outlet distributions for expected displacement mode cases are shown in figures 10.5f, 10.5h, 10.5j and 10.5l. Here, the results are thoroughly unfavourable to the displacement mode, with a majority of the cells ending-up in the wrong (zigzag) outlets O1 and O2. For the case $(Ca = 0.2, \Delta\lambda = 2.0)$, which is the furthest away from the critical separation curve, $\approx 50\%$ of the RBCs are collected in the designated displacement outlet 3, For all other cases nearly all RBCs end up in the outlets designated for zigzag particles.

We can observe that the displacement mode breaks down at the high volume fraction of $Ht = 45.6\%$. Looking at the cell distribution trends in the figures 10.5f, 10.5h, 10.5j and 10.5l, we can note that the displacement mode recovers when the simulation setup is further away from the critical separation curve. In general, the displacement mode does not cope well at higher volume fractions, and the expected outcomes get worse as we move closer to the critical bifurcation curve between displacement and zigzag modes. The zigzag mode however remains robust even at higher volume fractions, where the cells always end up in their designated outlets. We can therefore postulate that the DLD lends itself very well for the separation of larger particles from a dense background of smaller cells (e. g. RBCs). But, the opposite would prove difficult; i. e. it is difficult to separate smaller particles (e. g. platelets) from a dense background of larger cells (e. g. RBCs), in the DLD.

10.5 FAILURE PROBABILITIES

failure probabilities
Defined on the assumption that all success events amount to the cell following the trajectory traced in the single cell simulations, while failure events cause lateral deviations

In order to gain an insight into and quantify the robustness of one mode over the breakdown of the other, we identify failure events and define suitable *failure probabilities*. A *failure event* is defined as an event where the cell takes a "wrong turn", compared to its path expected in the dilute limit with the same initial conditions, geometry and deformability. For a cell flowing through the DLD, only two occurrences are possible in terms of its lateral motion. It flows over and above a pillar, or passes through the axial array gap between pillars and passes under the next pillar. These two outcomes are termed as zigzag and displacement events and can be counted for every particle-pillar interaction over the distance λ.

To elucidate further, a zigzag event is said to occur when a cell changes its array path for another path parallel to it. Zigzag events are marked by the sharp dips in the cell trajectory plots seen in figures 10.3 and 10.4. A displacement event is defined as the occurrence where the cell simply stays in its

array path (i. e. essentially everything other than the zigzag event). Now, it is quite easy to define a failure event as one where a displacement event occurs when a zigzag was expected and *vice versa*. Based on visual observation of the cell motion in the simulations, we can state that these failure events result from increased particle-particle interactions at higher Ht.

For example, in the displacement mode a failure event occurs when the cells fail to bump, when passing through the array gap, and therefore fail to travel along the same array path. Each failure event is associated with a lateral displacement penalty. When a cell fails to bump, it falls to the array path that is parallel and laterally ($y = -\lambda$) below its original path. In the simulations, we never observe a cell, expected to be in the displacement mode, get pushed on to the array path that lies laterally ($y = +\lambda$) above its current path. Therefore, we can always associate a lateral displacement penalty of $-\lambda$ with a failure event in the displacement mode.

The picture is quite different in the zigzag mode. Here, in the dilute limit, the cell is expected to undergo a number of displacement events, followed by a zigzag event every N pillars downstream. Therefore, there are two different kinds of failures in the zigzag mode; one where the cell does not undergo a zigzag event when one is expected, and the other when it is pushed onto the array path below once too often. In ether case, the failure penalty is again $\pm\lambda$. Hence, for both displacement as well as zigzag failures, the penalty is the same, up to its sign.

The two kinds of failures in the zigzag mode lead to unexpected lateral displacements of the same magnitude, but in the opposite directions. Thus, the crucial differentiator for the zigzag mode is that the two kinds of failures tend to cancel each other. The occurrence of one failure event can compensate for the occurrence of the other. This is contrary to the nature of displacement mode failure, where cells can only drop down on to the array path below. As mentioned earlier, we never observe a cell getting pushed an entire array path laterally up in the $+\lambda$ direction, in either of the modes.

This means that the failures can only accumulate in the displacement mode, while those in the zigzag mode can cancel one another. This makes the displacement mode susceptible to a breakdown, when the failure probability increases. The increase in failure rate is attributed to an increase in the non-deterministic effects as a result of increased particle-particle collisions, at higher Ht. On the other hand the zigzag mode survives at higher volume fractions, as on an average the cell failure modes cancel each other. This does not mean that individual cell trajectories remain unaffected. Here, individual cells can experience a total $\pm\lambda$ penalty that does not nullify over the device length, leading to the cell scatter as seen in the plots in figures 10.4d and 10.4f.

10.5.1 *Zigzag failure*

I introduce the parameter Δ_y to indicate the lateral displacement error in a cell's trajectory, at the n^{th} pillar. Δ_y is the difference between measured lateral

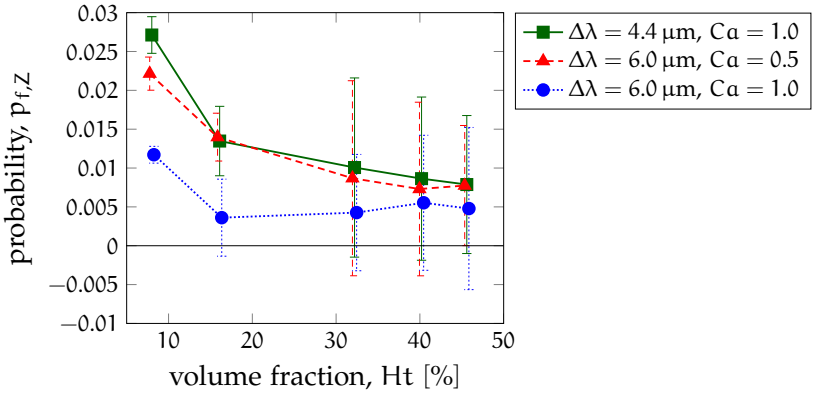

(a) Zigzag failure

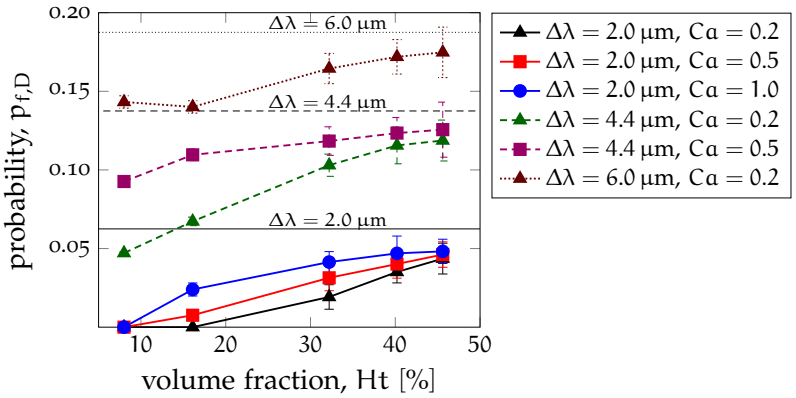

(b) Displacement failure

Figure 10.6: Failure probability plots as a function of increasing Ht. The mean probabilities for (a) zigzag failure $p_{f,Z}$, and (b) displacement failure $p_{f,D}$ are plotted for all the simulated cases, in the respective expected trajectory modes. Error bars indicate the standard deviation obtained from the cell ensemble in each simulation. The data points are moved slightly along the x axis to avoid error bar overlap. Lines connecting the data points are guides for the eyes only. In (b) the horizontal (black) lines indicate the limiting failure probability $p^{\infty}_{f,D} = \varepsilon = \Delta\lambda/\lambda$, for tested values of $\Delta\lambda$ (solid line for $\Delta\lambda = 2.0\ \mu m$, dashed for $\Delta\lambda = 4.4\ \mu m$ and dotted for $\Delta\lambda = 6.0\ \mu m$).

cell position and the expected lateral cell position at the n^{th} pillar. Obviously, a cell moving on its expected trajectory would yield $\Delta_y = 0$. For cells that end up laterally further upwards or downwards than expected, we get $\Delta_y > 0$ and $\Delta_y < 0$, respectively.

Further, I define zigzag failure probabilities $p^{+}_{f,Z}$ and $p^{-}_{f,Z}$ for the two kinds of failures seen in the zigzag mode. For a failure of the zigzag outcome, when a zigzag event turns to a displacement event, we assign the probability $p^{+}_{f,Z}$,

while for the reverse failure event, we assign $p^{-}_{f,Z}$. For a total of n pillar encounter for a cell, we can write

$$\Delta_y = n\lambda(p^{+}_{f,Z} - p^{-}_{f,Z}). \tag{10.2}$$

The equation signifies the summation of lateral displacement errors, over the positive and negative lateral directions, computed from the probabilities for a total of n events (pillars encounters for each cell). Each failure contributes $\pm\lambda$ to the lateral displacement error $\Delta\lambda$ which can be computed from the cell trajectories, as discussed. From equation 10.2 it is clearly seen that only the net failure probability $p_{f,Z} = p^{+}_{f,Z} - p^{-}_{f,Z}$ influences the final lateral cell position. This net probability $p_{f,Z}$ is a measure of the intrinsic failure rate for a device under given flow conditions ($Ca, \Delta\lambda, Ht$).

For a single cell, passing through the DLD device in the ideal zigzag mode, let n^{0}_{up} and n^{0}_{dn} be the number of times a cell moves up or down onto the adjacent array paths (relative to its current array path), respectively. Now, from our simulations setups at higher Ht, we can measure the actual number of times each cell swaps up or down between adjacent array paths as, n_{up} and n_{dn}, respectively. Here, the numbers indicated by subscripts $_{up}$ and $_{dn}$ are respectively the number of displacement and zigzag events in a cell's trajectory through the device. Therefore we can write

$$n = n^{0}_{up} + n^{0}_{dn} = n_{up} + n_{dn}. \tag{10.3}$$

From design considerations and flow lane divisions, we know that in the zigzag mode

$$\frac{n^{0}_{dn}}{n} = \frac{\Delta\lambda}{\lambda} = \frac{1}{N}. \tag{10.4}$$

Equation 10.4 reflects the fact that for an ideal zigzag mode without any net lateral displacement, the ratio of n^{0}_{up} to n^{0}_{dn} is uniquely constrained by the device geometry $\Delta\lambda$ and λ. In practice, I calculate the failure probability $p_{f,Z}$ for each individual cell in all the simulations from the observed values of Δ_y, using equation 10.2. This calculation is carried out when all cells reach device outlets at $x = 100\lambda$, and $n = 100$. Data from all the cells lets us compute an average failure probability and its variance in a particular simulation. $p_{f,Z}$ can also be computed from the number of events as

$$p_{f,Z} = \frac{n^{0}_{dn} - n_{dn}}{n} = \frac{n_{up} - n^{0}_{up}}{n}. \tag{10.5}$$

Figure 10.6a plots the average zigzag failure probability as a function of Ht, for all the simulation cases where the RBCs are expected to be in the zigzag mode. Error bars in the figure give standard deviation for the cell zigzag failure probabilities. Therefore, the error bars indicate the scale of cell

scatter at the outlets. From figure 10.6a we can see that the zigzag failure probabilities are relatively small, with the failure rate remaining $\leqslant 3\%$ for all cases. Here, the failure rate decreases with increase in Ht and then attains a near-constant stable value as Ht is increased further.

This shows that the zigzag mode stabilises at higher volume fractions. The reason for this stability is subtle. At higher volume fractions the RBCs tend to distribute uniformly and occupy most of the volume in the DLD. Their motion is akin to that of fluid elements flowing through the device, performing zigzag motions past the obstacles like those seen with pure fluid flow lanes. Therefore, the zigzag mode is the natural state for the DLD device, and at higher volume fractions the densely packed RBCs tend to follow the natural flow lane divisions.

Furthermore, the standard deviation of the zigzag probability is seen to increase, with an increase in Ht in figure 10.6a. This is because with an increase in the number of cells, the number of outliers that have a large $\pm\Delta_y$ penalty also increases, leading to a larger spread of the cells at the outlet. For a real DLD device, this suggests the need for larger zigzag mode cell collection outlets, whenever a higher volume fraction of particle suspension is used.

10.5.2 *Displacement failure*

In an ideal displacement mode trajectory, all pillar-particle encounters should result in the displacement events for the particle. Here, the cell remains within its array path at all times, and there are no zigzag events. Therefore, we can write $n^0_{up} = n$ and $n^0_{dn} = 0$, indicating that there cannot be more bumping events than the ideal case of n.

Since there are no observed events where the cell gets pushed up onto the array path with a positive penalty $+\lambda$, we can set $p^+_{f,D} = 0$. In the displacement mode, there is only one failure type that causes a negative lateral displacement penalty of $-\lambda$. The corresponding displacement failure probability is therefore, $p_{f,D} = p^-_{f,D}$. The lateral position error Δ_y in the displacement mode can be written as

$$\Delta_y = -n\lambda p_{f,D}. \tag{10.6}$$

The equation signifies the accumulation of negative lateral displacement errors in the $-y$ direction computed from the failure probabilities, for a total of n pillar crossings. Similar to the zigzag failure, the displacement failure can also be written in terms of the number of observed zigzag and displacement events as

$$p_{f,D} = \frac{n^0_{up} - n_{up}}{n} = \frac{n_{dn} - n^0_{dn}}{n} = \frac{n_{dn}}{n}. \tag{10.7}$$

Similar to the calculations in the zigzag mode, we compute the displacement failure probabilities for each of the cells in a given simulation setup.

Figure 10.6b plots the average displacement failure probability values, for all simulated cases expected to be in the displacement mode in the dilute limit, as a function of Ht. As before, the error bars in the figure indicate the standard deviation values for $p_{f,D}$. In addition, a horizontal line indicating the limiting failure probability $p^{\infty}_{f,D}$ value, for each device geometry with a given $\Delta\lambda$, is also shown. The limiting failure probability corresponds to a situation where the cells move along the horizontal and their trajectories cannot be distinguished from those in the zigzag mode. This limiting failure probability is therefore calculated as $p^{\infty}_{f,D} = \Delta\lambda/\lambda$ and indicates the worst-case scenario for the displacement mode. If the displacement failure probability reaches its limiting value, there is complete breakdown of the displacement mode.

From the figure 10.6b, we see that $p_{f,D}$ increases monotonically with an increase in Ht for all explored cases. The failure probability appears to asymptotically approach the limiting value for the device at high Ht. As expected, the highest failure rates are seen for $Ht = 45.6\%$, where the cells fill the entire volume of the device and behave as fluid parcels. In this case, the cells are so densely packed that most of them cannot undergo displacement mode at every pillar crossing. Their trajectories therefore appear similar to those particles in the zigzag mode, and the failure probability is consequently seen to increase and asymptotically approach the limiting value.

At lower volume fractions the simulation parameters $(Ca, \Delta\lambda)$ have a significant influence on $p_{f,D}$. With further increase in the volume fraction, the $p_{f,D}$ values for the different parameters are seen to converge based on $\Delta\lambda$. Also, we see that the failure probabilities increase with $\Delta\lambda$ in general. The physical reason can be understood from the fact that the ratio of the *first flow lane* width to the array gap β/G increases proportionally with $\Delta\lambda$. This means that more particles would potentially lie close to the separation streamline that divides the flow through the lateral pillar gap, between adjacent array paths. Hence, the likelihood of a particle being pushed off by its neighbours into the first flow lane, and thus leading to a zigzag failure event, increases.

first flow lane
The flow lane that lies closest to a pillar, and carries its fluid flux into the array path located below its present, in each array gap

Generally speaking, this variation of $p_{f,D}$ with $(Ca, \Delta\lambda)$ can be correlated with the distance of the phase-space point from the critical separation curve, as plotted in figure 10.2. From figure 10.6, the overall trends for $p_{f,Z}$ and $p_{f,D}$ suggest that the further removed we are from the critical separation curve (in figure 10.2), the lower is the failure probability. In the displacement failure cases, we can normalise the failure probabilities by the respective limiting failure probability $p^{\infty}_{f,D}$, to see this direct correlation emerge. Hence, the DLD device setups close to the critical separation curve are less robust upon an increase in particle volume fraction. We can hypothesise that using larger volume fractions of particles causes decreasing determinacy in the DLD, and there is no longer a sharp bifurcation between displacement and zigzag modes. The bifurcation curve in figure 10.2 thus loses its original meaning and can only be used as reference.

10.6 SUMMARY AND CONCLUDING REMARKS

In this chapter we look at the effect of haematocrit Ht on the performance of particle trajectory modes in the DLD device. The investigation is based solely on 3D numerical simulations of the DLD, with RBCs suspensions in aqueous plasma. The device setup used has previously been mapped by Krüger, Holmes and Coveney (2014) for deformability based separation of RBCs, in the dilute haematocrit limit. In the RBC suspension simulations, we track the trajectories of individual cells until each of them cross 100 pillars in the flow-wise direction. Also, four imaginary equal sized outlet bins are placed 100 pillars downstream of the starting RBC positions. From the cell trajectories and the outlet cell distributions, we see that the displacement mode breaks down while the zigzag mode remains robust at high RBC haematocrit Ht. This breakdown is attributed to increased particle-particle collisions at higher Ht.

Digging deeper into the issue, appropriate failure probabilities are defined for each trajectory mode, by taking reference cell trajectories in the dilute limit as the ideal "successful" path. The mean and standard deviations of these failure probabilities in each of the trajectory modes are significant performance indicators for the DLD device. The mean displacement failure probability increases monotonically with Ht, approaching its limiting value at $\mathrm{Ht} \approx 45.6\%$. At the limiting value, particles in the "failed" displacement mode would resemble those in a normal zigzag mode. In contrast, the zigzag failure probability remains relatively low, even at high Ht. With increasing Ht, the zigzag failure probability stabilises and decreases to a near constant value.

This difference stems from the fact that in the nature of failure in the two modes is different. In the displacement mode, failure is uni-directional and the penalty due to repeating failures adds up. However, in the zigzag mode failures can occur in opposing directions, and these tend to nullify each other over the length of the device. This means that the zigzag mode is robust, and works as expected at high volume fractions. Another important observation seen from the failure probabilities is that the devices set-up to operate close to the critical separation curve (from the phase separation map) are less robust to an increase in Ht, in comparison to those further away.

The results shows that even at small volume fractions of around $\mathrm{Ht} \approx 10\%$, the displacement mode will significantly deteriorate in performance. This result is in good agreement with the experimental observations by Lubbersen, Schutyser and Boom (2012). Critically, this means that the RBCs designated for the displacement outlets would end up in zigzag outlets, rendering separation very difficult in a real world device. This leads us to postulate that it would be easier to isolate a few larger particles (e. g. white blood cells) from a dense background of RBCs, then to separate out a similarly dense RBCs suspension from a few smaller particles (e. g. platelets) without dilution, in the DLD.

The key reason for the breakdown of the displacement mode at larger Ht lies in the DLD operating principle, which relies on deterministic interac-

tions between particles and pillars. Particle-particle collisions at increased Ht introduce non-deterministic effects on to the particle trajectories in the DLD. Therefore it is believed that these results are not specific to the DLD geometry, or to the nature of the particle suspension employed here. All separation devices relying on deterministic principles would suffer from such a dense suspension effect.

The essential point for future applications targeting dense particle suspensions in the DLD is to minimise the failure probability of the displacement mode (e. g. by using innovative pillar shapes). This would further necessitate an understanding of how particle collisions influence the failure probabilities.

Part IV

CONCLUSIONS AND OUTLOOK

Progress is made by trial and failure; the failures are generally a hundred times more numerous than the successes; yet they are usually left unchronicled…

— William Ramsay, Harper's Magazine (1904)

11 SUMMARY AND CONCLUSIONS

In this chapter I undertake a short overview of the research and its associated aspects contained in the thesis. Importantly, the chapter deals with the major conclusions from the three research areas covered in the thesis. The conclusions presented here are condensed from the research work contained in this thesis. In other words, the reader should refer back to the summary and conclusions contained in the individual research chapters in this thesis, in order to gain a comprehensive understanding of the conclusions reached from the work presented. However, an attempt has been made to keep this chapter modular, so that it can be read independently of the main body of this thesis.

This chapter is divided into two sections; the first in section 11.1 outlining a short summary of the research area, and the second in section 11.2 containing the most important conclusions drawn from the research work. Looking forward, some research ideas regarding the deterministic lateral displacement (DLD) technique worth pursuing in the near future are presented in the final chapter 12.

11.1 SUMMARY

The field of microfluidic Lab-on-a-Chip techniques has been in active development over the last couple of decades. Such techniques possess immense potential for point-of-care medical diagnostics and hold promise of bringing about a revolution in the current healthcare practices. Cells and bio-particles, being of the same scale as the geometric feature sizes in such microfluidic devices, have thus been the subject of majority of interest with these techniques. In particular, blood cells have received a large amount of interest due to their importance in multiple physiological processes and in disease diagnostics. This research work deals with understanding the behaviour of soft red blood cells (RBCs) trajectories within a specific microfluidic technique called deterministic lateral displacement (DLD).

The DLD was invented as a size-based separation technique for rigid particles, and has been mostly used for the separation, purification and enrichment of bio-particles such as RBCs. DLD consists of a series of obstacle pillars, arranged in a regular fashion, inside a wide ($\mathcal{O}(10^2)$–$\mathcal{O}(10^3)$ μm) microfluidic channel. The obstacle pillars are generally cylindrical in shape. The obstacles are placed such that the array orientation presents an angle to the average flow direction through the DLD microchannel, which is generally parallel to the side walls of the channel. The flow is usually driven with the help of micro-syringe pumps.

The separation principle of the DLD relies on the angle, α, between the average fluid flow direction and the array orientation. This angle creates unequal flow divisions through each array gap. Particles greater than a certain size that flow through the device are 'bumped by the obstacles, and move along the array incline. Larger particles moving along the array inclination are laterally displaced relative to the flow direction. These particle trajectories are classified as displacement (or bump) mode. Particles smaller than this 'critical' size escape the 'bumping' effect of the array obstacles and flow along the average fluid flow direction. The smaller particles zigzag around the obstacles in the array to stay on course of the average fluid flow direction. Their trajectories are therefore termed as zigzag mode. Eventually, the particles' lateral positions are sufficiently large and they can be collected in separated outlets.

The obstacles array orientation to flow direction can be achieved *via* two types of layouts; parallelogram and rotated-square. The names for these layouts come from the shape of the unit cell formed by four nearest neighbour obstacle centres. Generally, these two layouts are used interchangeably and the difference between them are not known.

Furthermore, from a bio-cellular application perspective, the use DLD technique with the RBCs is challenging because RBCs have a anisotropic biconcave discoid shape. The RBCs are one of the most deformable cells in the human body, adding further complexity to their mechanical behaviour in the DLD. They display characteristic motions such as tumbling and tank-treading, as well as experience hydrodynamic cross streamline migration pushing them away from fixed walls. RBC motion through the DLD is governed by additional physics that is not well understood.

I study the microhydrodynamics and the RBC dynamics through DLD arrays using 3D numerical simulations. In these simulations fluid is assumed to be viscous and incompressible, flowing around rigid fixed obstacles. The RBC is modelled as a deformable capsule with a 2D membrane that encloses a viscous fluid. The numerical recipe used couples hydrodynamic flow solver to RBC membrane deformation computations. I have used the lattice Boltzmann method to resolve the fluid flow and the finite element method to compute RBC membrane deformation energetics. The immersed boundary method explicitly couples the two solutions at each time step.

The simulations in this work are carried out, both over a single obstacle pillar with periodic boundary conditions (2D and 3D), as well as over entire obstacle arrays of the DLD. Experimental data is used to compliment and validate the numerical research wherever possible. However, I would like to assert that my work contained in this thesis deals solely with numerical investigations of the DLD, and the experimental results provided here are solely for the purpose of clarity and corroboration.

I have carried out simulations to investigate three main research questions. The first concerns anisotropic permeability in the DLD arrays, and the subtle differences between the parallelogram and the rotated-square layouts. Such underlying fluid dynamic effects cause unintended particle trajectories in the

DLD, in turn affecting separation. The remaining two questions deal with single and collective RBC dynamics in the DLD. The single cell study investigates the physical effects that lead to 'enhanced' bumping of RBCs in the DLD, which leads to their greater lateral displacement. Here, the effect of cell membrane deformability, and the resulting dynamical behaviour, on RBC lateral displacement in the DLD are probed. The collective RBC study looks at the effect of increased RBC haematocrit (or volume fraction) on the displacement and zigzag modes in the DLD. In this study, cell-cell interactions that lead to detrimental effects are analysed.

11.2 CONCLUSIONS

DLD ANISOTROPIC PERMEABILITY: The first study thoroughly investigates the anisotropic permeability of DLD arrays and is detailed in chapter 8. Physically , anisotropy of permeability signifies a mismatch between average pressure drop and the average fluid velocity direction. Anisotropic permeability can be seen as the intrinsic property of an array to induce a pressure gradient in in a direction normal to the applied pressure drop driving the fluid flow. This induced component of the pressure gradient has to be balanced by normal stresses at the no-slip walls of the array, to prevent flow deviation along the lateral direction. Array anisotropy can induce a "ladder-like" background recirculatory flow pattern, that causes local deviations in the primary flow streamlines. For correct DLD operation, the average flow must remain at a fixed angle α to the obstacle array. Such anisotropic flow deviations lead to locally varying critical separation diameter d_c in the arrays, and are experimentally observed to cause unintended particle trajectories in the DLD.

We discover that the parallelogram array with cylindrical pillars possesses intrinsic anisotropy, while the rotated-square array (also with cylindrical pillars) shows no anisotropy. The anisotropy in the parallelogram array exhibits a non-linear non-monotonic dependence on the array inclination (α) to flow. When the parallelogram layout is used, the flow can deviate locally along the prevailing direction of the anisotropic pressure, causing locally varying d_c. In the rotated-square layout, the flow remains parallel to the device side walls throughout, and d_c remains constant and predictable. Therefore, for particle separation applications, the use of the rotated-square layout is recommended over the parallelogram layout.

The anisotropic pressure gradient is problematic only when it causes flow deviations. In anisotropic arrays, this deviation in the primary flow streamlines is seen to manifest when certain design features are present. It is found that these features, termed as "enablers", provide regions where the fluid flux can recompense for its deviations within anisotropic arrays. A common "enabler" feature is the gap between array sections, often seen in cascaded DLD arrays. Furthermore, multiple causes of excessive anisotropy are also identified. It is established that unequal flow-wise and lateral array gaps, larger gap to pillar diameter ratio and non-circular post cross sections can lead to

severe anisotropy, even with the rotated-square layout. The anisotropy cause by pillar shape cross section, such as that from 'right-triangle', can be several orders of magnitude higher than that due to the array layout, and such pillars should be used with caution. Additionally, a number of design guidelines are proposed in order to mitigate the effect of array anisotropy on particle trajectories in the DLD.

RBC DYNAMICS AND HYDRODYNAMIC 'LIFT': In the next study in chapter 9, the mechanisms that lead to the RBCs undergoing displacement mode at elevated array inclinations than expected is probed. I investigate the role of RBC dynamic motions, such as 'tumbling' and 'tank-treading', in trajectory mode selection. In this study, the DLD device depth H is designed to be greater than the RBC diameter $H > 2r_{RBC}$ to allow the RBCs freedom to undergo characteristic dynamic motions. The three special pillar shapes trialled are termed as 'U-groove', 'C-ridge' and 'Square', their design following from previous experimental work (Zeming, Ranjan and Zhang, 2013). The simulations comprise flowing RBCs in the dilute limit through DLD arrays with varying inclinations and varying their membrane deformability over two orders of magnitude. The cell migrations and their dynamical motions are recorded and analysed.

The findings show that full-3D tumbling dynamics of rigid RBCs are important for trajectory mode selection in the DLD. Such tumbling dynamics can lead to bumping at elevated row shifts and therefore greater lateral displacement. I observe such elevated bumping for the rigid RBC in the pillar with the groove, which corroborates the experimental observations of a similar nature. This also shows the inadequacy of 2D simulations for resolving the dynamics of anisotropic cells such as the RBCs in arrays with complex pillar shapes.

With increase in the RBC deformability, the trend seen for the critical array inclination in arrays with the C-ridge and Square pillar shape reverses. The most likely cause for this bifurcation-reversal is the cross streamline particle migration acting on the cell as it crosses the array gaps. I show that soft particle migration velocity can get orders of magnitude larger when the cell becomes highly deformable. In these cases there is no physical contact between the cell and the pillar and the cell bumping action is entirely through hydrodynamic interactions. From the trajectory mode-bifurcation maps, it can be suggested that arrays with the Square pillar shape would serve well for detecting cellular deformability changes.

Here, a new physical mechanism that aids lateral displacement of deformable cells under specific conditions is uncovered. The findings in this study also bring us closer to an understanding of the reasons for bumping at higher array inclinations observed with grooved pillar cross sections. The understanding gained in this study can be applied towards design of deformability sensitive DLD arrays for the RBCs and other anisotropic bio-particles.

DLD DISPLACEMENT MODE BREAKDOWN: The final study tackles RBC collective behaviour in the DLD. Here, the effect of the RBC haematocrit Ht on the performance of particle trajectory modes in DLD arrays is investigated. The device setup selected for this investigation has previously been probed by Krüger, Holmes and Coveney (2014) for deformability dependent separation of RBCs in the dilute limit. Here, the DLD device has a shallow depth ($H = 4.8\ \mu m < 2r_{RBC}$) that confines the RBCs to present their largest diameter flowing through the array gap. The simulations track multiple cells through the device till they cross 100 pillars in the flow-wise direction. At the end of the 100^{th} pillar, four imaginary outlets are defined to collect these cells. Based on the cell trajectories that were previously mapped in the dilute limit, these outlets are pre-designated as zigzag and displacement.

The simulations show that increasing the volume fraction causes deviations in the cell trajectories. Therefore, appropriate failure probabilities are defined for each trajectory mode, by taking reference cell trajectories in the dilute limit as the ideal 'successful' path. The mean and standard deviations of these failure probabilities are significant performance indicators for the DLD device. The analysis shows that, the mean failure probability in the displacement mode increases monotonically with rising haematocrit, and tends towards its limiting value at the highest simulated haematocrit of $Ht = 45.6\%$. Limiting failure in the displacement mode would mean that the cell trajectory would undergo zero lateral displacement and would be indistinguishable from the zigzag path. In contrast, the failure probability in the zigzag mode remains relatively low, even at $Ht = 45.6\%$.

This difference stems from the nature of failure in the two modes. In the displacement mode, high Ht induced failure is uni-directional and the penalty due to repeated failures adds up. On the other hand, in the zigzag mode the failures can occur in opposing directions and tend to cancel each other over the length of the device. This shows that the zigzag mode is robust and works as expected at high haematocrit, while the displacement mode is susceptible to breakdown.

Critically, this means that at higher Ht the RBCs designated for the displacement outlet increasingly end up in the displacement outlet, making separation difficult. The performance of the displacement mode deteriorated significantly even at moderate volume fractions of $Ht \approx 10\%$. The RBCs designated for the zigzag outlet however tend to be collected correctly, even at the highest tested haematocrit $Ht = 45.6\%$. This leads to the postulate that it would be very difficult to isolate a few smaller particles from a dense background of larger particles without significant dilution of the suspension (e. g. platelets from blood). It should however be relatively easy to separate out a few larger particles from a dense background of smaller particles (e. g. white blood cells from blood).

The DLD relies on deterministic cell-pillar interactions leading to a size-based trajectory bifurcation, and was designed using dilute suspensions. The underlying reason for the breakdown of the displacement mode at larger Ht lies in increased cell-cell interactions, which introduce non-deterministic ef-

fects in the operating principle of the DLD. Therefore, these results are not specific to the RBCs employed in this study, but to all types of dense particle suspensions. The study identifies an important limitation on the usage of the DLD arrays. The vital point for future DLD applications targeting dense particle suspensions is to minimise the failure probability for the displacement mode (e. g. by using novel pillar shapes).

12

FUTURE OUTLOOK

In this chapter I surmise my thoughts on the most fruitful future route for research and development on deterministic lateral displacement (DLD) technology. Most of these ideas have been shaped from my PhD research work in the last four years. Though the DLD has attained considerable maturity as a separation technique, a number of challenges still remain. This chapter could provide useful direction to a researcher in microfluidics, who potentially plan on working with DLD separation arrays. As mentioned in chapter 3, DLD has some notable advantages over other microfluidic separation methods, while remains lacking in others. Serious research is needed to plug fundamental gaps in understanding and bring the technology to the clinical/commercial stage.

An important research question that is yet to be resolved concerns the mismatch between experimentally observed bead trajectory modes and their theoretical predictions. As seen in chapter 3, currently the best theory for predicting the critical diameter in a DLD array relies on the assumption of parabolic flow and does not account for particle presence. Hence, most experimental device are built based on the empirical power law given in equation 3.2, which is derived from experiments on a limited set of devices. A possible approach to tackle this issue would be to consider the presence of a particle when predicting the critical separation diameter.

The research on anisotropic permeability has opened up possibilities for designing arrays that capitalise on anisotropy in the DLD. We know that anisotropic flow deviations lead to a decrease in the critical separation diameter d_c, and the locally contained unintended bumping of particles in the zigzag mode. This could be turned to an advantage, as a means to reduce the critical size d_c without changing array parameters. We know that the array gap size is constrained by the diameter of the largest particle that needs to flow through the DLD arrays. The challenge here is to ensure predictable d_c throughout the anisotropic arrays. An idea that could be explored would be to use anisotropic pillar shapes such as the right-triangle along with post rotation to ensure uniform operation.

Pillar shape engineering has emerged as highly promising in the recent years, especially for the separation of bio-particles. These pillars can modify the flow field to induce dynamic effects in the particles, such as the tumbling dynamics seen for the red blood cells (RBCs) in this thesis. Bio-particles are rarely rigid and spherical, and the effect of these variables has not been explored thoroughly. The research on pillar cross-sections, designed to utilise the anisotropic bio-particles shapes, could start off by having features that mate with the particle shape in order to ensure favourable orientations through the array gaps.

Pillar shape optimisation for exploiting the wall-induced hydrodynamic lift phenomenon, identified in this work, could be another avenue to explore. We know that this lift force is bidirectional, pushing the particle away from the pillar in the upstream section of the gap, while pulling it towards the pillar in the downstream gap section. Therefore, pillar shape designs that induce the repulsive force component over longer lengths could be explored.

The aim of such research should be to provide design tools and guidelines for DLD chip fabrication. Nevertheless, only addressing the fundamental questions about particle behaviour in DLD arrays would not be sufficient to bring it to the marketplace. The DLD user community has to work towards establishing experimental protocols for various applications demonstrated by the DLD. The most promising area for such protocols to be established is the area of bio-cellular analysis, cytometry and medical diagnostics. Also, fabrication protocols that deal with the materials, manufacture and operation of DLD chips specifically should be established.

Furthermore, as with any other microfluidic technique, DLD research has mostly been carried out in isolation. It is more likely than not that future microfluidic chips could carry components from different techniques. being a passive particle separator, DLD lends itself for easy coupling with other micro-particle or cell manipulation techniques (see the recent protocol for isolation of circlating tumor cells (Karabacak et al., 2014)), and efforts should focus on integration of the DLD with other techniques on a single microfluidic platform. The DLD has shown tremendous potential for high resolution size based particle separation, however due to the niche nature of its applications, my feeling is that its future lies in integration with other broader range microfluidic separation techniques.

BIBLIOGRAPHY

Abkarian, M., M. Faivre and A. Viallat (2007). 'Swinging of Red Blood Cells under Shear Flow'. In: *Physical Review Letters* 98.18, p. 188302.

Abkarian, M., C. Lartigue and A. Viallat (2002). 'Tank Treading and Unbinding of Deformable Vesicles in Shear Flow: Determination of the Lift Force'. In: *Physical Review Letters* 88.6, p. 068103.

Aidun, C. K. and J. R. Clausen (2010). 'Lattice-Boltzmann Method for Complex Flows'. In: *Annual Review of Fluid Mechanics* 42.1, pp. 439–472.

Antfolk, M. and T. Laurell (2017). 'Continuous flow microfluidic separation and processing of rare cells and bioparticles found in blood – A review'. In: *Analytica Chimica Acta* 965, pp. 9–35.

Arthurs, K. M., L. C. Moore, C. S. Peskin, E. B. Pitman and H. E. Layton (1998). 'Modeling Arteriolar Flow and Mass Transport Using the Immersed Boundary Method'. In: *Journal of Computational Physics* 147.2, pp. 402–440.

Au, S. H., J. Edd, A. E. Stoddard, K. H. K. Wong, F. Fachin, S. Maheswaran, D. A. Haber, S. L. Stott, R. Kapur and M. Toner (2017). 'Microfluidic Isolation of Circulating Tumor Cell Clusters by Size and Asymmetry'. In: *Scientific Reports* 7.1, p. 2433.

Bagchi, P. (2007). 'Mesoscale Simulation of Blood Flow in Small Vessels'. In: *Biophysical Journal* 92.6, pp. 1858–1877.

Balagaddé, F. K., L. You, C. L. Hansen, F. H. Arnold and S. R. Quake (2005). 'Long-Term Monitoring of Bacteria Undergoing Programmed Population Control in a Microchemostat'. In: *Science* 309.5731, pp. 137–140.

Batchelor, G. K. (2000). *An Introduction to Fluid Dynamics*. Cambridge: Cambridge University Press.

Beebe, D. J., G. A. Mensing and G. M. Walker (2002). 'Physics and Applications of Microfluidics in Biology'. In: *Annual Review of Biomedical Engineering* 4.1, pp. 261–286.

Beech, J. P., B. D. Ho, G. Garriss, V. Oliveira, B. Henriques-Normark and J. O. Tegenfeldt (2018). 'Separation of pathogenic bacteria by chain length'. In: *Analytica Chimica Acta* 1000, pp. 223–231.

Beech, J. P., S. H. Holm, K. Adolfsson and J. O. Tegenfeldt (2012). 'Sorting cells by size, shape and deformability'. In: *Lab on a Chip* 12.6, pp. 1048–1051.

Bester, J., A. Buys, B. Lipinski, D. B. Kell and E. Pretorius (2013). 'High ferritin levels have major effects on the morphology of erythrocytes in Alzheimer's disease'. In: *Frontiers in Aging Neuroscience* 5.

Bhatnagar, P. L., E. P. Gross and M. Krook (1954). 'A Model for Collision Processes in Gases. I. Small Amplitude Processes in Charged and Neutral One-Component Systems'. In: *Physical Review* 94.3, pp. 511–525.

Bitbol, M. (1986). 'Red blood cell orientation in orbit C = 0'. In: *Biophysical Journal* 49.5, pp. 1055–1068.

Boltzmann, L. (1964). *Lectures on gas theory*. In collab. with Stephen G Brush. Berkeley: University of California Press.

Callens, N., C. Minetti, G. Coupier, M.-A. Mader, F. Dubois, C. Misbah and T. Podgorski (2008). 'Hydrodynamic lift of vesicles under shear flow in microgravity'. In: *EPL (Europhysics Letters)* 83.2, p. 24002.

Campos-González, R., A. M. Skelley, K. Gandhi, D. W. Inglis, J. C. Sturm, C. I. Civin and T. Ward (2018). 'Deterministic Lateral Displacement: The Next-Generation CAR T-Cell Processing? , Deterministic Lateral Displacement: The Next-Generation CAR T-Cell Processing?' In: *SLAS TECHNOLOGY: Translating Life Sciences Innovation*, p. 2472630317751214.

Cantat, I. and C. Misbah (1999). 'Lift Force and Dynamical Unbinding of Adhering Vesicles under Shear Flow'. In: *Physical Review Letters* 83.4, pp. 880–883.

Carey, T. R., K. L. Cotner, B. Li and L. L. Sohn (2018). 'Developments in label-free microfluidic methods for single-cell analysis and sorting'. In: *Wiley Interdisciplinary Reviews: Nanomedicine and Nanobiotechnology* 0.0, e1529.

Chakraborty, S. and S. K. Mitra, eds. (2011). *Microfluidics and Nanofluidics Handbook: Chemistry, Physics, and Life Science Principles*. CRC Press.

Chapman, S. (1918). 'V. On the kinetic theory of a gas. Part II.—A composite monatomic gas: diffusion, viscosity, and thermal conduction'. In: *Phil. Trans. R. Soc. Lond. A* 217.549, pp. 115–197.

— (1952). *The mathematical theory of non-uniform gases: an account of the kinetic theory of viscosity, thermal conduction, and diffusion in gases.* In collab. with T. G Cowling. Second edition.. Cambridge: Cambridge University Press.

Chen, S. and G. D. Doolen (1998). 'Lattice Boltzmann Method for Fluid Flows'. In: *Annual Review of Fluid Mechanics* 30.1, pp. 329–364.

Chen, Y., J. D'Silva, R. H. Austin and J. C. Sturm (2015). 'Microfluidic chemical processing with on-chip washing by deterministic lateral displacement arrays with separator walls'. In: *Biomicrofluidics* 9.5, p. 054105.

Civin, C. I., T. Ward, A. M. Skelley, K. Gandhi, Z. Peilun Lee, C. R. Dosier, J. L. D'Silva, Y. Chen, M. Kim, J. Moynihan, X. Chen, L. Aurich, S. Gulnik, G. C. Brittain, D. J. Recktenwald, R. H. Austin and J. C. Sturm (2016). 'Automated leukocyte processing by microfluidic deterministic lateral displacement'. In: *Cytometry Part A* 89.12, pp. 1073–1083.

Coupier, G., B. Kaoui, T. Podgorski and C. Misbah (2008). 'Noninertial lateral migration of vesicles in bounded Poiseuille flow'. In: *Physics of Fluids* 20.11, p. 111702.

Danker, G., P. M. Vlahovska and C. Misbah (2009). 'Vesicles in Poiseuille Flow'. In: *Physical Review Letters* 102.14, p. 148102.

Davis, J. A., D. W. Inglis, K. J. Morton, D. A. Lawrence, L. R. Huang, S. Y. Chou, J. C. Sturm and R. H. Austin (2006). 'Deterministic hydrodynamics: Taking blood apart'. In: *Proceedings of the National Academy of Sciences* 103.40, pp. 14779–14784.

Davis, J. A. (2008). 'Microfluidic separation of blood components through deterministic lateral displacement'. PhD thesis. Princeton University.

Deuling, H. J. and W. Helfrich (1976). 'Red blood cell shapes as explained on the basis of curvature elasticity'. In: *Biophysical Journal* 16.8, pp. 861–868.

Dillon, R., L. Fauci, A. Fogelson and D. Gaver III (1996). 'Modeling Biofilm Processes Using the Immersed Boundary Method'. In: *Journal of Computational Physics* 129.1, pp. 57–73.

Dimitrakopoulos, P. (2012). 'Analysis of the variation in the determination of the shear modulus of the erythrocyte membrane: Effects of the constitutive law and membrane modeling'. In: *Physical Review E* 85.4, p. 041917.

Dincau, B. M., A. Aghilinejad, T. Hammersley, X. Chen and J.-H. Kim (2018). 'Deterministic lateral displacement (DLD) in the high Reynolds number regime: high-throughput and dynamic separation characteristics'. In: *Microfluidics and Nanofluidics* 22.6, p. 59.

Dincau, B., A. Aghilinejad, J.-H. Kim and X. Chen (2017). 'Characterizing the High Reynolds Number Regime for Deterministic Lateral Displacement (DLD) Devices'. In: V010T13A033.

Dixit, H. N. and V. Babu (2006). 'Simulation of high Rayleigh number natural convection in a square cavity using the lattice Boltzmann method'. In: *International Journal of Heat and Mass Transfer* 49.3, pp. 727–739.

Doddi, S. K. and P. Bagchi (2009). 'Three-dimensional computational modeling of multiple deformable cells flowing in microvessels'. In: *Physical Review E* 79.4, p. 046318.

Duke, T. A. J. and R. H. Austin (1998). 'Microfabricated Sieve for the Continuous Sorting of Macromolecules'. In: *Physical Review Letters* 80.7, pp. 1552–1555.

Dupin, M. M., I. Halliday, C. M. Care, L. Alboul and L. L. Munn (2007). 'Modeling the flow of dense suspensions of deformable particles in three dimensions'. In: *Physical Review E* 75.6, p. 066707.

Dupire, J., M. Socol and A. Viallat (2012). 'Full dynamics of a red blood cell in shear flow'. In: *Proceedings of the National Academy of Sciences* 109.51, pp. 20808–20813.

Eggleton, C. D. and A. S. Popel (1998). 'Large deformation of red blood cell ghosts in a simple shear flow'. In: *Physics of Fluids* 10.8, pp. 1834–1845.

Evans, E. A. (1983). 'Bending elastic modulus of red blood cell membrane derived from buckling instability in micropipet aspiration tests'. In: *Biophysical Journal* 43.1, pp. 27–30.

Evans, E. and Y.-C. Fung (1972). 'Improved measurements of the erythrocyte geometry'. In: *Microvascular Research* 4.4, pp. 335–347.

Fachin, F., P. Spuhler, J. M. Martel-Foley, J. F. Edd, T. A. Barber, J. Walsh, M. Karabacak, V. Pai, M. Yu, K. Smith, H. Hwang, J. Yang, S. Shah, R. Yarmush, L. V. Sequist, S. L. Stott, S. Maheswaran, D. A. Haber, R. Kapur and M. Toner (2017). 'Monolithic Chip for High-throughput Blood Cell Depletion to Sort Rare Circulating Tumor Cells'. In: *Scientific Reports* 7.1, p. 10936.

Fåhræus, R. and T. Lindqvist (1931). 'The viscosity of the blood in narrow capillary tubes'. In: *American Journal of Physiology-Legacy Content* 96.3, pp. 562–568.

Fedosov, D. A., M. Peltomäki and G. Gompper (2014). 'Deformation and dynamics of red blood cells in flow through cylindrical microchannels'. In: *Soft Matter* 10.24, pp. 4258–4267.

Feng, Z.-G. and E. E. Michaelides (2009). 'Robust treatment of no-slip boundary condition and velocity updating for the lattice-Boltzmann simulation of particulate flows'. In: *Computers & Fluids* 38.2, pp. 370–381.

Fischer, T. M., M. Stöhr-Lissen and H. Schmid-Schonbein (1978). 'The red cell as a fluid droplet: tank tread-like motion of the human erythrocyte membrane in shear flow'. In: *Science* 202.4370, pp. 894–896.

Fischer, T. M. (2004). 'Shape Memory of Human Red Blood Cells'. In: *Biophysical Journal* 86.5, pp. 3304–3313.

Fogelson, A. L. and C. S. Peskin (1988). 'A fast numerical method for solving the three-dimensional stokes' equations in the presence of suspended particles'. In: *Journal of Computational Physics* 79.1, pp. 50–69.

'Front cover' (2018). In: *Lab on a Chip* 18.11, pp. 1507–1507.

Geislinger, T. M., B. Eggart, S. Braunmüller, L. Schmid and T. Franke (2012). 'Separation of blood cells using hydrodynamic lift'. In: *Applied Physics Letters* 100.18, p. 183701.

Geislinger, T. M. and T. Franke (2013). 'Sorting of circulating tumor cells (MV3-melanoma) and red blood cells using non-inertial lift'. In: *Biomicrofluidics* 7.4, p. 044120.

— (2014). 'Hydrodynamic lift of vesicles and red blood cells in flow — from Fåhræus & Lindqvist to microfluidic cell sorting'. In: *Advances in Colloid and Interface Science*. Special issue in honour of Wolfgang Helfrich 208 (Supplement C), pp. 161–176.

Geuzaine, C. and J.-F. Remacle (2009). 'Gmsh: A 3-D finite element mesh generator with built-in pre- and post-processing facilities'. In: *International Journal for Numerical Methods in Engineering* 79.11, pp. 1309–1331.

Ghosh, A., S. Sinha, J. A. Dharmadhikari, S. Roy, A. K. Dharmadhikari, J. Samuel, S. Sharma and D. Mathur (2006). 'Euler buckling-induced folding and rotation of red blood cells in an optical trap'. In: *Physical Biology* 3.1, p. 67.

Ginzbourg, I. and D. d'Humières (1996). 'Local second-order boundary methods for lattice Boltzmann models'. In: *Journal of Statistical Physics* 84.5, pp. 927–971.

Goldsmith, H. L., J. Marlow and F. C. MacIntosh (1972). 'Flow behaviour of erythrocytes - I. Rotation and deformation in dilute suspensions'. In: *Proc. R. Soc. Lond. B* 182.1068, pp. 351–384.

Gompper, G. and D. Kroll (1996). 'Random Surface Discretizations and the Renormalization of the Bending Rigidity'. In: *Journal de Physique I* 6.10, pp. 1305–1320.

Gompper, G. and M. Schick, eds. (2008). *Soft matter, Volume 4: Lipid Bilayers and Red Blood Cells*. Vol. 4. 4 vols. OCLC: ocm63389869. Weinheim: Wiley-VCH. 254 pp.

GPB Scientific (2018). URL: http://www.gpbscientific.com/technology.php.html (visited on 21/07/2018).

Green, J. V., M. Radisic and S. K. Murthy (2009). 'Deterministic Lateral Displacement as a Means to Enrich Large Cells for Tissue Engineering'. In: *Analytical Chemistry* 81.21, pp. 9178–9182.

Gu, H., M. H. G. Duits and F. Mugele (2011). 'Droplets Formation and Merging in Two-Phase Flow Microfluidics'. In: *International Journal of Molecular Sciences* 12.4, pp. 2572–2597.

Guckenberger, A., A. Kihm, T. John, C. Wagner and S. Gekle (2018). 'Numerical–experimental observation of shape bistability of red blood cells flowing in a microchannel'. In: *Soft Matter* 14.11, pp. 2032–2043.

Guo, Z., C. Zheng and B. Shi (2002). 'Discrete lattice effects on the forcing term in the lattice Boltzmann method'. In: *Physical Review E* 65.4, p. 046308.

Hage, D. S. (1999). 'Affinity Chromatography: A Review of Clinical Applications'. In: *Clinical Chemistry* 45.5, pp. 593–615.

He, X., S. Chen and R. Zhang (1999). 'A Lattice Boltzmann Scheme for Incompressible Multiphase Flow and Its Application in Simulation of Rayleigh–Taylor Instability'. In: *Journal of Computational Physics* 152.2, pp. 642–663.

Helfrich, W. (1973). 'Elastic Properties of Lipid Bilayers: Theory and Possible Experiments'. In: *Zeitschrift für Naturforschung C* 28.11, pp. 693–703.

Heller, M. and H. Bruus (2008). 'A theoretical analysis of the resolution due to diffusion and size dispersion of particles in deterministic lateral displacement devices'. In: *Journal of Micromechanics and Microengineering* 18.7, p. 075030.

Hempelmann, E. (2009). *Major proteins in the erythrocyte (red blood cell) membrane.* In collab. with T. Vickers.

Henry, E. (2017). 'Cell Sorting in Deterministic Lateral Displacement Devices'. text.thesis.doctoral. Universität zu Köln.

Henry, E., S. H. Holm, Z. Zhang, J. P. Beech, J. O. Tegenfeldt, D. A. Fedosov and G. Gompper (2016). 'Sorting cells by their dynamical properties'. In: *Scientific Reports* 6, p. 34375.

Higgs, D. R., N. Roy and D. Hay (2015). 'Erythropoiesis'. In: *Postgraduate Haematology*. Wiley-Blackwell, pp. 11–20.

Holm, S. H., J. P. Beech, M. P. Barrett and J. O. Tegenfeldt (2016). 'Simplifying microfluidic separation devices towards field-detection of blood parasites'. In: *Analytical Methods* 8.16, pp. 3291–3300.

Holm, S. (2018). 'Microfluidic Cell and Particle Sorting using Deterministic Lateral Displacement'. PhD thesis. Department of Physics, Lund University.

Holm, S. H., J. P. Beech, M. P. Barrett and J. O. Tegenfeldt (2011). 'Separation of parasites from human blood using deterministic lateral displacement'. In: *Lab on a Chip* 11.7, pp. 1326–1332.

Holmes, D., G. Whyte, J. Bailey, N. Vergara-Irigaray, A. Ekpenyong, J. Guck and T. Duke (2014). 'Separation of blood cells with differing deformability using deterministic lateral displacement'. In: *Interface Focus* 4.6, p. 20140011.

Huang, L. R., E. C. Cox, R. H. Austin and J. C. Sturm (2004). 'Continuous Particle Separation Through Deterministic Lateral Displacement'. In: *Science* 304.5673, pp. 987–990.

Inglis, D. W. (2009). 'Efficient microfluidic particle separation arrays'. In: *Applied Physics Letters* 94.1, p. 013510.

Inglis, D. W., J. A. Davis, R. H. Austin and J. C. Sturm (2006). 'Critical particle size for fractionation by deterministic lateral displacement'. In: *Lab on a Chip* 6.5, pp. 655–658.

Inglis, D. W., J. A. Davis, T. J. Zieziulewicz, D. A. Lawrence, R. H. Austin and J. C. Sturm (2008). 'Determining blood cell size using microfluidic hydrodynamics'. In: *Journal of Immunological Methods* 329.1, pp. 151–156.

Inglis, D. W., N. Herman and G. Vesey (2010). 'Highly accurate deterministic lateral displacement device and its application to purification of fungal spores'. In: *Biomicrofluidics* 4.2, p. 024109.

Inglis, D. W., M. Lord and R. E. Nordon (2011). 'Scaling deterministic lateral displacement arrays for high throughput and dilution-free enrichment of leukocytes'. In: *Journal of Micromechanics and Microengineering* 21.5, p. 054024.

Inglis, D. W., K. J. Morton, J. A. Davis, T. J. Zieziulewicz, D. A. Lawrence, R. H. Austin and J. C. Sturm (2008). 'Microfluidic device for label-free measurement of platelet activation'. In: *Lab on a Chip* 8.6, pp. 925–931.

Jeans, J. (1940). *An introduction to the kinetic theory of gases*. Cambridge science classics. Cambridge [Cambridgeshire]: Cambridge University Press. 311 pp.

Jiang, X., K. H. K. Wong, A. H. Khankhel, M. Zeinali, E. Reategui, M. J. Phillips, X. Luo, N. Aceto, F. Fachin, A. N. Hoang, W. Kim, A. E. Jensen, L. V. Sequist, S. Maheswaran, D. A. Haber, S. L. Stott and M. Toner (2017). 'Microfluidic isolation of platelet-covered circulating tumor cells'. In: *Lab on a Chip* 17.20, pp. 3498–3503.

Jing, T., R. Ramji, M. E. Warkiani, J. Han, C. T. Lim and C.-H. Chen (2015). 'Jetting microfluidics with size-sorting capability for single-cell protease detection'. In: *Biosensors and Bioelectronics* 66, pp. 19–23.

Joensson, H. N., M. Uhlén and H. A. Svahn (2011). 'Droplet size based separation by deterministic lateral displacement—separating droplets by cell-induced shrinking'. In: *Lab on a Chip* 11.7, pp. 1305–1310.

Kabacaoglu, G. and G. Biros (2017). 'Sorting same-size red blood cells in deep deterministic lateral displacement devices'. In: *arXiv:1711.07616 [cond-mat, physics:physics]*. arXiv: 1711.07616.

— (2018). 'Optimal design of deterministic lateral displacement device for viscosity contrast based cell sorting'. In: *arXiv:1805.08849 [physics]*. arXiv: 1805.08849.

Kantor, Y. and D. R. Nelson (1987). 'Crumpling transition in polymerized membranes'. In: *Physical Review Letters* 58.26, pp. 2774–2777.

Kantsler, V. and V. Steinberg (2006). 'Transition to Tumbling and Two Regimes of Tumbling Motion of a Vesicle in Shear Flow'. In: *Physical Review Letters* 96.3, p. 036001.

Kaoui, B., G. H. Ristow, I. Cantat, C. Misbah and W. Zimmermann (2008). 'Lateral migration of a two-dimensional vesicle in unbounded Poiseuille flow'. In: *Physical Review E* 77.2, p. 021903.

Kaoui, B., G. Biros and C. Misbah (2009). 'Why Do Red Blood Cells Have Asymmetric Shapes Even in a Symmetric Flow?' In: *Physical Review Letters* 103.18, p. 188101.

Karabacak, N. M., P. S. Spuhler, F. Fachin, E. J. Lim, V. Pai, E. Ozkumur, J. M. Martel, N. Kojic, K. Smith, P.-i. Chen, J. Yang, H. Hwang, B. Morgan, J. Trautwein, T. A. Barber, S. L. Stott, S. Maheswaran, R. Kapur, D. A. Haber and M. Toner (2014). 'Microfluidic, marker-free isolation of circulating tumor cells from blood samples'. In: *Nature Protocols* 9.3, pp. 694–710.

Keller, S. R. and R. Skalak (1982). 'Motion of a tank-treading ellipsoidal particle in a shear flow'. In: *Journal of Fluid Mechanics* 120, pp. 27–47.

Kim, S.-C., B. H. Wunsch, H. Hu, J. T. Smith, R. H. Austin and G. Stolovitzky (2017). 'Broken flow symmetry explains the dynamics of small particles in deterministic lateral displacement arrays'. In: *Proceedings of the National Academy of Sciences* 114.26, E5034–E5041.

Kim, Y., S. Lim, S. V. Raman, O. P. Simonetti and A. Friedman (2009). 'Blood Flow in a Compliant Vessel by the Immersed Boundary Method'. In: *Annals of Biomedical Engineering* 37.5, pp. 927–942.

Kim, Y., K. Kim and Y. Park (2012). 'Measurement Techniques for Red Blood Cell Deformability: Recent Advances'. In: *Blood Cell - An Overview of Studies in Hematology*. Ed. by T. Moschandreou. InTech.

Kraus, M., W. Wintz, U. Seifert and R. Lipowsky (1996). 'Fluid Vesicles in Shear Flow'. In: *Physical Review Letters* 77.17, pp. 3685–3688.

Krüger, T. (2012). *Computer Simulation Study of Collective Phenomena in Dense Suspensions of Red Blood Cells under Shear*. Wiesbaden: Vieweg+Teubner Verlag.

Krüger, T., M. Gross, D. Raabe and F. Varnik (2013). 'Crossover from tumbling to tank-treading-like motion in dense simulated suspensions of red blood cells'. In: *Soft Matter* 9.37, pp. 9008–9015.

Krüger, T., D. Holmes and P. V. Coveney (2014). 'Deformability-based red blood cell separation in deterministic lateral displacement devices—A simulation study'. In: *Biomicrofluidics* 8.5, p. 054114.

Krüger, T., H. Kusumaatmaja, A. Kuzmin, O. Shardt, G. Silva and E. M. Viggen (2017). *The Lattice Boltzmann Method: Principles and Practice*. Graduate Texts in Physics. Springer International Publishing.

Krüger, T., F. Varnik and D. Raabe (2011). 'Efficient and accurate simulations of deformable particles immersed in a fluid using a combined immersed boundary lattice Boltzmann finite element method'. In: *Computers & Mathematics with Applications*. Mesoscopic Methods for Engineering and Science — Proceedings of ICMMES-09 61.12, pp. 3485–3505.

Kulrattanarak, T., R. G. M. van der Sman, Y. S. Lubbersen, C. G. P. H. Schroën, H. T. M. Pham, P. M. Sarro and R. M. Boom (2011). 'Mixed motion in deterministic ratchets due to anisotropic permeability'. In: *Journal of Colloid and Interface Science* 354.1, pp. 7–14.

Kulrattanarak, T., R. G. M. van der Sman, C. G. P. H. Schroën and R. M. Boom (2010). 'Analysis of mixed motion in deterministic ratchets via experiment and particle simulation'. In: *Microfluidics and Nanofluidics* 10.4, pp. 843–853.

Leal, L. G. (2007). *Advanced Transport Phenomena: Fluid Mechanics and Convective Transport Processes*. Cambridge: Cambridge University Press.

Lim, H. W. G., M. Wortis and R. Mukhopadhyay (2002). 'Stomatocyte–discocyte–echinocyte sequence of the human red blood cell: Evidence for the bilayer– couple hypothesis from membrane mechanics'. In: *Proceedings of the National Academy of Sciences* 99.26, pp. 16766–16769.

Liu, C. and G. Hu (2017). 'High-Throughput Particle Manipulation Based on Hydrodynamic Effects in Microchannels'. In: *Micromachines* 8.3, p. 73.

Liu, Z., W. Zhang, F. Huang, H. Feng, W. Shu, X. Xu and Y. Chen (2013). 'High throughput capture of circulating tumor cells using an integrated microfluidic system'. In: *Biosensors and Bioelectronics* 47, pp. 113–119.

Long, B. R., M. Heller, J. P. Beech, H. Linke, H. Bruus and J. O. Tegenfeldt (2008). 'Multidirectional sorting modes in deterministic lateral displacement devices'. In: *Physical Review E* 78.4, p. 046304.

Loutherback, K., K. S. Chou, J. Newman, J. Puchalla, R. H. Austin and J. C. Sturm (2010). 'Improved performance of deterministic lateral displacement arrays with triangular posts'. In: *Microfluidics and Nanofluidics* 9.6, pp. 1143–1149.

Loutherback, K., J. D'Silva, L. Liu, A. Wu, R. H. Austin and J. C. Sturm (2012). 'Deterministic separation of cancer cells from blood at 10 mL/min'. In: *AIP Advances* 2.4, p. 042107.

Loutherback, K., J. Puchalla, R. H. Austin and J. C. Sturm (2009). 'Deterministic Microfluidic Ratchet'. In: *Physical Review Letters* 102.4, p. 045301.

Lubbersen, Y. S., R. M. Boom and M. A. I. Schutyser (2014). 'High throughput particle separation with a mirrored deterministic ratchet design'. In: *Chemical Engineering and Processing: Process Intensification* 77, pp. 42–49.

Lubbersen, Y. S., J. P. Dijkshoorn, M. A. I. Schutyser and R. M. Boom (2013). 'Visualization of inertial flow in deterministic ratchets'. In: *Separation and Purification Technology* 109, pp. 33–39.

Lubbersen, Y. S., M. A. I. Schutyser and R. M. Boom (2012). 'Suspension separation with deterministic ratchets at moderate Reynolds numbers'. In: *Chemical Engineering Science* 73, pp. 314–320.

Makler, M. T., C. J. Palmer and A. L. Ager (1998). 'A review of practical techniques for the diagnosis of malaria'. In: *Annals of Tropical Medicine and Parasitology* 92.4, pp. 419–433.

Martys, N. S. and H. Chen (1996). 'Simulation of multicomponent fluids in complex three-dimensional geometries by the lattice Boltzmann method'. In: *Physical Review E* 53.1, pp. 743–750.

Maxwell, J. C. (1867). 'IV. On the dynamical theory of gases'. In: *Philosophical Transactions of the Royal Society of London* 157, pp. 49–88.

McDonald, J. C., D. C. Duffy, J. R. Anderson, D. T. Chiu, H. Wu, O. J. A. Schueller and G. M. Whitesides (2000). 'Fabrication of microfluidic systems in poly(dimethylsiloxane)'. In: *ELECTROPHORESIS* 21.1, pp. 27–40.

McGrath, J., M. Jimenez and H. Bridle (2014). 'Deterministic lateral displacement for particle separation: a review'. In: *Lab on a Chip* 14.21, pp. 4139–4158.

McNamara, G. R. and G. Zanetti (1988). 'Use of the Boltzmann Equation to Simulate Lattice-Gas Automata'. In: *Physical Review Letters* 61.20, pp. 2332–2335.

McWhirter, J. L., H. Noguchi and G. Gompper (2009). 'Flow-induced clustering and alignment of vesicles and red blood cells in microcapillaries'. In: *Proceedings of the National Academy of Sciences* 106.15, pp. 6039–6043.

Mendoza, M., B. M. Boghosian, H. J. Herrmann and S. Succi (2010). 'Fast Lattice Boltzmann Solver for Relativistic Hydrodynamics'. In: *Physical Review Letters* 105.1, p. 014502.

Meßlinger, S., B. Schmidt, H. Noguchi and G. Gompper (2009). 'Dynamical regimes and hydrodynamic lift of viscous vesicles under shear'. In: *Physical Review E* 80.1, p. 011901.

Mittal, R. and G. Iaccarino (2005). 'Immersed Boundary Methods'. In: *Annual Review of Fluid Mechanics* 37.1, pp. 239–261.

Morton, K. J., K. Loutherback, D. W. Inglis, O. K. Tsui, J. C. Sturm, S. Y. Chou and R. H. Austin (2008). 'Crossing microfluidic streamlines to lyse, label and wash cells'. In: *Lab on a Chip* 8.9, pp. 1448–1453.

Moschou, D. and A. Tserepi (2017). 'The lab-on-PCB approach: tackling the μTAS commercial upscaling bottleneck'. In: *Lab on a Chip* 17.8, pp. 1388–1405.

Mountrakis, L., E. Lorenz and A. G. Hoekstra (2017). 'Revisiting the use of the immersed-boundary lattice-Boltzmann method for simulations of suspended particles'. In: *Physical Review E* 96.1, p. 013302.

Narla, M. (2015). 'Structure and Composition of the Erythrocyte'. In: *Williams Hematology*. Ed. by K. Kaushansky, M. A. Lichtman, J. T. Prchal, M. M. Levi, O. W. Press, L. J. Burns and M. Caligiuri. 9th ed. New York, NY: McGraw-Hill Education.

Navot, Y. (1998). 'Elastic membranes in viscous shear flow'. In: *Physics of Fluids* 10.8, pp. 1819–1833.

Noguchi, H. and G. Gompper (2005). 'Shape transitions of fluid vesicles and red blood cells in capillary flows'. In: *Proceedings of the National Academy of Sciences* 102.40, pp. 14159–14164.

Oliveira, A. R. M. d. and D. Szczerbowski (2009). 'Quinine: 470 years of history, controversy and science development'. In: *Química Nova* 32.7, pp. 1971–1974.

Olla, P. (1997). 'The Lift on a Tank-Treading Ellipsoidal Cell in a Shear Flow'. In: *Journal de Physique II* 7.10, pp. 1533–1540.

— (2000). 'The behavior of closed inextensible membranes in linear and quadratic shear flows'. In: *Physica A: Statistical Mechanics and its Applications* 278.1, pp. 87–106.

Ouared, R. and B. Chopard (2005). 'Lattice Boltzmann Simulations of Blood Flow: Non-Newtonian Rheology and Clotting Processes'. In: *Journal of Statistical Physics* 121.1, pp. 209–221.

Pamme, N. (2006). 'Magnetism and microfluidics'. In: *Lab on a Chip* 6.1, pp. 24–38.

Patankar, S., S. Sharma, P. K. Rathod and M. T. Duraisingh (2018). 'Malaria in India: The Need for New Targets for Diagnosis and Detection of Plasmodium vivax'. In: *PROTEOMICS – Clinical Applications* 12.4, p. 1700024.

Peskin, C. S. (1972). 'Flow patterns around heart valves: A numerical method'. In: *Journal of Computational Physics* 10.2, pp. 252–271.

— (1973). 'Flow patterns around heart valves: a digital computer method for solving the equations of motion'. In: *IEEE Transactions on Biomedical Engineering* BME-20.4, pp. 316–317.

— (1977). 'Numerical analysis of blood flow in the heart'. In: *Journal of Computational Physics* 25.3, pp. 220–252.

Peskin, C. S. (2002). 'The immersed boundary method'. In: *Acta Numerica* 11, pp. 479–517.

Pozrikidis, C. (2001). 'Effect of membrane bending stiffness on the deformation of capsules in simple shear flow'. In: *Journal of Fluid Mechanics* 440, pp. 269–291.

— (2003). 'Numerical Simulation of the Flow-Induced Deformation of Red Blood Cells'. In: *Annals of Biomedical Engineering* 31.10, pp. 1194–1205.

Quek, R., D. V. Le and K.-H. Chiam (2011). 'Separation of deformable particles in deterministic lateral displacement devices'. In: *Physical Review E* 83.5, p. 056301.

Ramanujan, S. and C. Pozrikidis (1998). 'Deformation of liquid capsules enclosed by elastic membranes in simple shear flow: large deformations and the effect of fluid viscosities'. In: *Journal of Fluid Mechanics* 361, pp. 117–143.

Ranjan, S., K. K. Zeming, R. Jureen, D. Fisher and Y. Zhang (2014). 'DLD pillar shape design for efficient separation of spherical and non-spherical bioparticles'. In: *Lab on a Chip* 14.21, pp. 4250–4262.

Rice, P. A., D. J. Fontugne, R. G. Latini and A. J. Barduhn (1970). 'Anisotropic permeability in porous media'. In: *Industrial & Engineering Chemistry* 62.6, pp. 23–31.

Ryan, D. H. (2015). 'Examination of Blood Cells'. In: *Williams Hematology*. Ed. by K. Kaushansky, M. A. Lichtman, J. T. Prchal, M. M. Levi, O. W. Press, L. J. Burns and M. Caligiuri. 9th ed. New York, NY: McGraw-Hill Education.

Sadd, M. H. (2014). *Elasticity: theory, applications, and numerics*. Third edition. Amsterdam ; Boston: Elsevier/AP, Academic Press is an imprint of Elsevier. 582 pp.

Salafi, T., K. Kwek Zeming and Y. Zhang (2017). 'Advancements in microfluidics for nanoparticle separation'. In: *Lab on a Chip* 17.1, pp. 11–33.

Santana, S. M., M. A. Antonyak, R. A. Cerione and B. J. Kirby (2014). 'Microfluidic isolation of cancer-cell-derived microvesicles from hetergeneous extracellular shed vesicle populations'. In: *Biomedical Microdevices* 16.6, pp. 869–877.

Seifert, U. (1997). 'Configurations of fluid membranes and vesicles'. In: *Advances in Physics* 46.1, pp. 13–137.

— (1999). 'Hydrodynamic Lift on Bound Vesicles'. In: *Physical Review Letters* 83.4, pp. 876–879.

Shan, X. and H. Chen (1993). 'Lattice Boltzmann model for simulating flows with multiple phases and components'. In: *Physical Review E* 47.3, pp. 1815–1819.

Shan, X., X.-F. Yuan and H. Chen (2006). 'Kinetic theory representation of hydrodynamics: a way beyond the Navier–Stokes equation'. In: *Journal of Fluid Mechanics* 550, pp. 413–441.

Skalak, R., A. Tozeren, R. P. Zarda and S. Chien (1973). 'Strain Energy Function of Red Blood Cell Membranes'. In: *Biophysical Journal* 13.3, pp. 245–264.

Skalak, R., N. Ozkaya and T. C. Skalak (1989). 'Biofluid Mechanics'. In: *Annual Review of Fluid Mechanics* 21.1, pp. 167–200.

Skotheim, J. M. and T. W. Secomb (2007). 'Red Blood Cells and Other Nonspherical Capsules in Shear Flow: Oscillatory Dynamics and the Tank-Treading-to-Tumbling Transition'. In: *Physical Review Letters* 98.7, p. 078301.

Sotiropoulos, F. and X. Yang (2014). 'Immersed boundary methods for simulating fluid–structure interaction'. In: *Progress in Aerospace Sciences* 65, pp. 1–21.

Spaid, M. A. A. and F. R. Phelan (1997). 'Lattice Boltzmann methods for modeling microscale flow in fibrous porous media'. In: *Physics of Fluids* 9.9, pp. 2468–2474.

Squires, T. M. and S. R. Quake (2005). 'Microfluidics: Fluid physics at the nanoliter scale'. In: *Reviews of Modern Physics* 77.3, pp. 977–1026.

Stone, H., A. Stroock and A. Ajdari (2004). 'Engineering Flows in Small Devices: Microfluidics Toward a Lab-on-a-Chip'. In: *Annual Review of Fluid Mechanics* 36.1, pp. 381–411.

Sturm, J. C., E. C. Cox, B. Comella and R. H. Austin (2014). 'Ratchets in hydrodynamic flow: more than waterwheels'. In: *Interface Focus* 4.6, p. 20140054.

Sturm, J. (2007). *Hypothesis on flow anisotropy in DLD arrays*. In collab. with D. W. Inglis. E-mail.

Temam, R. and A. Miranville (2005). *Mathematical Modeling in Continuum Mechanics*. 2nd ed. Cambridge: Cambridge University Press.

Tomaiuolo, G. (2014). 'Biomechanical properties of red blood cells in health and disease towards microfluidics'. In: *Biomicrofluidics* 8.5, p. 051501.

Tottori, N. and T. Nisisako (2018). 'High-throughput production of satellite-free droplets through a parallelized microfluidic deterministic lateral displacement device'. In: *Sensors and Actuators B: Chemical* 260, pp. 918–926.

Vernekar, R. and T. Krüger (2015). 'Breakdown of deterministic lateral displacement efficiency for non-dilute suspensions: A numerical study'. In: *Medical Engineering & Physics* 37.9, pp. 845–854.

Vernekar, R. R. and S. C. Mishra (2014). 'Analysis of transport of short-pulse radiation in a participating medium using lattice Boltzmann method'. In: *International Journal of Heat and Mass Transfer* 77, pp. 218–229.

Vernekar, R., T. Krüger, K. Loutherback, K. Morton and D. W. Inglis (2017). 'Anisotropic permeability in deterministic lateral displacement arrays'. In: *Lab on a Chip* 17.19, pp. 3318–3330.

Viallat, A. and M. Abkarian (2014). 'Red blood cell: from its mechanics to its motion in shear flow'. In: *International Journal of Laboratory Hematology* 36.3, pp. 237–243.

Viggen, E. M. (2014). 'The lattice Boltzmann method: Fundamentals and acoustics'. PhD thesis. Norges teknisk-naturvitenskapelige universitet, Fakultet for informasjonsteknologi, matematikk og elektroteknikk, Institutt for elektronikk og telekommunikasjon.

Vlahovska, P. M., T. Podgorski and C. Misbah (2009). 'Vesicles and red blood cells in flow: From individual dynamics to rheology'. In: *Comptes Rendus Physique*. Complex and biofluids 10.8, pp. 775–789.

Wang, J., M. Wang and Z. Li (2007). 'A lattice Boltzmann algorithm for fluid–solid conjugate heat transfer'. In: *International Journal of Thermal Sciences* 46.3, pp. 228–234.

Whitesides, G. M. (2006). 'The origins and the future of microfluidics'. In: *Nature* 442.7101, pp. 368–373.

Wolf-Gladrow, D. A. (2000). *Lattice-Gas Cellular Automata and Lattice Boltzmann Models: An Introduction*. Lecture Notes in Mathematics. Springer, Berlin, Heidelberg.

World Health Organization (2017a). *World malaria report 2016: summary*.

— (2017b). *World malaria report 2017*. Global Malaria Programme. OCLC: 1028745520.

Wunsch, B. H., J. T. Smith, S. M. Gifford, C. Wang, M. Brink, R. L. Bruce, R. H. Austin, G. Stolovitzky and Y. Astier (2016). 'Nanoscale lateral displacement arrays for the separation of exosomes and colloids down to 20 nm'. In: *Nature Nanotechnology* 11.11, pp. 936–940.

Wyatt Shields IV, C., K. A. Ohiri, L. M. Szott and G. P. López (2017). 'Translating microfluidics: Cell separation technologies and their barriers to commercialization'. In: *Cytometry Part B: Clinical Cytometry* 92.2, pp. 115–125.

Wyatt Shields IV, C., C. D. Reyes and G. P. López (2015). 'Microfluidic cell sorting: a review of the advances in the separation of cells from debulking to rare cell isolation'. In: *Lab Chip* 15.5, pp. 1230–1249.

Yager, P., T. Edwards, E. Fu, K. Helton, K. Nelson, M. R. Tam and B. H. Weigl (2006). 'Microfluidic diagnostic technologies for global public health'. In: *Nature* 442.7101, pp. 412–418.

Yan, S., J. Zhang, D. Yuan and W. Li (2016). 'Hybrid microfluidics combined with active and passive approaches for continuous cell separation'. In: *ELECTROPHORESIS* 38.2, pp. 238–249.

Yawata, Y. (2003). *Cell membrane: the red blood cell as a model*. OCLC: ocm51862936. Weinheim: Wiley-VCH. 439 pp.

Ye, S., X. Shao, Z. Yu and W. Yu (2014). 'Effects of the particle deformability on the critical separation diameter in the deterministic lateral displacement device'. In: *Journal of Fluid Mechanics* 743, pp. 60–74.

Yu, H., S. S. Girimaji and L.-S. Luo (2005). 'DNS and LES of decaying isotropic turbulence with and without frame rotation using lattice Boltzmann method'. In: *Journal of Computational Physics* 209.2, pp. 599–616.

Zeming, K. K., S. Ranjan and Y. Zhang (2013). 'Rotational separation of non-spherical bioparticles using I-shaped pillar arrays in a microfluidic device'. In: *Nature Communications* 4, p. 1625.

Zeming, K. K., T. Salafi, C.-H. Chen and Y. Zhang (2016). 'Asymmetrical Deterministic Lateral Displacement Gaps for Dual Functions of Enhanced Separation and Throughput of Red Blood Cells'. In: *Scientific Reports* 6, p. 22934.

Zhang, B., J. V. Green, S. K. Murthy and M. Radisic (2012). 'Label-Free Enrichment of Functional Cardiomyocytes Using Microfluidic Deterministic Lateral Flow Displacement'. In: *PLOS ONE* 7.5, e37619.

Zhang, J. (2011). 'Lattice Boltzmann method for microfluidics: models and applications'. In: *Microfluidics and Nanofluidics* 10.1, pp. 1–28.

Zhang, J., P. C. Johnson and A. S. Popel (2007). 'An immersed boundary lattice Boltzmann approach to simulate deformable liquid capsules and its application to microscopic blood flows'. In: *Physical Biology* 4.4, p. 285.

Zhang, Z., E. Henry, G. Gompper and D. A. Fedosov (2015). 'Behavior of rigid and deformable particles in deterministic lateral displacement devices with different post shapes'. In: *The Journal of Chemical Physics* 143.24, p. 243145.

Zheng, S., R. Yung, Y.-C. Tai and H. Kasdan (2005). 'Deterministic lateral displacement MEMS device for continuous blood cell separation'. In: *18th IEEE International Conference on Micro Electro Mechanical Systems, 2005. MEMS 2005*. 18th IEEE International Conference on Micro Electro Mechanical Systems, 2005. MEMS 2005, pp. 851–854.

Zhu, L. and C. S. Peskin (2002). 'Simulation of a Flapping Flexible Filament in a Flowing Soap Film by the Immersed Boundary Method'. In: *Journal of Computational Physics* 179.2, pp. 452–468.

COLOPHON

This document was typeset using the typographical look-and-feel `classicthesis` developed by André Miede. The style was inspired by Robert Bringhurst's seminal book on typography *"The Elements of Typographic Style"*. `classicthesis` is available for both LaTeX and LyX:

https://miede.de/

Final Version as of 27th May 2019 (`classicthesis` version 4.1).